

## 博士論文

論文題目 Indentation Response and Damage Monitoring of  
Foam-Core Sandwich Structures  
(フォームコアサンドイッチ構造の押し込み挙動  
と損傷モニタリング)

氏 名 シーヴォラ ユホ タパニ  
Siivola Juho Tapani

# **Indentation Response and Damage Monitoring of Foam-Core Sandwich Structures**

フォームコアサンドイッチ構造の押し込み挙動  
と損傷モニタリング

Juho Tapani Siivola  
Department of Advanced Energy  
The University of Tokyo

A thesis submitted for the degree of  
*Doctor of Science*

December 11th, 2013



---

## Contents

<b>Chapter 1. Introduction</b>	<b>1</b>
1.1. Foam core sandwich structures .....	1
1.2. Indentation and damage detection of sandwich structures .....	2
1.3. Objective and methods .....	4
1.4. Outline of thesis .....	5
<b>Chapter 2. Loading response of PMI foam</b>	<b>6</b>
2.1. Rigid closed cell foams .....	6
2.1.1. Deformation of foam under loading .....	7
2.1.2. Environmental effects .....	9
2.2. Experimental setup .....	10
2.2.1. Foam specimens .....	10
2.2.2. Conditioning .....	12
2.2.3. Test method .....	12
2.3. Moisture diffusion in PMI foam .....	14
2.4. Effect of loading rate .....	16
2.5. Test results .....	18
2.5.1. Compressive loading .....	18
2.5.2. Tension after compression .....	21
2.5.3. Microscopic observation .....	23
2.6. Foam properties .....	24
2.6.1. Defining foam properties .....	25
2.6.2. Foam properties .....	26
2.7. Conclusion .....	31
<b>Chapter 3. Indentation response of sandwich structures</b>	<b>32</b>
3.1. Indentation response of sandwich structures .....	32
3.1.1. Effect of environmental conditions .....	33
3.2. Experimental setup .....	34
3.2.1. Sandwich beam specimens .....	34
3.2.2. Conditioning .....	34
3.2.3. Test method .....	35
3.3. Moisture diffusion into sandwich beam specimens .....	36
3.4. Effect of hygrothermal conditions on face sheet and adhesive .....	37
3.5. Results .....	37
3.5.1. Indentation load-displacement response .....	37
3.5.2. Face sheet dent .....	45
3.6. Conclusion .....	47

---

<b>Chapter 4. Finite element indentation analysis</b>	<b>48</b>
4.1. Modeling indentation of sandwich structures .....	48
4.2. Modeling of foam core .....	49
4.3. Finite element analysis model.....	51
4.3.1. Materials .....	52
4.4. Results .....	55
4.4.1. Indentation load – displacement response .....	55
4.4.2. Face sheet dent .....	58
4.4.3. Strains in core-face sheet interface.....	60
4.4.4. Damage in core .....	61
4.5. Discussion on mesh and model parameters .....	63
4.6. Degraded properties of face sheet and adhesive layer.....	66
4.7. Conclusion .....	68
<b>Chapter 5. Improved model for indentation analysis</b>	<b>69</b>
5.1. Limitations of crushable foam material model .....	69
5.2. New improved model .....	70
5.2.1. Constitutive model .....	70
5.2.2. Integration in subroutine.....	72
5.2.3. Differentiating parts of loading cycle .....	75
5.2.4. Degradation of elastic modulus.....	75
5.2.5. Behavior during tensile loading .....	76
5.2.6. Outline of subroutine .....	76
5.3. Defining model parameters.....	78
5.3.1. Unloading.....	78
5.3.2. Tensile loading .....	79
5.4. Material model validation.....	82
5.5. Indentation simulation .....	85
5.5.1. Results .....	86
5.6. Conclusion .....	90
<b>Chapter 6. Monitoring of foam core sandwich structures</b>	<b>91</b>
6.1. Indentation / low velocity impact damage monitoring .....	91
6.2. Distributed strain measurement.....	92
6.3. Application into foam core sandwich structures .....	92
6.4. Monitoring system (LUNA OBR).....	94
6.4.1. Monitoring principle of fiber optic interferometry.....	94
6.4.2. Strain measurement .....	95
6.4.3. Measurement resolution.....	96
6.4.4. Determination of strain coefficient for strain measurements .....	97
6.4.5. Error distribution of monitoring system .....	97
6.5. Sandwich beam indentation monitoring experiments .....	100
6.5.1. Sandwich beam specimens.....	101
6.5.2. Test method .....	101

---

---

6.5.3. Strain measurement during indentation .....	102
6.5.4. Formation of residual strains .....	104
6.5.5. Effect of relaxation on strain distribution.....	105
6.5.6. Fiber damage during monitoring .....	106
6.5.7. Hygrothermal strains during manufacturing and conditioning.....	108
6.5.8. Results – Indentation loading tests .....	109
6.5.9. Comparison with numerical analysis results .....	113
6.6. Sandwich panel indentation monitoring experiment .....	118
6.6.1. Sandwich panel specimen .....	118
6.6.2. Test method .....	118
6.6.3. Finite element analysis model .....	120
6.6.4. Results.....	120
6.7. Damage detection demonstrator sandwich panel .....	129
6.7.1. Sandwich panel.....	129
6.7.2. Test method .....	130
6.7.3. Results – Taper region.....	133
6.7.4. Results – Mid region.....	137
6.8. Conclusion .....	140
<b>Chapter 7. Conclusion</b> .....	<b>141</b>
7.1. Future works .....	142
<b>References</b> .....	<b>144</b>
<b>Appendix A. Empirical model for foam parameters</b> .....	<b>149</b>
<b>Appendix B. Humidity and density of the foam</b> .....	<b>152</b>
<b>Appendix C. Impact test strain distribution data</b> .....	<b>155</b>
<b>Acknowledgements</b> .....	<b>162</b>



## Chapter 1. Introduction

### 1.1. Foam core sandwich structures

Composite foam core sandwich structures consist of foam core and composite face sheets that are relatively thin compared to the core, often made of fiber reinforced plastics as shown in Figure 1.1. The core is light weight and weak, while the faces are stiff and strong. The faces can be connected to the core by adhesive or by the resin of the face sheets. As the core separates the faces the structure can be thought to be analogous with an I-beam, where the core works as the web and the faces as the flanges. This way the core carries shear in the structure and supports the faces against wrinkling and buckling, while the faces carry the bending moments and in-plane loads [1].

Compared to solid composite laminates, composite sandwich structures offer stiffness and especially improved bending strength and stiffness properties while retaining the same low weight. Also under in-plane loading as the core supports the faces, buckling strength of the structure is improved. Therefore no stiffeners need to be added to the structure afterwards, thus leading to lower part count and simpler structure. Depending on the core material, sandwich structure can also provide thermal or acoustic insulation. Compared to honeycomb core materials, foams are easy to machine and due to their solid like structure and isotropic response, complicated shapes are also possible. Resin transfer molding

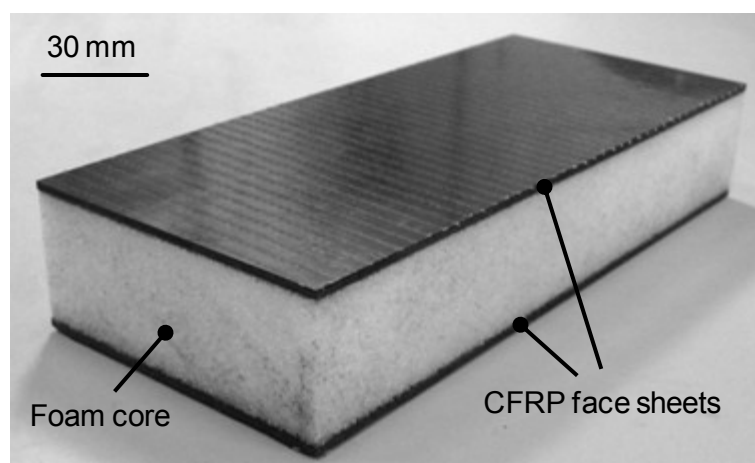


Figure 1.1 Foam core sandwich panel with CFRP face sheets.

methods besides typical adhesion or prepreg co-cure methods are also possible with closed cell foams and the sandwich structures can thus be manufactured with single curing process.

Due to their attractive properties, sandwich structures have been widely used in automobile, train, boat, aerospace, airplane, civil engineering, and wind energy applications. Lately increasing interest has been shown in using foam core sandwiches in the primary structures of aircraft structures [2, 3, 4, 5] which requires that improved performance and damage tolerance requirements are met. Many researchers have therefore studied the damage mechanisms in sandwich structures and ways to verify the integrity of the structures.

## 1.2. Indentation and damage detection of sandwich structures

Due to the thin faces and relatively weak core, sandwich structures are however rather weak against transverse loading. While high velocity and energy impacts can leave notable damage in the core and faces, and also lead to perforation of the structure, they are easy to detect as notable damage is left visible from outside. In airplane applications, for example, tool drop, hail, or contact with ground vehicles can cause indentation loadings or low-velocity impacts on the sandwich structures. These localized indentation loadings or low-velocity impacts can leave only barely visible damage on the outside, while the core and core-face sheet interface can be notably damaged, as shown in Figure 1.2. Even though the damage is barely visible, it can still significantly reduce the compressive strength of the sandwich structure [6].

The residual dent depth after impact or indentation has been used as a measure of severity of the damage, and thus barely visible impact damage (BVID) has been used as a threshold of the detectability of the damage. There is no general rule defining the depth of the indentation caused by BVID, and its definition varies from 0.2 to 2.5 mm based on

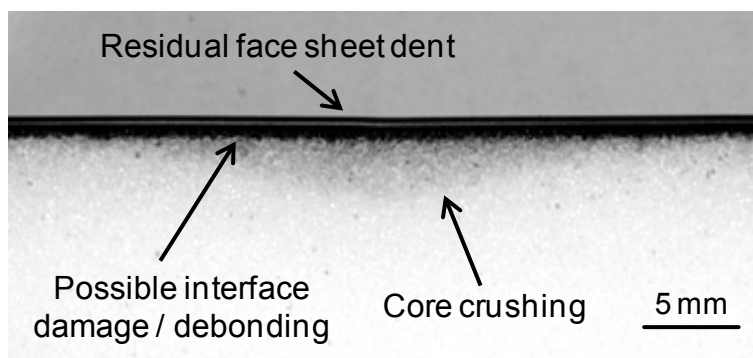


Figure 1.2 Cross section of indentation loaded foam core sandwich structure.

the literature source. The compression after impact (CAI) strength of a indentation or impact loaded sandwich panel cannot however be accurately estimated by using the residual dent depth [7, 8]. Even when the residual deformation on the face sheet is barely visible or not visible at all, debonding or significant damage in the core reducing the sandwich structures CAI can exist [9, 10]. It has also been shown that similar damage with barely visible residual dent occurs even if high density foam core or thicker face sheets are used [11]. The residual strength of the structures should therefore be evaluated using the damage area.

Figure 1.3, for example, shows the typical response of a structure when considering the relation of the energy of the impact and the detectability of the impact damage. Low energy impacts leave mostly damage below the BVID threshold. When the impact energy increases, the damage becomes visible. Relaxation of the core of the sandwich structure can however reduce the depth of the residual dent, which makes the damage barely visible.

A damage monitoring system is thus needed to detect the damages inside the sandwich structures. Conventional non-destructive inspection (NDI) methods take time and cannot always be used at hard to reach locations. Structural health monitoring systems (SHM) embedded into the structures have therefore gaining interest and in recent years various SHM systems for composite structures have been proposed and studied. The purpose of the SHM system is to monitor the condition of the structures and assess their integrity before the damage becomes critical. This can also extend the operation time of the structures between maintenances as repairs could be done when needed.

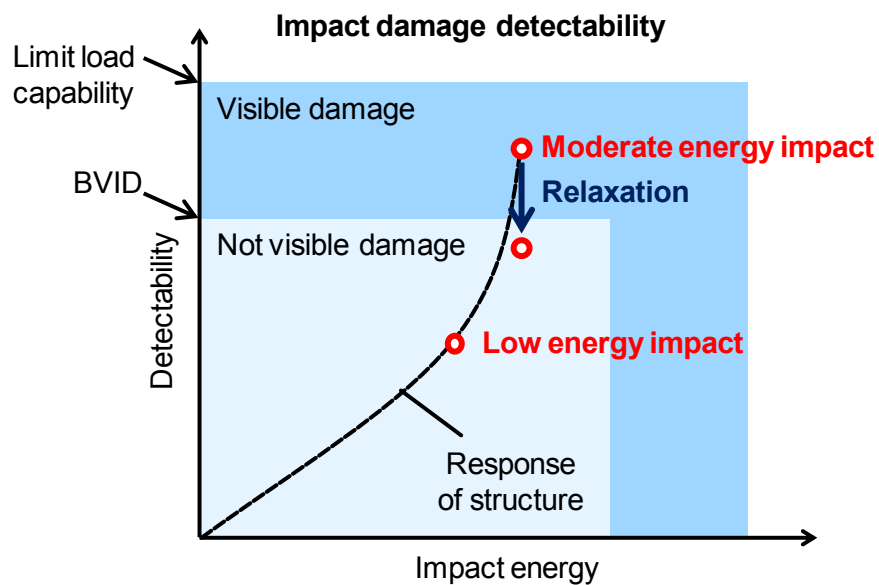


Figure 1.3 Detectability of impact damage based on impact energy.

Due to the various applications, foam core sandwich structures can also experience wide range of temperature and humidity conditions during operation and already during the manufacturing phase. The conditions can notably affect the behavior of the core material and thus negatively affect the performance of the whole structure. More information is however needed on the loading response and damage formation of sandwich structures under various temperature and humidity conditions. This information can be taken into account when designing sandwich structures to be used in various conditions, and also the effect of the environment on the damage formation is important for damage monitoring purposes, so that the monitoring system can accurately detect the damage at any operation conditions.

### **1.3. Objective and methods**

There are now two main objectives for this thesis:

- Study on the indentation response and residual state of foam core sandwich structures, and the effect of temperature and humidity conditions.
  
- Monitoring of indentation and low-velocity impact damage in sandwich structures.

The indentation response is studied experimentally and by finite element analysis. As the indentation response of the sandwich structures depend on the loading response of the core material which can be significantly affected by the environmental conditions, the loading response of the foam material under various hygrothermal conditions needs to be also studied. This information can then be used to explain the indentation response and also utilized in the finite element analysis. The numerical analysis focuses on predicting the indentation response under the set environmental conditions. Also prediction of the residual state of the sandwich structure after indentation is of importance for damage detection purposes.

To monitor damage in sandwich structures, a distributed strain monitoring system using embedded optical fiber sensors is applied. Monitoring of damage in the sandwich structures is then studied experimentally by indentation loading tests. As the damage detection ability depends on the residual state of the sandwich structures, the experimental and analysis results of the indentation behavior can be then used in assessing the capability of the monitoring system. The system is then verified by low-velocity impact tests on real-life demonstrator specimen.

## **1.4. Outline of thesis**

This thesis consists of seven chapters. Excluding the introduction in Chapter 1 and conclusion in Chapter 7, the contents can be mainly divided into three parts. In the first part (Chapter 2 and 3) the loading response of foam material and indentation response of its sandwich structures are studied experimentally. The loading response of the foam is observed under various temperature and humidity conditions. Based on these tests, the effect of the conditions on the foams loading response and mechanical properties is evaluated. Indentation tests are then conducted under various temperature and humidity conditions and the results are then related to the foams loading response.

The second part (Chapter 4 and 5), uses finite element analysis to predict the indentation and unloading response of sandwich structures at various humidity conditions. The properties of the core material are based on the experimental data, and the predicted indentation results are verified against the experimental indentation test data. Issues with the numerical analysis methods are also discussed and a new improved model is proposed to solve some of these issues.

The third part (Chapter 6) deals with the damage monitoring of the sandwich structures. As the detectability of damage in the sandwich structures is related to the response during indentation or impact loading, the indentation test and analysis results are used in evaluating the used monitoring method. The monitoring systems response during indentation loading tests is first observed experimentally and compared with analysis predictions to study the systems damage detection capability. In the end, low-velocity impact tests are conducted with a large scale sandwich panel to verify the systems damage detection ability in real life applications.

Finally, Chapter 7 summarizes the contents and main contributions of this thesis. Suggestions for future works on the studied topics are also presented.

## Chapter 2. Loading response of PMI foam

In this chapter the loading response of polymethacrylimide (PMI) foam is studied. Uniaxial compression and tension loading tests are conducted to define the loading response and mechanical properties of the foam at various temperature and humidity conditions.

### 2.1. Rigid closed cell foams

Mechanical properties of rigid polymer foams are mainly defined by geometric and material parameters. Geometric parameters define the cell structure of the foam and material parameters the properties of the parent polymer material. Closed cell foams have a closed cell structure that consists of cell walls which form a random cellular structure as shown in Figure 2.1. The microscopic structure of the foam gives it good strength, stiffness, and energy absorption properties while keeping its relative density low. The complicated cell structure however means that the mechanical behavior of the foam is also complex. The relative density of the foam depends on the cell size and cell wall thickness. Therefore high density foams have often smaller cells with thick faces, which thus leads to increased buckling strength of the cell walls and thus increased strength of the foam overall.

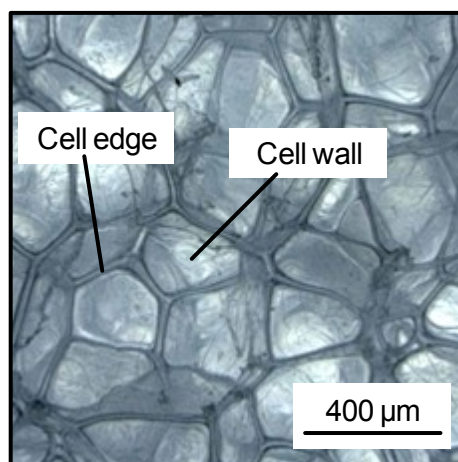


Figure 2.1 Micrograph showing the cell structure of PMI foam.

This study focuses on closed cell, rigid polymethacrylimide (PMI) foam, commercially known as Rohacell (Evonik Rohm GmbH). The Rohacell foams can be thermoformed to complex shapes and can withstand high temperatures and pressures, which allows for advanced manufacturing methods to be used. It has various grades with different densities and cell sizes for different applications. Due to the good mechanical and fatigue properties of the Rohacell foams, they have potential to be used in even high performance aerospace and aircraft structures.

### **2.1.1. Deformation of foam under loading**

Macroscopic behavior of polymer based foams depends on the polymer material behavior and the microstructure of the foam. Behavior of foams under compressive and tensile loading can thus be observed at microscopic and macroscopic level. The uniaxial loading behavior of closed cell polymer based foam material is now explained.

Typical tests using foam samples notable larger than the foams cell size give the macroscopic response of the material, such as the stress-strain response. This portrays the average response of the foam and is nearly the same for various cell configurations as long as the size of the foam sample is large enough. A typical stress-strain curve of rigid closed cell foam under compression-tension loading cycle can be seen in Figure 2.2. Each part of this curve is now related to the microscopic phenomena occurring in the foam as depicted in Figure 2.3. Based on this, the compressive loading response can now be divided into three regions as follows:

1. Elastic: Seemingly elastic deformation of the foam, during with the cell walls oriented in the loading direction bend elastically while the transverse ones are stretched. At certain loading the foam yields. At this point the weakest cell walls buckle, causing the buckled cells and surrounding cells to collapse, leading to notable drop in the stress response.
2. Plastic plateau: After yielding of the foam, a long plateau region is observed. This is caused by the progressive collapse of cell walls under increasing compressive loading. As the cell walls collapse, they can buckle, break or form plastic hinges or combination of any of the previous [12]. As the weakest cells have collapsed, their ability to carry loading is significantly reduced and the loading thus concentrates on the surrounding cells or other weak points in the foam. This way the cells in the foam keep crushing progressively leading to almost constant stress-strain response on macroscopic level. It has been also suggested that as the cells keep collapsing and the load carrying capability of the cell walls is notably reduced, the air trapped inside the cells starts to affect the compressive response [12]. If the cell walls stay intact after collapse, the air stays trapped inside the cell and can thus resist the compressive loading until the cell walls break. This can be seen as slight increase in the macroscopic stress-strain response at the end of the plastic plateau region.

3. **Densification:** After most of the cells have collapsed, the cell walls come to contact with each other. With increasing loading the cell walls start to interact with each other and the parent polymer material starts to carry the compressive loading, thus gradually increasing the stiffness of the crushed foam close to that of the parent polymer.

Besides these three parts during the compressive loading, we can also look at the unloading and tensile parts of the loading cycle.

**Unloading:** During unloading the elastic compression of the polymer material is removed and bended cell walls spring back. Due to the plastic deformation in the foam, some residual deformation will however remain even after any loading has been removed.

**Tension (after compression):** When the foam is loaded in tension after compressive loading, the crushed cell walls are being stretched back to their initial state. Due to the damages and viscoelastic deformations in the cell walls, the needed tensile loading is notably lower than the compressive loading was. However, when the global strain of the foam starts to get closer to zero, increased loading is needed to stretch and straighten the plastic hinges formed during compression in the cell walls.

The compressive and tensile loading of various polymer foams has been studied extensively in the past, but now the focus is put on the PMI foams. For example, Li and Mines [13, 14], and Zenkert et.al. [15, 16] have previously conducted quite extensive experiments on the Rohacell 51 WF foam under various loading conditions, such as uniaxial tension, uniaxial compression and shear, and also studied the hydrostatic compression and combined shear-compression loading cases. Based on the experiments

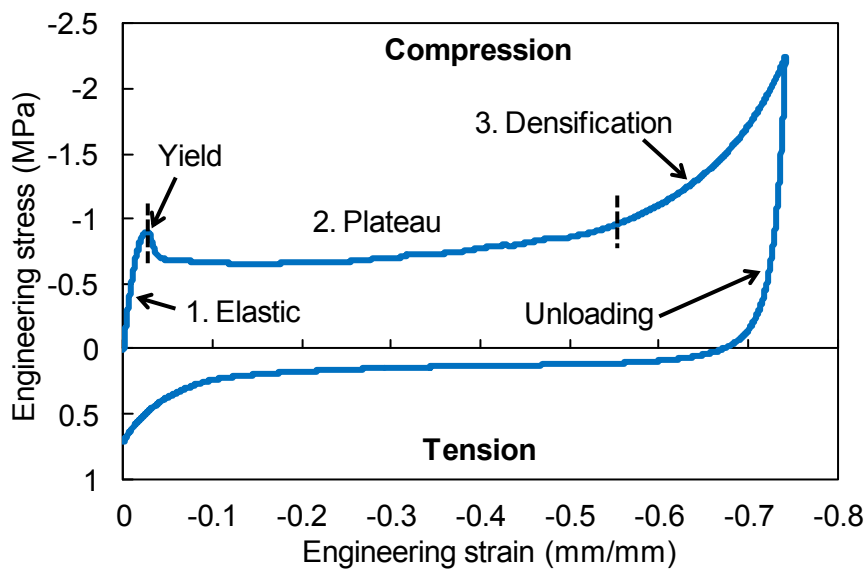


Figure 2.2 Typical stress-strain curve of rigid closed cell polymer foam during uniaxial compression-tension loading cycle.

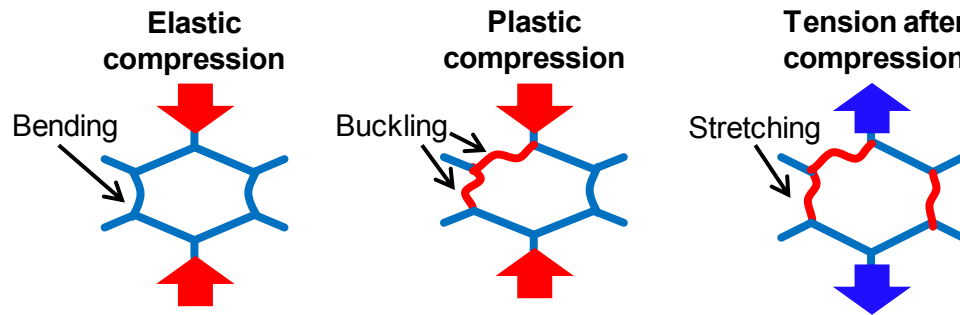


Figure 2.3 Microscopic response of ideal cell in closed-cell foam during compression and tension after compression.

they provided an analytical model for the prediction of global elastic and plastic strains in compression loaded foam material. Later Arezoo et. al. expanded the experiments to other densities and related the results with the microscopic response of the foam [17].

The properties of polymer foams can be notably degraded after compressive loading [18]. The tensile response after compression has however been addressed only briefly in previous works. Li and Mines [13], and Koissin and Shipsha [19] have given some experimental results on the tensile behavior and even provided simple model to partially fit the tensile stress-strain curve [19], but the subject has however got little further attention.

### 2.1.2. Environmental effects

In polymer based foams, the polymer material itself can be affected by various environmental conditions, such as temperature and humidity, leading to abnormal behavior. As with many materials, high temperature softens the parent polymer material of the foam. This again weakens the cell walls against loading on microscopic level, leading to degraded properties of the foam also on macroscopic level. Moisture can similarly affect the performance of the foam as water is absorbed by the polymer material.

Some studies exist on the effect of temperature and humidity conditions on the loading response of polymer based foams. Especially the effect of temperature conditions on the foam properties has gained attention lately [20, 21, 22]. Stiffness of the foams was seen to degrade almost linearly up to the glass transition temperature of the parent polymer material, after which the properties were reduced notably. Studies have also shown how polymer based foams become stronger and stiffer but also brittle at low temperatures [20, 22]. High temperatures on the other hand degrade the stiffness of the foam and it becomes rubbery at temperatures exceeding its glass transition temperature.

Moisture can affect the polymer foam in a few ways. Moisture in the foam can notably reduce its stiffness and strength properties. Increased moisture content can also lead to

swelling of the foam, thus causing increased internal strains and stresses in the structure. During indentation loading the response is defined by the loading response of the foam and thus the plasticization of the foams polymer material has the biggest effect. In closed cell foams, the moisture uptake happens by pure diffusion into the polymer material [23]. Because the imide groups in polymethacrylimide are highly polar, water molecules can easily connect to the polymer chains by Van der Waals force. As the water is absorbed into the polymer, the polymer is plasticized and its stiffness is notably reduced.

Diffusion of the moisture into the foam materials has gained attention and the moisture content at various temperature and humidity conditions has been studied quite extensively both experimentally and with numerical and analytical methods [23, 24, 25, 26, 27, 28, 29]. Effect of moisture on the glass transition temperature, and strength and stiffness properties of various polymer foams has also been studied to some extent [27, 30, 31]. However, to the author's knowledge, any studies on the combined effect of the temperature and humidity on the compressive and tensile loading response of polymer foams has not yet been conducted. The focus of this study is therefore put on the effect of high temperatures and various humidity conditions on the loading response and mechanical properties of rigid closed cell foams.

## **2.2. Experimental setup**

### **2.2.1. Foam specimens**

Closed cell rigid polymethacrylimide (PMI) foam Rohacell 51 WF (Evonik Rohm GmbH) was used in the experiments throughout this study. As was explained previously, the WF foams are aerospace grade foams that can withstand high temperatures and pressures, which allows for wide range of manufacturing methods to be used. Measured average density and manufacturer given density of the used foam are listed in Table 2.1.

25 x 25 mm foam core blocks were cut from a larger 35 mm thick panel using diamond coated blade saw. This gives cross-section area of 625 mm<sup>2</sup> for the specimens, which is the minimum area suggested by standard ASTM: C297/C297M-04 for compression tests of foam materials. These blocks were then further cut so that the thickness of each specimen was around 17 mm as shown in Figure 2.4. The thickness direction of the foam specimens was the same as the thickness direction of the larger panel. After the specimens were cut to size, they were dried in an oven at 120°C for at least 24 hours to remove any aging shrinkage [27] and to reach a stable and dry initial condition, after which they were adhered to steel jigs using a film adhesive AF 163-2K (3M Co.) and cured in oven for at least 2 hours at 120°C. Finished test specimen is depicted in Figure 2.5.

Table 2.1 Density of the used foam material.

Foam grade	Density (Measured)	Density (Manufacturer [32])
WF 51	59.9 kg/m <sup>3</sup>	52 kg/m <sup>3</sup>

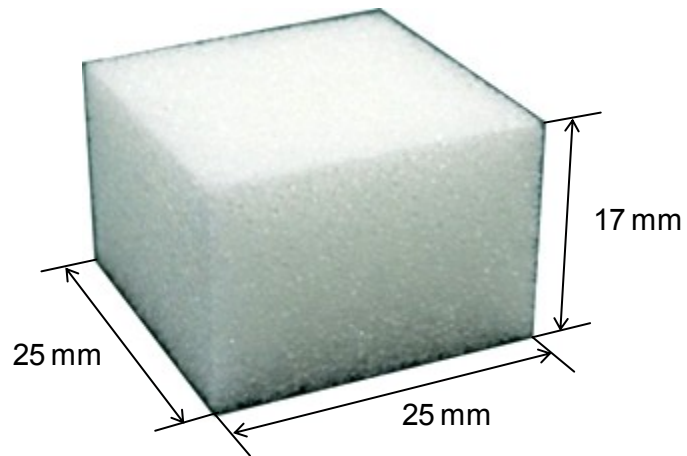


Figure 2.4 Dimensions of foam core specimen.

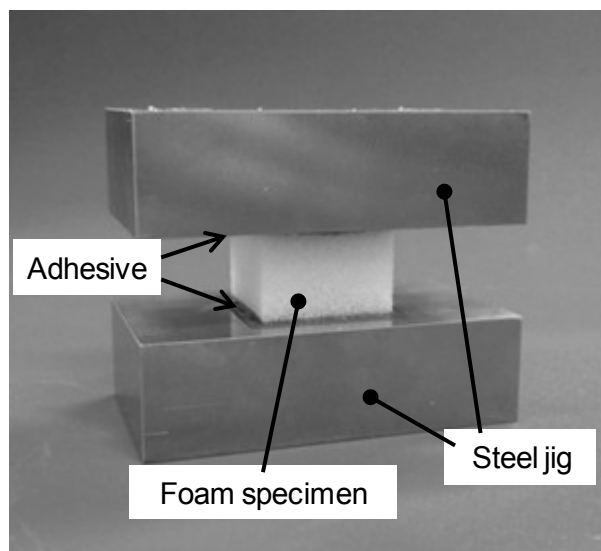


Figure 2.5 Foam core specimen adhered to steel jigs.

### **2.2.2. Conditioning**

The specimens were conditioned for 24 hours at three distinct humidity conditions before testing. These conditions are from now on called dry, ambient and wet conditions. For dry conditions the specimens were kept in an oven at around 120°C where the humidity was measured to be around 10%RH. For ambient conditions the specimens were kept at room conditions at room temperature. The humidity and temperature at ambient conditions was measured at around 55%RH and 30°C. For the wet conditions, the specimens were put in a closed container which was partially filled with water, and the temperature of the container was kept at 30°C. Due to the water at the bottom of the container, the humidity was measured to be around 95%RH. The specimens were not in direct contact with the water so that no notable amount of water gathered at the open cells on the sides of the specimen. Different temperatures could have been used during the wet conditioning, which would have led to different moisture contents as the moisture uptake is increased at higher temperatures. However, only 30°C temperature was now used to get similar moisture content for each specimen regardless of the following temperature conditioning.

After humidity conditioning, the specimens were heated in the environmental chamber of the testing machine. The specimens were let to heat for around 10 to 20 minutes before testing, so that the temperature in the chamber became stable and the temperature of the foam was assumed to be nearly uniform. During the heating some drying of the specimens will occur, but as the heating time was nearly same for all specimens, the moisture content should be similar for specimens having undergone same humidity conditioning.

Some conditioning tests were also conducted by immersing foam specimens in to water. During these tests it was noticed that the immersed foam deformed notably if the temperature was over 80°C. Wet foam or foam with high moisture content at high temperature seems to shrink so that the foam structure changes to something similar to re-entrant structure. The humidity conditioning temperature was thus limited to 30°C.

### **2.2.3. Test method**

The foam specimens adhered to the steel plates were attached to a jig inside an environmental chamber of a universal testing machine (INSTRON 5566). Quasi-static loading was the applied to the specimen by using a constant loading speed of the cross-head. Uniaxial compression and compression-tension tests were then conducted at various temperature conditions and the response of the foam was observed using stress-strain curves obtained from the tests. The stress was calculated using the load obtained from the load cell of the testing machine and the initial cross-section area of the specimens. Cross head displacement data was used to calculate the global strain of the specimens. Photographs of the testing setup are shown in Figure 2.6.

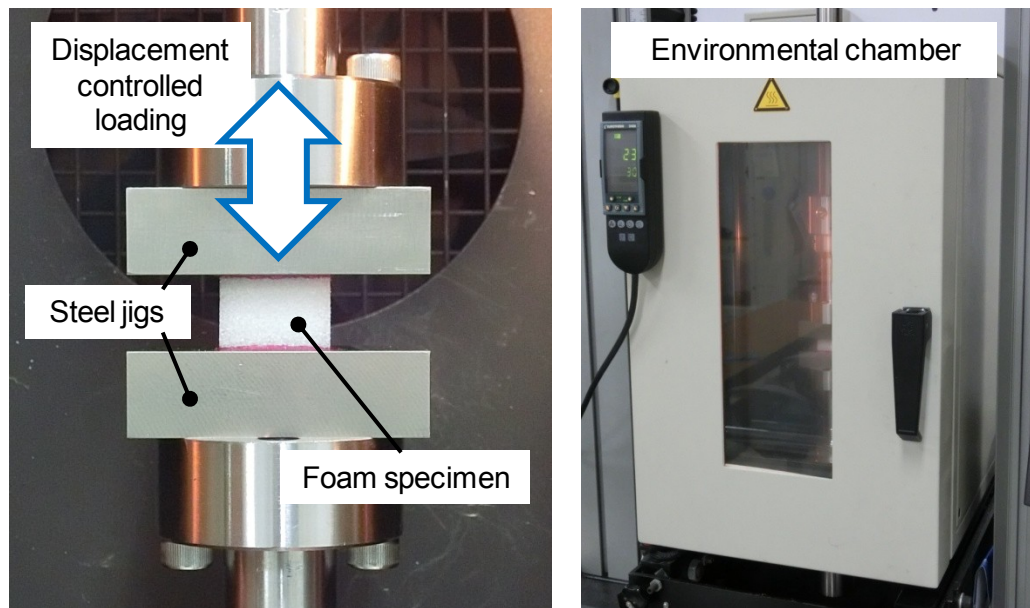


Figure 2.6 Testing setup of foam core specimens.

Loading speed of 5mm/min giving a strain rate of approximately  $0.005 \text{ s}^{-1}$  was used for the tests. Other loading speeds were also used to observe the effect of the strain rate. Lower strain rates gave lower stresses but the stress relaxation of the foam can have effect on the stress response. Therefore extremely slow strain rate is not feasible to be used in the experiments. Also higher strain rates give higher stress response, but then the crushing becomes dynamic which would require further consideration when looking at the results. Based on these observations, the chosen loading speed seems to be reasonable when looking at the properties of the foam samples under loading.

The loading was applied in two cycles so that the tensile behavior could be observed in the middle of the loading. First compressive loading was applied to the foam until around 30% compressive strain was reached, after which the loading was removed and the foam was tensioned until the strain returned to zero. During the second cycle, compressive loading was applied until around 75% compressive strain was reached, after which the loading direction was again changed and the foam was tensioned until the strain returned to zero. By combining the compressive part of these two cycles, the compressive response of the foam could be achieved until 75% compressive strain. Typical stress-strain curves are depicted in Figure 2.7 with the combined compressive stress-strain curve.

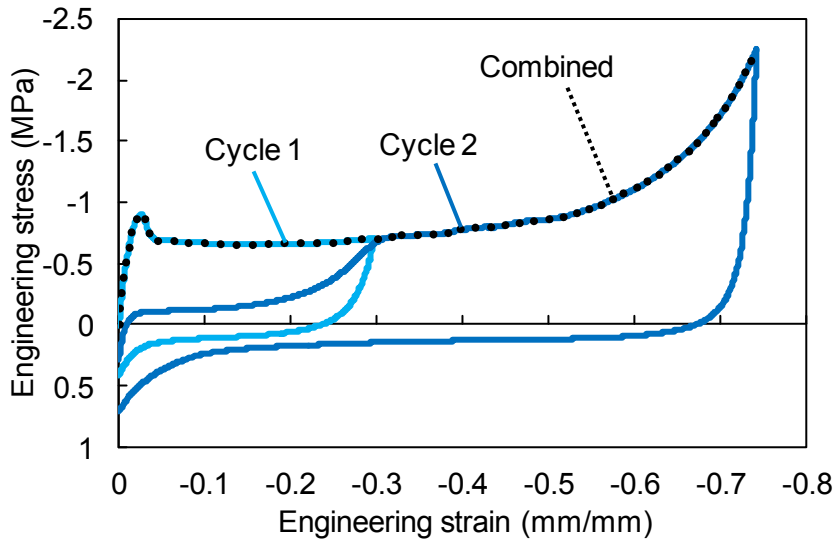


Figure 2.7 Typical stress-strain curves obtained from the foam loading tests.

### 2.3. Moisture diffusion in PMI foam

The main effect of humid environment on foam core materials is that moisture from the surrounding environment will diffuse into the polymer material of the foam. This increases the moisture content of the foam, which is the percentage weight gain of the foam due to absorbed moisture. Therefore it is important to have some estimation of the moisture content of the foam material. Basically the moisture content of the foam depends on the relative humidity and temperature of the environment. High humidity means that there will be more moisture to diffuse into the polymer. Temperature on the other hand affects the speed of diffusion. At higher temperatures the diffusion process will be accelerated as the diffusion constant increases. After some time, the increase of moisture content will become asymptotic and a level of saturation will be reached.

Diffusion process progresses over time, so that the amount of moisture diffused into the material also changes over time. For polymer foam materials, moisture absorption model [33] based on one-dimensional Fickian theory is often used. The model gives the moisture content percentage  $M_t$  of the foam at any time as

$$M_t = M_\infty \left\{ 1 - \frac{8}{\pi^2} \sum_{n=0}^{\infty} (2n+1)^{-2} \exp \left[ -\frac{D(2n+1)^2 \pi^2 t}{h^2} \right] \right\} \quad (2.1)$$

$$D = \pi \left[ \frac{h}{4M_\infty} \right]^2 \left[ \frac{M_2 - M_1}{\sqrt{t_1} - \sqrt{t_2}} \right]^2 \quad (2.2)$$

where  $D$  is the diffusion coefficient of the material,  $M_\infty$  is the moisture content at

equilibrium,  $h$  is the thickness of the specimen and  $t$  is time.

To study the moisture content of the used foam over time, foam block specimens were placed in various humidity conditions and their weight was observed over time. Before the tests, the specimens were dried at 120°C in an oven for at least 24 hours. Weight of the dried specimens was then weighted and they were placed in the set humidity and temperature conditions. During the conditioning the specimens were weighted at certain times to define their moisture content.

Moisture content of the foam specimens at ambient and wet conditions over time are shown in Figure 2.8. Specimens at the ambient conditions seem to reach saturation quite fast after the beginning of the conditioning. Moisture content of the wet specimens however keeps increasing notably faster than the ambient specimens, and it seems to take much longer to reach the saturation state. Moisture content of the dry specimens was assumed to stay near zero during the conditioning, so they were not tested.

The one dimensional Fickian diffusion model of Equation 2.1 was fitted to the experimental data as shown in Figure 2.8. The thickness  $h$  in the diffusion model was taken as the shortest dimension of the specimens, which is 17 mm for the foam block specimens. The model now seems to predict the moisture content of the specimens quite well and the moisture content at saturation and diffusion coefficient of the model for the tested conditions are listed in Table 2.2.

Moisture content of the foam at ambient conditions seems to settle at around 4 weight percent over long time period. Even short period at wet conditions can lead to quite notable moisture contents. It should though be noted that as the diffusion of the moisture occurs at the surfaces of the specimens, the size of the specimens will also affect the moisture content. It has been observed before that the moisture penetrates only few millimeters from the surfaces of polymer foams [25]. The area of the free surface available for moisture to diffuse thereby seems to be one factor defining the diffused moisture content. Therefore, as the foam specimens are adhered to the jig in the foam loading tests which reduces the free surfaces available for moisture uptake, lower moisture content can be possible than in the moisture diffusion tests.

As the foam compression test specimens are heated to the desired temperature before testing, some drying of the foam occurs. Placing conditioned foam blocks into the heated environmental chamber of the testing machine for around 20 minutes showed that the moisture content of the wet specimens dropped by approximately 8% and the ambient specimens by 1 %. Definition of the exact moisture condition of the specimens in the loading tests is thus rather difficult. Some estimation of their moisture content can however be made using the obtained data. The moisture content of the specimens at ambient and wet conditions after the 24 hour conditioning was now estimated to be approximately 3.8% and 14% respectively when no drying during heating is taken into account.

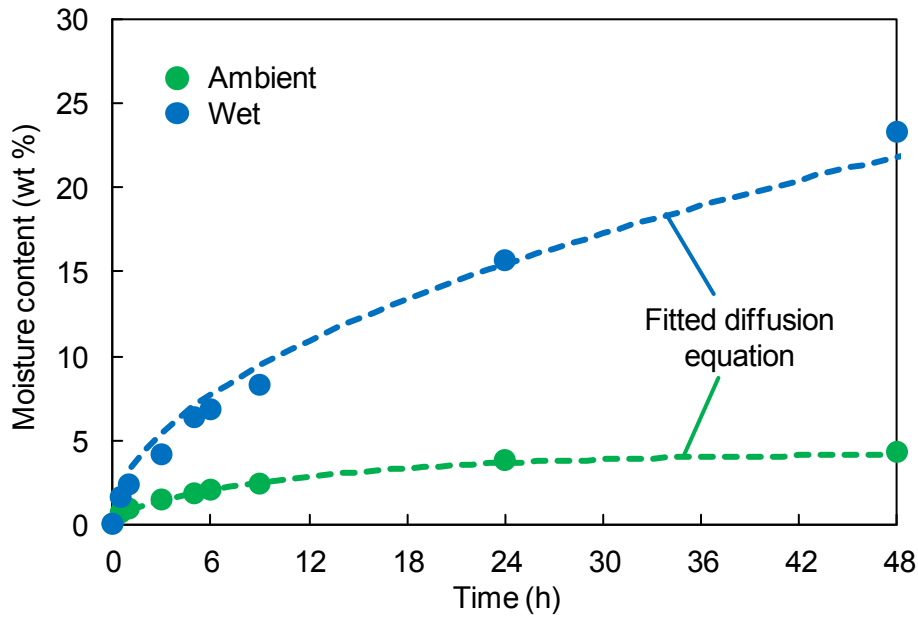


Figure 2.8 Moisture content of foam specimens at different humidity conditions.

Table 2.2 Saturated moisture content  $M_{\infty}$  and diffusion coefficient  $D$  of foam specimens at various conditions.

Condition	$M_{\infty}$	$D$
30°C / 55%	4.23%	0.000609 mm/s
30°C / 95%	121.69%	0.00000106 mm/s

## 2.4. Effect of loading rate

The feasibility of the chosen loading rate used in the experiments was confirmed by conducting uniaxial compressive loading tests with various strain rates. Figure 2.9 shows the compressive stress-strain curves and Figure 2.10 the measured yield and plateau stresses against the tested strain rates at ambient conditions. The yield stress increases logarithmically with increasing strain rates. The chosen strain rate of  $0.005 \text{ s}^{-1}$  is now located in the mid-region of the tested strain rate values. This would indicate that the chosen strain rate is slow enough to avoid any dynamic effects, but also fast enough to avoid viscoelastic stress relaxation effects during loading.

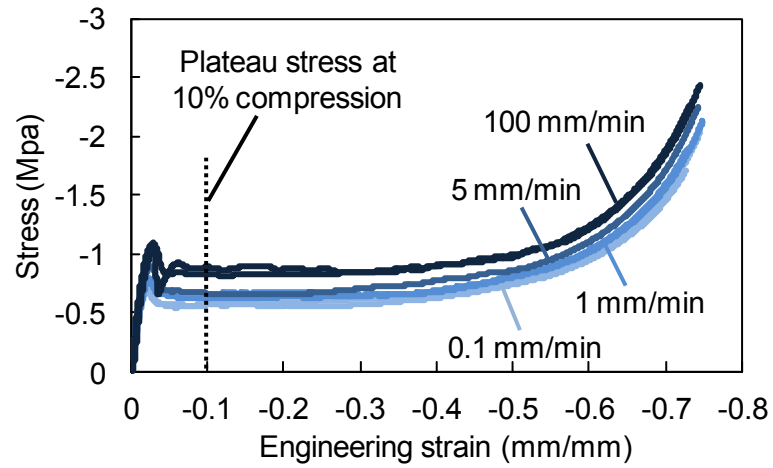


Figure 2.9 Compressive stress-strain response of foam at various loading rates at 30°C ambient conditions.

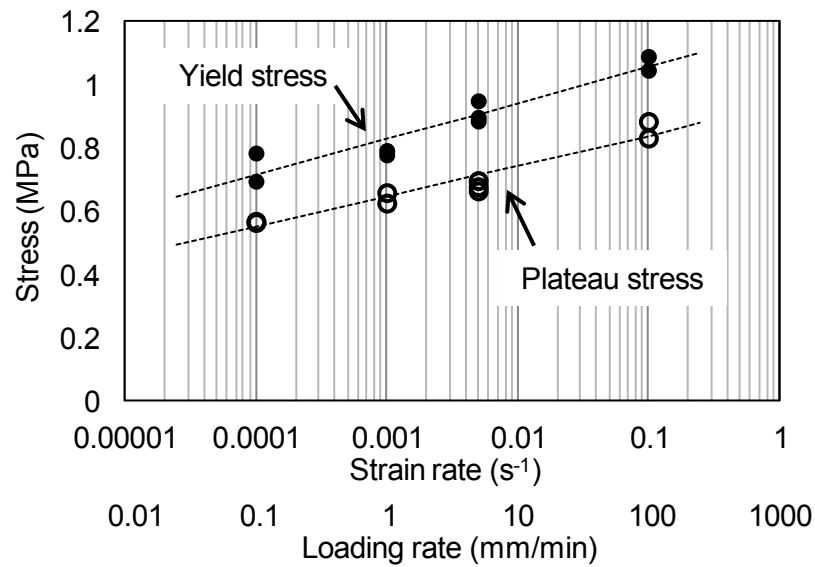


Figure 2.10 Yield and plateau stress of the foam at various loading rates at 30°C ambient conditions.

## 2.5. Test results

### 2.5.1. Compressive loading

Stress-strain curves for foams specimens conditioned at dry, ambient and wet conditions and tested at 30°C are shown in Figure 2.11. It can be seen that high humidity conditioning clearly degrades the strength of the foam as the yield stress and stress response during plastic plateau are notably reduced. On the other hand, drying of the foam leads to higher compressive strength and stress response as the moisture in the foam is removed and its plasticizing effect is thus reversed.

Looking at the plateau regions, it can be seen that the curve of the wet specimen is smooth due to the soft, plastic response of the wet polymer material. Contrary to this, quite notable fluctuation is visible in the dry specimens curve. This is thought to be due to brittle response of the dry foam, which causes the stress to fluctuate as the cell walls are suddenly broken under compressive loading. Stress also seems to start increasing earlier during the plateau region in the wet specimens while in the dry specimens the plateau is almost flat until the densification begins. This might be caused by the air trapped inside the cells of the foam. In dry foam the cell walls are brittle and break easily under loading, so the air can escape the cell and does not contribute to the macroscopic loading response. In the wet foam, however, the cell walls are more ductile and thus stay intact during collapse. The air therefore stays trapped inside the collapsed cells and starts to contribute to the macroscopic loading response during further compression, which can be seen as increased stress in the plateau region. Similar response can be seen at higher temperatures as shown for different humidity cases at 80°C temperature in Figure 2.12. The curves for the dry specimens become smoother as the polymer of the foam also becomes more ductile at higher temperatures.

Figure 2.13 shows the effect of temperature on the dry specimens. Increased temperature decreases the strength of the foams as can be expected as the polymer of the foam becomes softer. Slight fluctuation in the plateau region can be also seen on higher temperatures of the dry specimens. Therefore even with increased temperature the behavior of the polymer still seems to be somewhat brittle. On the wet foam specimens increase in the temperature also further reduces the loading response of the foam, as shown in Figure 2.14. Response at higher temperatures seems similar with each other and it might indicate that after certain temperature the properties of the dry foam will not degrade any further. Confirmation of this would however require further tests at high temperature conditions.

Figure 2.15 shows the combined effect of high temperature and humidity on the compressive loading response of the foam compared to the effect of temperature or humidity only. The combined effect is now clearly more significant than the effect of temperature or humidity on their own. Therefore, even if the degrading effect of high temperature on the foam properties is taken into account, moisture can lead to even greater reduction in the foam properties than expected.

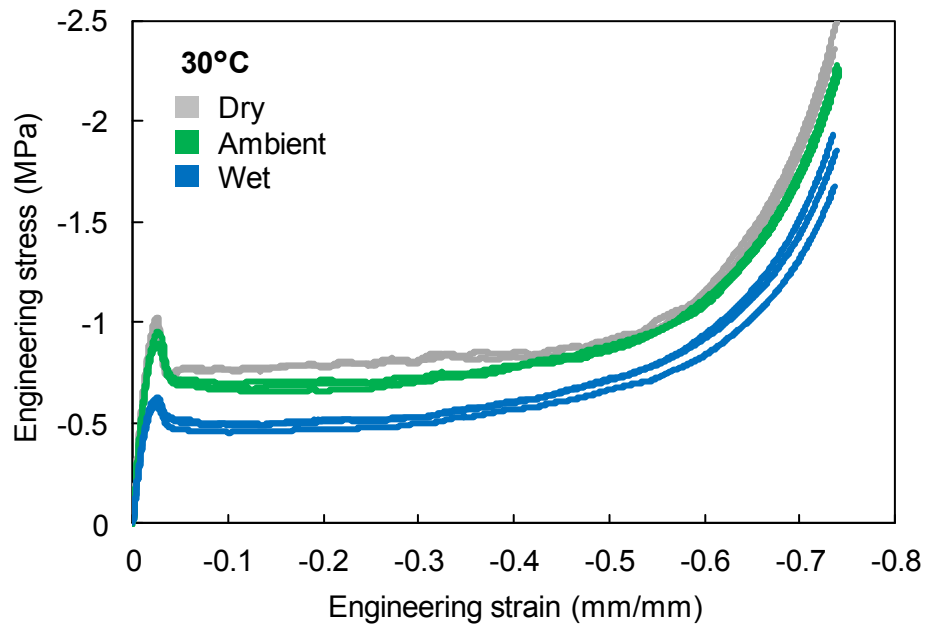


Figure 2.11 Compressive stress-strain response of foam at various humidity conditions at 30°C temperature.

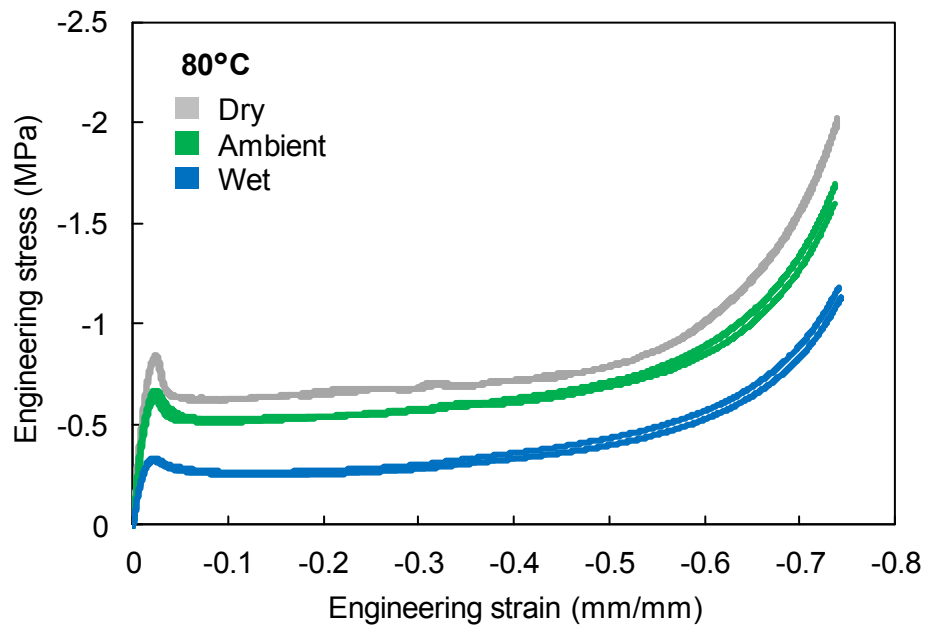


Figure 2.12 Compressive stress-strain response of foam at various humidity conditions at 80°C temperature.

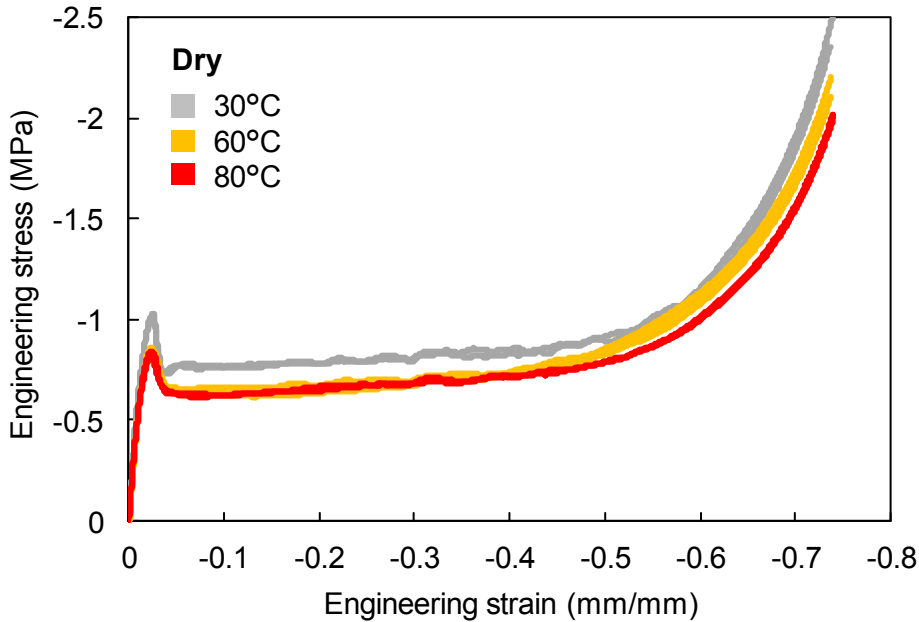


Figure 2.13 Compressive stress-strain response of dry foam at various temperature conditions.

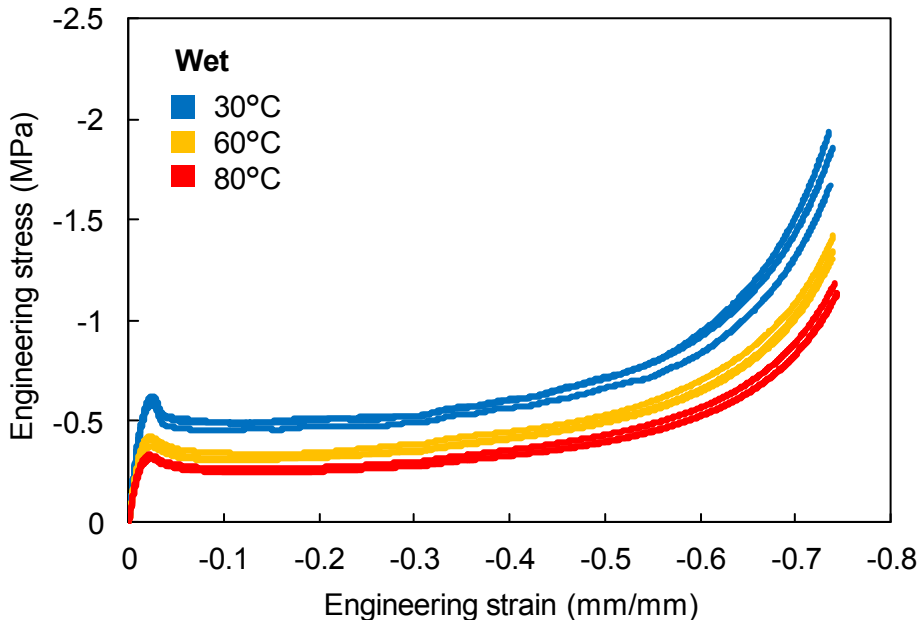


Figure 2.14 Compressive stress-strain response of wet foam at various temperature conditions.

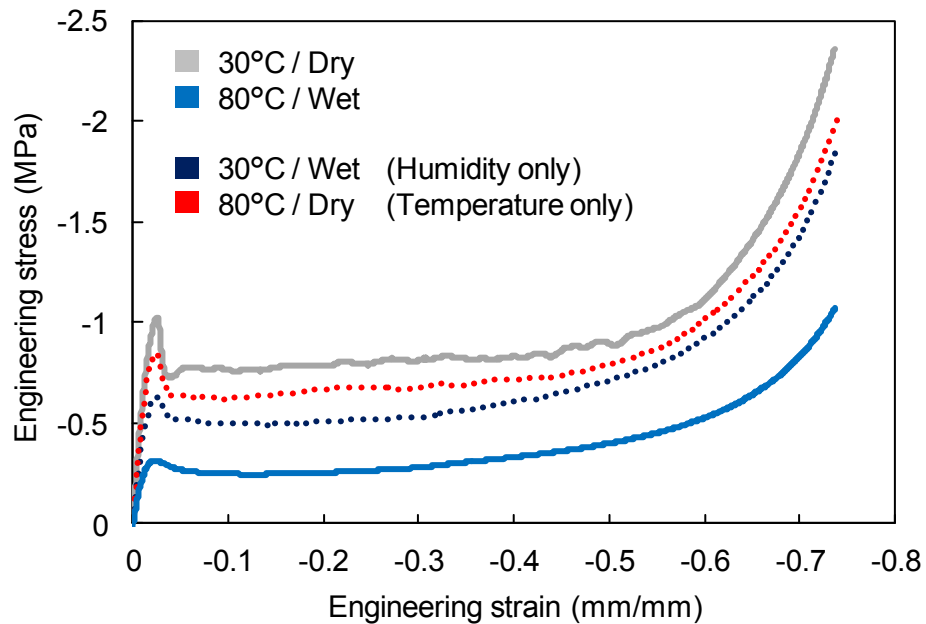


Figure 2.15 Compressive stress-strain response of foam at high temperature, high humidity and combined high temperature and humidity conditions.

### 2.5.2. Tension after compression

Stress-strain curves for uniaxial compression-tension loading cycle tests under various humidity conditions at 30°C and 80°C are shown in Figure 2.16. From these curves we can look at the tensile loading after the foam has been compressed. At 30°C temperature the wet specimens show highest tensile stresses. This means that higher tensile loading is needed to stretch the crushed core compared to dry and ambient conditions. This is most probably caused by notable plastic deformation of the cell walls in the foam during compression due to the soft and ductile response of the polymer. Due to the softness of the polymer, the deformation can also easily spread on a larger area causing more plastic deformation to occur in the foam. Increased loading is then needed to stretch and straighten the plastically deformed cell walls.

In the dry and ambient foams the polymer is more brittle and the cell walls can thus break under compressive loading more easily. After the cell walls have broken, they cause no resistance under tensile loading and thus lower tensile stress is needed. Also, as the polymer in the dry and ambient foams is more rigid, the plastic deformation under compression is limited to the weakest cells and cell walls and does not progress so easily to the surrounding cells.

At higher temperatures, such as 80°C, the tensile response is quite similar for all humidity cases. This can be partly explained by the softening of the polymer at the high temperature.

In the wet specimens, however, the adhesive used to adhere the foam specimens to the steel jigs is also weakened by the high humidity. This has no notable effect during compression, but during tension the adhesive can start to yield during tension leading to lower tensile loadings. The adhesive was also seen to debond at the end of the tensile loading, which can also be seen in the stress-strain curves as the tensile stress notably decreases as the strain comes close to zero.

Similar stress-strain curves for uniaxial compression-tension loading cycle tests of dry and wet foam specimens under various temperature conditions are shown in Figure 2.17. For dry specimens the tensile response seems to be similar for all temperature conditions. As plastic deformation has occurred, the temperature therefore seems to have no significant effect during the stretching of the deformed cell walls.

On the wet specimens however, lower tensile stress is observed for high temperature specimens. This might again be caused by degraded properties of the adhesive at high temperature and humidity conditions. It could also be possible that as the polymer is plasticized by the moisture and further softened by the high temperature, that the cell walls became so much softer that they are stretched more easily and thus lower tensile load is required.

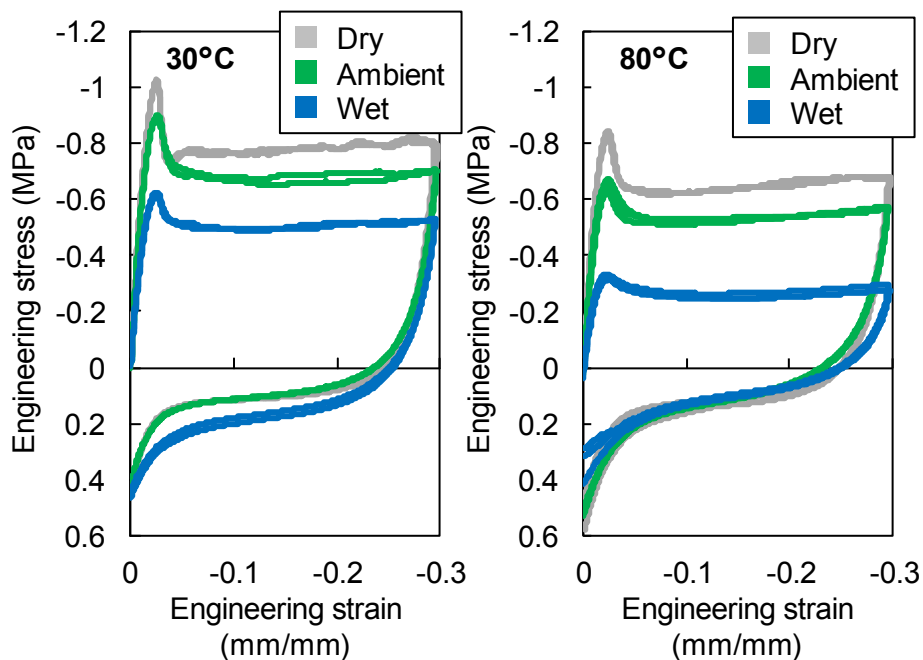


Figure 2.16 Stress-strain response of foam during uniaxial compression-tension loading cycle at various humidity conditions.

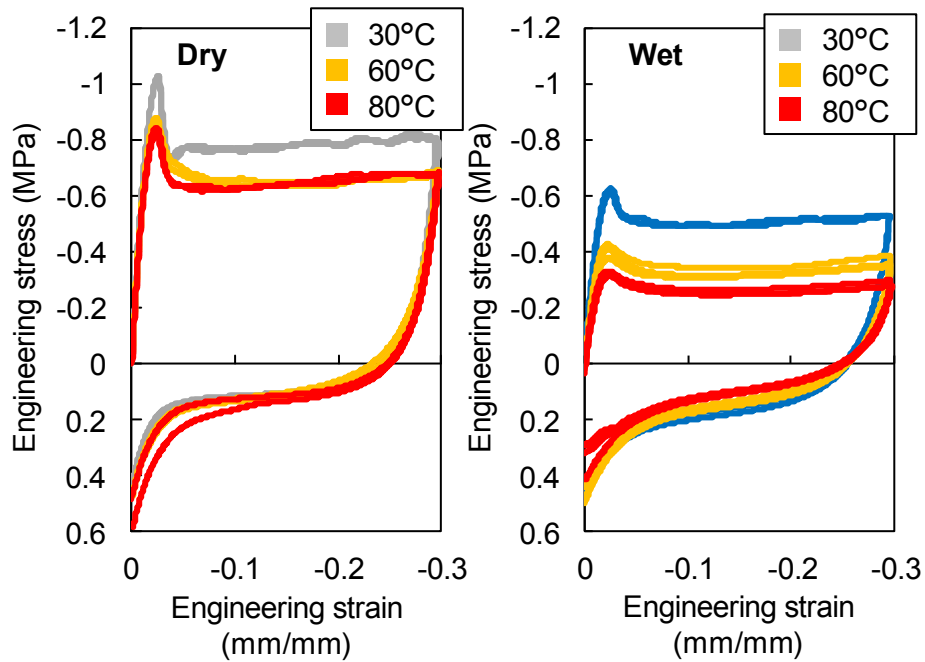


Figure 2.17 Stress-strain response of foam during uniaxial compression-tension loading cycle at various temperature conditions.

### 2.5.3. Microscopic observation

The foam specimens were also observed microscopically after the loading tests. The specimens were observed as they were after the tests, so that no further damage would be induced by, for example, cutting of the specimens. As the microscopic observation could be conducted only on the surfaces of the foam, the outermost cells that were already damaged during preparation of the foam specimens were ignored.

The outcome of the observations was that in the dry specimens several cases of broken cell walls and cell edges could be seen. Some examples of observed damage are shown in Figure 2.18. On the other hand, the wet specimens had highly deformed cell walls which still remained intact with no visible damage, as shown in Figure 2.19. It therefore confirms that the behavior of the dry foam seems to be brittle while the behavior of the wet foam more seems to be very ductile.

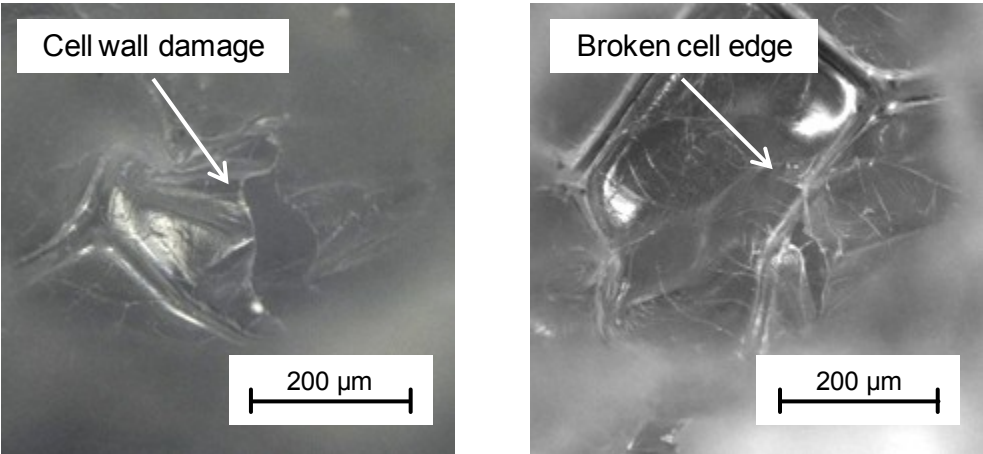


Figure 2.18 Typical damage in compression loaded dry foam specimens.

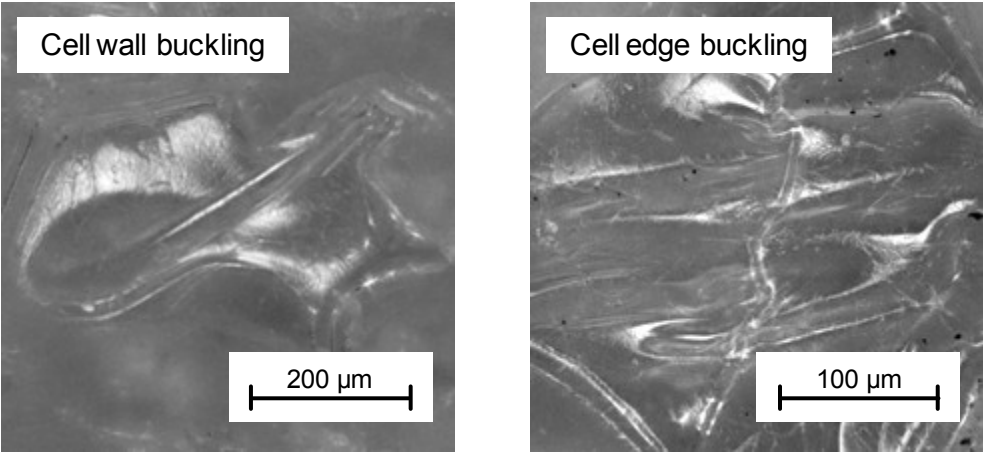


Figure 2.19 Typical damage in compression loaded wet foam specimens.

### 2.6. Foam properties

The characteristic properties of the foam were defined at various temperature and humidity conditions. These are macroscopic properties that can be used to evaluate performance of the foam. The observed properties are now the yield stress, elastic modulus, densification strain and plateau stress of the foam. Also the behavior after yielding was studied.

### 2.6.1. Defining foam properties

First, the macroscopic compressive yield stress of the foam can be estimated from the first local maximum in the stress-strain curve after the initial elastic deformation. This is the stress where the first cell walls buckle plastically and the crushing of the core begins, and defines the strength of the foam under compression.

Due to the nonlinear behavior of the foam during the initial elastic part of the compressive loading, the macroscopic compressive elastic modulus of the foam needs to be approximated. Simplest way to define the elastic modulus is to take the tangent modulus at the beginning of the loading or the secant modulus between zero loading and the yield point. These values however are often too high or low when used in numerical analysis, so a definition is needed to estimate a value that is somewhere between these values. Now, a 0.5% offset was used to get a value for the elastic modulus that is between the aforementioned values. Definition of this offset modulus is shown in Figure 2.20. First, the tangent modulus is defined at the beginning of loading. This tangent is then offset by 0.5% and the point where it crosses with the strain-strain curve is used to define the new secant elastic modulus. The modulus obtained from the 0.5% offset seems to give a good approximation of a value in the middle of the initial elastic modulus and the elastic modulus defined using the yield point as shown in Figure 2.21 for example for the 60°C ambient case.

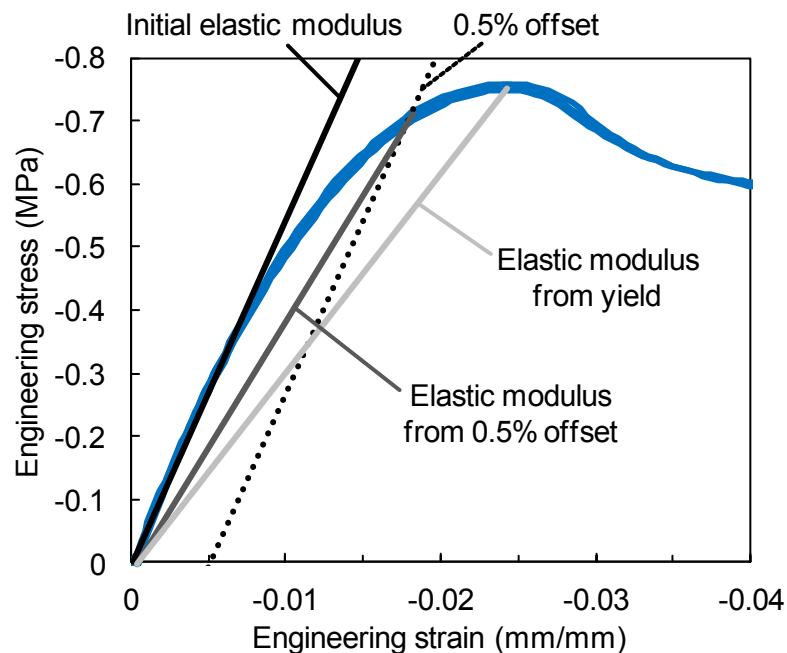


Figure 2.20 Definition of compressive elastic modulus of foam material from stress-strain data.

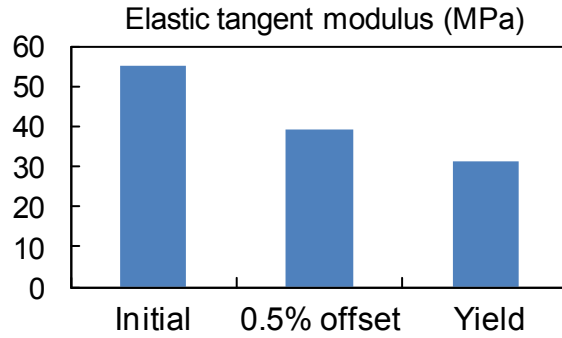


Figure 2.21 Elastic tangent modulus estimated by different definitions.

Values for densification strain and plateau stress can be obtained using energy efficiency method [34]. Energy dissipation efficiency  $E_d$  describes the energy absorbed by the foam up to given strain  $\varepsilon_a$  normalized by the stress value at that strain and can be defined as

$$E_d(\varepsilon_a) = \frac{\int_0^{\varepsilon_a} \sigma(\varepsilon) d\varepsilon}{\sigma_a} \quad (2.3)$$

Densification strain can then be defined using Equation 2.2 as the maximum strain value at which the condition of Equation 2.4 is satisfied. After this point the increase in absorbed energy is smaller than the increase in stress in the foam material. Therefore it can be assumed that most of the foam has collapsed reducing the foams energy absorption capability, and the densification of the foam has begun as the collapsed cell walls are compressed against each other.

$$\left. \frac{dE_d(\varepsilon_a)}{d\varepsilon} \right|_{\varepsilon_a = \varepsilon_i} = 0 \quad (2.4)$$

Plateau stress of the foam can then be calculated using the densification strain as

$$\sigma_{pl} = \frac{\int_0^{\varepsilon_d} \sigma(\varepsilon) d\varepsilon}{\varepsilon_d} \quad (2.5)$$

### 2.6.2. Foam properties

The elastic modulus and compressive yield stress values estimated from the experimental results of the specimens at tested temperature and humidity conditions are shown in Figure 2.22 and Figure 2.23. At maximum around 5% variation could be seen in the measured

values caused by differences in the specimens, but also by variance in the temperature and moisture content of the specimens. It can be seen that both properties degrade almost linearly with increasing temperature. Increasing the temperature from 30°C to 80°C leads to 10 to 30% reduction in the stiffness and strength of the foam depending on the humidity conditions, with high humidity leading to bigger reduction. On the other hand, increasing humidity can degrade the properties even more significantly. Difference between dry and wet conditions can be more than 50% at high temperatures. The yield strain was varied only slightly between conditions and stayed at around 2.4%. Based on this data it should also be noted that by just leaving dried foam in ambient room conditions, its stiffness and compressive strength can be reduced by around 10%.

The energy dissipation efficiency curves for the dry, ambient and humidity conditions at 30°C are plotted in Figure 2.24 with the respective stress-strain data. Using the definition in Equation 2.4, it seems that the densification strain is nearly same for all humidity conditions. Similar observation can be made for different temperature conditions as shown in Figure 2.25. The densification strain therefore seems to be related to the geometric properties of the foam rather than to its mechanical properties. However, some differences in the loading behavior of the foam at various conditions preceding densification can be seen. For example, by looking at the energy efficiency curves for different humidity conditions in Figure 2.24, the curves start to diverge after the foam has been compressed by 30%. This difference might be caused by the air trapped in the cells starting to affect the loading response. As was explained in section 2.5.1, at higher strains the air in the cells is pressurized and it also starts to carry part of the loading as long as the cell walls stay intact. As the cell walls are more ductile in the wet specimens, gas remains inside the cells

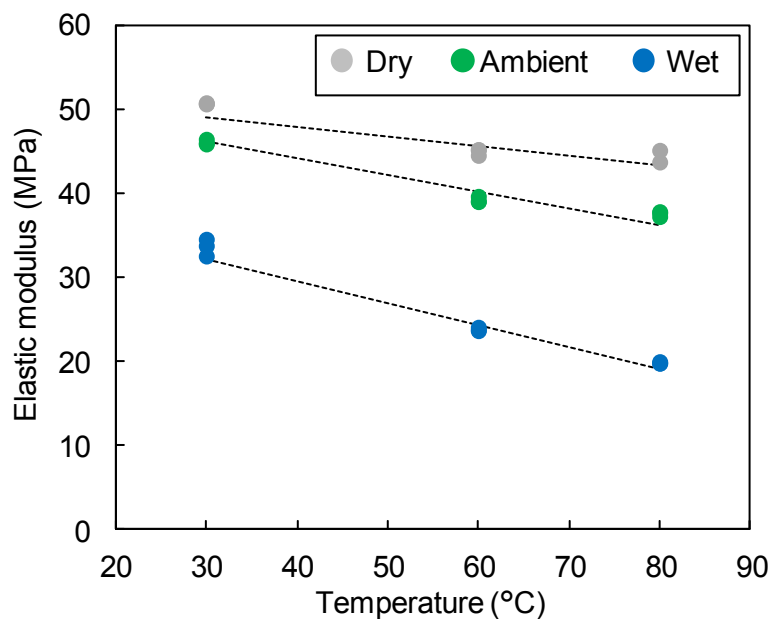


Figure 2.22 Elastic modulus at various conditions.

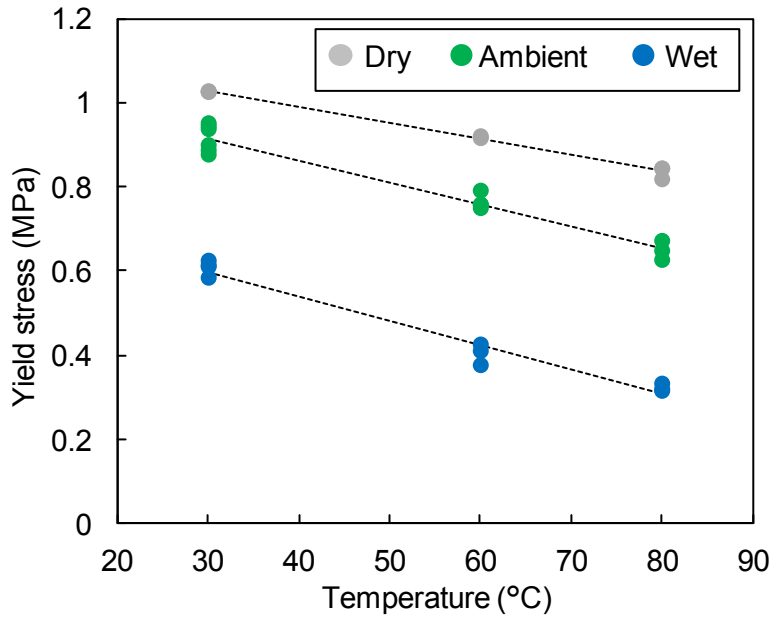


Figure 2.23 Yield stress at various conditions.

Plateau stresses estimated using Equation 2.5 at various temperature and humidity conditions are shown in Figure 2.26. As the energy dissipation efficiency curves and densification strain values are nearly similar for all conditions, the calculated plateau stresses show little variance. Better way to estimate the plateau stress therefore is to look at the stress value in the beginning of the plateau region, for example at 10% compressive strain. These plateau stress values are shown in Figure 2.27 and seem to follow the yield stress values quite closely.

To further study the response of the foam after yielding, it can be expressed using a hardening model [35] defined as

$$\sigma = \sigma_p + \gamma \frac{\varepsilon}{e_D} + \alpha \ln \left[ \frac{1}{1 - \left( \frac{\varepsilon}{e_D} \right)^\beta} \right], \quad e_D = 1 - \left[ \frac{\rho_f}{\rho_{f0}} \right] \quad (2.6)$$

where  $\sigma_p$  is the initial level of the plateau region,  $\gamma$  is a linear strain hardening coefficient, and  $\alpha$  and  $\beta$  are the scale factor and shape factor, respectively, for the non-linear part. The compaction strain  $e_D$  is calculated using the relative density of the foam  $\rho_f$  and the density  $\rho_{f0}$  of the parent material, and for the tested foam is 0.95. Using the previously obtained plateau stress values for the  $\sigma_p$  coefficient, the model is then fitted with the plateau and densification regions of the experimental results.

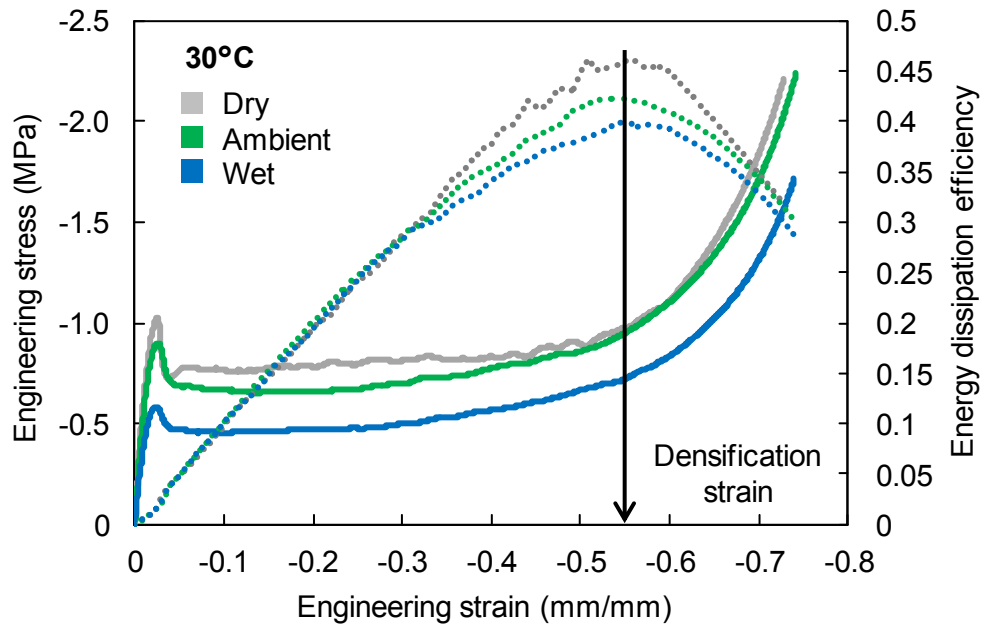


Figure 2.24 Energy dissipation efficiency curves for different humidity conditions.

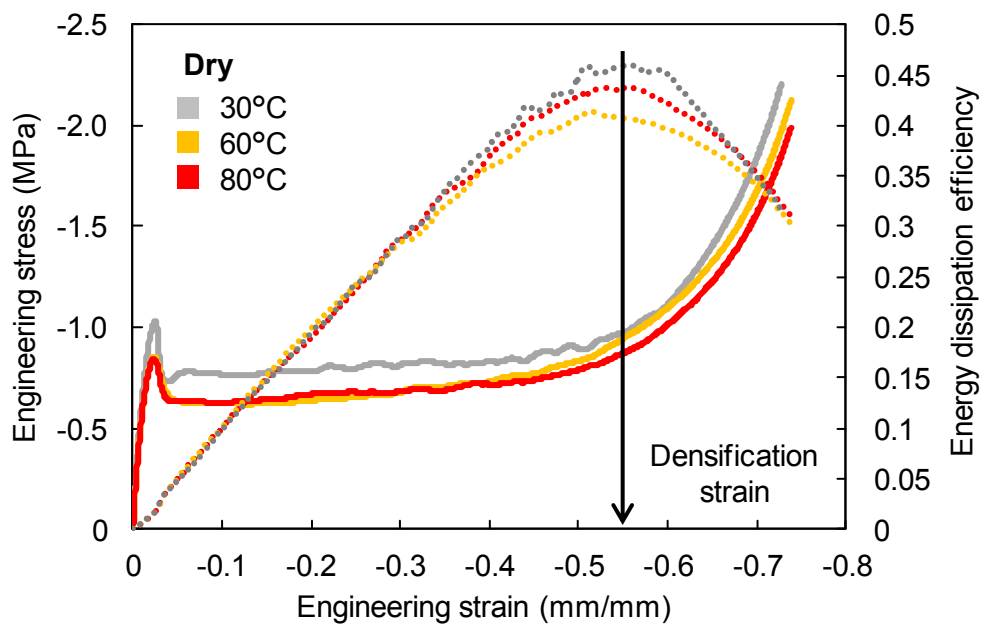


Figure 2.25 Energy dissipation efficiency curves for different temperature conditions.

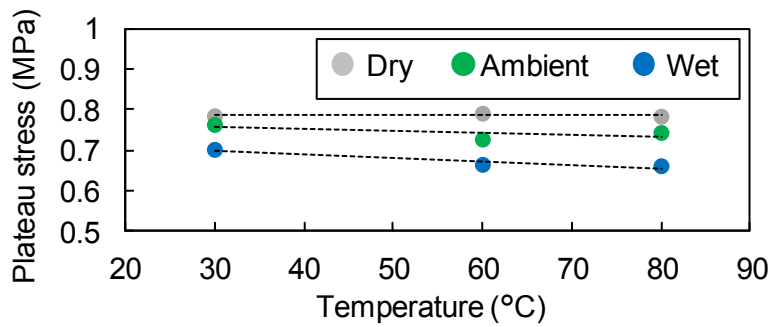


Figure 2.26 Average plateau stress by Equation 2.5 at various conditions.

Looking at the fitted parameter values, it could be seen that the value of the linear hardening parameter  $\gamma$  increased with increasing humidity, meaning that the angle of the plateau steepened. At the same time the angle of the densification region decreased slightly and thus transformation from the plateau region to the densification region became smoother. Between different temperatures there was some variation in the values of  $\alpha$  and  $\beta$  coefficients, while values of  $\gamma$  were almost same.

Effect of temperature and humidity conditions on the mechanical properties of the foam were obtained from the experimental results. The degrading effect of high temperature and humidity was now clearly evident. If the moisture content of the foam specimens can be measured with good precision, the mechanical properties of the foam in the whole tested temperature and humidity range can be predicted, as demonstrated in Appendix A. It should be also possible to extend the current results to other foam densities as discussed in Appendix B.

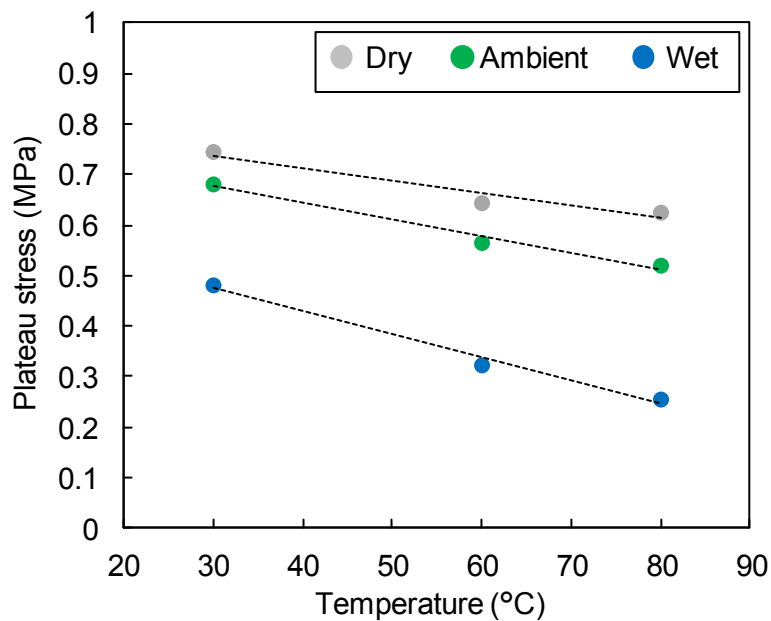


Figure 2.27 Average plateau stress at 10% compressive strain at various conditions.

## **2.7. Conclusion**

The loading behavior of Rohacell 51 WF PMI foam was observed under various temperature and humidity conditions. Uniaxial compression and compression-tension cycle loading tests were conducted with conditioned specimens. High temperature and humidity lead to degraded properties due to softening and plasticization of the polymer material in the foam. Brittle response of dry foam was observed, but it became ductile at higher humidity conditions as was also confirmed with microscopic observations. The stresses during tensile loading after compression were also increased by increasing humidity due to extensive plastic deformation of the foam during compression. At higher temperatures the tensile response was almost similar for all humidity conditions. Finally the material parameters for the foam were defined using the experimental results.

## **Chapter 3. Indentation response of sandwich structures**

In this chapter the indentation response of foam core sandwich beams is studied experimentally. Indentation loading tests are conducted at various temperature and humidity conditions. The loading response is then observed and the results are discussed with regard to the loading behavior of the foam materials at similar conditions.

### **3.1. Indentation response of sandwich structures**

A sandwich structure under localized indentation loading experiences, depending on the boundary conditions, global deformation due to the overall bending of the structure and local deflection of the face sheet at the location of the applied loading [1]. Sandwich structures are especially sensitive against the local deflection of the face sheet, as it can easily initiate compressive damage in the relatively weak core. Therefore, ignoring the global deformation and focusing on the local indentation response, the indentation event can be explained as depicted in Figure 3.1. As indentation loading is applied to the sandwich structure, the face bends locally under the loading. This also causes transverse loading in the core under the location of indentation. The loading is highest immediately under the loading point and changes further away accordingly with the profile of the bended face sheet. When the compression loading in the core is large enough, crushing of the core initiates near the face sheet. As the loading continues, the crushing of the core progresses in the through thickness direction of the sandwich structure, but also in the in-plane direction as the dent on the face sheet becomes larger.

After the loading has been removed, the face sheet, if it is not significantly damaged, tries to return to its initial state thus pulling the crushed core underneath the face. The plastically deformed crushed core on the other hand tries to resist the pull from the face sheet, causing a residual dent to remain in the face sheet. [36].

Stress relaxation in the core also begins to occur over time after the loading has been removed [36, 37, 38]. Because of this the foam starts to lose its capability to resist the pull from the face sheet. Therefore the face sheet can further stretch the crushed core and the dent becomes shallower. This means that there might remain no visible damage visible in the face, while the core can be notably damaged right under the face sheet and thus have notable effect degrading the strength of the sandwich structures [7, 39].

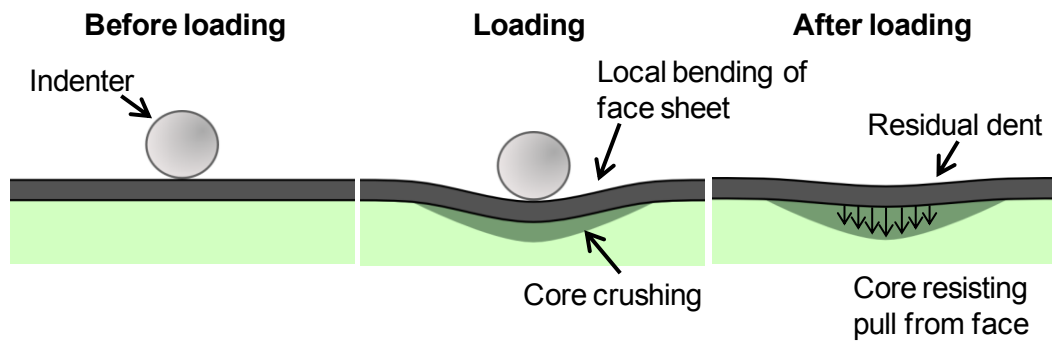


Figure 3.1 Local indentation loading response of sandwich structure.

The indentation response of sandwich structures depends on the face sheet stiffness and thickness, and on the properties of the core [11]. Thick or stiff face sheet will deform less locally under indentation loading, which again causes less compressive loading to transfer to the core. Thin or flexible face sheets on the other hand can deform notably, thus causing notable compression and core crushing damage under the indentation location. Then again, stiffer core material has higher strength against crushing and provides more support for the face sheet leading to smaller deformations. It has also been shown that low velocity impact response of laminates [40] and sandwich structures [41] can be evaluated well with quasi-static indentation tests. Quasi-static indentation tests are also easier to perform, control and simulate. The indentation test results can therefore be also applied to low velocity impact cases when considering loading cases where the residual deformation is near the barely visible threshold.

Many experimental and analytical studies have been done on the indentation and low-velocity impact response of foam core sandwich structures in the last decades [42, 43, 44, 45, 46, 47, 48, 49] but quite little attention has been given to the unloading response and the residual state remaining after indentation [36, 50, 51].

### 3.1.1. Effect of environmental conditions

The effect environmental conditions on the indentation or low-velocity impact response of foam core sandwich structures has not gained significant attention. Some indentation tests of PMI foam core sandwich structures have been conducted at low temperature conditions [52]. As the response of the foam became brittle in low temperature, brittle debonding damage was observed in the indented sandwich beams.

Even though the core in sandwich panels is often totally covered by the face sheets thus preventing direct contact between the core material and humidity in the environment, it

still will not stop the moisture from reaching the core. Experimental tests have shown that CFRP face sheets only slowed down the diffusion process, but the moisture still could reach the core and raise its moisture content depending on the environmental conditions [23, 27]. Also small cracks and voids in the faces can provide a route for the moisture to reach the core.

Various number of studies have considered the moisture diffusion in sandwich structures [23, 27, 28, 29, 31, 53, 54, 55] and the effect of humidity on interfacial fracture and debonding properties [29, 31, 54, 56] while fewer have looked at the impact or indentation response [28, 53]. The current study is therefore focused on the effect of temperature and humidity conditions on the indentation loading response of foam core sandwich structures, considering also the combined effect of temperature and humidity.

## **3.2. Experimental setup**

### **3.2.1. Sandwich beam specimens**

For the indentation tests, sandwich beam specimens were manufactured. Beams were selected as they are easy to manufacture and have seemingly two dimensional response. The beam specimens consisted of CFRP face sheet and foam core (Rohacell 51 WF) adhered together using adhesive film as depicted in Figure 3.2. The face sheets were manufactured beforehand using T700S/2592 (Toray Co.) CFRP prepreg sheets. 8 ply unidirectional laminates were manufactured in autoclave and then cut to size (20 mm × 200 mm) using diamond blade saw. This provided good quality laminates with constant and controllable thickness. Thickness of the face sheets was measured to be on average 1.15 mm. The face sheets are now thin enough to cause crushing of the core under loading, but still thick enough to prevent damage from occurring in the face sheet itself under tested indentation conditions. The face sheet laminates were then adhered to the core using AF 163-2K (3M Co.) adhesive film. The used core blocks were 35mm thick, 180 mm long and 20 mm wide. The core-face sheet combination was then adhered to steel jig using the same adhesive film. This provides fully backed support for the beam thus preventing global deformation.

### **3.2.2. Conditioning**

Conditioning of the sandwich specimens was done similar to the foam specimens in Chapter 2.2.2. After the core material was cut and dried at 120°C, it was assembled into a sandwich beam. The beams were then placed in the set humidity conditions and kept there for 24 hours. After humidity conditioning, the beam was heated to set temperature right before testing.

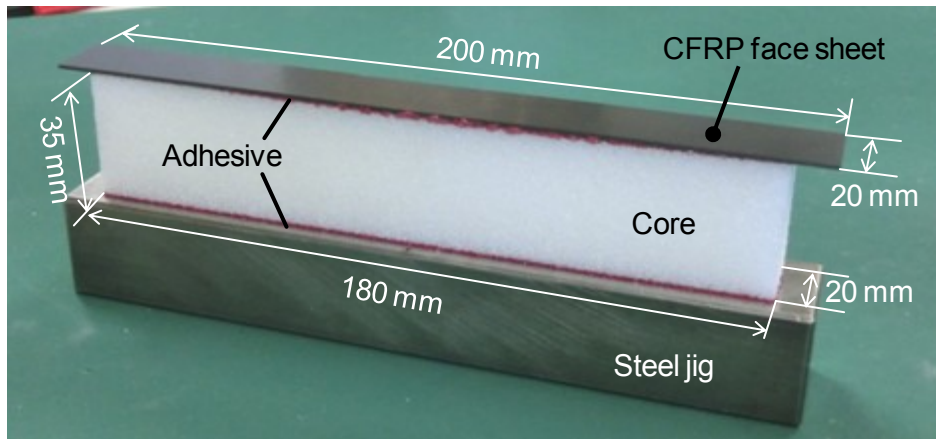


Figure 3.2 Sandwich beam specimen.

### 3.2.3. Test method

Indentation loading tests of the sandwich beams were conducted using a universal testing machine (INSTRON 5566). The experimental setup is shown in Figure 3.3. Quasi-static indentation loading was applied to the center of the sandwich beam specimens using a 10 mm diameter cylindrical steel indenter. The loading was applied at displacement controlled rate of 5 mm/min until 5 mm displacement was reached after which the loading was removed. The cross head displacement and load from the load cell were recorded to produce load-displacement data of the tests. The loading data is scaled by the width of the beams to get comparable values between specimens.

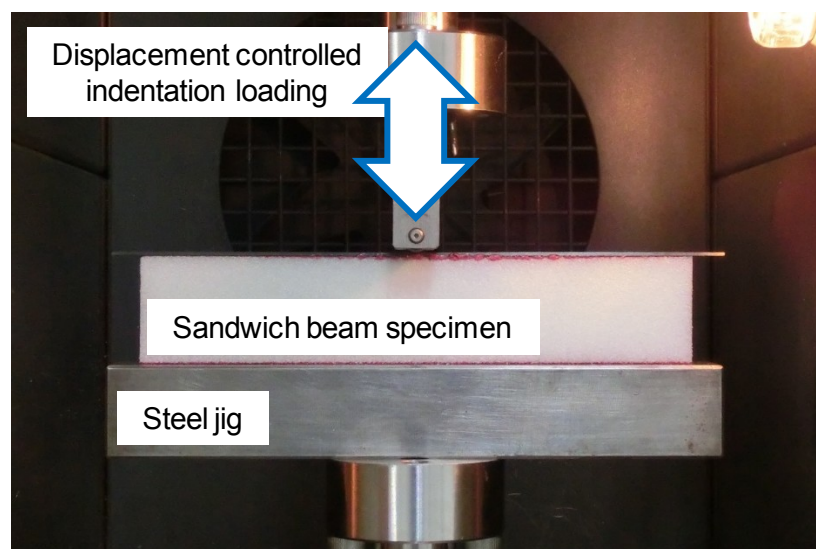


Figure 3.3 Experimental setup of sandwich beam indentation tests.

Two kinds of indentation tests were now conducted: Maximum indentation displacement and maximum indentation loading tests. In maximum indentation displacement tests, the loading was applied until maximum indentation displacement of 5 mm was achieved, after which the loading was removed. This indentation displacement was chosen so that significant maximum deformation was achieved without initiating notable damage in the face sheet or adhesive layer. In maximum indentation loading tests the loading was applied until maximum loading of 600 N (approximately 30 N/mm) was reached, after which the loading was removed. This level of loading was chosen so that the indentation deformation would stay in reasonable limits at all tested hygrothermal conditions.

### 3.3. Moisture diffusion into sandwich beam specimens

The moisture content of the sandwich beam specimens was studied similarly to the foam block specimens in Chapter 2. The foam core part of the sandwich beam was placed in wet and ambient conditions and the moisture content was measured over time. The results are shown in Figure 3.4. The moisture content of the foam block specimens tested at same conditions are also shown for reference with the curves fitted using the Fickian diffusion model in Equation 2.1. The wet condition was now slightly different than in the foam core tests due to slightly higher temperature, and thus resulting in higher moisture content of the specimens. Rapid increase in the moisture content of the wet specimens can be seen in the first hours of the test. This is probably not solely caused by the diffusion, but by some moisture condensed on the open cells at the surfaces of the foam. The specimens were blotted with a cloth before weighing, but some moisture possibly has remained in the faces of the foam at the early stages of the test.

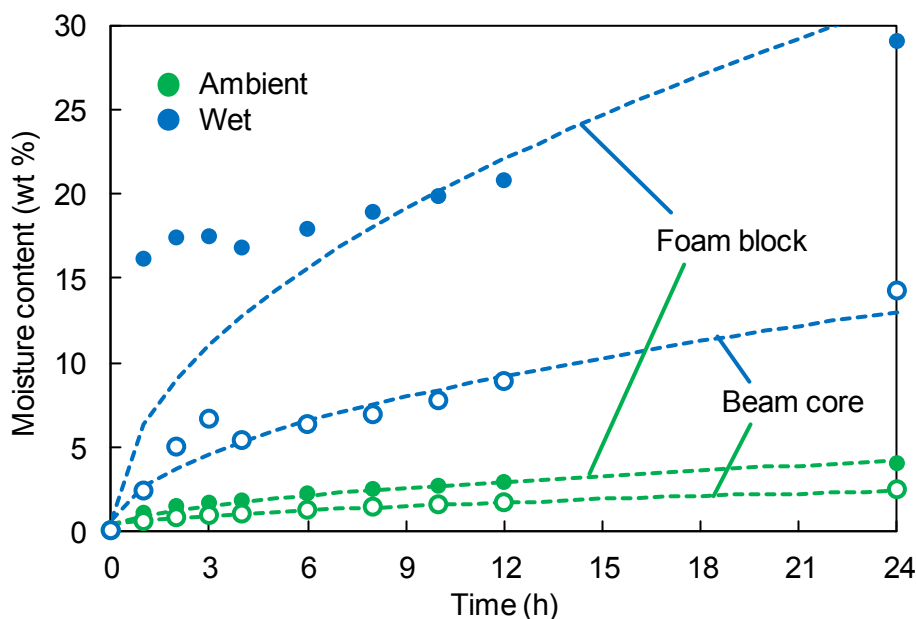


Figure 3.4 Moisture uptake of sandwich beam core over time.

The moisture content of the ambient and wet specimens is quite notably different after the 24 hour conditioning. The beam specimens moisture content is however lower than that of the foam block specimens. Especially for the wet conditions, significant difference can be seen after 24 hours. This is probably caused by the difference in the size of the foam core in the beams and the foam block specimens.

### **3.4. Effect of hygrothermal conditions on face sheet and adhesive**

The effect of temperature and humidity on the CFRP face sheet was also studied briefly. Three point bending tests were done with conditioned CFRP laminates to determine their flexural properties based on the test method in ASTM D790. 8 ply unidirectional T700S/2592 laminate beams were tested at ambient 30°C, dry 80°C and wet 30°C conditions to evaluate the effect of high temperature and high humidity on the bending response. From the three point bending data, the tangent elastic modulus of the specimens was calculated. From these tests it was seen that the high temperature caused around 5% reduction and high humidity around 8% reduction in the tangent elastic modulus of the laminates.

The adhesive film also can be affected by environmental conditions. No experiments were now conducted, but according to the manual of AF 163-2 adhesives [57], the mechanical properties of cured adhesive films can drop by more than 50% of the initial values when temperature is raised from 24°C to 80°C.

The environmental conditions can therefore have effect on the mechanical properties of the face sheet laminates and adhesive layer, and thus on the indentation response of the sandwich structures. However the reduction in the properties of the face sheet is relatively small compared to the reduction in the foam materials properties, but the properties of the adhesive layer might have some effect on the strains in the adhesive layer. Effect of the degraded properties of face sheet and adhesive layer are later studied in the analysis chapter.

## **3.5. Results**

### **3.5.1. Indentation load-displacement response**

Typical indentation load-displacement curves of the specimens under tested humidity conditions at 30°C and 80°C are shown in Figure 3.5 and Figure 3.6. The initial linear elastic part of the load-deflection curves is related to the elastic properties of the foam. After damage initiates in the core, notable change in the slope of the curve can be noticed. From this point on, the load-deflection behavior depends on the face sheets properties and the behavior of the foam material during progressive crushing of the cells.

Corresponding with the uniaxial compression tests of the foam material, indentation strength of the beams decreases with increased humidity. Similarly, as dry uniaxial loading specimens showed higher plateau stresses, higher indentation loading response can also be seen in the dry beam specimens. Some fluctuation in the load response of the dry specimen can be seen after damage initiation. This can be partly caused by the brittle breaking of the core, but also from damage formation in the face sheet, as the dry core provides more support for the face making deformation more local and thus leading to higher bending stresses. On higher humidities the fluctuation seems to disappear and the loading curves become smooth as the foam becomes softer and more ductile from plasticization due to humidity. Effect of humidity is similar also at higher temperatures as can be seen for the 80°C case in Figure 3.6 with the overall stiffness reduced due to the temperature.

Residual deformation of the dry and ambient specimens seem to be similar with each other. This means that the tensile response seems to be less affected at low moisture contents, as was shown in section 2.5.2. For the wet specimen the magnitude of residual dent is notably higher than for the other humidities. Due to the plasticization of the polymer at high humidities, the tensile response changes, as was also seen in the foam loading experiments in section 2.5.2. This causes the foam to resist the pull from the face sheet leading to deeper residual dent in the face. The residual dent will be discussed in more detail in the following section.

Figure 3.7 and Figure 3.8 show typical load-displacement curves for the maximum indentation loading tests at the tested humidity conditions at 30°C and 80°C temperatures. Now, as the maximum indentation load is the same for all specimens, largest difference can be seen in the indentation displacement response. As the stiffness and yield stress of the dry and ambient foams is relatively high, the maximum indentation displacement is smaller. On the wet specimen however the maximum indentation displacement is more than two times larger than in the dry or wet specimens because the compressive loading response of the foam is greatly reduced by the humidity. The larger indentation displacement also means that the face sheet deformation will be larger and thus the core will be damaged on a wider area. At 80°C temperature condition the difference between the humidity conditions is even more notable. Maximum indentation displacement of the wet specimen is now almost six times larger than in the dry and ambient specimens. The combined effect of temperature and humidity therefore seems to be rather severe.

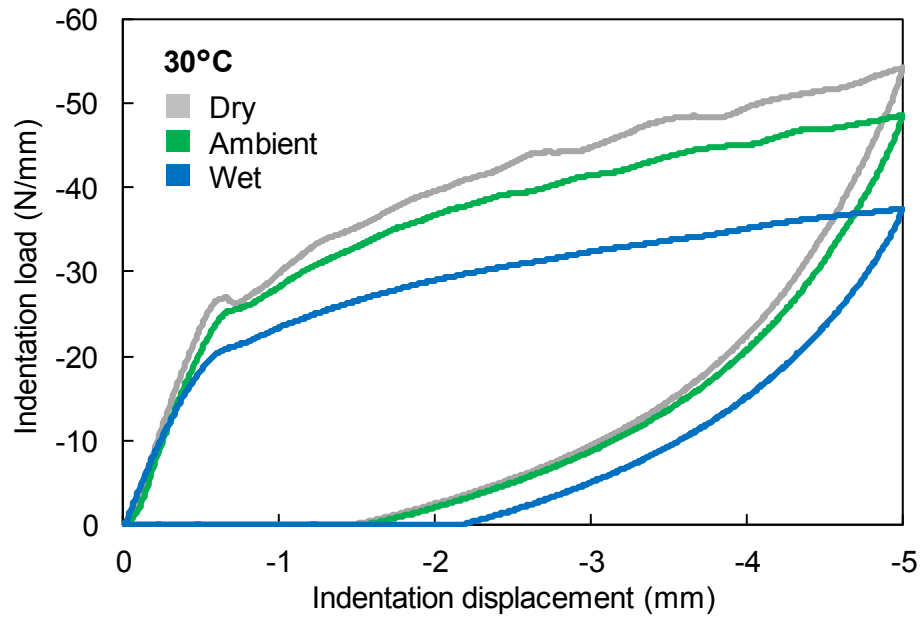


Figure 3.5 Indentation load-displacement response of sandwich beams at 30°C for maximum indentation displacement tests.

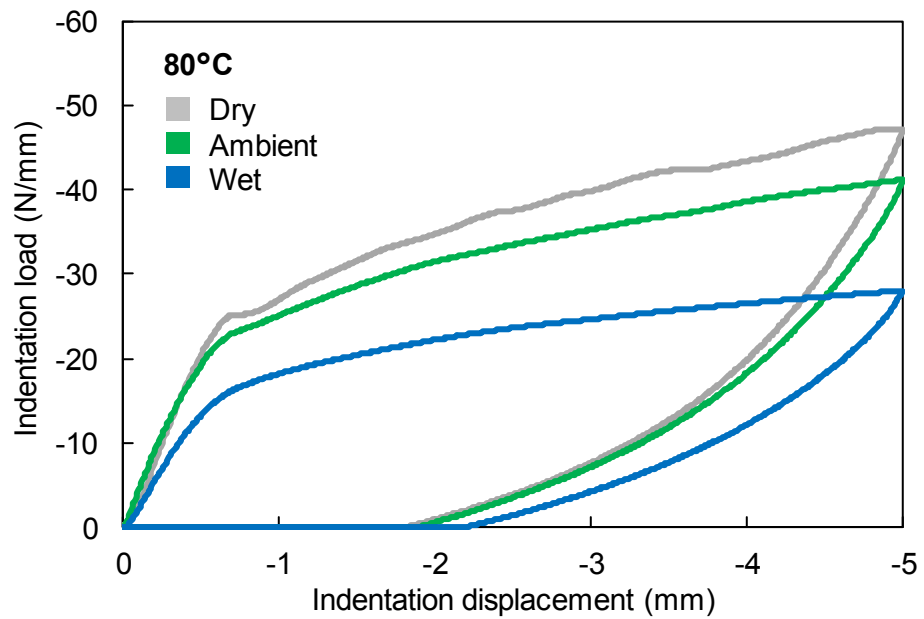


Figure 3.6 Indentation load-displacement response of sandwich beams at 80°C for maximum indentation displacement tests.

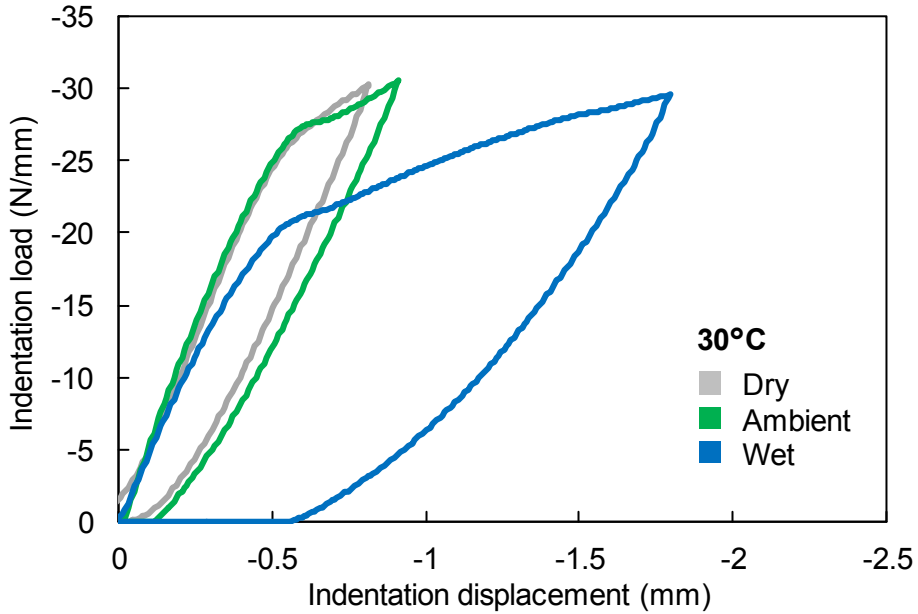


Figure 3.7 Indentation load-displacement response of sandwich beams at 30°C for maximum indentation loading tests.

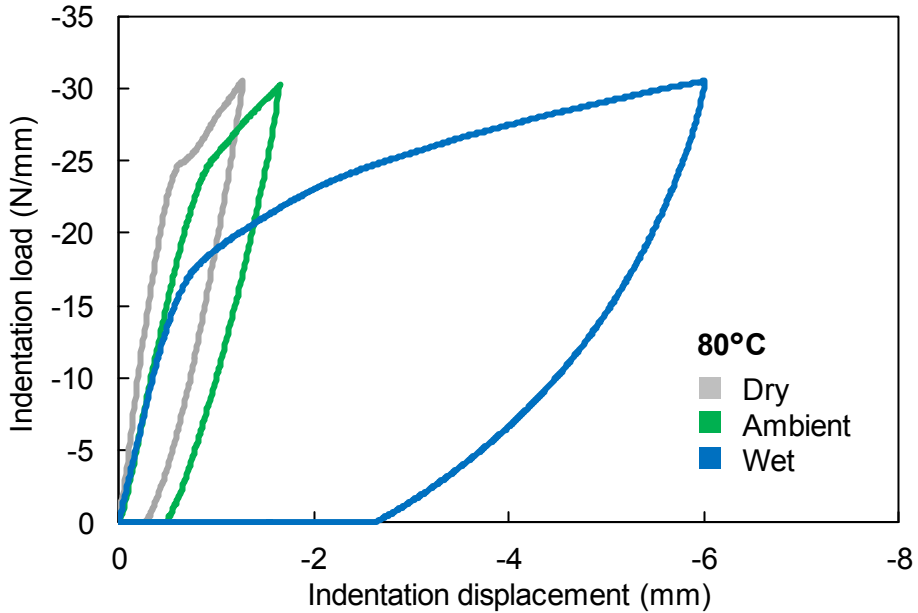


Figure 3.8 Indentation load-displacement response of sandwich beams at 80°C for maximum indentation loading tests.

Typical indentation load-displacement curves of dry and wet specimens under various temperature conditions are shown in Figure 3.9 and Figure 3.10. With increasing temperature the strength of the sandwich beam is reduced as the foam softens under high temperature. In the dry conditions the response of 60°C and 80°C specimens is similar with each other. This response is consistent with the response of dry foam at high temperatures. It therefore seems that around the 60°C to 80°C temperature range the crushing response of the foam does not change notably. Also on the wet beam specimens the loading response keeps degrading with increasing temperature. This comes from the observation that the properties of the foam degrade almost linearly with increasing temperature. Some fluctuation can be seen on the dry beam specimens load-indentation displacement curves. Again the foam seems to be more brittle when its dry even at higher temperatures. The curves of the wet specimens are much smoother due to the effect of humidity on the foams response.

The maximum indentation loading tests the response of dry and wet specimens at various temperature conditions are shown in Figure 3.11 and Figure 3.12. As increased temperature softens the polymer material of the foam, the maximum indentation displacement is increased with larger deformation in the face sheet and core. Response of the higher temperature conditions is quite similar with each other, as was also seen in the maximum indentation displacement tests, and again corresponds with the foams compressive response at these conditions.

Figure 3.13 and Figure 3.14 compare selected temperature and humidity cases to show the combined effect of high temperature and humidity on the indentation response of sandwich beams. It can be seen that high temperature or humidity itself can degrade the indentation strength and stiffness of the beams quite notably, but the combined effect of high temperature and humidity can be even more severe. This is again corresponding with the response of the foam materials behavior at similar conditions, but the properties of the face sheet and adhesive layer can also be slightly degraded due to the hygrothermal conditions. These results clearly show the highly degrading effect that high temperature and humidity can have on the indentation response when combined, as the response under high temperature or humidity conditions only is nowhere near as notable as the response under combined effect of both.

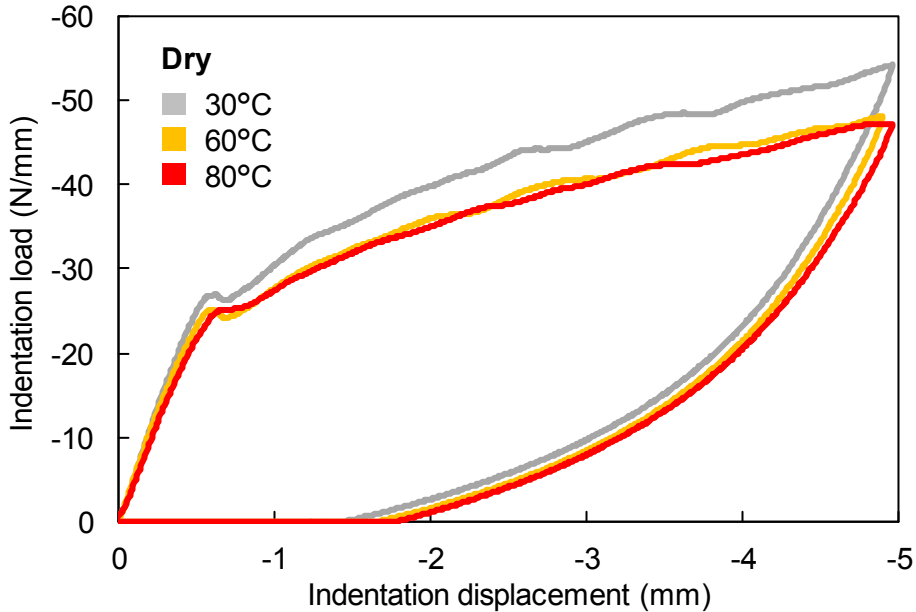


Figure 3.9 Indentation load-displacement response of dry sandwich beams for maximum indentation displacement tests.

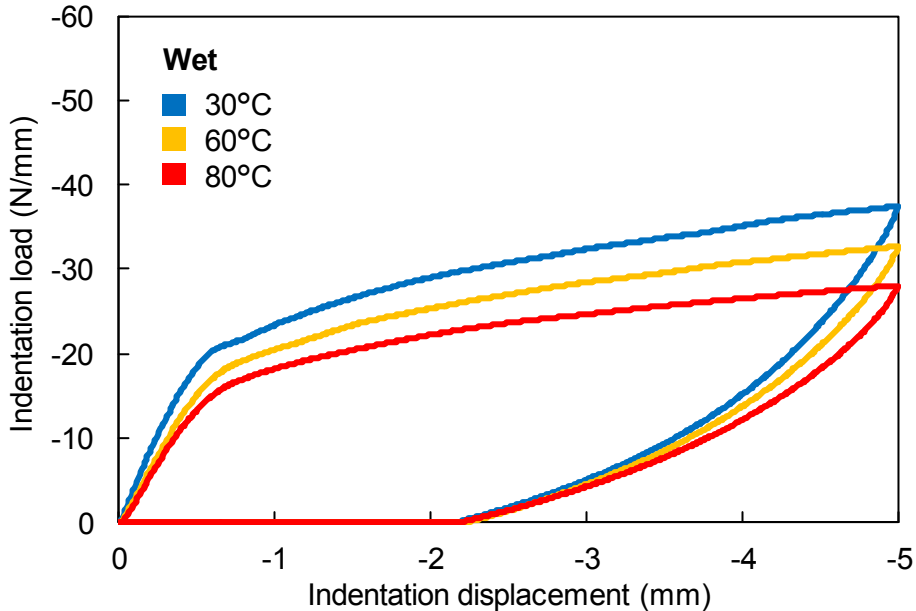


Figure 3.10 Indentation load-displacement response of wet sandwich beams for maximum indentation displacement tests.

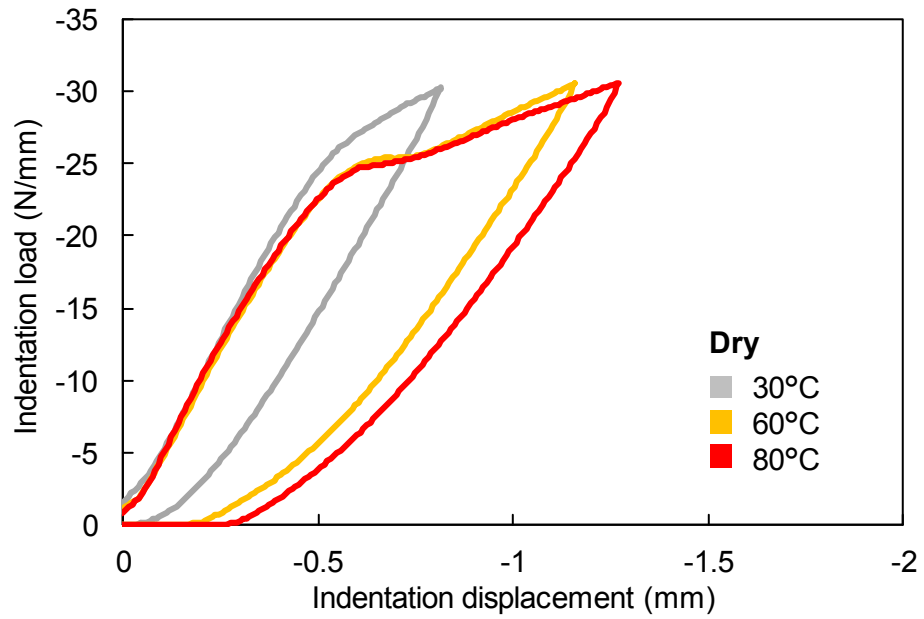


Figure 3.11 Indentation load-displacement response of dry sandwich beams for maximum indentation loading tests.

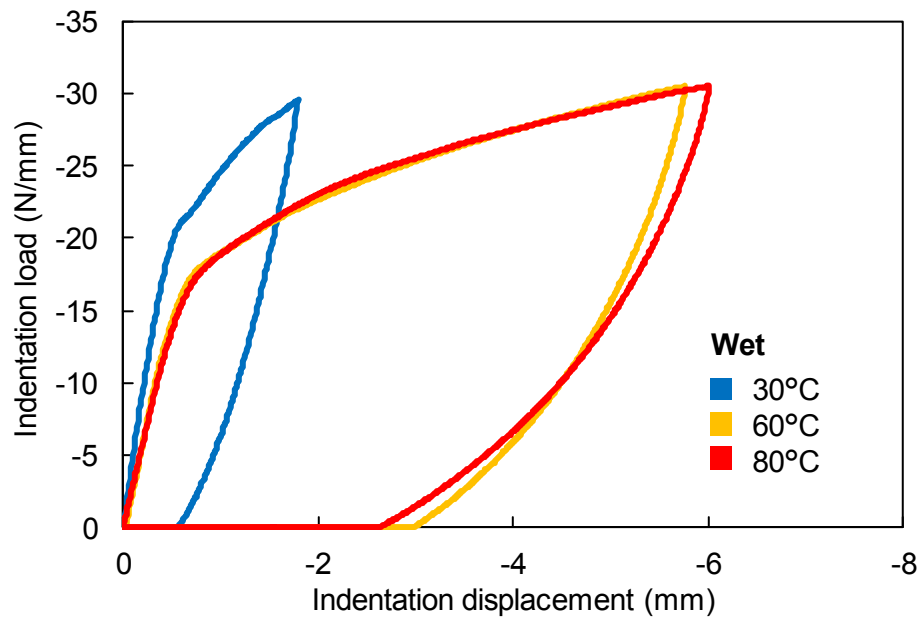


Figure 3.12 Indentation load-displacement response of wet sandwich beams for maximum indentation loading tests.

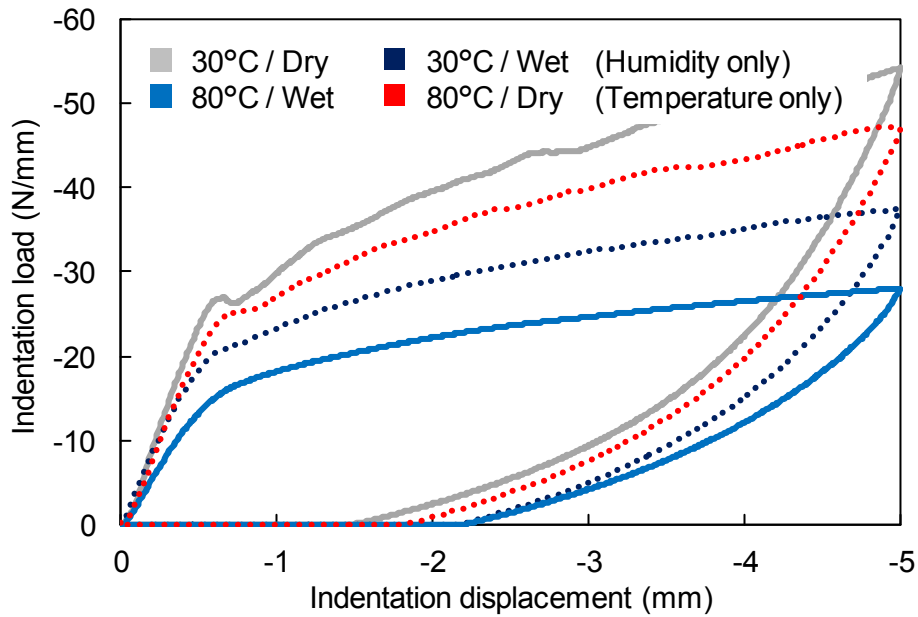


Figure 3.13 Indentation load-displacement response of sandwich beams under various temperature and humidity conditions for maximum indentation displacement tests.

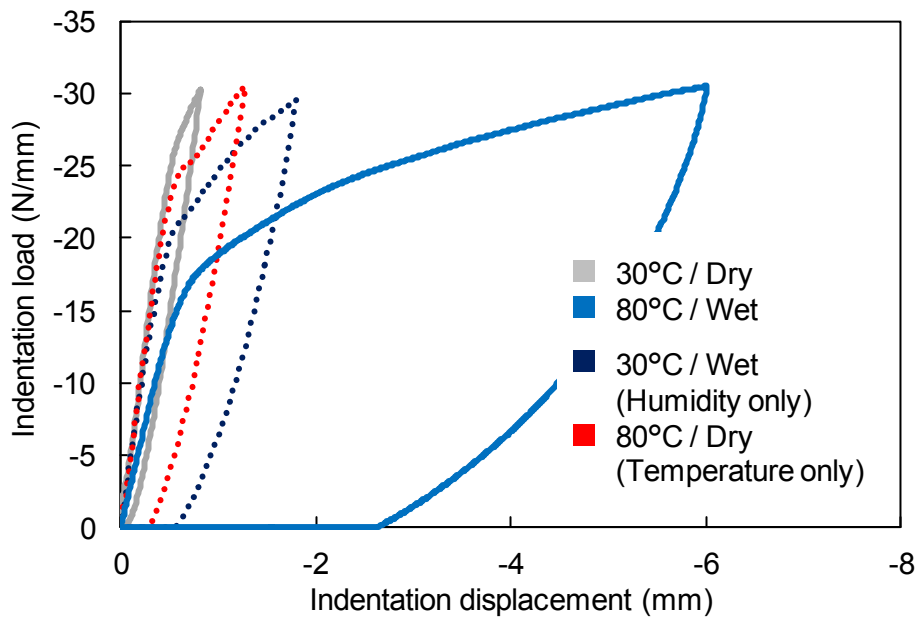


Figure 3.14 Indentation load-displacement response of sandwich beams under various temperature and humidity conditions for maximum indentation loading tests.

### 3.5.2. Face sheet dent

The residual dent depth at tested conditions immediately after unloading is shown in Figure 3.15 for the maximum indentation displacement tests. This clearly shows how the residual deformation increases slightly but gradually with increasing temperature as the foam softens leading to increased amount of plastic deformation in the foam. Difference between the 60°C and 80°C temperature cases is though quite small. Deeper residual dent is also observed at higher humidity conditions. However, when the humidity gets high enough, the residual dent depth seems to settle at a certain value regardless of the temperature conditions. The humidity now seems to dominate the foams response and the increased temperature has limited effect on the indentation response.

The maximum and residual dent depths for the maximum indentation loading tests at the tested conditions are shown in Figure 3.16 and Figure 3.17. With increasing temperature the maximum dent depth becomes slightly larger. Looking at the humidity conditions, the difference between dry and ambient conditions is not very notable. However, at wet conditions the maximum dent depth and thus maximum deformation in the sandwich beam specimen becomes notably larger as the properties of the foam are degraded. Trend with the residual dent depths is similar with the maximum dent depths. As the deformation in the face sheet is larger in the high temperature and humidity specimens, this leads to increased plastic deformation in the core, which again results in deeper residual dent. Again the difference between the wet conditions and the dry and ambient conditions is quite remarkable.

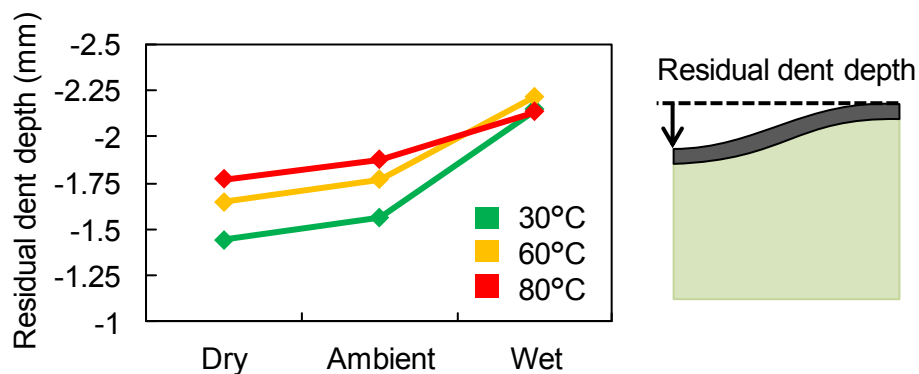


Figure 3.15 Residual dent depth at various temperature and humidity conditions in the maximum indentation displacement tests.

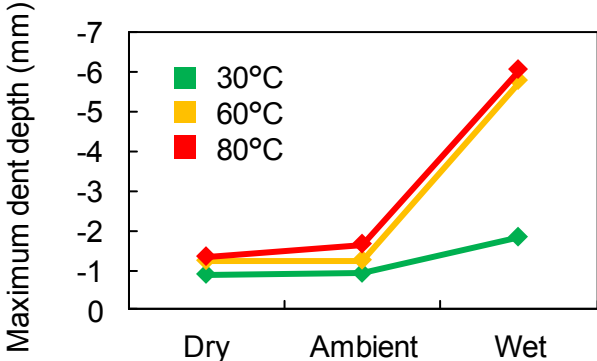


Figure 3.16 Maximum dent depth at various temperature and humidity conditions in the maximum indentation loading tests.

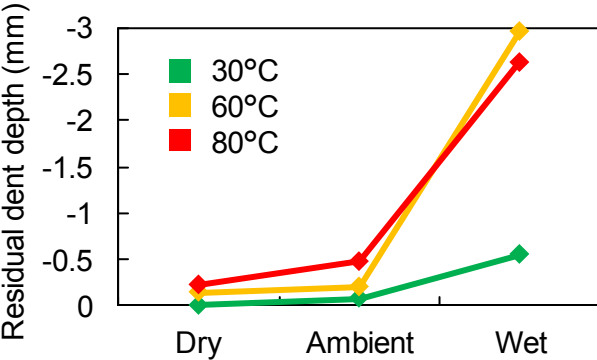


Figure 3.17 Residual dent depth at various temperature and humidity conditions in the maximum indentation loading tests.

It should be noted again that the properties of the face sheet and adhesive layer can also be slightly degraded at high temperature and humidity conditions thus further reducing the indentation strength of the beams. This kind of effect is now assumed to be small compared to the degradation of the foams material, but might still have affected the current results. However, from these results it can be concluded that the indentation response of the sandwich beams seems to be directly related to the loading response of the foam material. If the moisture condition of the core material is known the indentation response of the sandwich structure can then be predicted.

### **3.6. Conclusion**

Indentation loading tests were conducted with foam core sandwich beam specimens. The specimens were conditioned at various temperature and humidity conditions before testing. High temperature and humidity weakened the properties of the core which lead to larger deformation in the face sheet, and thus damaging the core on larger area. Residual dent was also seen to be increased in the high temperature and humidity specimens as higher loading is needed to stretch the crushed core due to extensive plastic deformation. Overall, the indentation loading response was seen to be closely related to the loading response of foam material.

## **Chapter 4. Finite element indentation analysis**

In this chapter, a numerical finite element model based on the sandwich beam specimens tested in Chapter 3 is constructed. By using the material properties obtained in the experiments in Chapter 2 for the foam, the indentation behavior of the sandwich beams is predicted. Effect of the foam core properties on the indentation behavior can thus be verified. Besides predicting the indentation loading behavior of sandwich beams under varying temperature and humidity conditions, the model now allows for detailed observation of damage formation in the core and strains in the core-face sheet interface.

### **4.1. Modeling indentation of sandwich structures**

Various problems regarding sandwich structures have been studied by finite element analysis (FEA) in the past and a comprehensive review is given by [58]. When modeling the indentation or impact of sandwich structures, one of the main considerations is how to model the core material. As the structure of the foam core is very complicated, it is difficult to reproduce its response under varying loading conditions. Many authors have constructed numerical models for closed cell foam materials on micro scale using, for example, unit cell structures [59, 60, 61, 62], Voronoi models [63, 64, 65, 66], and lately by using X-ray computer tomography based meshes [67, 68, 69]. These microscale structures however are very complex and thus the size of the simulated model is very limited.

It is often sufficient to predict the response of the foams using constitutive macromechanical models. Although information on the microscopic behavior of the cells and cell walls regarding damage initiation and progression is lost, quite many constitutive models based on experimental results have been proposed [70, 71, 72, 73] and have shown to give good prediction of the response of sandwich structures. For example, the crushable foam material model included in the ABAQUS finite element analysis software has been used in modeling the indentation and impact response of foam core sandwich structures with good results [36, 50, 74, 75, 76, 77]. The indentation behavior of foam core sandwich structures in this study is thus predicted by finite element analysis using an elasto-plastic model for the foam material.

## 4.2. Modeling of foam core

To model the behavior of the foam, the crushable foam model of ABAQUS [78] was now used. Basically the crushable foam model with isotropic hardening is based on the model of Deshpande and Fleck [70] originally derived for metallic foams and gives the same response in tension and compression. However, ABAQUS also provides an option with volumetric hardening, which uses a slightly modified form of the Deshpande and Fleck's model by accounting for different response in tension and compression. This is more realistic for foams, which often have different strength in tension and compression. The yield surface of the crushable foam model with volumetric hardening is defined by Equation 4.1.

$$F = \sqrt{q^2 + \alpha^2(p - p_0)^2} - B = 0 \quad (4.1)$$

$$q = \sqrt{\frac{3}{2} s_{ij} s_{ij}} \quad (4.2)$$

$$p = -\frac{\sigma_{kk}}{3} \quad (4.3)$$

$$s_{ij} = \sqrt{\sigma_{ij} + pI} \quad (4.4)$$

Here  $q$  is the von Mises stress,  $p$  the hydrostatic (pressure) stress and  $s$  the deviatoric stress (second invariant of stress deviator). The yield surface forms an ellipse in the meridional stress (hydrostatic stress-Mises stress) plane depicted in Figure 4.1.

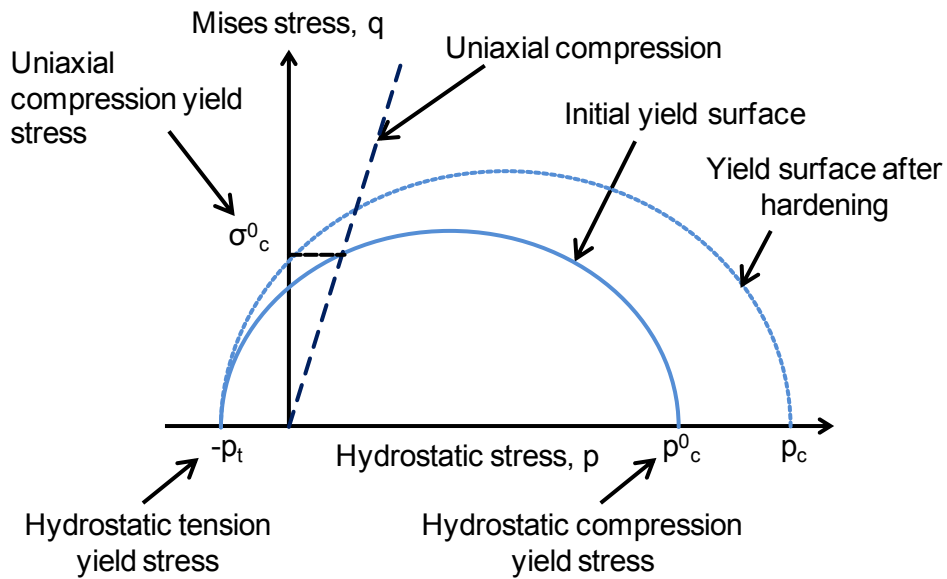


Figure 4.1 Yield surface of ABAQUS crushable foam model [78].

Shape of the yield surface is defined by the parameters A, which is the horizontal size of the ellipse on the p-axis, and B, which is the vertical size of the yield ellipse on the q-axis.  $\alpha$  is a shape factor that defines the relative magnitude of the axes and  $p_0$  the center of the yield ellipse on the p-axis. A, B,  $\alpha$ , and  $p_0$  are defined as

$$A = \frac{p_c + p_t}{2} \quad (4.5)$$

$$B = \alpha A \quad (4.6)$$

$$\alpha = \frac{B}{A} \quad (4.7)$$

$$p_0 = \frac{p_c - p_t}{2} \quad (4.8)$$

where  $p_t$  is the strength of the foam in hydrostatic tension and  $p_c$  the strength in hydrostatic compression. Here compressive stresses are assumed to be positive, which is common practice when considering materials mainly loaded in compression.

Initial shape of the yield surface can be calculated using strength ratio parameters  $k$  and  $k_t$ , which are defined using uniaxial compressive stress  $\sigma_{c0}$ , hydrostatic compressive stress  $p_{c0}$ , and hydrostatic tensile stress  $p_{t0}$  as follows

$$k = \frac{\sigma_{c0}}{p_{c0}} \quad (4.9)$$

$$k_t = \frac{p_t}{p_{c0}} \quad (4.10)$$

For a valid surface, values of these parameters must be in the range  $0 < k < 3$  and  $k_t \geq 0$ . The shape factor alpha can then be defined as

$$\alpha = \frac{3k}{\sqrt{(3k_t + k)(3 - k)}} \quad (4.11)$$

For the plastic flow, a non-associated flow rule is defined so that the flow potential is chosen as

$$G = \sqrt{q^2 + \frac{9}{2}p^2} \quad (4.12)$$

The value 9/2 is now defined based on the plastic Poisson's ratio of the foam. As with many

---

types of foams when they are compressed, there is minimal expansion in the other directions, and so the Poisson's ratio is close to zero. This is achieved using the value  $9/2$  in the plastic flow rule.

During plastic deformation the point  $p_t$  is assumed to be fixed, and the point  $p_c$  on the  $p$ -axis moves based on the hardening behavior. The yield surface evolves in geometrically self-similar manner so that  $\alpha$  stays constant. This means that the tensile direction behaves as perfectly plastic and the compressive direction hardens or softens based on the value of  $p_c$  during loading. Evolution of the value  $p_c$  as function of volumetric compacting plastic strain during plastic loading is done based on hardening data input by the user. As hydrostatic compression tests are often difficult to conduct, the hydrostatic hardening behavior can be specified using uniaxial compression data. Also, as the Poisson's ratio is close to zero during compression, it can be assumed that the uniaxial strain equals volumetric strain in uniaxial compression. Therefore, by assuming uniaxial compression and inserting  $\sigma = \sigma_c(\varepsilon_{ax}^{pl})$  into Equation 4.1 defining the yield surface, we can get an expression for the hydrostatic compressive stress as

$$p_c(\varepsilon_{vol}^{pl}) = \frac{\sigma_c(\varepsilon_{ax}^{pl}) \left[ \sigma_c(\varepsilon_{ax}^{pl}) \left( \frac{1}{\alpha^2} + \frac{1}{9} \right) + \frac{p_t}{3} \right]}{p_t + \frac{\sigma_c(\varepsilon_{ax}^{pl})}{3}} \quad (4.13)$$

The hardening data for the crushable foam model can therefore be calculated from stress-strain curves of uniaxial compression experiments.

### 4.3. Finite element analysis model

Two dimensional model of the sandwich beam specimen, as shown in Figure 4.2, was constructed based on the test specimens in Chapter 3 using ABAQUS finite element analysis software. Due to symmetry only half of the beam was modeled with corresponding symmetric boundary conditions at the symmetry plane. Also, as the sandwich beam specimens were adhered to the rigid support, the model was also rigidly constrained on the bottom side to prevent global bending deformation.

The face sheet, adhesive layer and core were modeled separately. Each layer of the face sheet was also modeled to obtain more detailed strain distribution near the core-face sheet interface. The core was divided into 2 elements in the through thickness direction and the whole model was divided into 90 elements in the beam longitudinal direction. The mesh was found to be sufficient in predicting the transverse loading behavior of the core. Four node plane strain elements with full integration were used for the whole model.

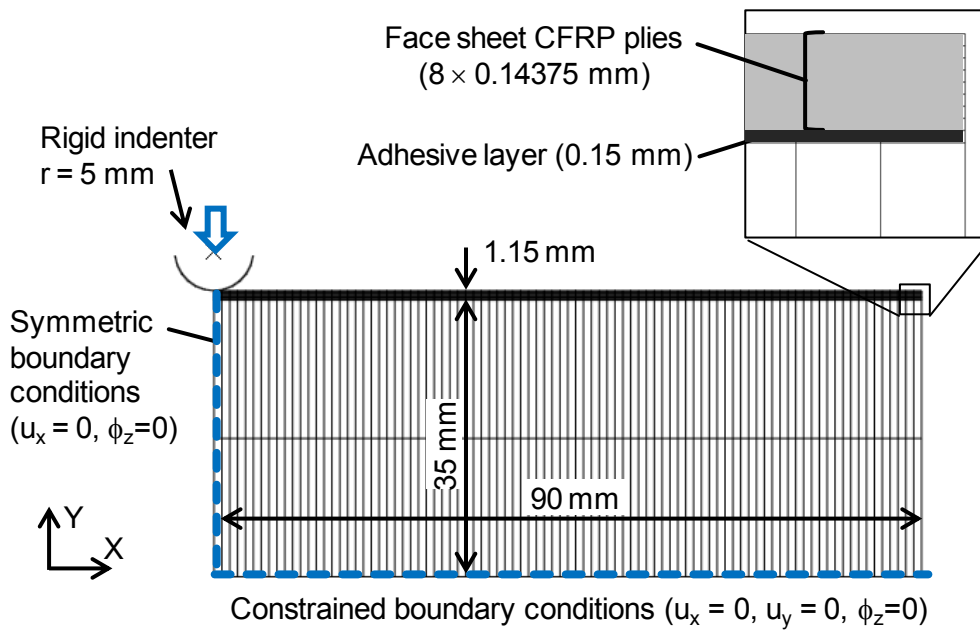


Figure 4.2 Finite element analysis model of sandwich beam indentation.

Simulation was done using the Standard solver of ABAQUS. Large deformations were taken into account by using the nonlinear geometry option. Loading was applied on the beam using a rigid cylindrical indenter with diameter 10 mm and a frictionless contact condition defined between the indenter and face sheet. A displacement controlled boundary condition was applied to the rigid indenter to simulate the indentation tests.

Similarly to the indentation experiments, two kinds of simulations were conducted: Maximum indentation displacement and maximum indentation loading simulations. In maximum indentation displacement, the loading was applied until maximum indentation displacement of 5 mm was achieved, after which the loading was removed. In maximum indentation loading simulations the loading was applied until maximum loading of 600 N (approximately 30 N/mm) was reached, after which the loading was removed.

#### 4.3.1. Materials

Core of the sandwich beam was modeled using the crushable foam material model of ABAQUS explained in previous section. The parameter  $k$  was set as 1.03659 based on the uniaxial stress and pressure stress values experimentally defined for Rohacell 51 WF by Li, Mines et. al. [13]. ABAQUS manual [78] suggests a value of 0.1 for the parameter  $k_t$  defining the tensile behavior of the foam. As the tensile loading behavior is important when simulating the unloading behavior of indentation loaded sandwich structures, the

parameter  $k_t$  was adjusted based on experimental data. As shown in Figure 4.3, tensile yield stress was approximated from the stress-strain curves obtained from the foam loading experiments. Using this tensile stress value, the yield surface of the crushable foam model was adjusted by changing the value of the parameter  $k_t$  until the obtained tensile yield stress was on the yield surface. Hardening data was defined by taking points along the stress-strain curves of the uniaxial compression data in section 2.5.1. The crushable foam model requires hardening input as volumetric plastic strain and volumetric stress, and therefore the stress-strain data was transformed into suitable format as explained in section 4.2. For the elastic part of the foam, the Poisson's ratio was defined as zero and the elastic modulus was taken from the experimental data in Chapter 2. Used parameter values for the tested cases are listed in Table 4.3.

The face sheet laminates were modeled as purely elastic as the loading was assumed to be so low that no notable damage will initiate in the faces. Therefore a linear elastic material model using engineering constants was used for each layer of the face sheet representing one ply of prepreg. Material properties for one unidirectional ply made of T700/2952 CFRP prepreg are shown in Table 4.1. The adhesive layer between the core and the face sheet was modeled with isotropic linear elastic material. Material properties of the adhesive layer are shown in Table 4.2.

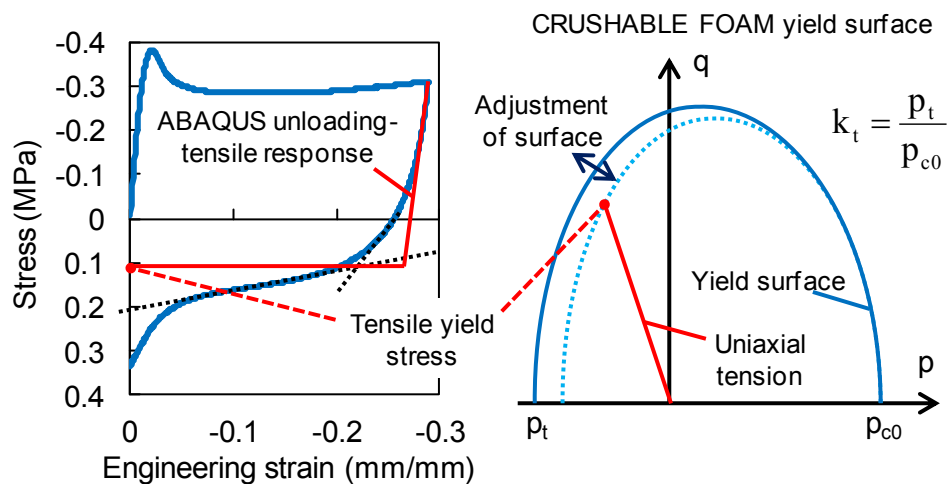


Figure 4.3 Adjustment of the yield surface based on the approximated tensile yield stress of the foam.

Table 4.1 Elastic material properties for T700S/2952 CFRP (one ply) [79].

Young's modulus	$E_1$	135 GPa
	$E_2, E_3$	8.5 GPa
Poisson's ratio	$\nu_{12}$	0.34
	$\nu_{13}, \nu_{23}$	0.49
Shear modulus	$G_{12}$	4.8 GPa
	$G_{13}, G_{23}$	2.7 GPa

1: Fiber direction

2: Fiber transverse direction (in-plane)

3: Through thickness direction

Table 4.2 Elastic material properties of adhesive layer [57].

Young's modulus	$E$	1.1 GPa
Poisson's ratio	$\nu$	0.33

Table 4.3 Material parameters used for the crushable foam material.

		$E$ (MPa)	$\sigma_y$ (MPa)	$k_t$
30°C	Dry	49.18	1.026	0.030
	Ambient	46.44	0.912	0.028
	Wet	32.53	0.606	0.079
60°C	Dry	44.86	0.877	0.035
	Ambient	39.15	0.755	0.043
	Wet	23.05	0.404	0.090
80°C	Dry	44.32	0.830	0.039
	Ambient	36.71	0.648	0.046
	Wet	19.80	0.322	0.075
For all conditions		$\nu = 0$	$k = 1.03659$	

## 4.4. Results

### 4.4.1. Indentation load – displacement response

The predicted load-displacement curves of the indentation simulations at 30°C and 80°C are presented together with the experimental results in Figure 4.4 and Figure 4.5 for the maximum indentation displacement tests, and in Figure 4.6 and Figure 4.7 for the maximum indentation loading tests. During indentation loading the finite element analysis prediction seems to correspond well with the experimental results. The initial elastic response is also close to the experimental data, which verifies that the chosen elastic modulus of the foam seems to be feasible.

On the wet specimen at 80°C temperature the prediction is quite notably off from the experimental values, which might be caused by the moisture content of the beams foam core being lower than the moisture content of the foam specimens whose properties were used when modeling the beam. The moisture content of the foam core in the model is therefore higher than that of the experiments leading to lower stiffness and strength, and thus lower indentation response.

During unloading the prediction diverges from the experimental results. On the maximum indentation loading case it can however be seen that the smaller the deformation is, the closer the prediction is to the experimental results. This is obviously due to the loading response of the core being mostly comprised of compression, elastic unloading and elastic tension, and thus the plastic tensile response has less effect on the overall response. In all of the cases the residual indentation depth however seems to be somewhat close to the experimental ones. The adjustment of the tensile yield parameter of the crushable foam material model therefore seems to give decent prediction of the unloading response.

As summary the crushable foam model seems to give good prediction of the indentation response during the loading phase. High temperature and humidity condition gave less accurate prediction probably due to the moisture content of the sandwich beam being different than that of the foam whose material properties were used. The prediction of the unloading response is also less accurate, although prediction of the residual state seems to be somewhat accurate.

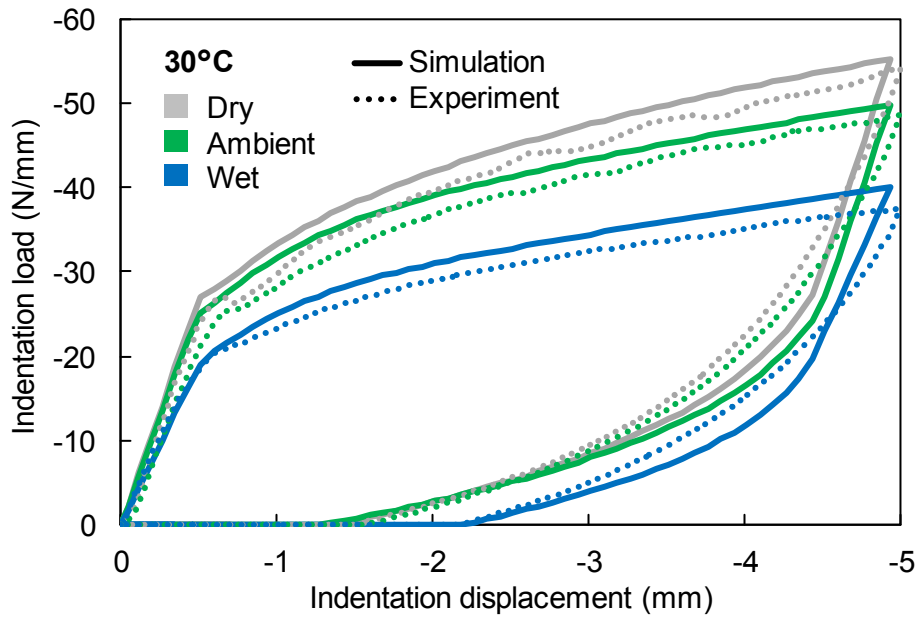


Figure 4.4 Predicted indentation load-displacement response of sandwich beams at 30°C loaded to maximum displacement.

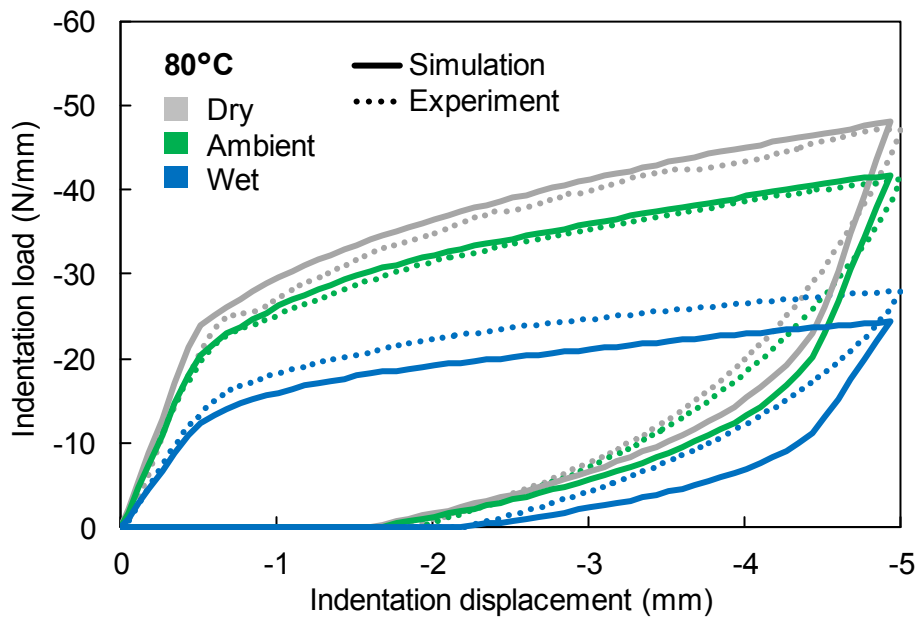


Figure 4.5 Predicted indentation load-displacement response of sandwich beams at 80°C loaded to maximum displacement.

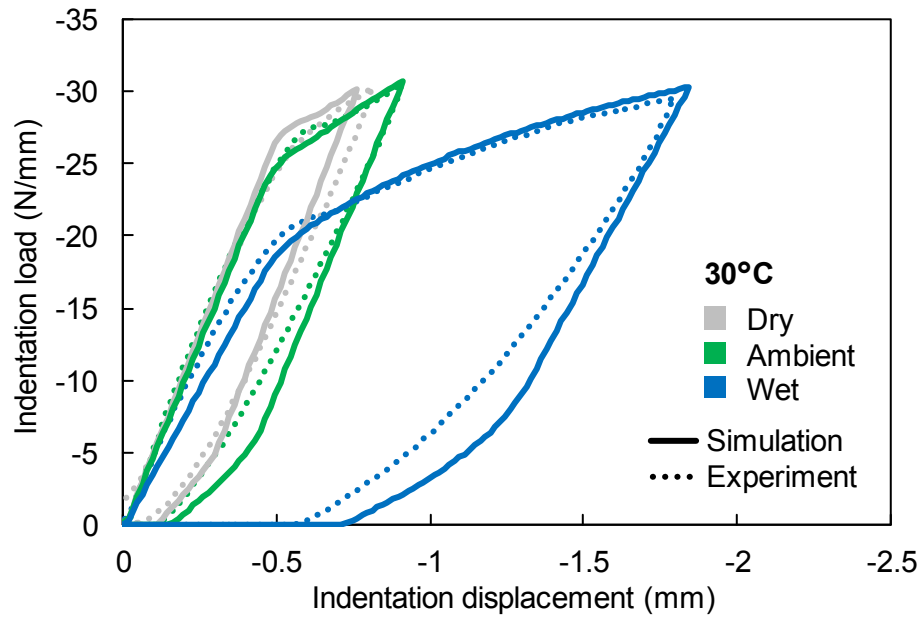


Figure 4.6 Predicted indentation load-displacement response of sandwich beams at 30°C loaded to maximum loading.

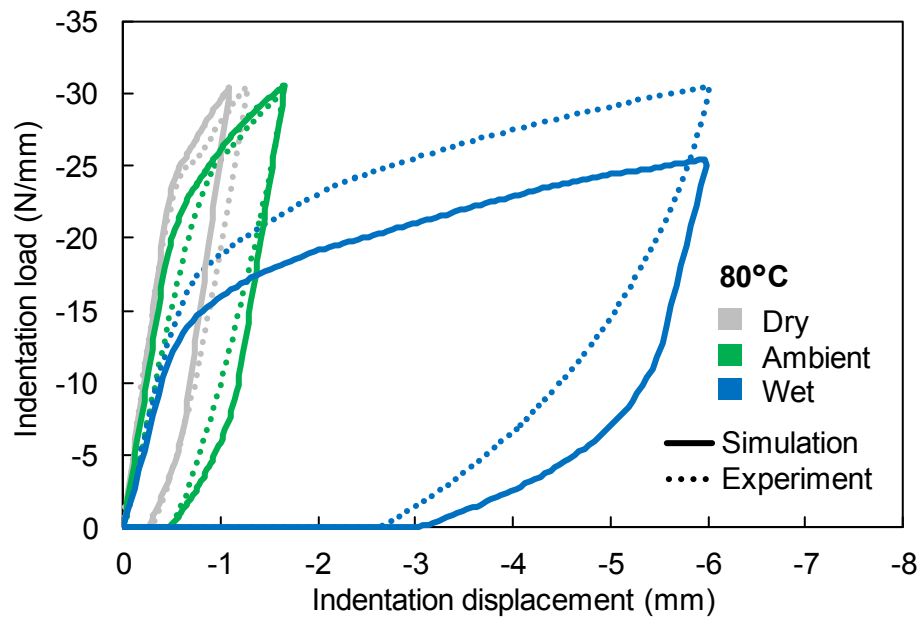


Figure 4.7 Predicted indentation load-displacement response of sandwich beams at 80°C loaded to maximum loading.

**4.4.2. Face sheet dent**

Dent profiles for 30°C specimens are shown in Figure 4.8 and Figure 4.9. For the maximum indentation displacement tests the effect of humidity can be seen as wider dent during loading due to the weakened core. For maximum indentation loading tests significant difference can be seen between the humidity conditions based on the stiffness and strength of the foam material. After the loading has been removed, the dent in the wet specimens is deeper and wider due to plastic deformation in the core. Similar response is seen at higher temperatures also, with the dent being widest at the high temperature and humidity conditions.

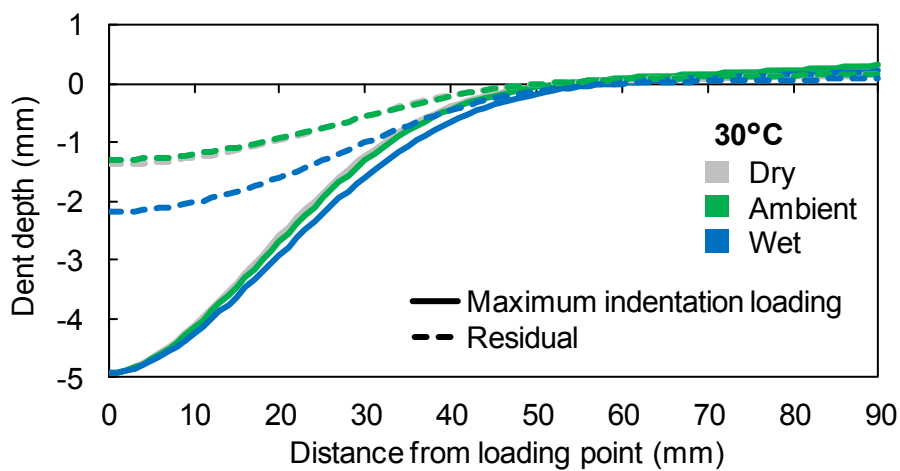


Figure 4.8 Predicted dent profiles during and after indentation for maximum indentation displacement tests.

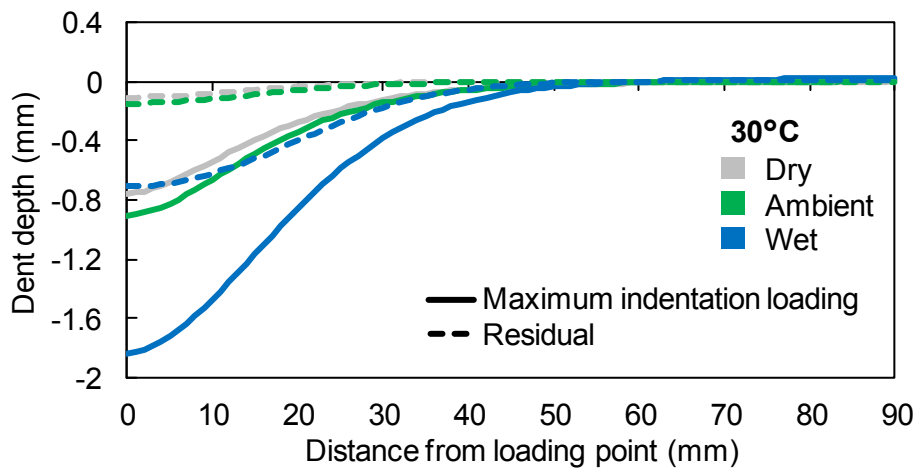


Figure 4.9 Predicted dent profiles during and after indentation for maximum indentation loading tests.

As the residual dent is one of the signs of indentation damage, Figure 4.10 and Figure 4.11 compare the predicted residual dent depth with experimental results for the maximum indentation displacement and maximum indentation loading cases. In general

the predicted residual dent depths are slightly smaller than observed in the maximum indentation displacement case. This is mostly due to the simplified tensile response of the foam material, as it cannot sufficiently resist the pulling force from the face sheet. On the other hand, the predicted dent depths are larger in the maximum indentation loading case. This is again due to the tensile yield stress value being too high for the amount of deformation in the core.

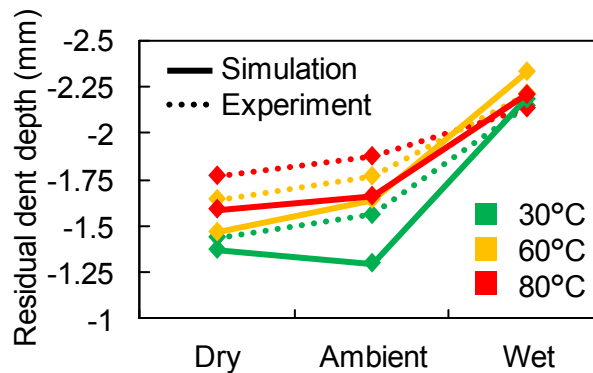


Figure 4.10 Predicted and experimental residual dent depths for the maximum indentation displacement case.

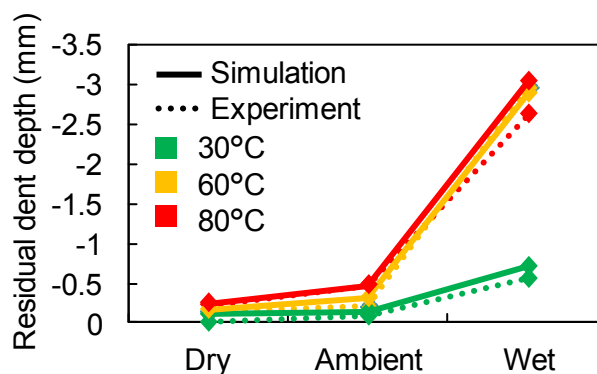


Figure 4.11 Predicted and experimental residual dent depths for the maximum indentation loading case.

The trend is however similar with the experiments in that the residual dent becomes deeper with increased temperature and humidity, due to the tensile yield stress of the core increasing accordingly. In the 80°C wet condition of the maximum indentation loading case the predicted dent depth is though larger than the experiments. This is caused by tensile yielding occurring at the edges of the beam due to high indentation displacement during the test. The yielded elements can no longer support the face sheet at the edges of the beam, and the residual dent thus becomes deeper than expected.

The predicted residual dent depth depends largely on the tensile response of the foam. As the crushable foam model uses only one constant parameter,  $k_t$ , in defining the tensile yield stress, the value of the  $k_t$  parameter should be carefully adjusted based on the maximum deformation in the foam. This however would require different values for each element as the amount of compressive deformation in the core varies along the length of the beam.

#### **4.4.3. Strains in core-face sheet interface**

Next, the strains in the core-face sheet interface are discussed. Highest strains in the sandwich beams longitudinal direction are observed in the adhesive layer due to the bending of the face sheet. Figure 4.12 and Figure 4.13 show the maximum and residual longitudinal strains in the adhesive layer for the maximum indentation loading case as 30°C temperature condition for the maximum indentation displacement and maximum indentation loading tests respectively. The strains are mostly related with the face sheet dent. Looking at the maximum indentation displacement case, it can be seen that the strains during maximum indentation are decreased with increasing humidity. This is due to the weakened properties of the foam, leading to wider face sheet dent and thus lower bending induced strains. The residual strains are however higher due to the increased plastic deformation in the core. In the maximum indentation loading tests the strains during maximum indentation are increasing at higher humidity conditions due to the larger deformation of the face sheet. Again the residual strains are also higher for the wet case as the core experiences notable plastic deformation.

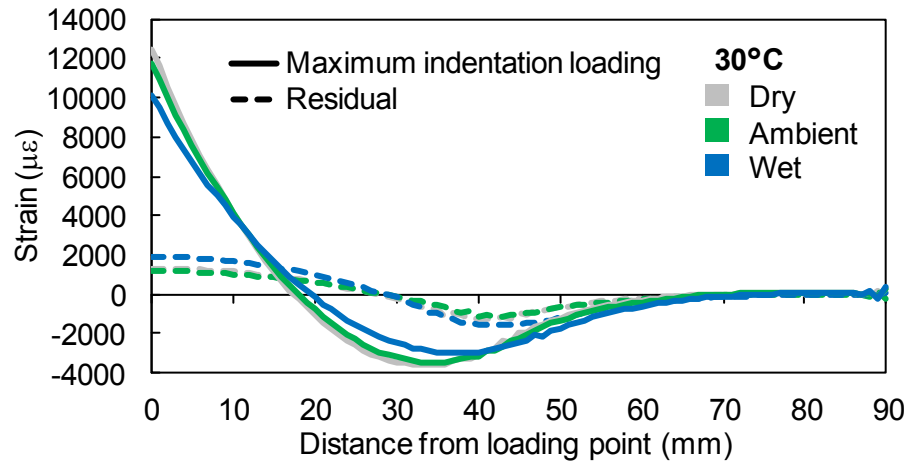


Figure 4.12 Longitudinal strains in the adhesive layer for the maximum indentation displacement tests.

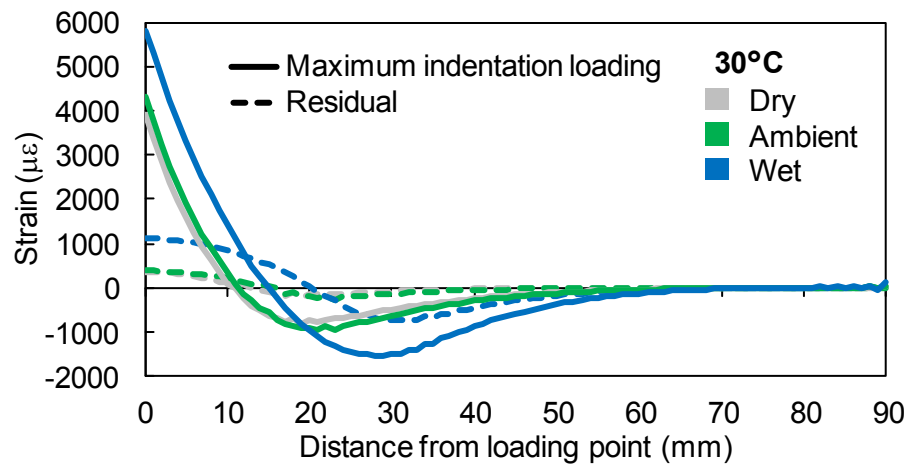


Figure 4.13 Longitudinal strains in the adhesive layer for the maximum indentation loading tests.

#### 4.4.4. Damage in core

The damage area of the core can be estimated by looking at the plastic strains in the core as shown in Figure 4.14. As yielding initiates in the core elements, their plastic strain becomes nonzero. This can therefore be taken as an indicator of damage initiation in the core. Figure 4.15 shows the half size of the damaged core area from the loading point, which is the distance where the plastic strain of the core elements becomes zero, during maximum indentation loading. It shows how the damaged core area widens with increasing temperature and humidity as the yield stress and stiffness of the core is reduced. Quite notable differences can be seen at wet conditions, while the difference is similar between dry and ambient conditions. The effect of temperature seems to increase at higher humidity conditions. The size of the damaged area is also related with the face sheet dent, as the width of the dent obviously changes according to the damaged area.

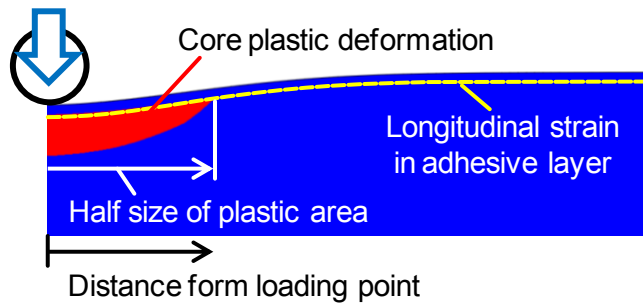


Figure 4.14 Estimation of damage in core from area of plastic deformation.

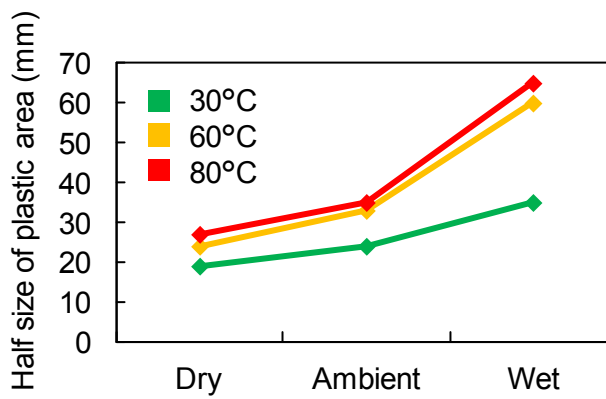


Figure 4.15 Predicted half size of plastic area in the core at various temperature and humidity conditions.

The formation of residual strains can be observed by looking at the strains in the adhesive layer during the unloading phase as shown in Figure 4.16 for the 30°C ambient maximum indentation displacement case. The maximum strain peak at the loading flattens out and the highest strains are reduced to close to 10% of the maximum values. The tensile strain area also widens during the unloading as the face sheet is unbent and the compressive strains near the edge of the damaged core area are reduced and move further away from the loading point. The compressive strain peak seems to settle near the edge of the damaged core area. The residual strain distribution could therefore be used as a way to define the size of the damage in the core. Figure 4.17 shows the residual strain distribution in the adhesive layer at various humidity conditions compared with the plastic strain distribution indicating damage in the core. The tensile strain peak of the residual strain distribution seems to be located near the edge of the damaged core area with the highest strain area being on the damaged core side. This information is later on useful for the damage detection purposes.

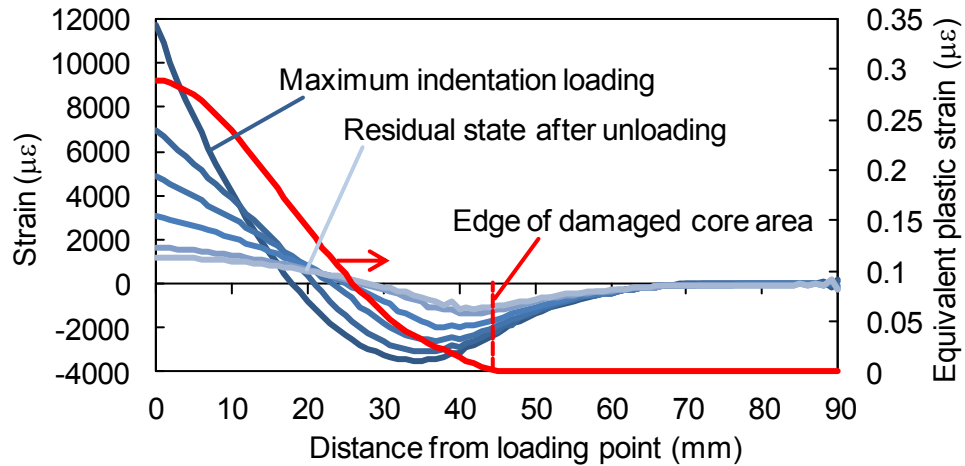


Figure 4.16 Strain distribution in the adhesive layer during unloading.

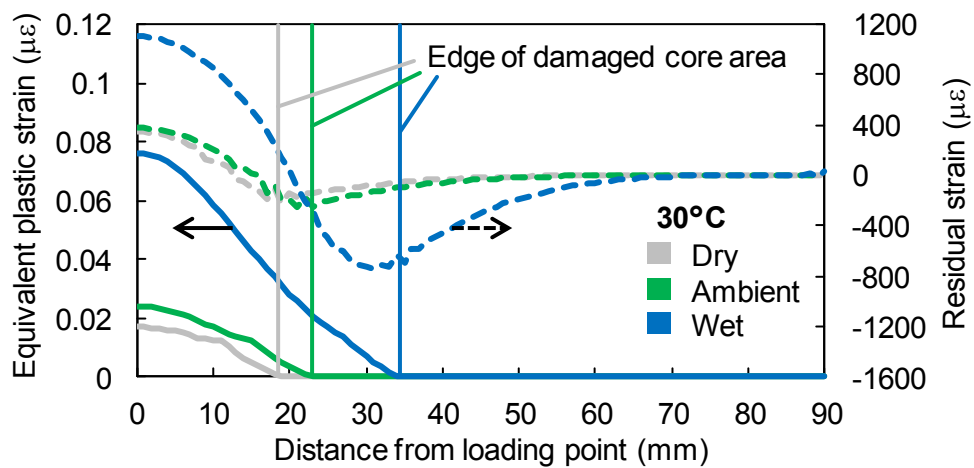


Figure 4.17 Core plastic strain distribution compared with residual strain distribution in the adhesive layer.

#### 4.5. Discussion on mesh and model parameters

Increasing the number of element in the thickness direction of the core causes convergence problems during solution calculations. This can be somewhat helped by loosening the convergence condition tolerances of the solver. One issue also causing problems during the solution calculations is softening behavior in the foams plastic loading response. Sudden softening of the foam after the yield causes sudden large deformations in the yielded elements and increased loading in the surrounding elements. This can be overcome by ignoring the yield peak in the foam materials compressive stress-strain response and thus modeling the foam with pure hardening. This leads to lower yield stress to be used, but allows higher density meshes to be used.

However, another problem arises from the smaller elements. Due to the elements being smaller the stresses in the core at the edges of the beam near the face sheet, where the face exerts tensile loading on the core during maximum indentation loading, are notably higher than with more coarse mesh. Now as the tensile yield stress of the foam is adjusted based on the tensile response after compression, the yield stress is much smaller than it would be for undamaged foam as illustrated in Figure 4.18. This causes the foam core elements to yield under tension at the edges of the beam near the face sheets and thus gives unrealistic results as depicted in Figure 4.19. To avoid this, the  $k_t$  parameter of the crushable core material model needs to be adjusted so that the tensile yield stress is high enough to prevent this kind of yielding. The higher tensile yield stress then however leads to less accurate prediction of the unloading response after indentation loading is removed.

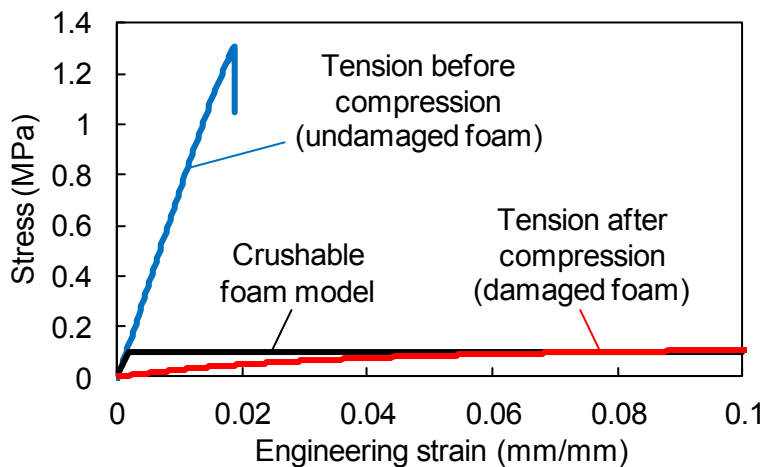


Figure 4.18 Tensile response of foam before and after compression.

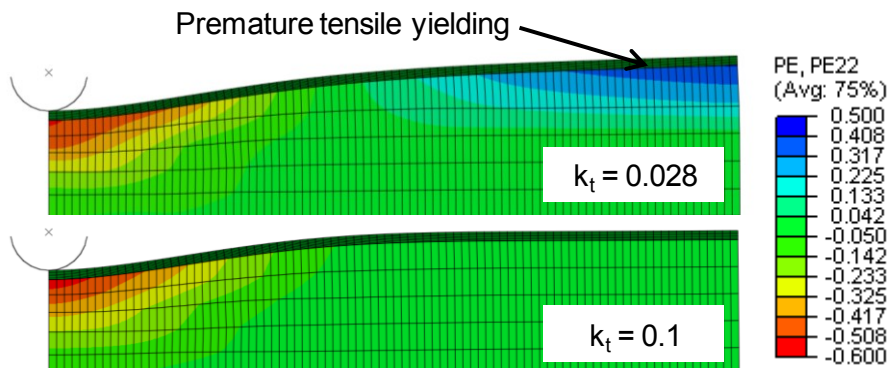


Figure 4.19 Transverse plastic strains in the upper part of the core during maximum indentation loading.

Figure 4.20 shows the indentation load-displacement curves for the used model which follows the experimental hardening behavior of the foam, and model with pure hardening behavior and denser mesh (10 elements through thickness). The value for the parameter  $k_t$  for the pure hardening model was chosen as 0.1 for all conditions. Due to the yield stress peak being ignored in the foams loading behavior, the slope of the curves when the core crushing initiates becomes shallower. Also the loading is slightly reduced in the beginning due to the pure hardening behavior having lower plastic stresses at the beginning of yielding. Most notable difference can be seen during the unloading. As higher tensile yield stress value needed to be used for the pure hardening model, the unloading response changes accordingly. The residual deformation also converges to same point due to the  $k_t$  parameter being same for all conditions and causes the residual strain distributions in the adhesive layer to differ notably from the model with experimental hardening data as shown in Figure 4.21.

The crushable foam model is therefore most suited to model the compressive response of the foam, but has limitations when trying to accurately predict the tensile response after compressive damage.

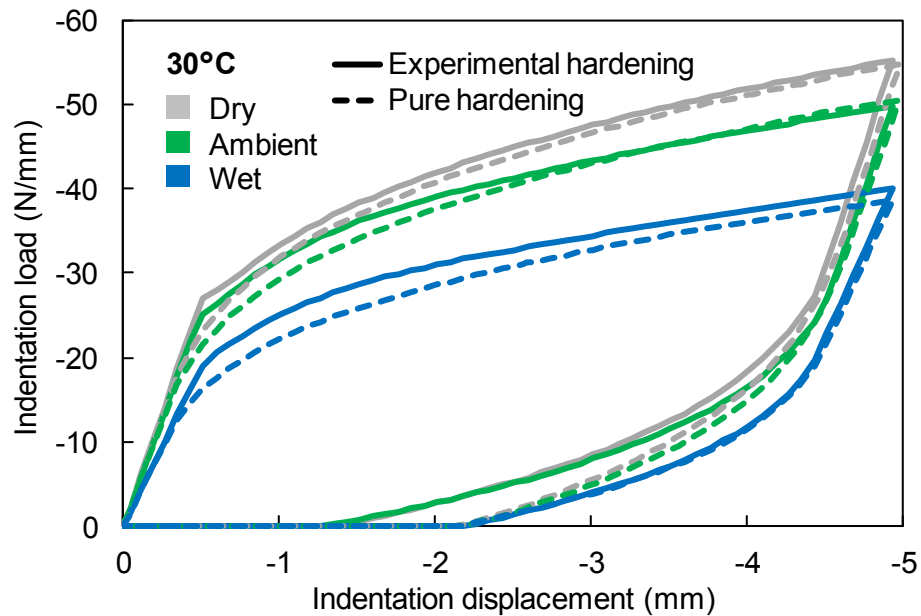


Figure 4.20 Indentation load-displacement curves for models with different mesh density and hardening behavior.

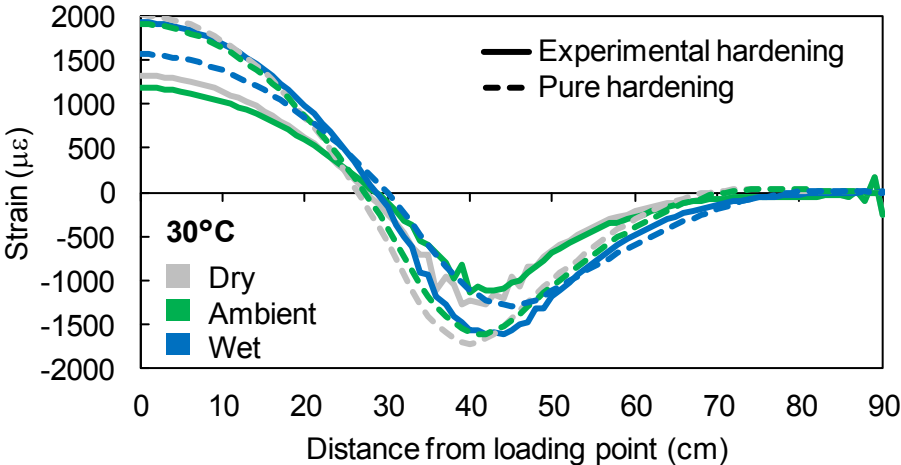


Figure 4.21 Residual strain distributions for models with different mesh density and hardening behavior.

### 4.6. Degraded properties of face sheet and adhesive layer

As was mentioned in section 3.4, the high temperature and humidity conditions can degrade the properties of the composite face sheet and the adhesive layer, and thus have effect on the indentation response of the sandwich structure. This was now also studied using the FEA model by degrading the elastic properties of the face sheet by 10% and the adhesive by 50% to simulate extremely degraded condition. The effect on the indentation load-displacement response is shown in Figure 4.22. The loading response of the degraded model is now slightly lower, but still does not differ significantly from the original model. The maximum strains in the adhesive layer during the maximum loading and after unloading were increased by approximately 6% due to the lower stiffness of the adhesive. Example of the effect on the residual strain distribution is shown in Figure 4.23.

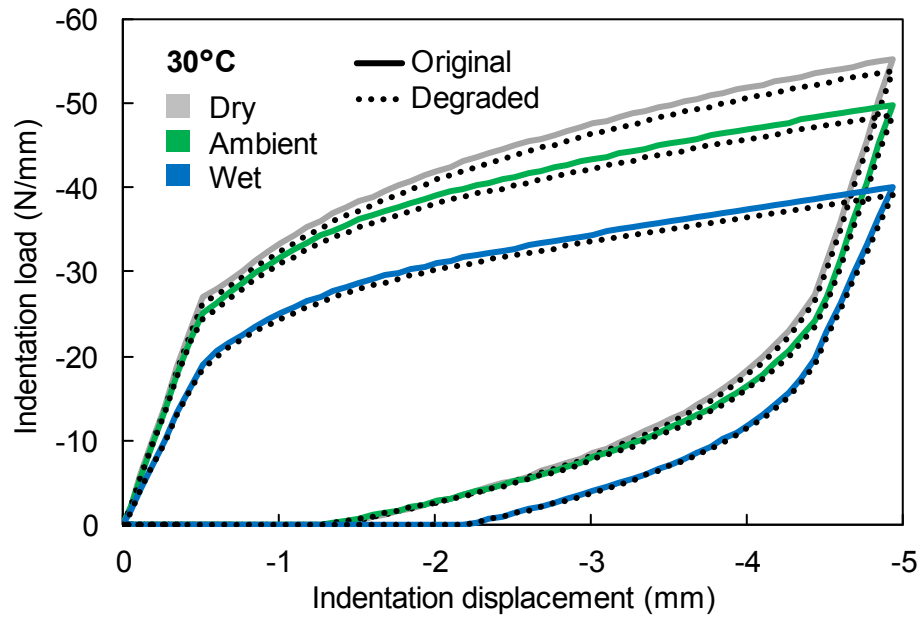


Figure 4.22 Effect of degraded face sheet and adhesive layer properties on the indentation load-displacement response.

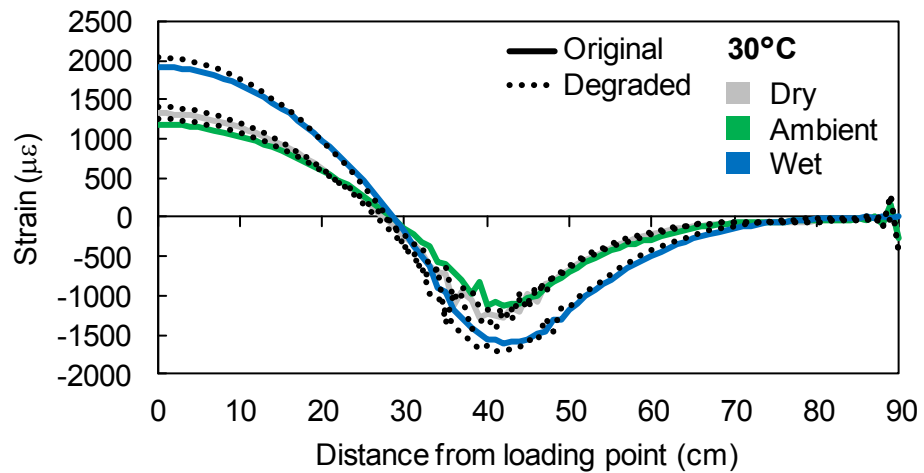


Figure 4.23 Effect of degraded face sheet and adhesive layer properties on the residual strain distribution.

## **4.7. Conclusion**

The indentation loading response of sandwich beam specimens was studied by finite element analysis. Behavior of the core was modeled using crushable foam material model in the ABAQUS software. The parameters of the model were adjusted against the experimental data obtained from the foam loading experiments. Indentation response of the sandwich beams specimens was then predicted at various temperature and humidity conditions. The predicted response correlated well with experimental data during the loading phase. Damage formation and the internal state of the sandwich beams during indentation loading could therefore be examined with regards to the experimental results. Due to the crushable core models limitations, the response during unloading and residual state prediction were less accurate but gave still approximate results due to careful calibration with experimental data. Other modeling aspects regarding the indentation of sandwich structures were also discussed.

## **Chapter 5. Improved model for indentation analysis**

In this chapter the shortcomings of the crushable foam material model in ABAQUS are discussed. Focus is especially put on the prediction of the unloading behavior in indentation loading analysis. An improved model is then constructed to overcome some of these limitations in the original material model. The new model is calibrated using experimental data and used to predict the response of sandwich beam during indentation loading cycle. Results are then compared with experimental results and predictions made using the crushable foam material model.

### **5.1. Limitations of crushable foam material model**

Previous studies have also shown that the crushable foam model gives good results during the loading phase, but as was discussed in section 4.5, the crushable foam model of ABAQUS has some limitations and is not so good when predicting the unloading response and residual state [50]. These mostly concerned the unloading and tensile response of the foam material. For example, it has been previously shown that the unloading modulus of the Rohacell 51 WF foam degrades with increasing compressive strain [80]. However, this kind of behavior is not included in the crushable foam model thus leading to less accurate prediction of the unloading response. Also, the tensile response of the crushable foam model is notably simplified and the tensile response differs notably from experimentally observed behavior. The tensile response can be adjusted to some extent to estimate the experimental response, but this often leads to problems with smaller element sizes, as the tensile yield stress becomes lower than expected. A new improved model is therefore now presented to overcome these limitations and to obtain more accurate prediction of the unloading behavior and of the residual state after unloading.

## 5.2. New improved model

### 5.2.1. Constitutive model

The new material model was implemented into ABAQUS as an explicit VUMAT FORTRAN user subroutine. The explicit solver was chosen as it provides easy implementation of the material model and can later be easily extended for high strain rate problems, such as high velocity impacts. The model is now only implemented for two dimensional plane strain elements, so that it is comparable with the Crushable foam model of ABAQUS which in two dimensional cases is limited to only plane strain elements.

During elastic deformation the behavior is modeled as isotropic based on Hooke's law. The stiffness parameters  $K$  (bulk modulus),  $G$  (shear modulus) and  $\lambda$  (Lamé constant) are defined using elastic modulus  $E$  and Poisson's ratio  $\nu$  as

$$\begin{aligned}
 K &= \frac{E}{3(1-2\nu)} \\
 G &= \frac{E}{2(1+\nu)} \\
 \lambda &= K + \frac{2}{3}G = \frac{E\nu}{(1+\nu)(1-2\nu)}
 \end{aligned} \tag{5.1}$$

The Hooke's law can then be written as

$$\boldsymbol{\sigma} = \mathbf{C}\boldsymbol{\varepsilon}$$

$$\begin{Bmatrix} \sigma_{11} \\ \sigma_{22} \\ \sigma_{33} \\ \sigma_{12} \\ \sigma_{23} \\ \sigma_{13} \end{Bmatrix} = \begin{bmatrix} 2G + \lambda & \lambda & \lambda & 0 & 0 & 0 \\ \lambda & 2G + \lambda & \lambda & 0 & 0 & 0 \\ \lambda & \lambda & 2G + \lambda & 0 & 0 & 0 \\ 0 & 0 & 0 & 2G & 0 & 0 \\ 0 & 0 & 0 & 0 & 2G & 0 \\ 0 & 0 & 0 & 0 & 0 & 2G \end{bmatrix} \begin{Bmatrix} \varepsilon_{11} \\ \varepsilon_{22} \\ \varepsilon_{33} \\ \varepsilon_{12} \\ \varepsilon_{23} \\ \varepsilon_{13} \end{Bmatrix} \tag{5.2}$$

Where  $\mathbf{C}$  is the stiffness matrix. For plane strain this becomes

$$\begin{Bmatrix} \sigma_{11} \\ \sigma_{22} \\ \sigma_{33} \\ \sigma_{12} \end{Bmatrix} = \begin{bmatrix} 2G + \lambda & \lambda & \lambda & 0 \\ \lambda & 2G + \lambda & \lambda & 0 \\ \lambda & \lambda & 2G + \lambda & 0 \\ 0 & 0 & 0 & 2G \end{bmatrix} \begin{Bmatrix} \varepsilon_{11} \\ \varepsilon_{22} \\ \varepsilon_{33} \\ \varepsilon_{12} \end{Bmatrix} \tag{5.3}$$

It should be noted that the VUMAT subroutine uses shear strain tensor components and not engineering shear strains. Also, for foams the Poisson's ratio is often close to zero,

which causes the Lamé constant to be zero. Therefore the stiffness matrix simplifies and becomes diagonal and can be replaced with a simple stiffness parameter  $C = 2G$ .

The plastic behavior of the new model is built based on the ABAQUS Crushable foam material model. Therefore the yield criterion and its parameters are the same as shown in Equation 4.1 to Equation 4.11. The plasticity model begins with the assumption that the total strain increment can be decomposed into elastic and plastic increments

$$d\boldsymbol{\varepsilon} = d\boldsymbol{\varepsilon}^e + d\boldsymbol{\varepsilon}^p \quad (5.4)$$

Using the stress-strain relationship, we can write

$$d\boldsymbol{\sigma} = \mathbf{C}d\boldsymbol{\varepsilon}^e = \mathbf{C}(d\boldsymbol{\varepsilon} - d\boldsymbol{\varepsilon}^p) \quad (5.5)$$

Based on non-associated flow during plastic deformation, the plastic strain increment can be written as

$$d\boldsymbol{\varepsilon}^p = d\lambda \frac{\partial G}{\partial \boldsymbol{\sigma}} \quad (5.6)$$

where  $d\lambda$  is the plastic multiplier. This can then be substituted into the stress-strain relationship which becomes

$$d\boldsymbol{\sigma} = \mathbf{C} \left( d\boldsymbol{\varepsilon} - d\lambda \frac{\partial G}{\partial \boldsymbol{\sigma}} \right) \quad (5.7)$$

and thus plastic stress increment can be written as

$$d\boldsymbol{\sigma}^p = \mathbf{C}d\lambda \frac{\partial G}{\partial \boldsymbol{\sigma}} \quad (5.8)$$

To define the plastic multiplier, we can look at the consistency condition, which tells that during plastic loading the stress point should remain on the yield surface, meaning that the yield condition should be zero. This can be written as

$$F(\boldsymbol{\sigma} + d\boldsymbol{\sigma}) = F(\boldsymbol{\sigma}) + \frac{\partial F}{\partial \boldsymbol{\sigma}}^T d\boldsymbol{\sigma} = 0 \quad (5.9)$$

Since during plastic loading  $F(\boldsymbol{\sigma}) = 0$ , we get

$$\frac{\partial F^T}{\partial \boldsymbol{\sigma}} d\boldsymbol{\sigma} = 0 \quad (5.10)$$

Now substituting the stress increment from Equation 5.7 into this gives

$$\frac{\partial F^T}{\partial \boldsymbol{\sigma}} \mathbf{C} \left( d\boldsymbol{\varepsilon} - d\lambda \frac{\partial G}{\partial \boldsymbol{\sigma}} \right) = 0 \quad (5.11)$$

This can then be solved for the plastic multiplier as

$$d\lambda = \frac{\frac{\partial F^T}{\partial \boldsymbol{\sigma}} \mathbf{C} d\boldsymbol{\varepsilon}}{\frac{\partial F^T}{\partial \boldsymbol{\sigma}} \mathbf{C} \frac{\partial G}{\partial \boldsymbol{\sigma}}} \quad (5.12)$$

After the plastic multiplier has been solved, it can be used to calculate the plastic strain increment and thus the plastic strain increment.

### 5.2.2. Integration in subroutine

The explicit solver of ABAQUS integrates through time by using many small time increments and the time increment is limited by the stability limit of the integration procedure. As time increments are very small, explicit methods are sufficient during plasticity integration of the VUMAT subroutine.

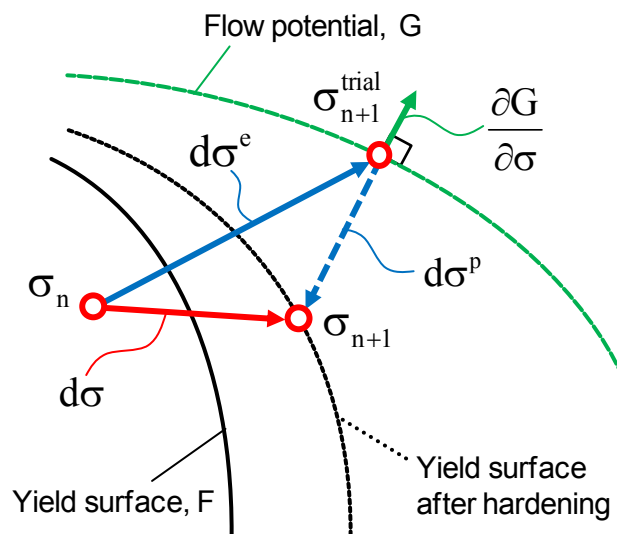


Figure 5.1 Illustration of the stress return method.

As input, the VUMAT subroutine gets the stress tensor components in the beginning of the step and the total strain and time increment of the current step. Based on these, the subroutine should then calculate the stresses at the end of the step by integrating the rate constitutive equations in incremental procedure. The integration method used here is simple return mapping algorithm based on elastic predictor and plastic corrector stresses. The method and definition of the stresses used are illustrated in Figure 5.1.

First, initial trial stress is calculated using the given strain increment using Hooke's law from Equation 5.2.

$$\boldsymbol{\sigma}_{n+1}^{\text{trial}} = \boldsymbol{\sigma}_n + \mathbf{C}d\boldsymbol{\varepsilon}_{\text{trial}} \quad (5.13)$$

Hardening parameters are then calculated using the previous stresses after which the yield condition is evaluated for the new trial stress

$$F(\boldsymbol{\sigma}_{n+1}^{\text{trial}}, \mathbf{H}) > 0 \quad (5.14)$$

where  $H$  indicates the hardening parameters. If no yielding occurs, the stresses are updated and the solver moves to the next increment. Otherwise, if yielding initiates, a plastic corrector needs to be defined. We now have to take the hardening parameters into account when defining the plastic multiplier. As the strain increments are very small for the explicit method, we can assume that the trial stress is still close to the yield surface, and use first order Taylor expansion to obtain approximation of new value for the yield function at the final stress state. This gives

$$\begin{aligned} F(\boldsymbol{\sigma}_{n+1}, H_{n+1}) &= F(\boldsymbol{\sigma}_{n+1}^{\text{trial}}, h_{n+1}^{\text{trial}}) + \frac{\partial F}{\partial \boldsymbol{\sigma}_{n+1}^{\text{trial}}} (\boldsymbol{\sigma}_{n+1} - \boldsymbol{\sigma}_{n+1}^{\text{trial}}) \\ &+ \frac{\partial F}{\partial H_{n+1}^{\text{trial}}} (H_{n+1} - H_{n+1}^{\text{trial}}) \end{aligned} \quad (5.15)$$

The new value of the yield function should be zero as the stress should return to the yield surface at final state and by using the stresses defined in Figure 5.1, this can be written as

$$F(\boldsymbol{\sigma}_{n+1}^{\text{trial}}, H_{n+1}^{\text{trial}}) + \frac{\partial F}{\partial \boldsymbol{\sigma}_{n+1}^{\text{trial}}} d\boldsymbol{\sigma}^p + \frac{\partial F}{\partial H_{n+1}^{\text{trial}}} dH = 0 \quad (5.16)$$

Evolution equation for hardening parameters can be written as

$$dH = d\lambda h \quad (5.17)$$

where  $d\lambda$  is the plastic multiplier and  $h$  is the rate form of the hardening law. Inserting

this and the plastic stress increment from Equation 5.8 into Equation 5.6 gives

$$F(\boldsymbol{\sigma}_{n+1}^{\text{trial}}, H_{n+1}^{\text{trial}}) + \frac{\partial F}{\partial \boldsymbol{\sigma}_{n+1}^{\text{trial}}} \mathbf{C} d\lambda \frac{\partial G}{\partial \boldsymbol{\sigma}_{n+1}^{\text{trial}}} + \frac{\partial F}{\partial H_{n+1}^{\text{trial}}} d\lambda h = 0 \quad (5.18)$$

The plastic multiplier can then be solved from this as

$$d\lambda = \frac{F(\boldsymbol{\sigma}_{n+1}^{\text{trial}}, H_{n+1}^{\text{trial}})}{\frac{\partial F}{\partial \boldsymbol{\sigma}_{n+1}^{\text{trial}}} \mathbf{C} \frac{\partial G}{\partial \boldsymbol{\sigma}_{n+1}^{\text{trial}}} - \frac{\partial F}{\partial H_{n+1}^{\text{trial}}} dh} \quad (5.19)$$

which can be simplified to

$$d\lambda = \frac{F}{\frac{\partial F}{\partial \boldsymbol{\sigma}} \mathbf{C} \frac{\partial G}{\partial \boldsymbol{\sigma}} - \hat{H}}, \quad \hat{H} = \frac{\partial F}{\partial H} dh \quad (5.20)$$

To solve the plastic multiplier, the differentials  $\partial F/\partial \boldsymbol{\sigma}$ ,  $\partial G/\partial \boldsymbol{\sigma}$  and the hardening parameter  $\hat{H}$  need to be known. Using the definition of the yield function and flow potential from Equation 4.1 and Equation 4.12 the differentials become

$$\frac{\partial F}{\partial \boldsymbol{\sigma}} = \frac{\partial F}{\partial p} \frac{\partial p}{\partial \boldsymbol{\sigma}} + \frac{\partial F}{\partial q} \frac{\partial q}{\partial \boldsymbol{\sigma}} = \frac{\alpha^2(p - p_0)}{3F} + \frac{3\mathbf{s}}{2F} \quad (5.21)$$

$$\frac{\partial G}{\partial \boldsymbol{\sigma}} = \frac{\partial G}{\partial p} \frac{\partial p}{\partial \boldsymbol{\sigma}} + \frac{\partial G}{\partial q} \frac{\partial q}{\partial \boldsymbol{\sigma}} = \frac{3\boldsymbol{\sigma}}{2G} \quad (5.22)$$

Hardening is now defined by  $p_c$  and  $p_t$ , so the hardening parameter  $H$  becomes

$$\hat{H} = \frac{\partial F}{\partial p_c} dp_c + \frac{\partial F}{\partial p_c} \frac{\partial p_c}{\partial p_t} dp_t \quad (5.23)$$

where

$$\frac{\partial F}{\partial p_c} = \frac{\alpha}{2} - \frac{\alpha^2(p - p_0)}{2F} \quad (5.24)$$

and using Equation 4.1

$$\frac{\partial p_c}{\partial p_t} = -\frac{q^2}{\alpha^2(p_t + p)^2} \quad (5.25)$$

After the plastic multiplier is solved, the plastic strain and plastic stress increments from Equation 5.6 and Equation 5.8 can be calculated. The new stresses can then be solved by deducting the plastic stresses from the trial stresses.

$$\boldsymbol{\sigma}_{n+1} = \boldsymbol{\sigma}_{n+1}^{\text{trial}} - d\boldsymbol{\sigma}^p \quad (5.26)$$

Due to the small time step of the Explicit solver it can be assumed that the trial state is close to the yield surface and therefore the plastic stress correction is done only once, thus reducing computation time.

### 5.2.3. Differentiating parts of loading cycle

To be able to apply various conditions during different times of loading, the compression-tension loading cycle was first divided into five distinct parts:

1. Initial elastic loading
2. Plastic crushing plateau
3. Unloading
4. Elastic tensile loading after crushing
5. Plastic tensile loading after crushing

The tension and compression parts of the loading could be identified using the hydrostatic pressure stress  $p$  which is now positive under compressive stresses and negative under tensile stresses. The loading direction during compression can be defined by using the following statement

$$\begin{aligned} \boldsymbol{\varepsilon} \cdot \dot{\boldsymbol{\varepsilon}} &> 0 \text{ during loading} \\ \boldsymbol{\varepsilon} \cdot \dot{\boldsymbol{\varepsilon}} &\leq 0 \text{ during unloading} \end{aligned} \quad (5.27)$$

Finally the elastic and plastic compression could be separated by looking at the volumetric plastic strain, which differs from zero after the crushing of the core begins.

### 5.2.4. Degradation of elastic modulus

To account for changes in the elastic modulus during different parts of loading, a scaling factor  $B_s$  is added to the elastic modulus  $E$ . The scaling factor  $B_s$  can be added to the stress-strain relationship as follows:

$$\boldsymbol{\sigma} = B_s \mathbf{C} \boldsymbol{\varepsilon} \quad (5.28)$$

The value of  $B_s$  varies based on the loading condition and if the stiffness decreases or increases. However, its value is changed only during regions of elastic loading or unloading. During plastic deformation the value of  $B_s$  is kept at 1 so that it doesn't affect the plasticity calculations.

### **5.2.5. Behavior during tensile loading**

The compressive hardening behaves similarly to the crushable foam model so that new hardening stress is acquired from the user input hardening curve based on the volumetric plastic strain. The tensile behavior now differs notably from the crushable foam model. The tensile loading is now divided into elastic and plastic part. During the elastic part, the elastic modulus is scaled using a scaling factor as shown in Equation 5.28.

Hardening behavior is now included also in the tensile direction. When the material yields in tensile direction, the hydrostatic tensile yield stress  $p_t$  is adjusted similarly to the compressive direction using uniaxial stress-strain data and Equation 4.13 .

Also, it should be remembered that the tensile loading behavior changes depending on whether compression has occurred or not. For the quasi-static indentation problem, it is assumed that the damage in the core happens mainly by compression, and the tensile stresses will not exceed the tensile yield stress of undamaged core. Therefore if tensile loading now happens before compressive plastic deformation, the check for yield is simply ignored to prevent too early yield by tension. More sophisticated definition for tensile damage criterion for undamaged and crushed core is left for future study.

### **5.2.6. Outline of subroutine**

Basic outline of the whole user subroutine procedure is illustrated in Figure 5.2.

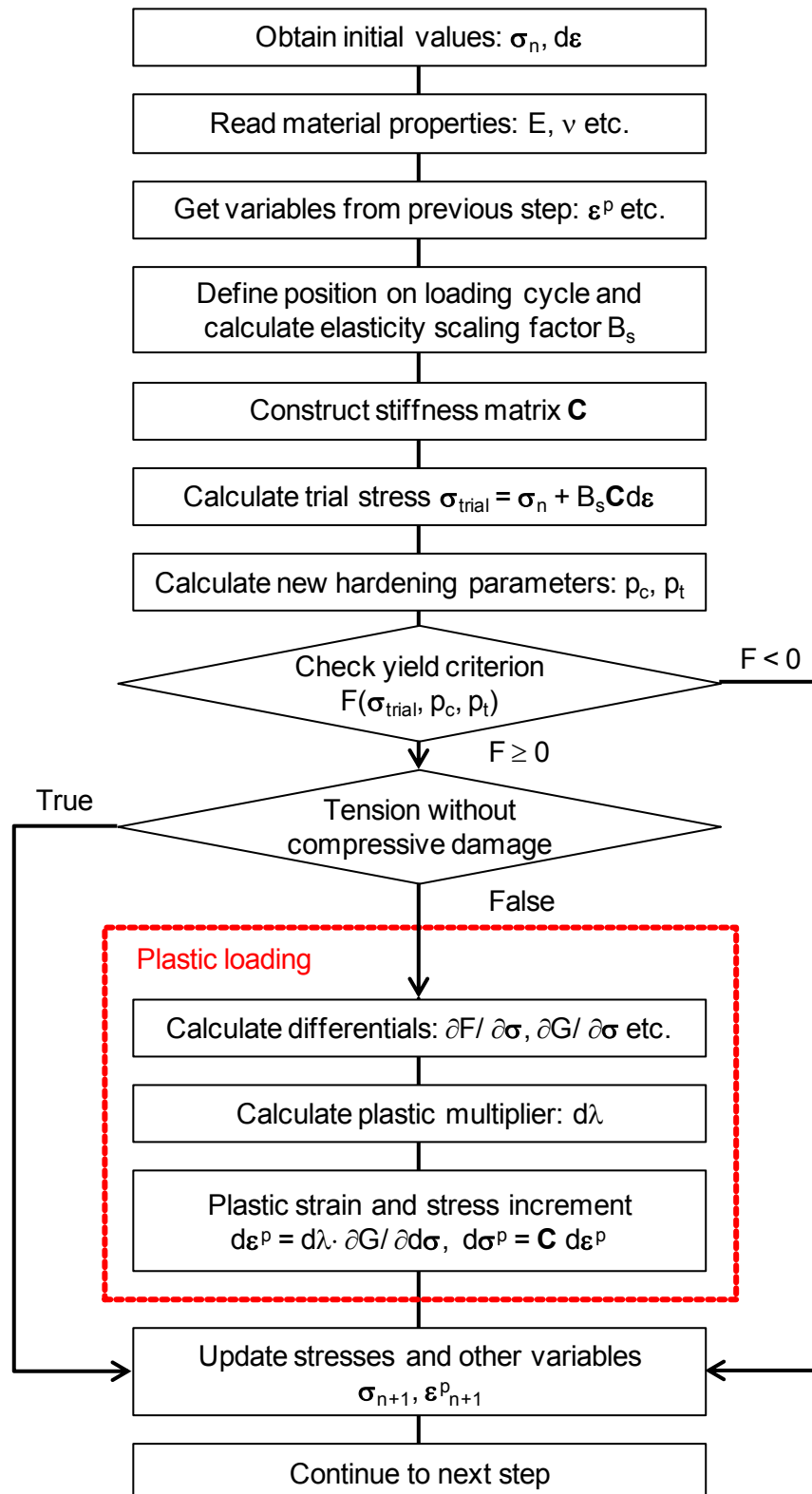


Figure 5.2 Flow chart of the VUMAT user subroutine.

### 5.3. Defining model parameters

The parameters for unloading and tensile behavior used in the model were defined experimentally. To obtain the needed parameters, loading cycle tests were conducted with foam specimens. The foam was compressed until set compressive strain and the unloaded until the strain became zero again. These compression-tension loading cycles were repeated while the maximum compressive strain of the cycle was increased gradually. This way the unloading behavior and tensile behavior after compression could be observed at various maximum compressive strains as shown in Figure 5.3. The stress-strain curves from the cycle tests seem to correspond well with curves obtained by only one cycle, so no notable effect from fatigue could be seen. In the following sections the unloading and tensile behavior is observed, and the model parameter data is defined using the experimental results for the 30°C ambient humidity condition. The same procedure can also be used for data from other temperature and humidity conditions.

#### 5.3.1. Unloading

Looking at the unloading parts of the loading cycle test, the unloading modulus can be estimated as a tangent between the maximum stress point at the beginning of unloading and the point of zero stress at the end of unloading as depicted in Figure 5.4. This gives the unloading modulus as a function of the maximum compressive strain. The unloading modulus was normalized using the initial compressive modulus to obtain a dimensionless value that can be used as the scaling parameter in Equation 5.28. As the ABAQUS subroutine uses logarithmic strains, the normalized unloading modulus was plotted against the maximum logarithmic plastic strain as shown in Figure 5.5. The response is

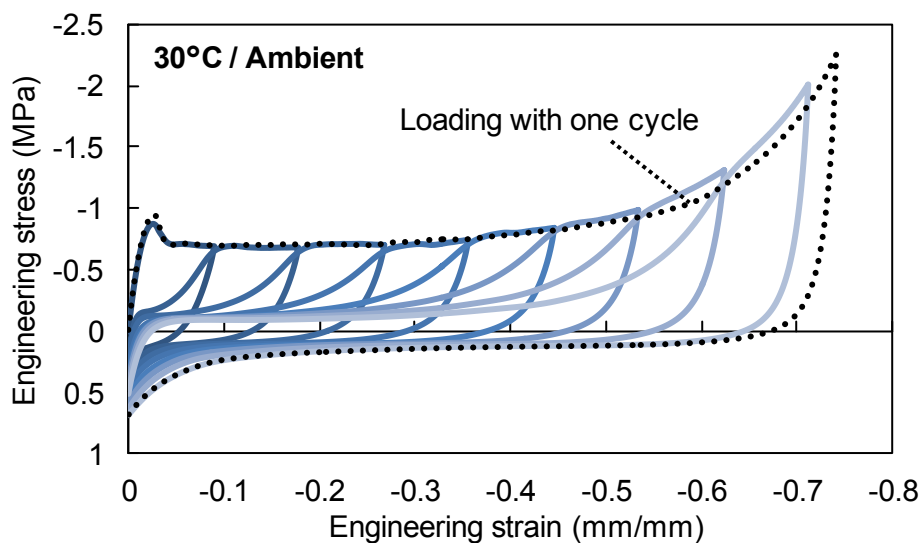


Figure 5.3 Stress-strain response of loading cycle test.

similar to that reported previously by Flores-Johnson et. al. [80] for Rohacell 51 WF, although the values differ slightly due to the different definition of the initial elastic modulus. The data is now fitted with two curves to obtain good correspondence over the observed strain region. A logarithmic fitting curve was used for small strains and a second order fitting curve for higher strains as shown in Figure 5.5. These curves were then implemented into the subroutine to define the degradation of the elastic modulus.

### 5.3.2. Tensile loading

The tensile parts of the loading cycles are now divided into seemingly elastic and plastic parts. The tensile parts can be considered separately from the compressive parts as shown in Figure 5.6. The elastic part of one cycle is estimated by calculating the strain energy at the unloading of the tensile stress at the beginning of next cycle assuming that this energy equals the strain energy during the elastic tensile deformation as also illustrated in Figure 5.6. This way the tensile yield stress can be calculated for each cycle, and using the yield stress, the elastic modulus at tension can be estimated. The tensile elastic modulus when normalized using the initial elastic modulus is shown in Figure 5.7 with the fitting curve used in the subroutine. The average tensile yield stress is now 0.075 MPa.

Subtracting the elastic part from the tensile curves, and normalizing the data with regard to the strains, plastic tensile loading curves as shown in Figure 5.8 are obtained. The plastic tensile behavior is now approximated with a bilinear curve. This represents the parts of the tensile loading where, first, the collapsed cell walls are stretched at slightly increasing loading. As the cell walls have mostly recovered their initial shape, plastic deformation and plastic hinges still remain, which require notably increased loading while the cell walls are stretched.

The hardening modulus for the first part is assumed to be constant 0.88 for all cycles. The hardening modulus of the second part however changes with each cycle as the final stress level at zero strain changes. The change between the two parts of the bilinear curve was set to happen at 0.15 normalized strain. Thus, using the final stress values at zero strain and the point where the hardening changes, the hardening modulus for the second part could be estimated using a linear function as shown in Figure 5.8.

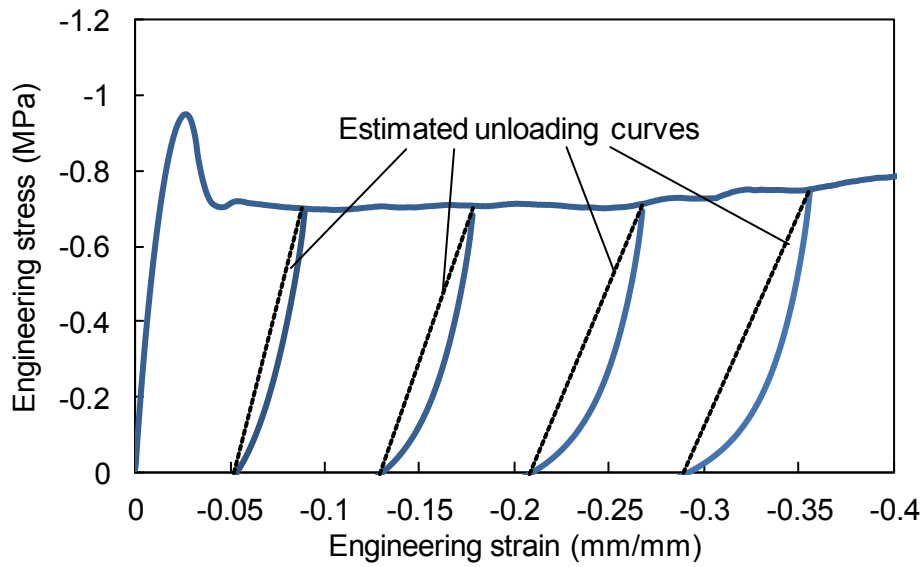


Figure 5.4 Estimation of unloading modulus from the experimental loading cycle data.

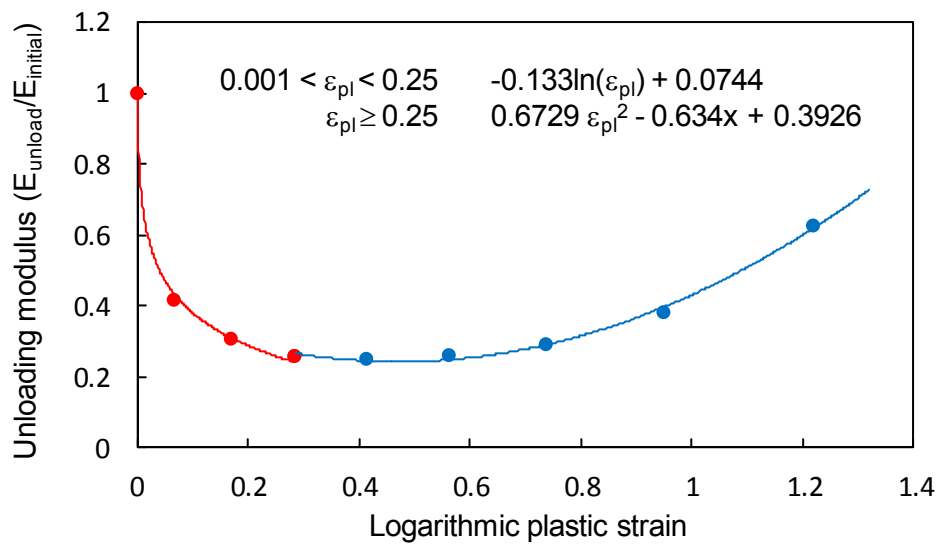


Figure 5.5 Normalized unloading modulus against maximum logarithmic plastic strain during compression.

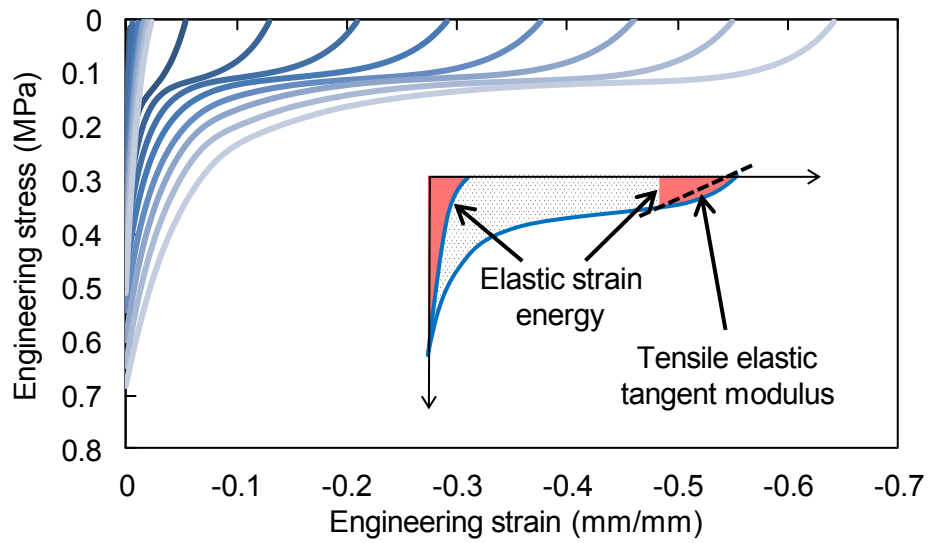


Figure 5.6 Tensile parts of the loading cycle data and definition of the elastic part.

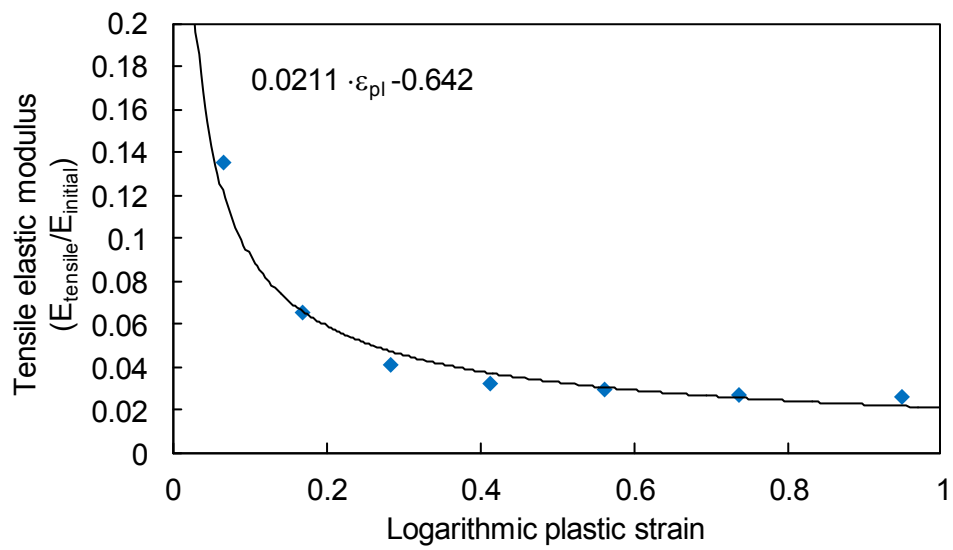


Figure 5.7 Normalized tensile elastic modulus against maximum logarithmic plastic strain during compression.

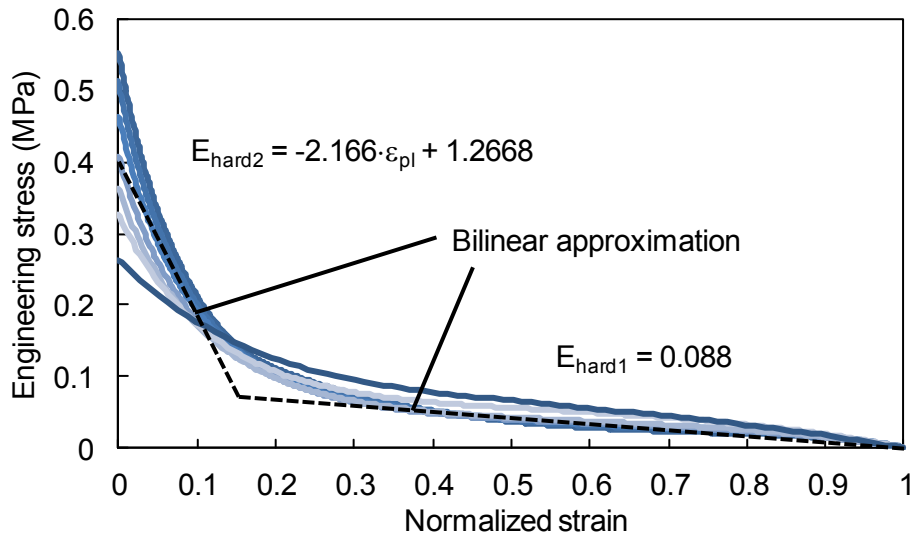


Figure 5.8 Plastic tensile stress with bilinear approximation.

#### 5.4. Material model validation

The constructed material model was tested and validated with ABAQUS's Explicit solver using one four node square plane-strain element with reduced integration. Uniaxial, hydrostatic and shear loading cases, as depicted in Figure 5.9, were simulated and the results were compared with results given by crushable for the same loading cases. The material properties of the foam at 30°C ambient conditions were used.

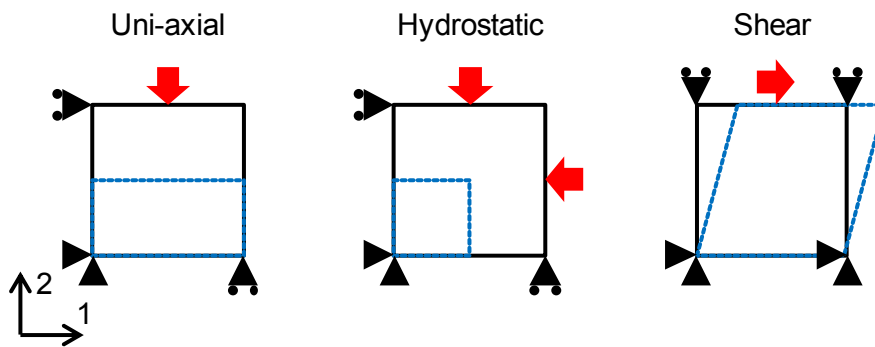


Figure 5.9 Tested loading cases using one element.

Figure 5.10 compares the uniaxial stress-strain response of the models during a compression-tension loading cycle. The compressive parts are almost identical for both models as they follow the user input hardening curve. During the unloading and tensile parts the differences are clear. The elastic unloading and elastic tensile modulus of the crushable foam model stay the same as the initial elastic modulus during the whole simulation. In the new model the unloading and tensile modulus are degraded using the scaling parameter  $B_s$  as explained previously and the value of the factor  $B_s$  during one compression-tension loading cycle is shown in Figure 5.11. The elastic modulus is notably degraded during the unloading and initial tensile loading, leading to notably different behavior. The tensile hardening behavior also significantly differs from the perfectly plastic behavior of the crushable foam model. The uniaxial stress-strain response of the new model is compared with experimental data in Figure 5.12. The new model seems to predict the loading behavior rather well.

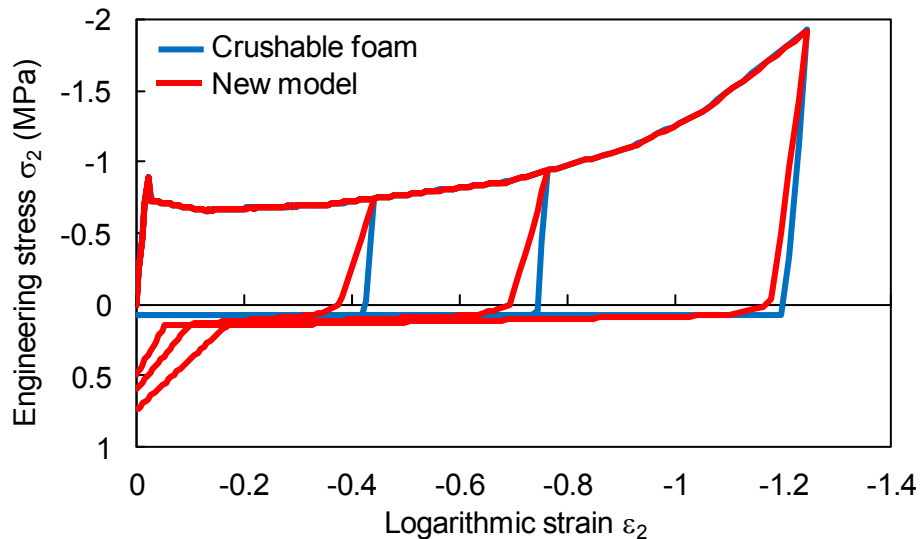


Figure 5.10 Predicted compression-tension loading cycle response of crushable foam model and new model.

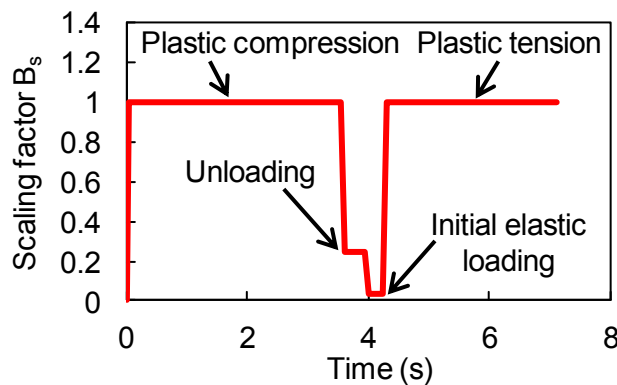


Figure 5.11 Scaling factor  $B_s$  during compression-tension loading cycle.

Comparison of the tensile response of the new model and crushable foam model area shown in Figure 5.13. The tensile yield stress of the crushable foam model is the same whether compressive yielding has occurred or not. This can be seen now as premature yielding during tension without any previous compressive loading. The new model disregards tensile yielding if no compressive yielding has occurred. At this moment the tensile stress will keep increasing infinitely with increasing loading, but a tensile damage criterion for the brittle damage in tension is to be implemented into the model in future. Also during tensile loading after compression, the crushable foam model keeps following the perfectly plastic behavior while the new model has tensile stiffness even with tensile strains.

As can be seen from Figure 5.14, the hydrostatic loading response of the new model differs from the crushable foam model similarly with the uniaxial tests as expected. The shear loading response is nearly identical for both models, as no notable changes are done that could affect the shear behavior.

The constructed new model seems to work as expected and should be able to predict the unloading and tensile response of the foam more accurately than what the crushable foam can do. This is studied in the next section by simulation of sandwich beam indentation loading test.

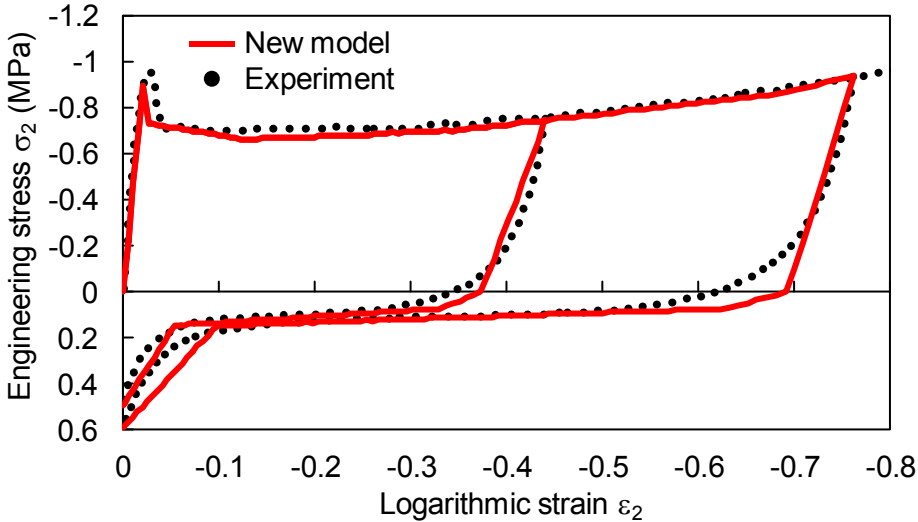


Figure 5.12 Comparison of uniaxial loading response of new model and experimental data.

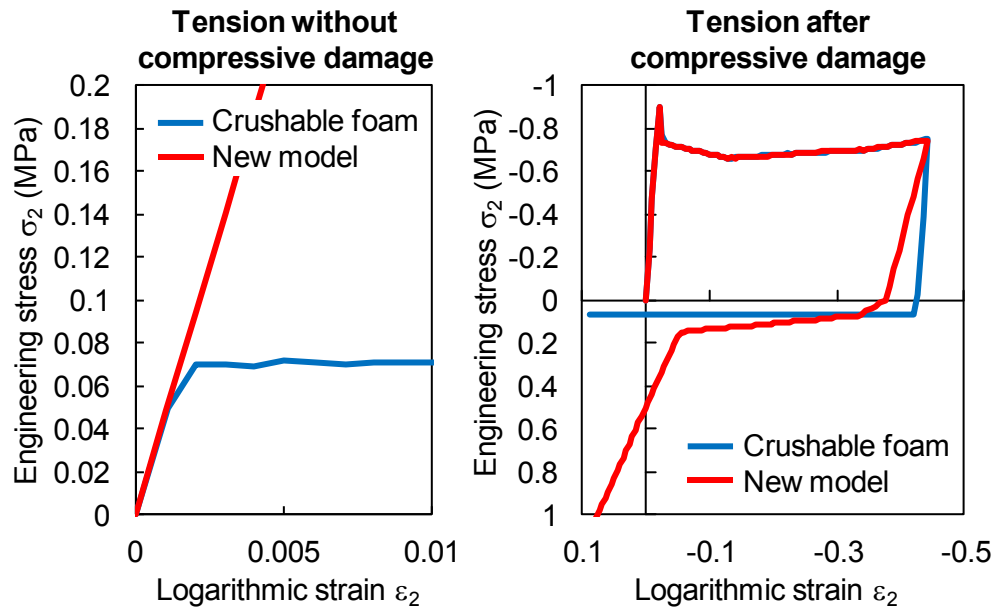


Figure 5.13 Tensile response of crushable foam model and new model.

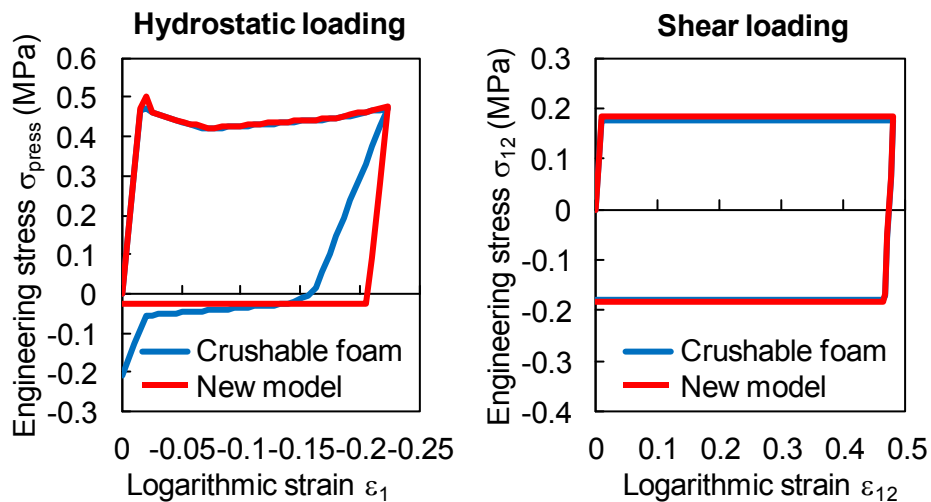


Figure 5.14 Hydrostatic and shear response of crushable foam model and new model.

## 5.5. Indentation simulation

Indentation loading of sandwich beams was simulated similarly to Chapter 4. However, the Explicit solver of ABAQUS was now used, and therefore the elements used reduced integration. Also, as the indentation loading is quasi-static, the density of the foam material was scaled so that a reasonable solution could be obtained. The loading speed could also be increased to reduce the solution time as the material models are strain-rate independent. Only the 30°C ambient condition was studied for the maximum indentation displacement and maximum indentation loading tests.

### 5.5.1. Results

Figure 5.15 and Figure 5.16 show the indentation load-displacement curves obtained using the new model compared with experimental results and those predicted using the crushable foam model in Chapter 4. The response during loading is similar between both models, as the compressive behavior follows the same behavior. The new model now gives notably improved prediction of the unloading response. The slope of the curve at the beginning of the unloading is notably different from the previous prediction using crushable foam model due to the degraded elastic modulus. The linear approximation of the unloading response is still slightly different from the experimental behavior of the foam and this can be seen clearly in the maximum indentation loading test in Figure 5.15. As the indentation unloading is now mostly by the unloading of the compressed foam, the linear behavior of the model slightly underestimates the stiffness. However, the tensile hardening fitted with the experiments brings latter part of the unloading curve also close to the experimental data.

Residual dent profiles for the models with the experimental residual dent depth value at the loading point are shown in Figure 5.17 and Figure 5.18. The experimental values are taken from the indentation load-indentation data, and the values thus have some error due to the sampling rate of the test system and relaxation of the core. The residual dent depths predicted by the new model are however clearly closer to the experimental values. Especially with small indentation displacement, as in the maximum indentation loading case, the crushable foam model seems to predict too deep dent depth suggesting that the tensile yield stress is too high. For the maximum indentation displacement case some deformation can be seen remaining away from the loading point at the edges of the beam with the crushable foam model. This is caused by premature tensile yielding of the core, which is now effectively prevented by the new model.

The residual strains in the adhesive layer for the models are compared in Figure 5.19 and Figure 5.20. Due to the tensile hardening of the core during unloading, the strains are now higher compared to the crushable foam model for the maximum indentation displacement case. This also corresponds with the deeper residual dent. For the maximum indentation loading test the strains given by the new model are slightly smaller and similarly shows shallower residual dent.

The new model seems to give improved prediction of the indentation response of sandwich beams. Especially the unloading behavior is notably closer to experimental results when compared to the crushable foam model. Comparison of the strain distributions with experimental data is done later in Chapter 6 which discusses the strain monitoring of sandwich structures.

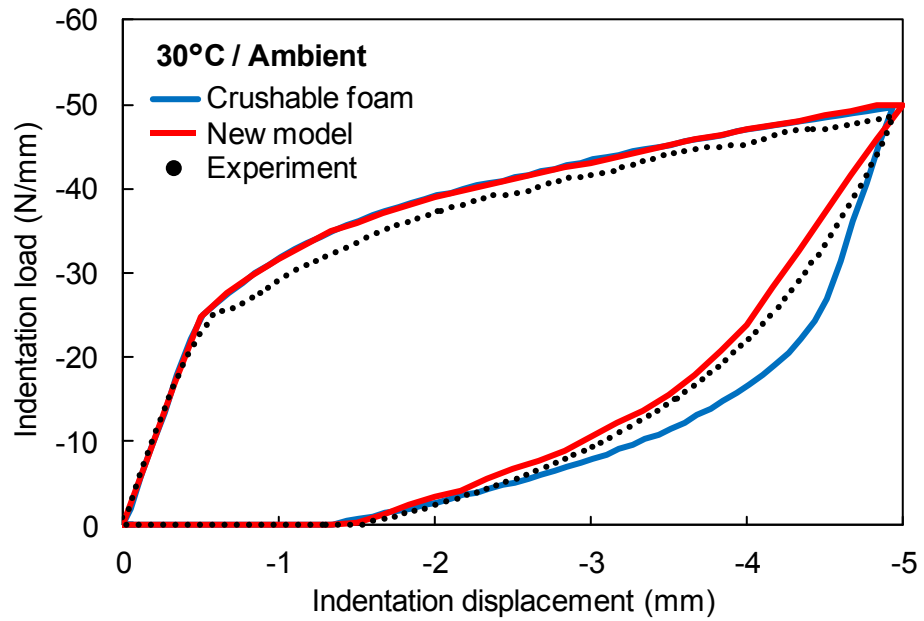


Figure 5.15 Comparison of predicted indentation load-displacement response for maximum indentation displacement test.

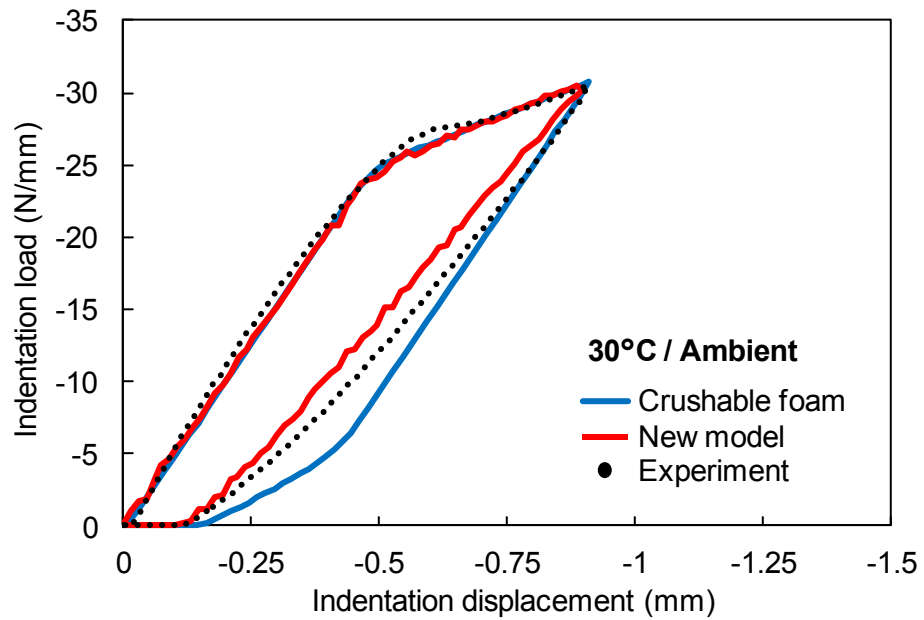


Figure 5.16 Comparison of predicted indentation load-displacement response for maximum indentation loading test.

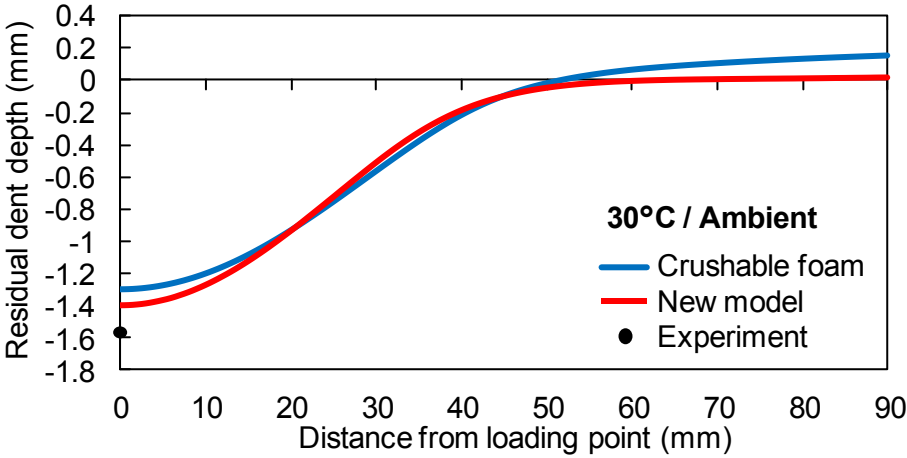


Figure 5.17 Predicted residual dent profiles for maximum indentation displacement test.

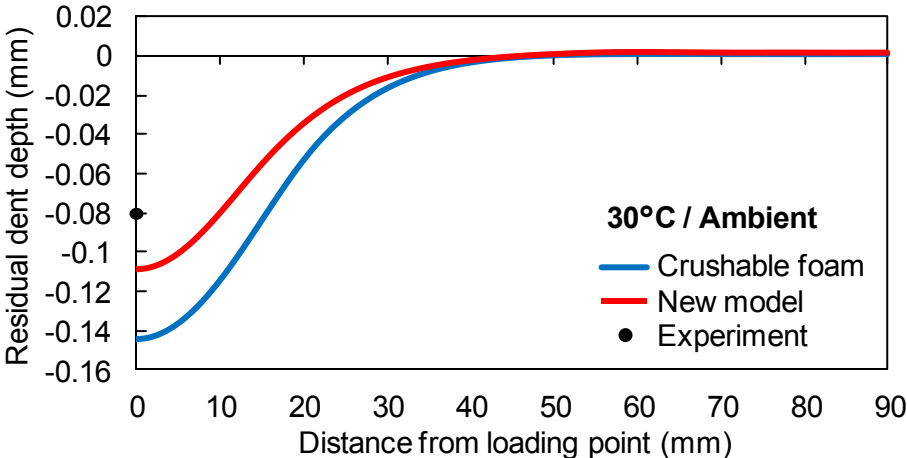


Figure 5.18 Predicted residual dent profiles for maximum indentation loading test.

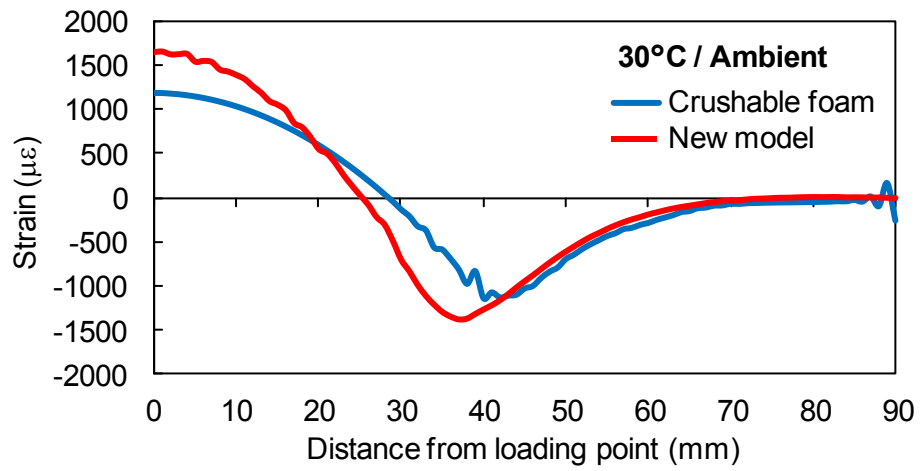


Figure 5.19. Comparison of predicted residual strain distributions for maximum indentation displacement test.

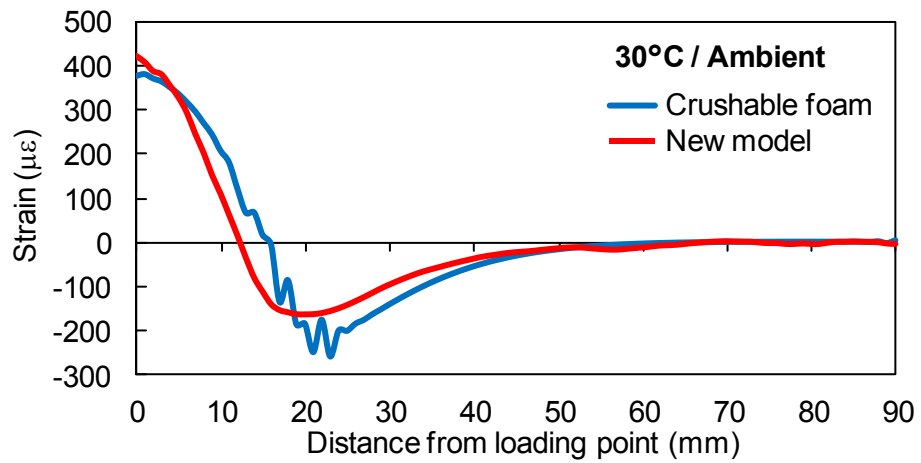


Figure 5.20 Comparison of predicted residual strain distributions for maximum indentation loading test.

## 5.6. Conclusion

A new improved material model for the foam material was constructed based on the crushable foam plasticity model. The new model included hardening also for the tensile loading and took the degradation of elastic modulus during compression into account. The degradation and tensile hardening parameters were adjusted based on cyclic compression-tension experiments done with the foam material. In addition, tensile behavior of uncrushed and crushed foam was separated so that premature tensile yielding of the foam can be avoided.

For an example case, the indentation loading cycle of a sandwich beam was studied. The new improved model predicted the indentation-load displacement behavior and residual dent depth better than the crushable foam model. The new model can therefore give improved prediction on the indentation loading response of sandwich structures. Especially the unloading behavior and residual dent formation can be predicted with significantly improved accuracy.

## **Chapter 6. Monitoring of foam core sandwich structures**

In this chapter a distributed strain monitoring system using fiber optic sensors is applied to foam core sandwich structures. The system is studied by conducting indentation tests with sandwich beams and panels. Strain distribution in the specimens is measured continuously during indentation loading. Comparing the monitoring data with numerical analysis predictions, the damage detection capability is evaluated. Finally the system's ability to detect low velocity impact damages in real life sandwich panel structure is verified using a large scale demonstrator.

### **6.1. Indentation / low velocity impact damage monitoring**

Detection of indentation or low velocity impact damage in sandwich structures is difficult by conventional methods, as often no clear sign of the impact remains on the face sheets, while the core can be significantly damaged therefore notably reducing the strength of the structure [7, 9]. To detect these damages in sandwich structures caused by indentation or impact loadings, various structural health monitoring methods have been studied in the past. These methods mainly consist of detection of damage using the dynamic response of the structures, using wave propagation in the structures, and by using optical fiber sensors. A good review is given, for example, in [81].

Fiber optic based systems seem promising as the fibers are embedded into the structure, they can provide information about the condition inside the structure throughout its whole life cycle from manufacturing to operation. Also due to their small size, the fiber optic sensors cause no notable effect on the mechanical properties of the structures. Previously fiber optic based distributed strain monitoring systems have been applied to sandwich structures to detect impact damages [82, 83, 84], but precise and sensitive detection of the damage location and size is still lacking.

In this study, fiber optic sensing system with high spatial resolution is embedded into the sandwich structures. The used sensors measure the strain distribution along the fiber they can provide information over the whole structure, thus allowing for example easy detection of damage location.

## 6.2. Distributed strain measurement

Typical strain sensors, like strain gages, measure the strain at one location over the short length of the sensor itself. Distributed strain monitoring means that the strain is measured over the whole length of the sensor. The sensor is divided into sections or sampling points, shown in Figure 6.1 at which the strain is measured. Distance between each sampling point is defined as the sensor spacing, which also defines the resolution of the system. The measured strain is the average strain over the length of the section, defined as the gage length, and the sections can overlap each other.

On fiber optic sensing systems, the spacing and length of the sections can be adjusted to achieve most suitable performance. Longer spacing and sensing length allows lower performance equipment, as the precision is also lower. The measurement speed can though also be increased this way, as less data is obtained and less time is therefore needed to process that data. There is still however limitations in current monitoring systems on how small sensor spacing and gage length can be used.

## 6.3. Application into foam core sandwich structures

In indentation and low velocity impact cases the local deformation of the face sheet causes high compressive and tensile stresses on the top and bottom surfaces the face sheet which will still be present even after unloading if some residual dent remains. Also yielding in the adhesive layer or damage in the core near the interface may occur, resulting in additional or reduced strains near the interface area. These considerations suggest that the core-face sheet interface seems to be to most feasible location for the optical fiber to be embedded.

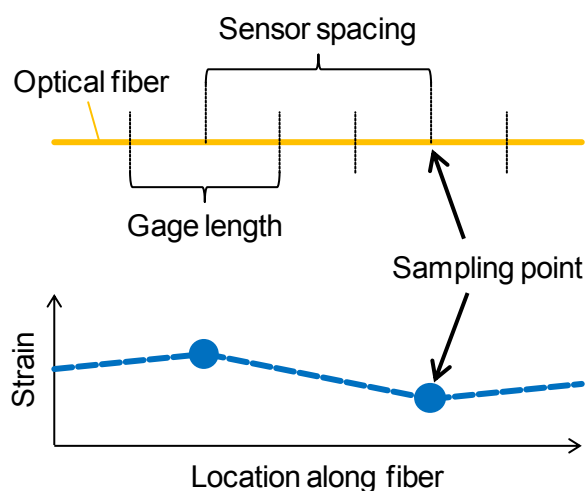


Figure 6.1 Distributed strain measurement with fiber-optic sensor.

The expected strain condition in the core-face sheet interface, and therefore also in the embedded fiber optic sensor, during indentation or after unloading is depicted in Figure 6.2. During indentation the face sheet bends under the indenter. This causes the bottom of the face sheet to be in tension at the location of indentation. However, as the bending happens locally, the areas further away from the indentation point stay undeformed. This creates compressive strain on the bottom of the face sheet on the areas between the undeformed region and the indentation location. If a residual dent remains in the face after the loading is removed, similar strain conditions should remain in the interface. Plastic deformation in the adhesive layer, face sheet or the foam core near the indented face can however also affect the strain distribution. However, over time stress relaxation in the core occurs, which will make the residual dent shallower and therefore reduce the strains.

Embedment inside the structure would also allow monitoring during the manufacture phase of the structures. This data can then be used to evaluate the condition of the adhesion or to detect any voids or strain concentrations in the core-face sheet interface, thus verifying the manufacturing quality of the structure.

The monitoring system now needs to be either fast enough to detect the high strains during the indentation or low velocity impact event, or sensitive enough to detect the strain distribution caused by the residual dent even after some relaxation has occurred. To fulfill these qualifications, a high spatial resolution distributed sensing system based on Rayleigh backscattering is presented in the following section.

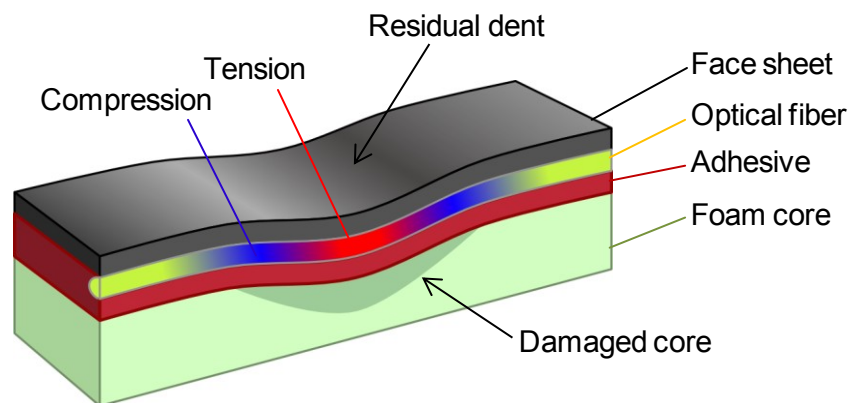


Figure 6.2 Expected strain distribution in the embedded fiber optic sensor after indentation or impact damage.

## 6.4. Monitoring system (LUNA OBR)

Optical backscatter reflectometry (OBR) based strain monitoring system was used in this study. It uses distributed sensing technique developed by LUNA and can provide millimeter range spatial resolution with high measurement speed allowing for in-situ monitoring of the tests. Under these measurement settings the measurement range is however limited to tens of meters, but sufficient for the used test specimens sizes. Next the basic working principle of the measurement system is explained and some of its parameters are discussed.

### 6.4.1. Monitoring principle of fiber optic interferometry

Basic explanation of the monitoring principle based on optical reflectometry is now explained based on [85, 86, 87, 88]. Optical reflectometry techniques can be roughly divided into three categories: optical time domain reflectometry (OTDR), optical frequency domain reflectometry (OFDR), and optical low coherence reflectometry (OLCR). Based on the method used there are limits in range, resolution, speed, sensitivity and accuracy of the measurements. For example, OTDR has long range of several kilometers but low resolution while OFDR has higher resolution but limited measurement range. The used system uses the OFDR method which is based on swept-wavelength interferometry (SWI). It can provide millimeter-range resolution over a range of up to hundreds of meters.

The monitoring system consists of a tunable laser source (TLS), an interferometer, which is the fiber under test (FUT), and a detector, which are depicted in Figure 6.3. The frequency of the tunable laser is swept linearly over time to create a chirped light signal. This signal is then split into two paths at a coupler. One goes to the fiber under test and one to the static reference fiber. As the signal is propagating through the FUT, part of it is reflected back due to Rayleigh scattering. The backscattered signal returning from the FUT and the signal from the reference fiber are then combined and they coherently interfere at the optical detector. Due to the time delay between the signals, there is a phase difference between the reference signal and the backscattered signal. Therefore as the laser frequency is tuned, interference fringes are generated. These interference fringes can be detected and related to the optical amplitude and phase response of the fiber under test. Using Fourier transformation, fringes in the spectral domain can be transformed into the time domain which can be further scaled using the speed of light to correspond with the length of the fiber. This gives the amplitude of the reflections as function of length of the FUT. Therefore both the frequency domain and time domain data can be obtained using the OFDR method.

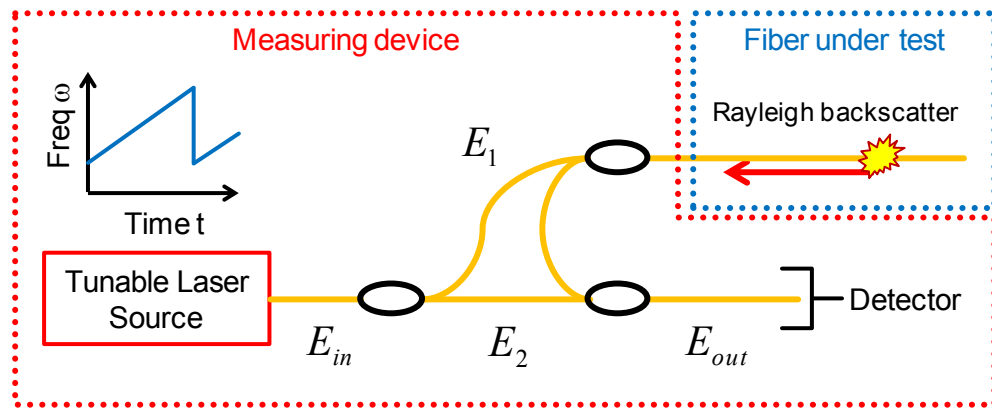


Figure 6.3 Schematic of optical backscatter reflectometer fiber network.

#### 6.4.2. Strain measurement

Strain measurement along the fiber is based on the fact that there is a random but static distribution in the index of refraction in the fiber core over the whole length of the fiber. The amplitude of the scattered signal over the length of the fiber is therefore a random but static property which is unique for each fiber. Changes in temperature or strain then change the local period of the Rayleigh scatter, which can be seen as shift of the backscattered Rayleigh spectrum. The Rayleigh scattering spectra at the sampling points along the fiber are obtained by reverse Fourier transformation from the time domain data over increments defined by the gage length. The distance between each sampling point is defined as the sensor spacing, as defined in the LUNA manual [88].

The strain distribution along the fiber can then be calculated by looking at the Rayleigh scattering spectrum at each sampling point along the fiber and comparing it with a reference state obtained before strain was applied as illustrated in Figure 6.4. Shift in the spectrum, obtained by cross-correlating the measured spectrum with reference spectrum, is related to the change in temperature and strain at the measurement point and can be defined as

$$\frac{\Delta\lambda}{\lambda} = -\frac{\Delta\nu}{\nu} = K_T\Delta T + K_\varepsilon\varepsilon \quad (6.1)$$

where  $\lambda$  is the mean optical wavelength,  $\nu$  the mean optical frequency, and  $K_T$  and  $K_\varepsilon$  are the temperature and strain calibration constants which depend on the used fiber. If we assume that there is no change in temperature, the strain can be calculated as

$$\varepsilon = -\frac{\bar{\lambda}}{cK_\varepsilon}\Delta\nu = \bar{K}_\varepsilon\Delta\nu \quad (6.2)$$

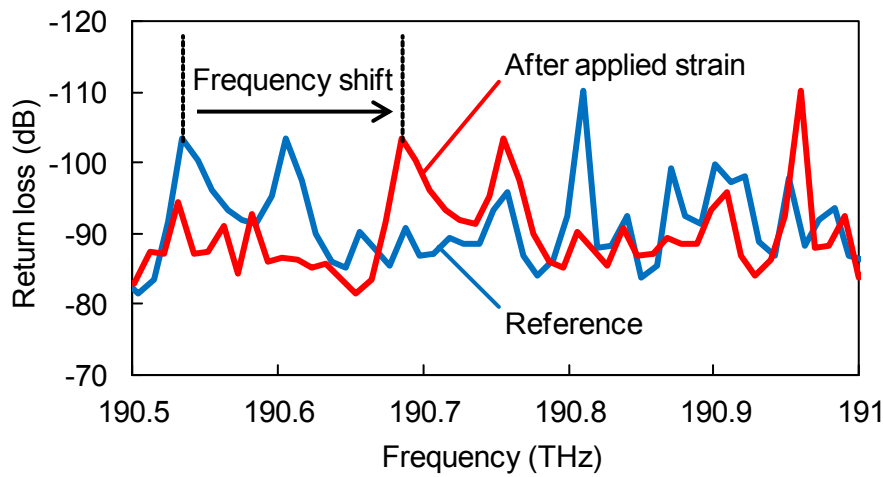


Figure 6.4 Frequency shift of Rayleigh scattering spectrum due to applied strain.

where  $\bar{\lambda}$  is the center wavelength of the measurement and  $c$  is the speed of light. These form the conversion factor  $\bar{K}_e$  which can be obtained experimentally by relating applied strain and frequency shift of the Rayleigh scatter spectrum.

Similarly at constant strain conditions the temperature change can be calculated as

$$\Delta T = -\frac{\bar{\lambda}}{cK_T} \Delta v = \bar{K}_T \Delta v \quad (6.3)$$

By using these relations, the spectral shift data can be converted to strain or temperature data.

### 6.4.3. Measurement resolution

As the frequency domain information over the gage length is obtained by discrete Fourier transformation from the time domain data, the length of the gage in the time domain affects the spectral resolution of the frequency-domain [88]. In the Fourier transformation the resolution bandwidth of the frequency domain is

$$RBW = \frac{1}{\Delta t_f} \quad (6.4)$$

Where  $\Delta t_f$  is the width of the portion in time domain transferred to frequency domain. As the time domain data is scaled into the fiber length values using

$$z = \frac{c}{2n_g} t \quad (6.5)$$

Where  $z$  is the spatial dimension along the fiber,  $c$  is the speed of light in vacuum,  $n_g$  is the group index of refraction of the fiber under test and  $t$  is the time. The spatial dimension thus depends linearly on the time, and therefore the resolution bandwidth of the frequency domain of Equation 6.4 also depends on the gage length in spatial domain. Therefore the gage length affects the resolution in the frequency domain so that larger gage length gives higher frequency resolution.

Suitable settings for the monitoring system should be selected based on the phenomenon to be measured. When observing very small strain changes happening over a decently wide area, a larger gage length will provide better results. If the strain is highly local, the large gage length can on the other hand average out the detailed strain distribution information and thus a smaller gage length can provide more detailed results.

#### **6.4.4. Determination of strain coefficient for strain measurements**

The strain coefficient used to convert frequency shifts of the measurements to strain was defined experimentally for the used optical fibers by conducting tensile test. A 5 mm strain gage and optical fiber made by joining fibers of both used batches were adhered to an aluminum plate as depicted in Figure 6.5. The strain gage was adhered to the center of the plate and the optical fibers on both sides of the strain gage. The optical fibers were adhered at two points using epoxy adhesive.

The aluminum plate was then loaded in tension using a tensile testing machine. The loading was increased in 500  $\mu\epsilon$  steps as observed by the strain gage, and the strain along the fibers was measured at each strain level. Comparing the measurement at each strain level with measurement at previous strain level, the frequency shift distribution in the fibers corresponding with the 500  $\mu\epsilon$  increase was achieved. Average frequency shift over the tensioned region was then calculated for each frequency shift data. Finally the strain coefficient was obtained by correlating the strain values with the frequency shift data as shown in Figure 6.6. The obtained strain coefficient values are shown in Table 6.1.

#### **6.4.5. Error distribution of monitoring system**

At constant strain and temperature conditions the frequency shift of the backscattered spectra over the whole fiber should be zero. However, because of some random error in the measurements, the measured frequency shifts varies slightly with each measurement. To define the amount of error, standard deviation at each measurement point along the

fiber can be calculated. By plotting the frequency of each error magnitude occurring in the measurements, the error distribution of the system can then be defined.

The procedure used to obtain the error distribution was based on one for Pulse Pre-Pump Brillouin optical time domain analysis (PPP-BOTDA) based system [89]. Different to the PPP-BOTDA system used in [89], the current Rayleigh scattering based system does not give a unambiguous peak at each measurement point, but a random spectrum which depends on the fluctuations in the core index of refraction of the fiber at the measured location. Therefore, for example, an average peak frequency cannot be calculated. The procedure was thus modified to be applicable to the current monitoring system.

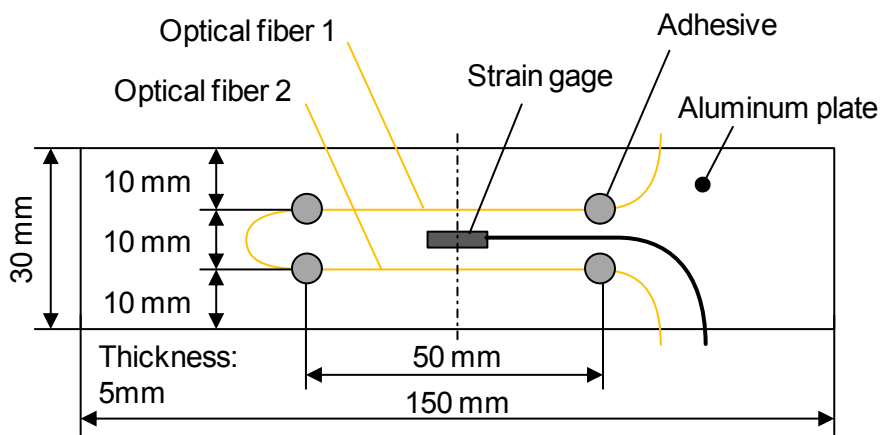


Figure 6.5 Schematic of the test specimen used to define strain coefficients for the used optical fibers.

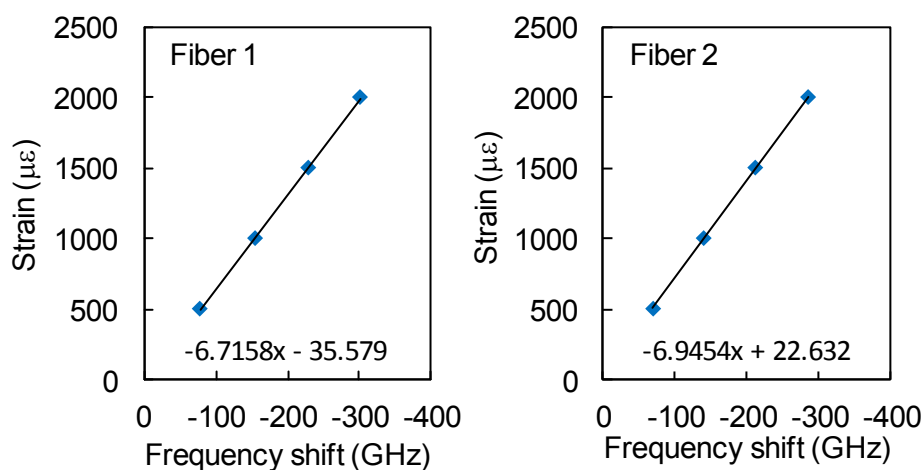


Figure 6.6 Spectral shift distributions of fiber sections corresponding with fibers 1 and 2 against tensile strain levels measured by strain gage.

Table 6.1 Strain coefficients of used optical fibers.

	Fiber 1	Fiber 2
Strain coefficient $\bar{K}_\varepsilon$	-6.716 GHz/ $\mu\varepsilon$	-6.945 GHz/ $\mu\varepsilon$

Using a fiber without any applied strain or temperature, N pairs of measurements were taken at same and constant conditions. The frequency shift was then calculated for each measurement pair, so that the first measurement of the pair was used as the reference data and the second measurement was compared to the first one. From these, the strain deviation at each sampling point was calculated using the strain coefficient of the fiber for each measurement pair.

$$\hat{\varepsilon}_{ik} = \bar{K}_\varepsilon v_{ik} \quad (6.6)$$

Here i indicates sampling point along the measured fiber and k is the number of the measurement pair. The average of strain deviation was then calculated at each sampling point as

$$\hat{\varepsilon}_i^{Ave} = \frac{\sum_{k=1}^N \hat{\varepsilon}_{ik}}{N} \quad (6.7)$$

Comparing the deviation of strain at each sampling point with the average of strain deviation, the random error can be obtained.

$$v_{ik}^{F0} = \hat{\varepsilon}_{ik} - \hat{\varepsilon}_i^{Ave} \quad (6.8)$$

Plotting a histogram of the random error values from all measurements gives the error distribution of the measurement.

Error distribution was now defined for two distinct measurement settings using 5 pairs of consecutive measurements that were taken at ambient room temperature conditions of a fiber with no strain applied. Gage lengths of 1 mm, 5 mm and 10 mm were used with 0.6 mm sensor spacing. Strain deviation histograms based on the calculated random error  $v_{ik}^{F0}$  for each gage length are shown in Figure 6.7. Standard deviation of the error is less than 1  $\mu\varepsilon$  for the 5 mm and 10 mm gage lengths, whereas it is around 12  $\mu\varepsilon$  for the shortest gage length of 1 mm. This is due to the bandwidth resolution of the Fourier transformation which increases with longer gage lengths as was explained in section 6.4.3.

With longer gage lengths the error of the system seems to be notable smaller than the PPP-BOTDA system for which the standard deviation of the error was measured to be

9.37  $\mu\epsilon$  [89]. The error for the 1 mm gage length is still acceptable for the current use, as the measured strains are assumed to be over 100  $\mu\epsilon$ .

### 6.5. Sandwich beam indentation monitoring experiments

Indentation tests were conducted using sandwich beams with fiber optic sensor embedded in the adhesive layer. The sandwich beam specimens provide good information on the monitoring ability of indentation damage. The results can also be compared with numerical results from previous chapter, thus providing a good tool for verification.

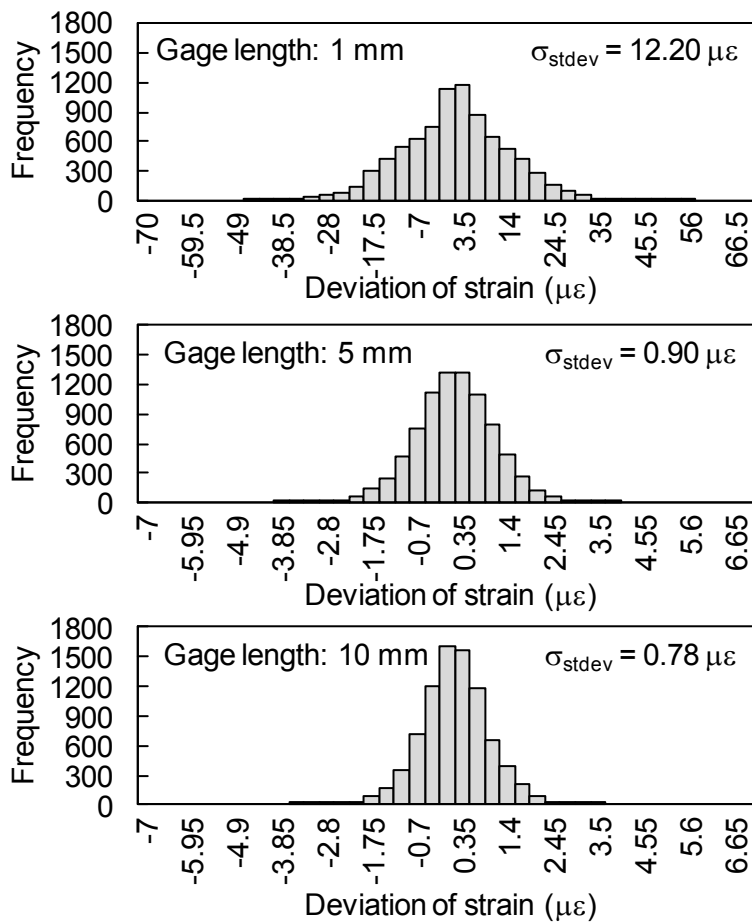


Figure 6.7 Strain deviation histograms for selected gage lengths.

### 6.5.1. Sandwich beam specimens

The sandwich beam specimens were similar with those in section 3.2.1. Only difference is that a high delta optical fiber (Heatop 300, Totoku Electric Co., Ltd., outer diameter: 150  $\mu\text{m}$ , cladding diameter: 125  $\mu\text{m}$ ) was embedded between the face sheet and the adhesive layer of the sandwich beams as shown in Figure 6.8.

### 6.5.2. Test method

Sandwich beam indentation tests were conducted similar to Chapter 3. Indentation loading was applied at the center of the beams using a cylindrical steel indenter under various temperature and humidity conditions. During and after the indentation loading, strain distribution was continuously measured at the embedded part of the fiber using the LUNA OBR 4600 monitoring system. Reference data was obtained before the tests to which the data obtained during the tests was compared to, so that the strains could be calculated.

Maximum indentation displacement and maximum indentation loading test were conducted similar to Chapter 3. In maximum indentation displacement tests, the loading was applied until maximum indentation displacement of 5 mm was achieved, after which the loading was removed. In maximum indentation loading tests the loading was applied until maximum loading of 600 N was reached, after which the loading was removed.

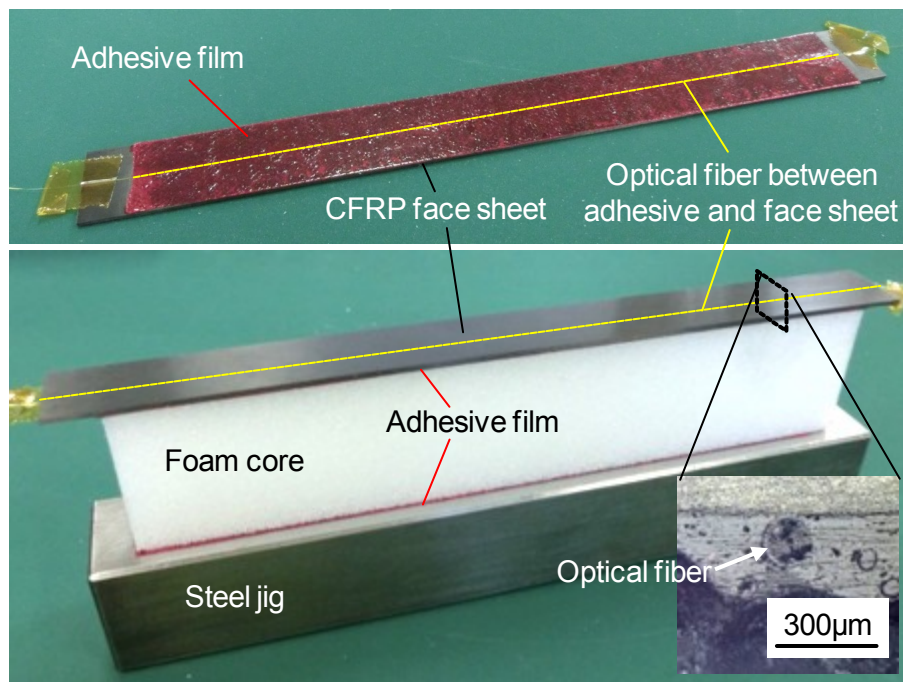


Figure 6.8 Sandwich beam specimen with embedded optical fiber.

### 6.5.3. Strain measurement during indentation

Figure 6.9 and Figure 6.10 illustrate the typical results from continuous strain monitoring during the indentation loading tests. The arrows in Figure 6.9 indicate selected locations during the indentation test. These locations are at the beginning of the test, before damage initiation in the core, after damage initiation, at the maximum indentation displacement and immediately after unloading. Strain distribution corresponding with the indicated locations are shown in Figure 6.10. In the beginning of the loading the strain distribution is near zero over the whole length of the beam. As the reference state is taken right before the tests, no thermal strains or other residual strains from the manufacturing phase are taken into account. As the loading begins, the strain distribution starts to show a sharp tensile peak at the location where the indentation loading is applied due to the face sheet bending and the bottom of the face sheet being in tension. Increasing the loading bends the face further while the core crushes, and thus the tensile strain peak becomes larger and wider. After the loading has been removed, the tensile peak flattens, but a notable strain distribution is still observed as residual dent remains in the face sheet.

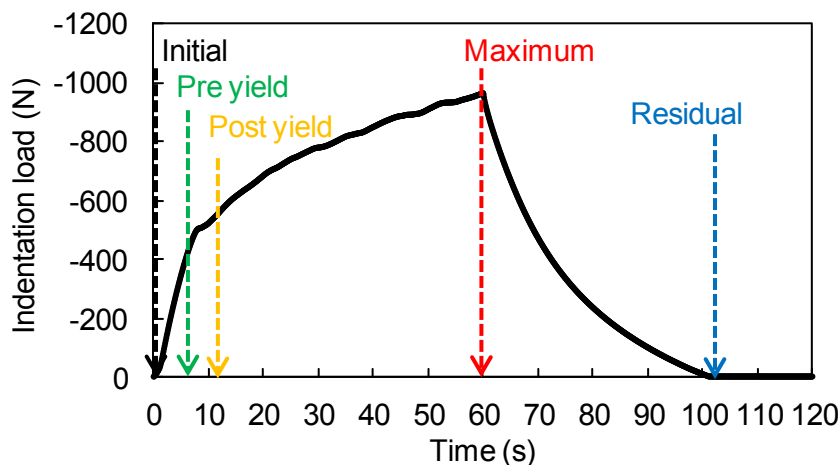


Figure 6.9 Loading response during typical sandwich beam indentation test.

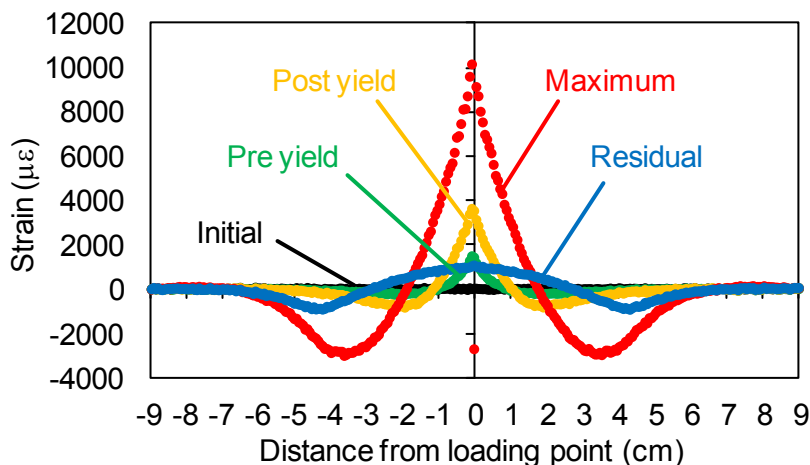


Figure 6.10 Strain distribution during different parts of sandwich beam indentation test.

The monitoring system is capable of continuous strain measurement during the indentation tests and seems to provide very detailed and reasonable results. The maximum strains and residual strains can thus be quite easily extracted from the measurement data based on the measurement time and indentation loading data.

The maximum and residual strain distribution are compared with those measured by PPP-BOTDA system and strain gages embedded between the adhesive layer and the face sheet in Figure 6.11 [90]. The PPP-BOTDA measurements were taken using the systems maximum spatial resolution of 2 cm with 1 cm sensor spacing. The measured strain values from the embedded strain gages are close with the strain distribution measured using the current OBR system and indicates that the system can detect the strains in the adhesive-face sheet interface correctly. The PPP-BOTDA strain distribution however differs notably and the strain levels are also significantly lower. This is probably due to the rather large spatial resolution of the system, which evens out the high strain peak at the point where indentation loading is applied. The resolution and accuracy of the OBR system is now clearly better than that of the PPP-BOTDA system and is more suitable in monitoring the highly local strains in the case of indentation loading of sandwich structures.

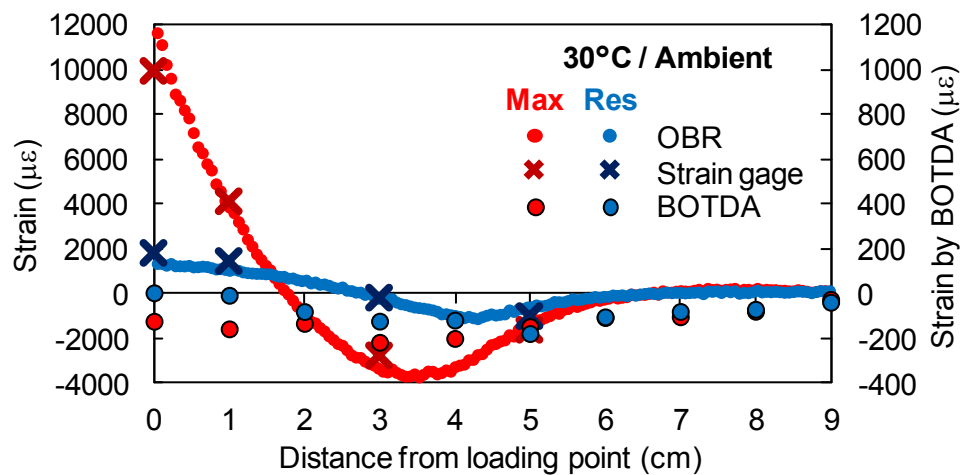


Figure 6.11 Comparison of measured strain distributions using different measurement methods.

**6.5.4. Formation of residual strains**

As the detectability of the damage in the sandwich structure depends on the detectability of the residual strains, an indentation test was conducted where the maximum loading was increased gradually and the residual strains were then measured after each loading cycle. Figure 6.12 shows the load-indentation curves of the test and Figure 6.13 the corresponding residual strain distributions of selected cycles. Up to 500 N loading the deformation was mostly elastic with no residual deformation remaining. Therefore no residual strains were observed, as can be seen for the 500 N case in Figure 6.13. After crushing of the core initiated at 600 N loading cycle, a clear indication of damage was also seen in the residual strains. With increasing loading the residual strains also became gradually larger.

The strained area also widened as the damage area in the core also widened with higher indentation loading and thus larger indentation displacement. The results however do not present the residual strains immediately after unloading but do include some relaxation and are thus show slightly lower than should be expected. The used monitoring system now seems to be capable of detecting the initiation of the core crushing damage based on the observation of residual strains.

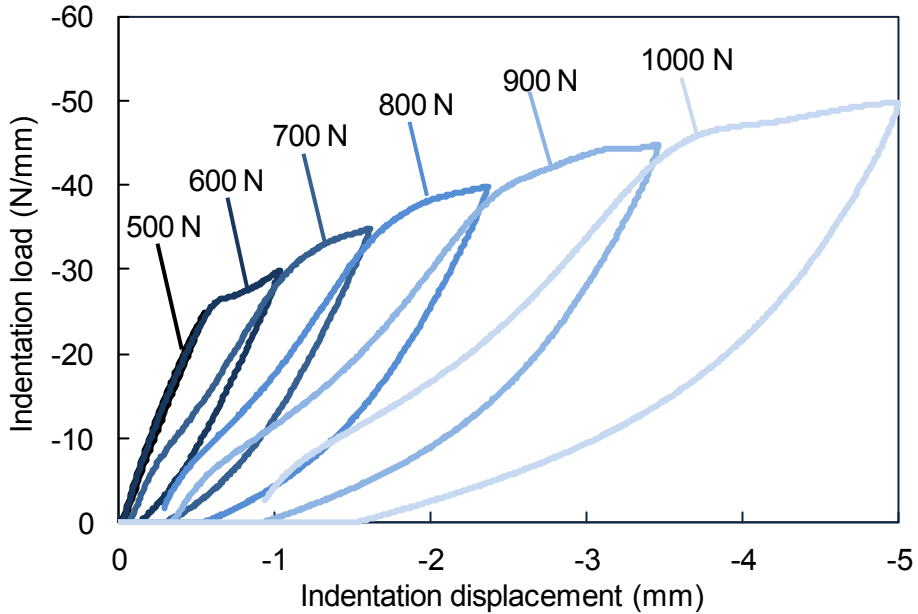


Figure 6.12 Indentation load-displacement of the sandwich beam during loading cycles.

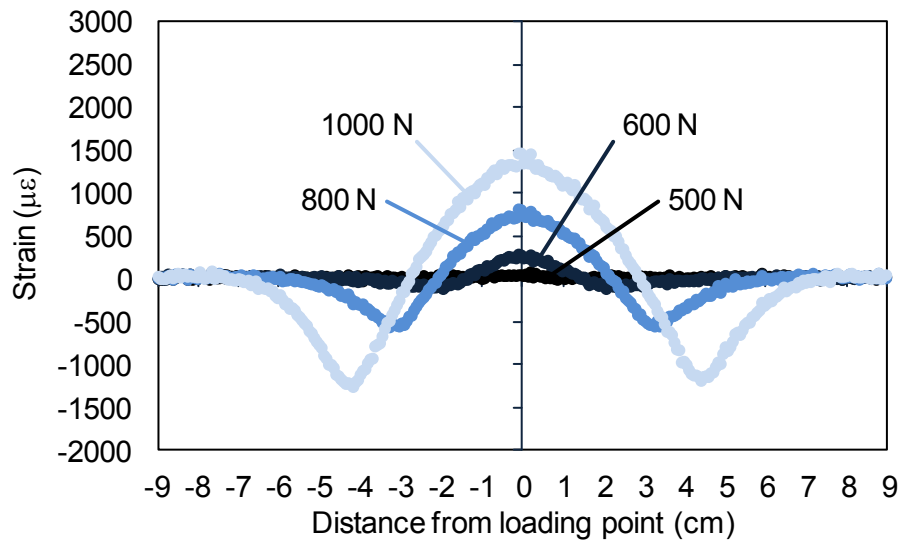


Figure 6.13 Measured residual strain distributions after selected loading cycles.

#### 6.5.5. Effect of relaxation on strain distribution

The relaxation behavior of the strains was also studied on a ambient conditioned beam at 30°C. After indentation loading was removed the strain distribution was monitored over period of time and selected results are shown in Figure 6.14. Also the maximum peak strain at the point of applied indentation loading over time is presented in Figure 6.15. The strains become lower over time due to stress relaxation in the core which leads to shallower residual dent. Besides stress relaxation in the core, the residual state can also be affected by the face sheet. Thicker face sheet having higher bending stiffness will exert higher pulling force into the crushed foam which might lead to faster reduction in the depth of the residual dent. The effect of the face sheet is however not included in the current study.

A significant drop in the strains can be seen over the first 10 minutes after the loading was removed with the maximum strain being reduced by 25% during the first minute, and by almost 50% during the first 10 minutes after unloading. Over time the strains keep decreasing and eventually 24 hours later the maximum strains are only around 30% of the initial strains immediately after unloading. The stress relaxation of the foam can thus significantly affect the detectability of the indentation damage over time. It should be noted, that the location of the compressive strain peak does not move notably during relaxation, meaning that the size of the damage can still be estimated quite accurately.

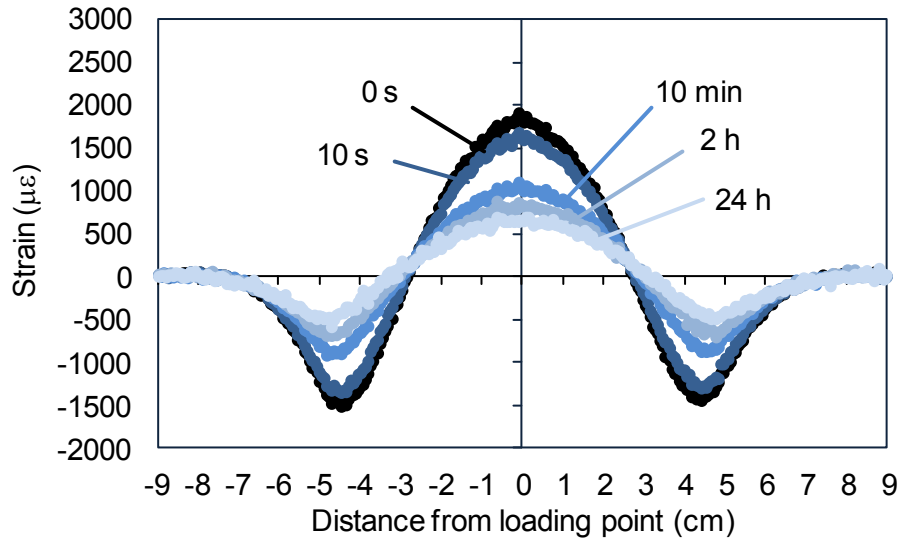


Figure 6.14 Residual strain distribution over time after unloading.

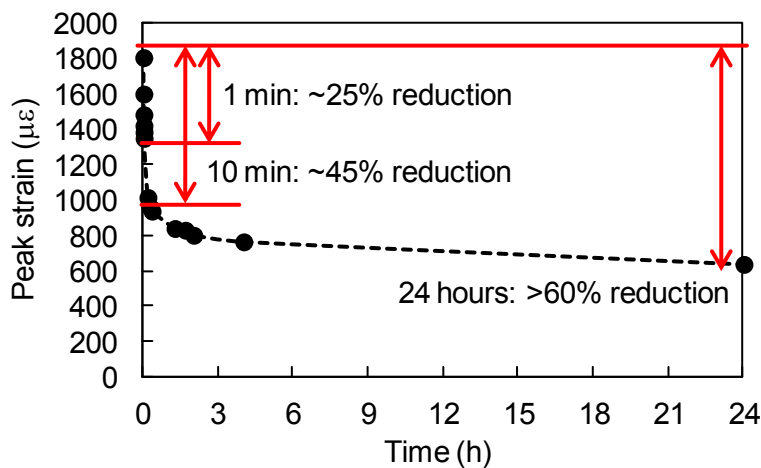


Figure 6.15 Reduction in maximum peak strain at indentation location over time due to relaxation.

### 6.5.6. Fiber damage during monitoring

Compared to other fiber optic sensing systems, the current system does not need to create a closed loop of the fiber. In the closed fiber loops systems, if the fiber is damaged the loop is also broken and the measurement cannot be performed at all. With the used system, however, if the fiber happens to be damaged or cut, the system is still usable up to the damage location. This would also allow for accurate detection of the location where the fiber has broken, so that needed measures to repair the fiber can be taken.

Next, results from an example case where the embedded fiber broke during indentation

loading of a sandwich beam are shown. Figure 6.16 shows the amplitude of the backscattered or reflected light along fiber. After the fiber has broken, a clear peak can be seen at the location of the breakage due to the light reflecting back from the broken end of the fiber. Figure 6.17 shows the measured strain distribution around the damage location. Immediately before the damage a clear strain peak is still observed at the location of the indentation loading. After the fiber has broken, the part of the fiber after the breakage shows only noise. The strain measurement is still however possible up to the damage location and the other half of the strain peak is still visible in the results. The other half of the broken fiber could still be monitored by connecting the other end of the fiber to the measurement system.

The OBR system seems to be suitable for damage detection applications. In the case of damage in the optical fiber, the location of the breakage can be identified and repaired. Also, breakage of the fiber still allows monitoring up to the damage location and does not paralyze the whole system.

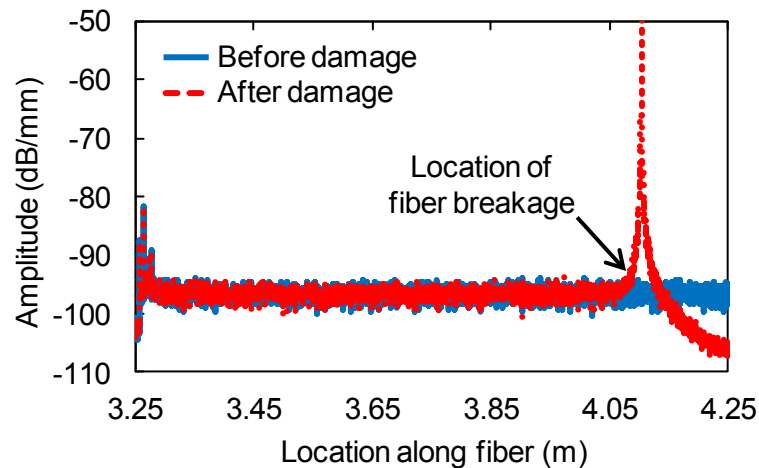


Figure 6.16 Amplitude response of backscattered/reflected light along the embedded fiber before and after fiber breakage.

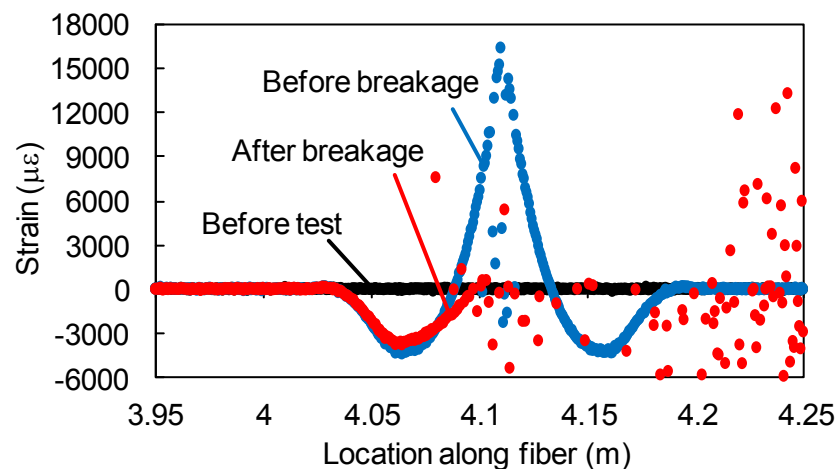


Figure 6.17 Strain distribution at the fiber breakage location before and after damage.

### 6.5.7. Hygrothermal strains during manufacturing and conditioning

Hygrothermal strains can occur during the manufacturing and conditioning of the sandwich structures. Due to differences in the thermal and moisture expansion coefficients, notable strains and stresses can be induced in the interface between the face sheet and the core material. For example, during adhesion of the core and face sheet at high temperature the core and the face sheet expand, with the core expanding slightly more. When the sandwich structure is cooled down to room temperature after the adhesion, the core and face sheet shrink back to their initial size. However, as the adhesive was cured at high temperature condition when the core and face sheet were expanded, some residual strain will remain at the core-face sheet interface as the core tries to shrink more than the adhesively joined face sheet now allows.

To observe these strains occurring during manufacturing and conditioning, measurements were done during manufacturing before adhesion and after conditioning right before the indentation tests. By comparing these two measured states, the hygrothermal strains in the core-face sheet interface were estimated, assuming that cure shrinkage of the adhesive is insignificant. Figure 6.18 shows the measured strain distributions at selected conditions. At highest, strains up to 300  $\mu\epsilon$  can be observed based on the conditions. These are rather small when considering that the maximum strains during indentation can reach thousands of  $\mu\epsilon$ . However, it should be noted that during the manufacturing of the sandwich beams some tension is applied to the fiber when it is set on its place. This tension in the fiber is then gradually released over time as the fiber can slightly move between the face sheet and the adhesive layer, especially in the beginning of the adhesion when the adhesive starts to flow. The state measured before adhesion can thus contain strains due to the tensioning of the fiber, and as this state is used as the reference when obtaining the strains before the indentation tests, the obtained strains might show slightly too high compressive strains.

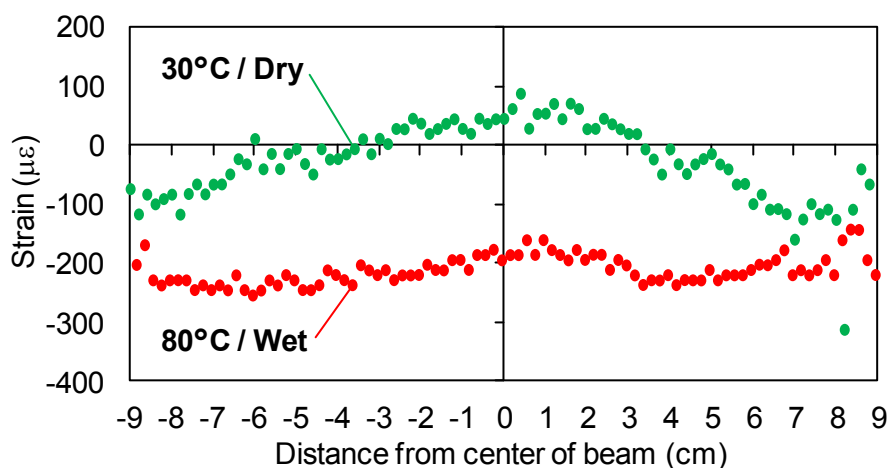


Figure 6.18 Strain distributions measured after adhesion and conditioning, right before the indentation tests.

### 6.5.8. Results – Indentation loading tests

Figure 6.19 and Figure 6.20 show the strain distribution during maximum indentation and immediately after unloading for various humidity conditions at 30°C temperature. It can be seen that the maximum strain immediately below the indentation location becomes slightly smaller with increasing humidity. This is due to the dent becoming slightly wider as the weakened core is crushed on wider area. This is also supported by the observation that the compressive strain area seems to spread on a slightly wider area with increasing humidity. Some strain values near the maximum strain can be seen to be significantly off from the general trend of the strain. This is probably caused by the very high and local, almost singular strain peak at the indentation loading point, which leads to problems when the system tries to cross-correlate the measurement data.

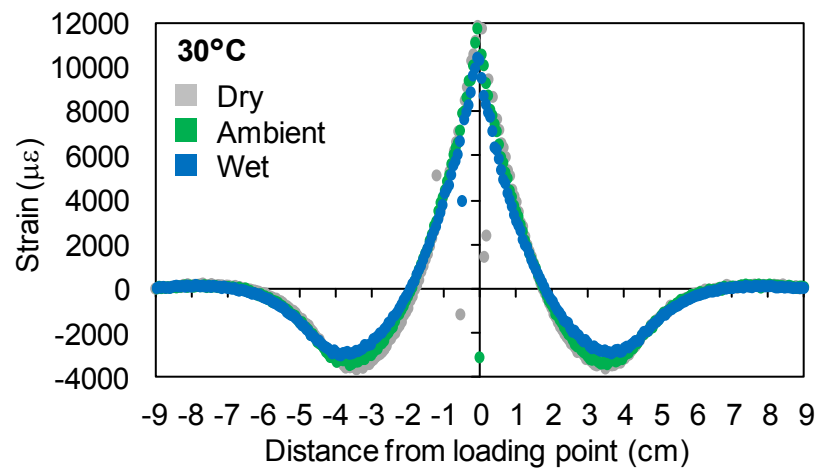


Figure 6.19 Measured strain distribution during maximum loading at 30°C for maximum indentation displacement tests.

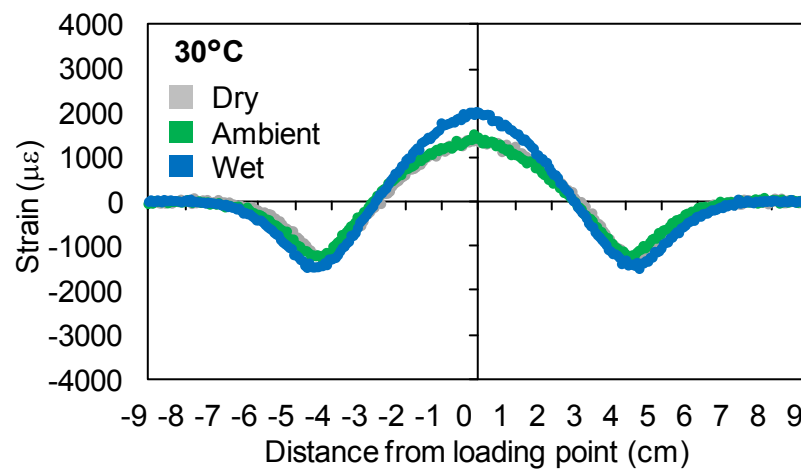


Figure 6.20 Measured residual strain distribution after unloading at 30°C for maximum indentation displacement tests.

After unloading quite notable amount of residual strain remains. The wet specimen shows higher strains than the dry and ambient specimens which have similar strain distributions. This is in correspondence with the indentation test results where the wet beam specimen had deepest residual dent depth, which now leads to higher residual strains. The residual strain distribution is also spread on a slightly wider area corresponding with the crushed core area.

Similar strain distribution data for 80°C temperature case is shown in Figure 6.21 and Figure 6.22. As with the 30°C case, increased humidity leads to lower and wider maximum strain distribution. Difference between different humidity conditions is now much more clearer compared to the 30°C results due to the combined effect of temperature and humidity.

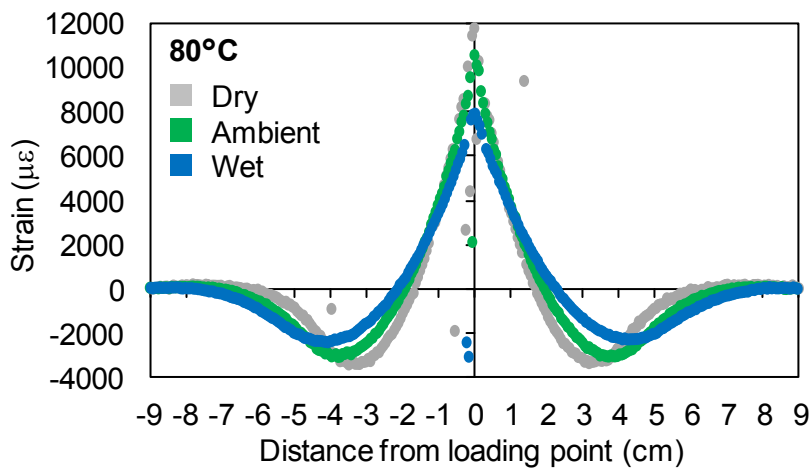


Figure 6.21 Measured strain distribution during maximum loading at 80°C for maximum indentation displacement tests.

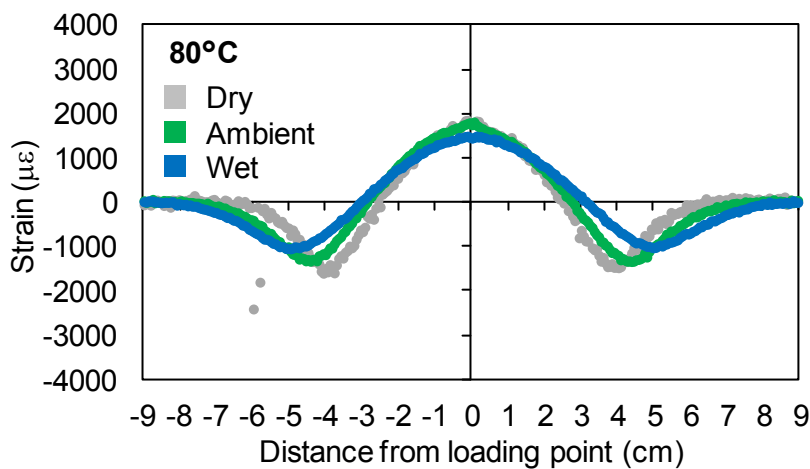


Figure 6.22 Measured residual strain distribution after unloading at 80°C for maximum indentation displacement tests.

Looking at the residual strains, the strained area spreads similar to the maximum strains. However, the maximum strains become lower with increased humidity which seems to be contrary to the results at 30°C. The degrading effect of high temperature and humidity combined cause the core to crush at much larger area compared to the low humidity conditions. The deformation of the face sheet is therefore less local leading to a shallower residual dent, which again reduces the magnitude of the residual strains.

Figure 6.23 and Figure 6.24 show the maximum and residual strain distribution for various humidity conditions at 30°C temperature for the maximum indentation loading tests. Notable differences can be seen between each humidity case. This is because the maximum deflection of the face sheet varies notably between each humidity condition. The foam of the wet specimen is the weakest so the wet sandwich beam will have the largest deformation in the face sheet during indentation and thus highest strains. The magnitude of the strains is now closely related to the indentation displacement. The strain peak also becomes notably wider in the wet specimen as the weak core is damaged on larger area.

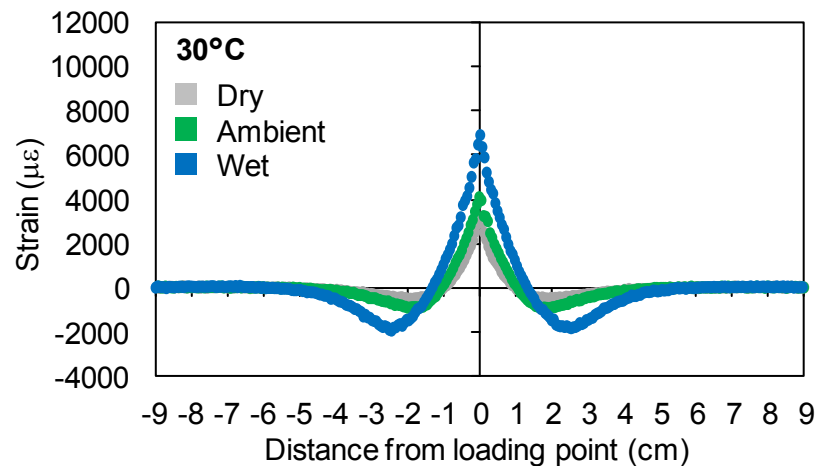


Figure 6.23 Measured strain distribution during maximum indentation loading at 30°C .

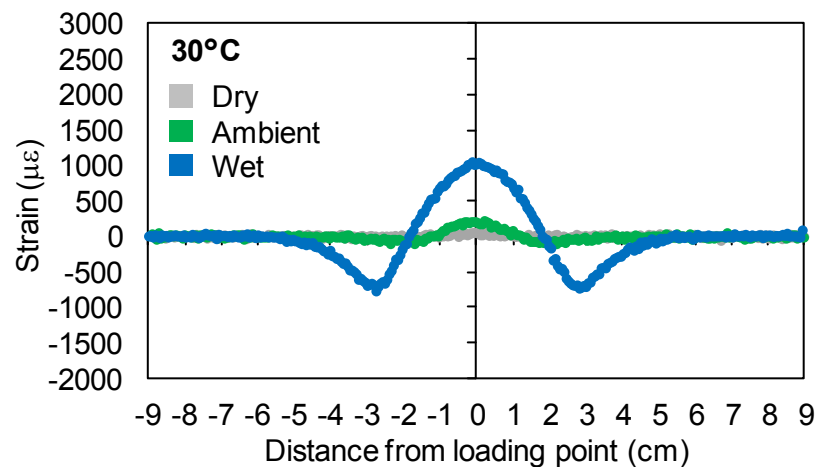


Figure 6.24 Measured residual strain distribution after unloading at 30°C for maximum indentation loading tests.

Looking at the residual states, the deformation in the dry specimen is quite small and just barely large enough to initiate damage in the foam core. Therefore almost no residual strain remains in the core-face sheet interface. The wet specimen on the other hand shows large residual strains corresponding with large residual dent due to notable plastic deformation in the foam core.

Figure 6.25 and Figure 6.26 show the strain distributions for 80°C temperature conditions. The response is mostly similar with the 30°C results. The magnitude of the strains is increased due to larger deformation of the in the face sheet. For the same reason the magnitude of the residual strains are also increased and notable residual strains are now observed for the dry case also.

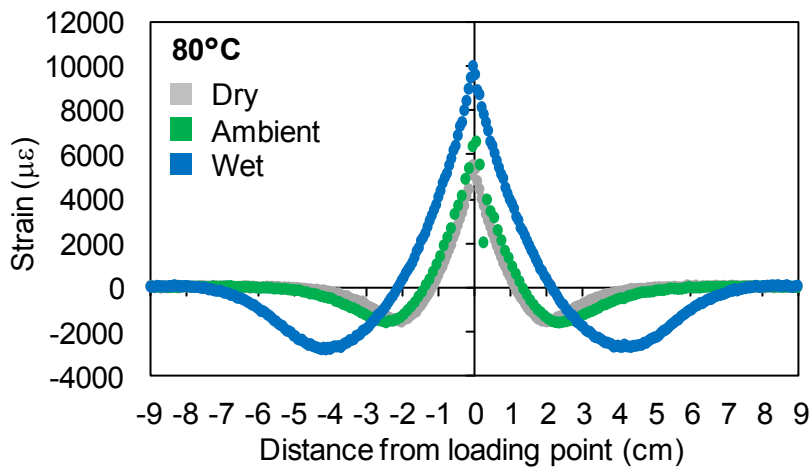


Figure 6.25 Measured strain distribution during maximum indentation loading at 80°C.

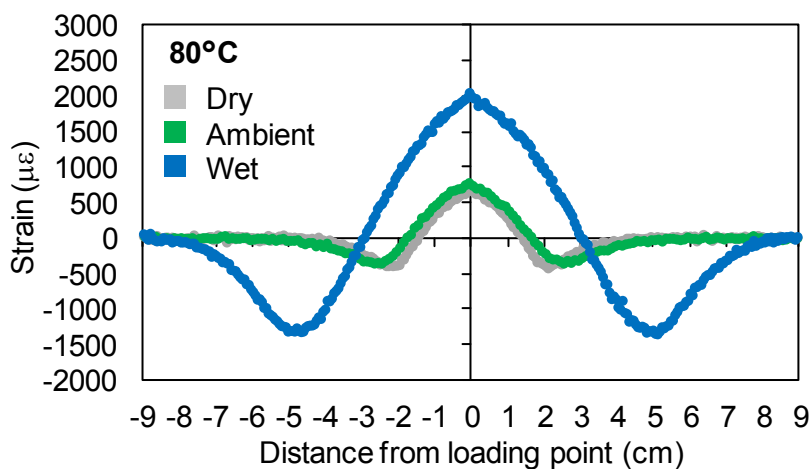


Figure 6.26 Measured residual strain distribution after unloading at 80°C for maximum indentation loading tests.

### 6.5.9. Comparison with numerical analysis results

The measured strain distribution were compared with numerical analysis results from Chapter 4. Comparison of strains during maximum indentation loading for the 30°C test cases are shown in Figure 6.27. The predicted values are now very close to the experimental values. The strain distribution during the loading phase can therefore be predicted well with FEA using the crushable foam model due to the hardening behavior based on experimental data.

Prediction of the residual strain distribution can however be more difficult due to the simplified tensile response of the material model. Figure 6.28 shows the comparison of predicted and measured residual strain distributions for the 30°C temperature cases. The predicted results are close to the experimental ones but give lower strains. The maximum tensile and compressive strains, for example, are around 300 to 500  $\mu\epsilon$  lower than the measured. Similar behavior could be seen with results from higher temperature conditions. The residual strains from the maximum indentation loading tests also are quite close with the predicted values as shown in Figure 6.29. However, looking at the compressive strain peak, the size of the damaged area seems to be smaller than predicted.

It should be noted that as was shown in section 6.5.5 the strains are quite quickly reduced during the first minutes after unloading due to relaxation. Therefore the measured strains are most likely slightly lower than expected immediately after unloading. Also, it is rather difficult to exactly determine the time of unloading from the measurement data and the measurement strain distributions might be few seconds before or after the actual unloading point.

Also, for comparison, Figure 6.30 and Figure 6.31 show the residual strain distributions for the 30°C ambient condition predicted using the new improved foam core model. Using the new material model for the foam core, the strains are higher than what the crushable foam model predicts, and thus closer to the experimental results. Location of the compressive strain peak is however slightly closer to the loading point compared to the experimental results. This might indicate that the predicted damage area is slightly smaller than expected. The strains during maximum loading are practically identical with the ones predicted using crushable foam material model. The new model therefore seems to have potential in giving improved predictions on the residual state of indentation loaded sandwich structures.

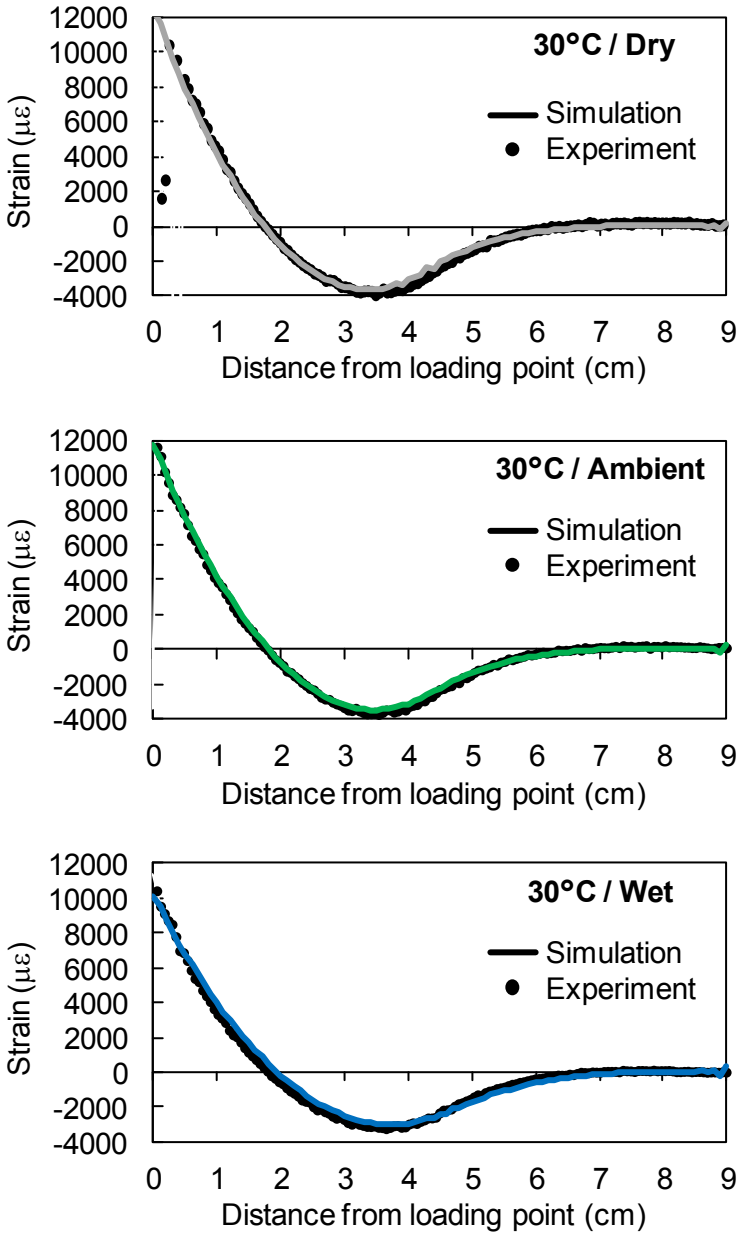


Figure 6.27 Predicted and measured strain distributions during maximum indentation loading for maximum indentation displacement tests.

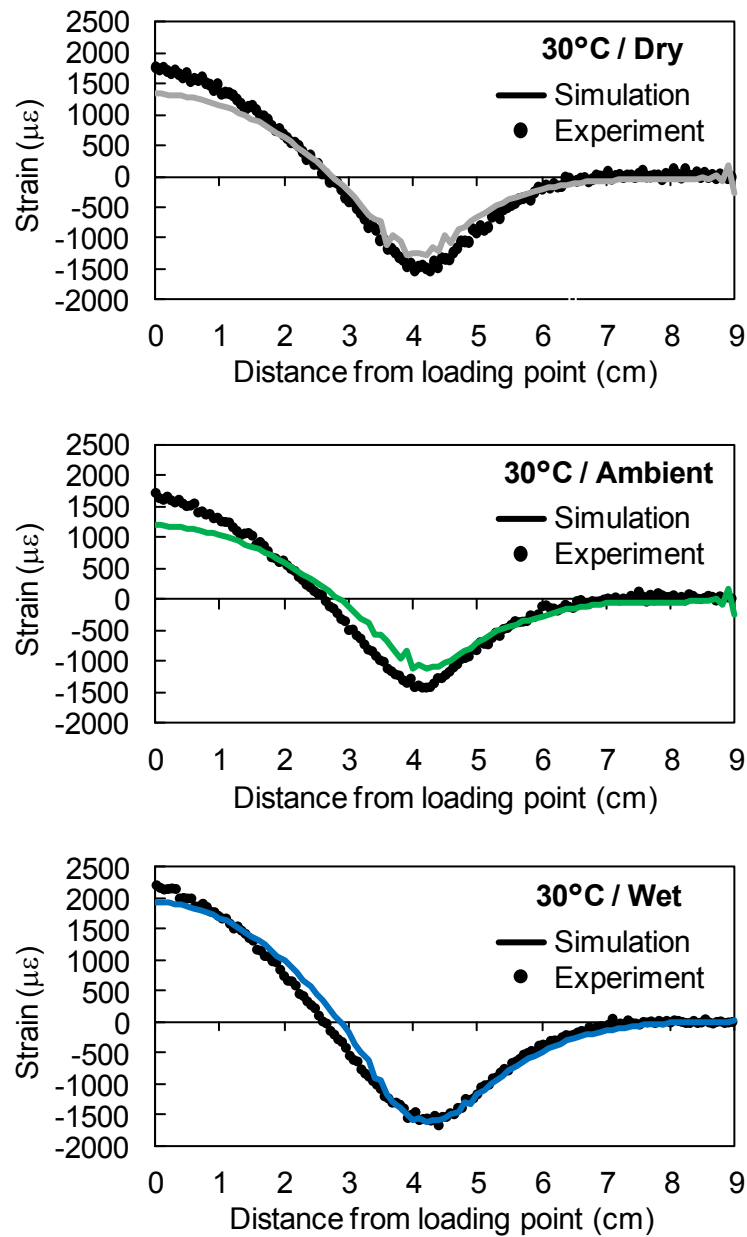


Figure 6.28 Predicted and measured residual strain distributions for maximum indentation displacement tests.

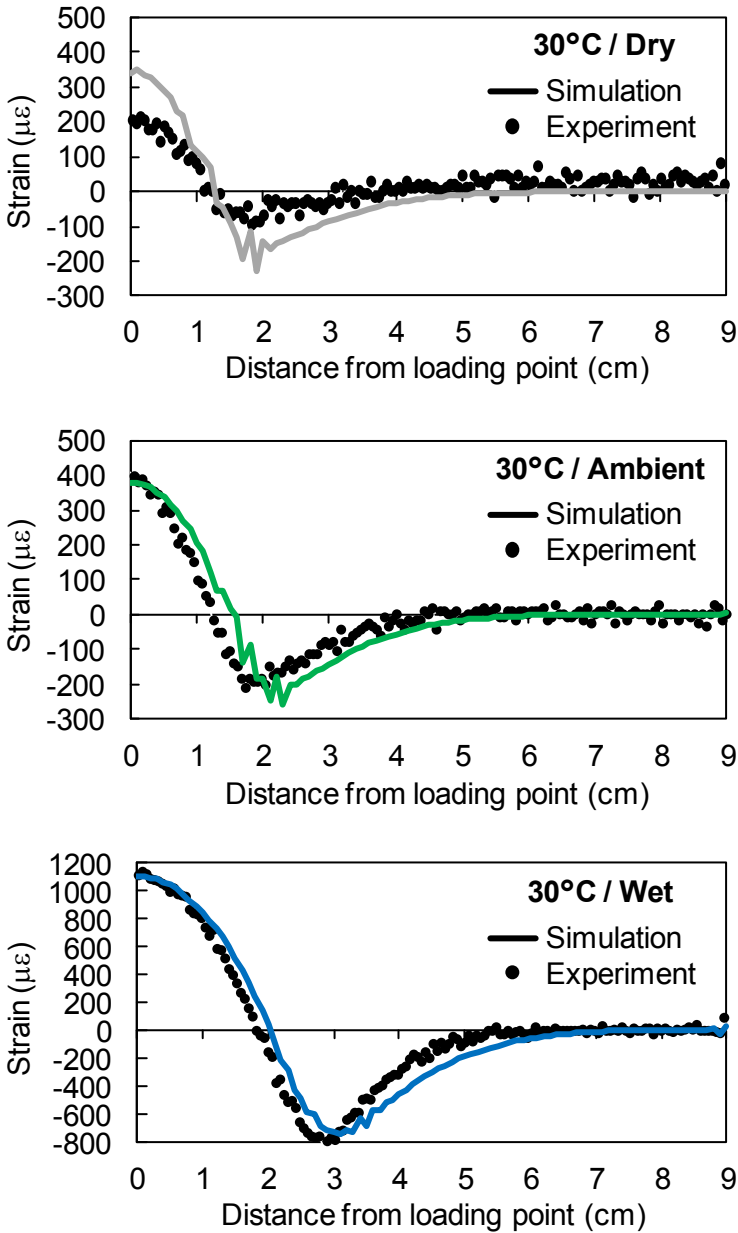


Figure 6.29 Predicted and measured residual strain distributions for maximum indentation loading tests.

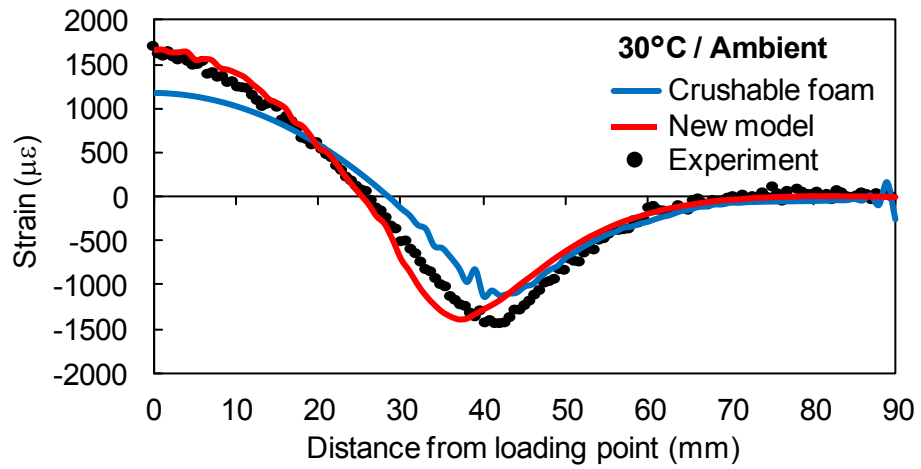


Figure 6.30 Comparison of predicted residual strains by new foam core model and crushable foam model and experimental results for maximum indentation displacement test.

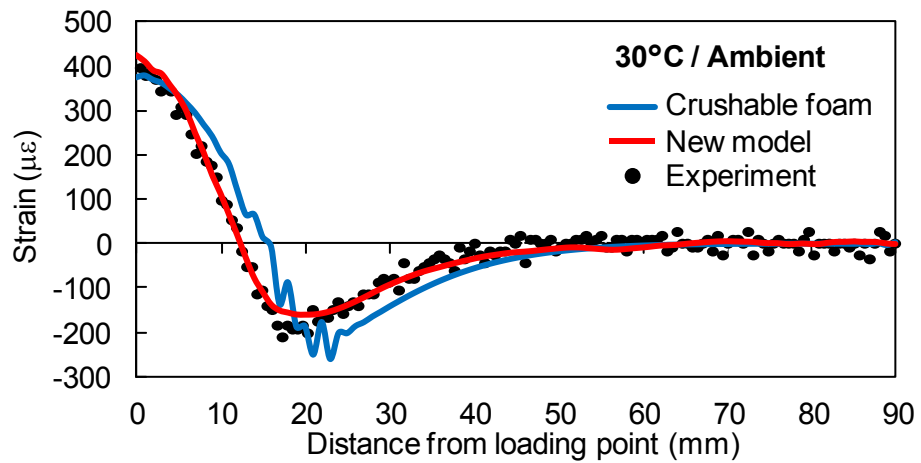


Figure 6.31 Comparison of predicted residual strains by new foam core model and crushable foam model and experimental results for maximum indentation loading test.

## 6.6. Sandwich panel indentation monitoring experiment

Compared to sandwich beams, sandwich panels provide higher stiffness against indentation due the face sheet providing support against bending in two dimensions. The panel therefore experiences more local deformation than beam. Now due to the more local damage the monitoring capability might be affected compared to the sandwich beam specimens. Experiments are therefore conducted with a sandwich panel specimen to verify the indentation damage detection ability.

### 6.6.1. Sandwich panel specimen

Sandwich panel as depicted in Figure 6.32 was manufactured with optical fiber (Heatop 300, Totoku Electric Co., Ltd., outer diameter: 150  $\mu\text{m}$ , cladding diameter: 125  $\mu\text{m}$ ) embedded between the adhesive layer and face sheet similar to the sandwich beam specimens in section 6.5. The fiber was embedded starting from the middle of the panel immediately under the impact location and the adjacent parallel fibers were embedded 5 mm apart. The fibers were embedded only on one half of the panel as the strain distribution is assumed to be symmetric. The panel was manufactured similar to the beam specimens previously and consisted of CFRP face sheet and foam core adhered together using adhesive film. The face sheets were manufactured beforehand using T700S/2592 (Toray Co.) CFRP prepreg sheets. 8 ply cross-ply  $[0/90]_4$  laminates were manufactured in autoclave and then cut to size (100 mm  $\times$  100 mm) using diamond blade saw. Thickness of the face sheets was on average 1.15 mm. The face sheet laminates were then adhered to 35 mm thick Rohacell 51 WF core of same size using AF 163-2K adhesive film. The core-face sheet combination was then adhered to a steel plate using the same adhesive film. This provides fully backed support against global deformation.

### 6.6.2. Test method

In the tests, quasi-static indentation loading was applied to the center of the panel using a hemispherical 10 mm diameter steel indenter with constant loading displacement speed of 5 mm/min. The maximum indentation loading was increased gradually with each indentation loading-unloading cycle from 100 N to 2000 N. The strain distribution was measured continuously during each indentation-unloading cycle using the LUNA OBR 4600 monitoring system.

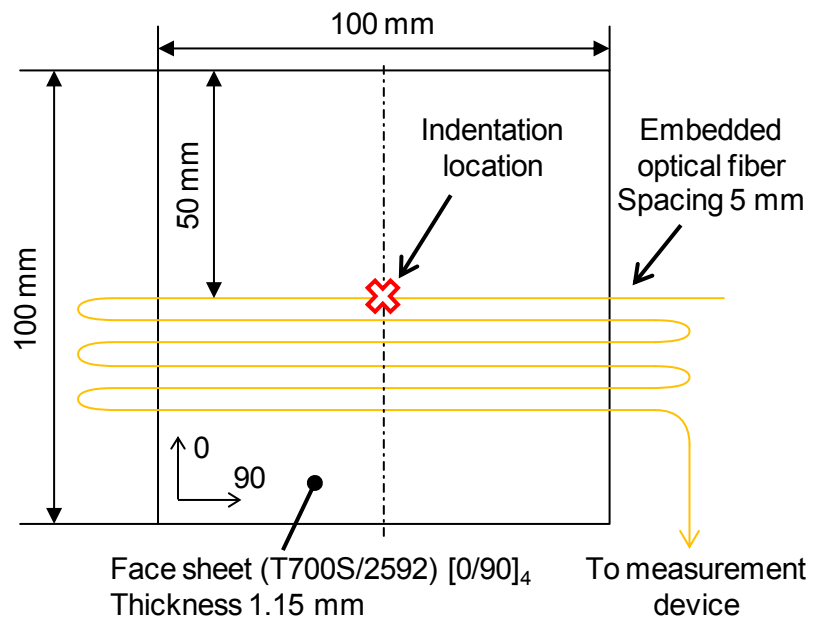


Figure 6.32 Schematic of sandwich panel specimen.

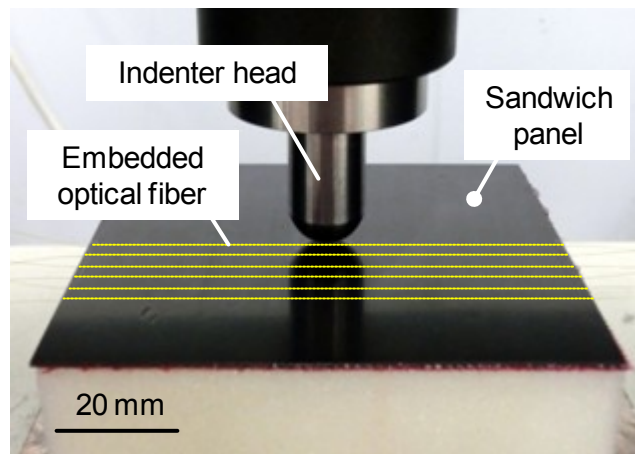


Figure 6.33 Indentation test setup of sandwich panel specimen.

### 6.6.3. Finite element analysis model

A finite element model of the sandwich panel was also constructed using the ABAQUS software to evaluate the monitoring results. The panel was modeled using 3 dimensional 8-node elements with reduced integration. Due to the symmetry of the panel, only one quarter was modeled with appropriate symmetric boundary conditions. The used model is depicted in Figure 6.34. Mesh size in the X-Z plane was 1×1 mm. The face and adhesive layer were modeled as elastic and the core as elasto-plastic using the crushable foam material model. The material parameters were the same as in the sandwich beam model in section 4.3.1 at 30°C ambient conditions. Loading was applied to the panel using a hemispherical rigid indenter until desired maximum indentation displacement was reached.

### 6.6.4. Results

The indentation load-displacement curves of the loading cycles are shown in Figure 6.35. Looking at the loading parts, it can be seen how the response becomes nonlinear after nearly linear response in the beginning. This behavior is quite similar with sandwich beam specimens where a change in the indentation stiffness can be seen as the core is crushed and begins to deform plastically. Later at increasing indentation loads, a visible decrease can be seen in the loading response after maximum loading of 1000 N. Looking at the residual dent progression in Figure 6.36, it can also be seen that the dent becomes suddenly deeper after the load decrease. This might therefore be caused by some permanent damage in the adhesive layer or the face sheet, or by the core damage suddenly propagating on larger area.

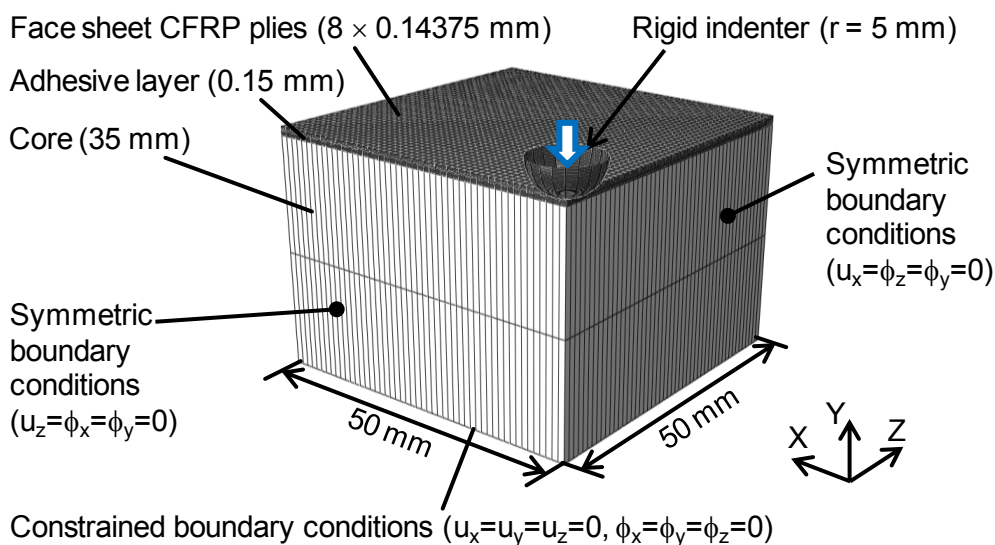


Figure 6.34 Finite element analysis model of sandwich panel indentation.

The residual dent progression in Figure 6.36 also shows that, if taking the limit of BVID dent depth as 0.01 to 0.02 inches (0.25 to 0.51 mm), loading of 1 to 1.5 kN is needed for the indentation damage to become visible for the current sandwich panel. The detectability of the damage can now be evaluated against this specification.

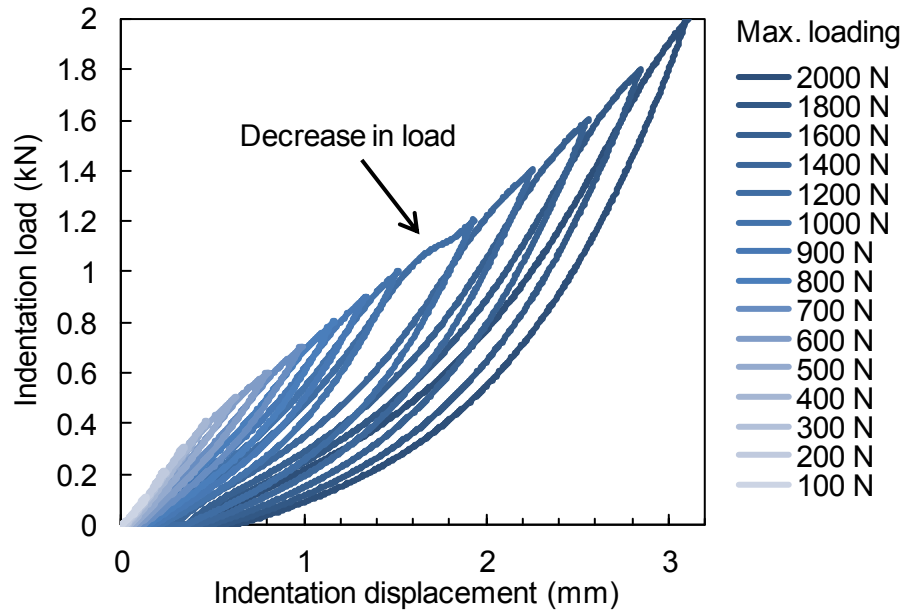


Figure 6.35 Indentation load-displacement response of sandwich panel specimen.

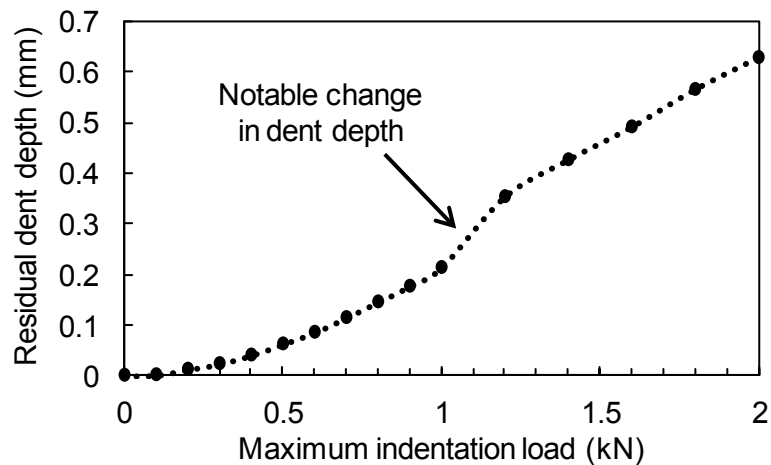


Figure 6.36 Progression of residual dent depth during indentation loading test of sandwich panel.

First, the strain results were observed to see when the indentation damage becomes detectable with the current system, that is when the strain results show clear indication of the damage. Table 6.2 shows the loading that resulted in clearly visible indication of damage in the residual strain distribution along the fibers. Examples of the residual strain distributions along selected fibers after first indication of damage are given in Figure 6.37. Within 10 mm from the indentation location, the damage is detectable at 300 N maximum loading. The residual dent depth after the 300 N loading cycle is around 0.025 mm, so the system can detect the indentation damage almost immediately it has initiated and well before it becoming visible.

Based on the data in Table 6.2 and corresponding residual dent depths in Figure 6.36, graph for the damage detectability can be constructed as shown in Figure 6.38. The figure shows the maximum indentation loadings and residual dent depths of smallest detectable damages at various fiber spacing's, when assuming that the damage occurs between the parallel fibers. This can now be used for the current sandwich configuration to define sufficient spacing of the parallel fiber to be embedded in the structure. For example, 10 to 20 mm fiber spacing would be able to detect the damage initiation after 300 N loading. Barely visible damages with 0.5 mm deep residual dent could still be detected with 50 mm spacing of the fiber sensors.

Table 6.2 Indentation loadings after which damage is detectable from residual strain distribution for each fiber from the loading point.

Fiber distance from loading	First indication of damage
0 mm	100 N
5 mm	300 N
10 mm	300 N
15 mm	800 N
20 mm	1000 N
25 mm	1400 N

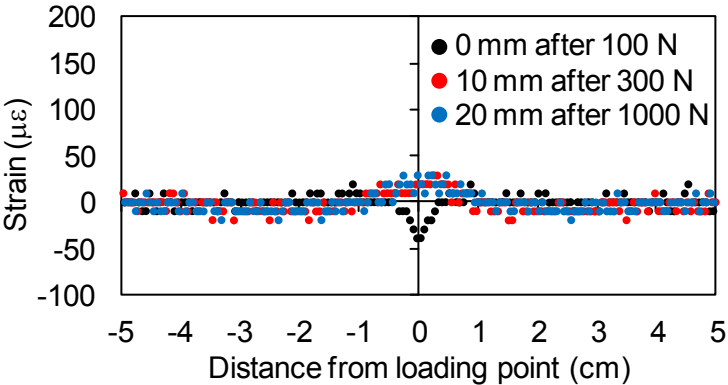


Figure 6.37 Residual strain distributions after first indication of damage.

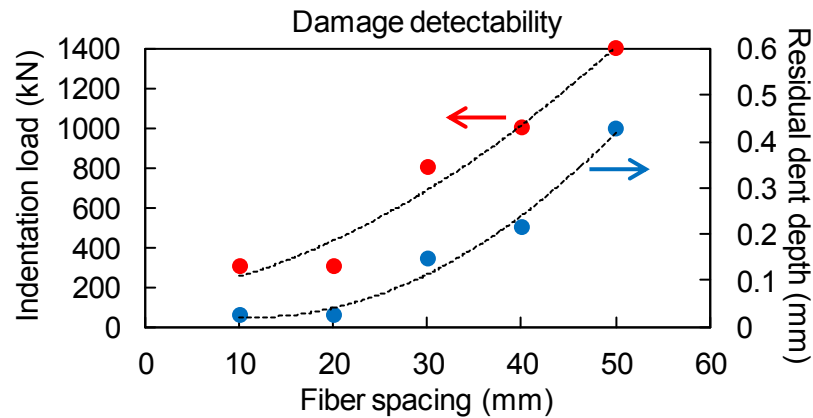


Figure 6.38 Detectability of damage with various fiber spacing based on the maximum indentation loading and residual dent depth.

Next, changes in the strains were observed during the loading cycles. Figure 6.39 shows the strain distributions at maximum loading during early phases of the loading at maximum indentation loads from 400 N to 600N. The strain response is similar with the beam specimens as the strains are increased with increasing loading and the strained area becomes slightly larger due to increasing denting of the face sheet. After 500 N the strains seem to increase slightly faster. This might be caused by the damage in the core spreading on area large enough to affect the indentation stiffness of the panel. Also, very local high strains arise immediately under the loading point which cause problems with the correlation algorithm of the monitoring system and can be seen as notable noise in the strain results. Looking at residual strains in Figure 6.40, the residual strains also increase with increasing maximum loading similar to the beam specimens. There however seems to be some flattening of the strain peak at the loading point after 500 N loading which is probably caused by local damage immediately under the loading point.

Notable change in the indentation load-displacement curve was seen after 1000 N maximum loading. After 1000 N loading the strain distribution during maximum loading near the loading point starts to spread on wider area while the strain magnitude stays almost same, as shown in Figure 6.41. This also corresponds with the sudden increase in the residual dent after 1000 N loading and could indicate that the damage in the core expands on wider area leading to wider dent in the face sheet which would spread the strain on larger area without increasing the maximum strains. Also after the sudden jump in the strains, the residual strains stop increasing and start to spread on wider area similar to the strains at maximum loading as can be seen from Figure 6.42.

Figure 6.43 shows the residual dent in the face sheet of the sandwich panel after the maximum loading of 2000 N. It can be seen that the remaining visible deformation in the face sheet is very local. The diameter of the residual dent is approximately 10 mm. The sandwich panel was cut after the tests and cross section along the fiber embedded at the

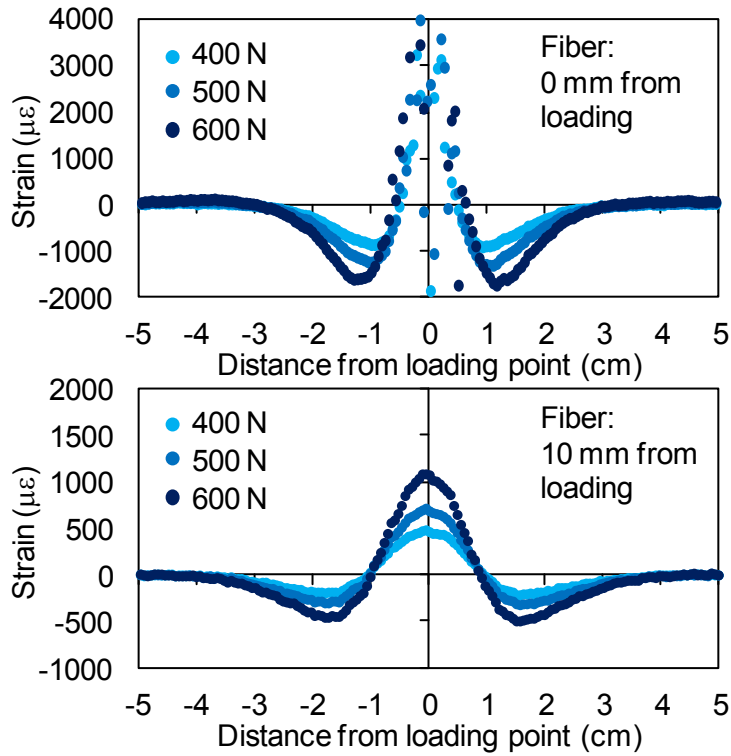


Figure 6.39 Strain distribution at maximum indentation loading at low indentation loading levels.

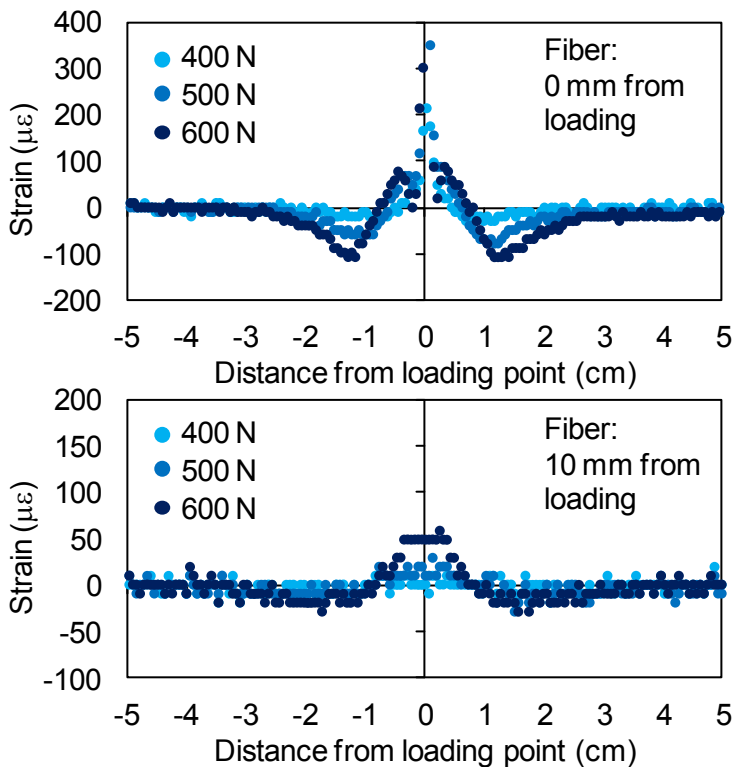


Figure 6.40 Residual strain distributions immediately after unloading at low indentation loading levels.

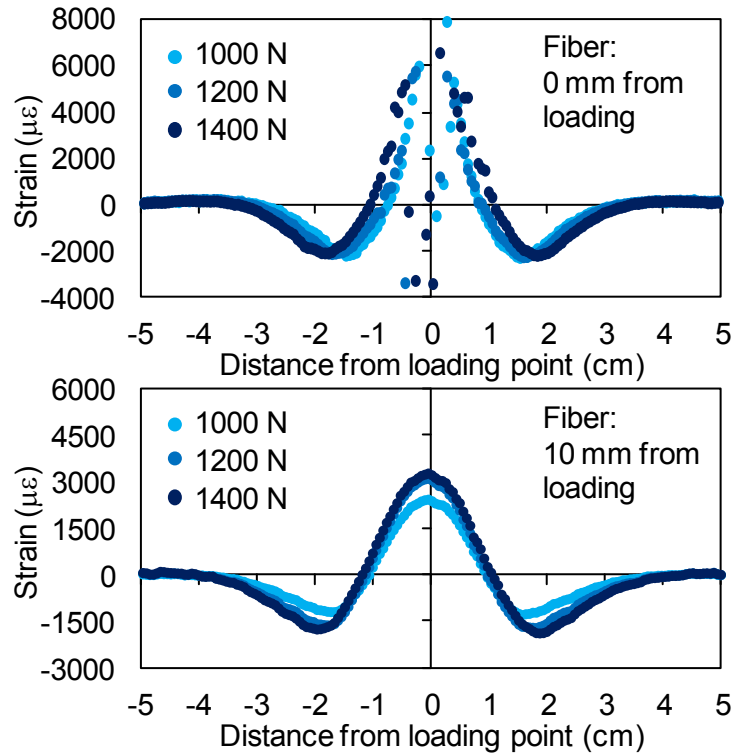


Figure 6.41 Strain distributions at maximum indentation loading at high indentation loading levels.

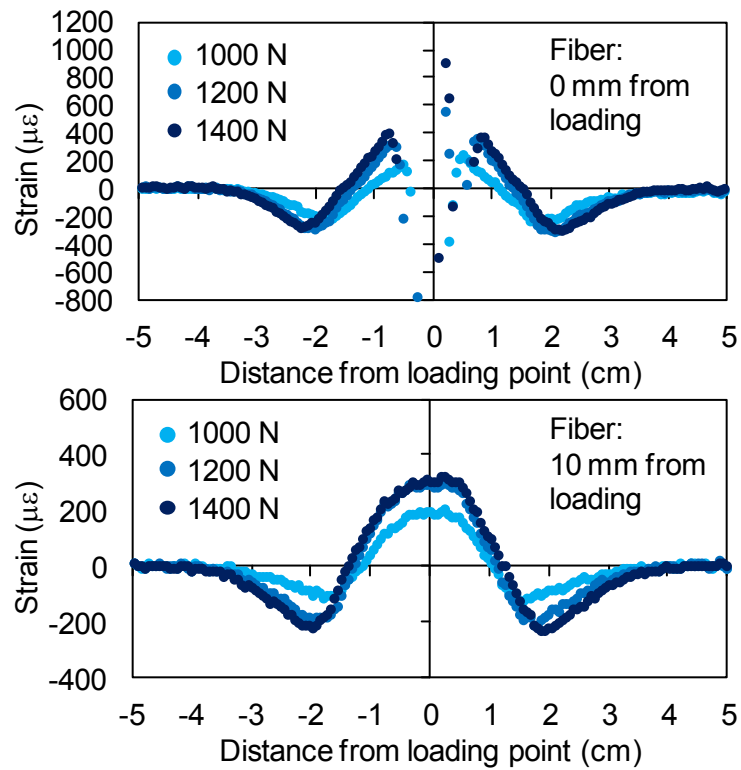


Figure 6.42 Residual strain distributions immediately after unloading at high indentation loading levels.

middle of the panel is shown in Figure 6.44. No clearly visible damage was observed in the face sheet or adhesive layer, and the damage was therefore mostly crushing of the core. The area of the core damage seem to reach 20 to 30 mm away from the loading point. The damage area should now correspond with the residual strain as was explained in section 4.4.4 and it seems to do so, as compressive strain peaks are seen around 25 mm away from the loading point in the residual strain distributions in Figure 6.45. These observations also show how the diameter of the damaged area in the core is approximately 6 times larger than the diameter of the dent visible in the face sheet.

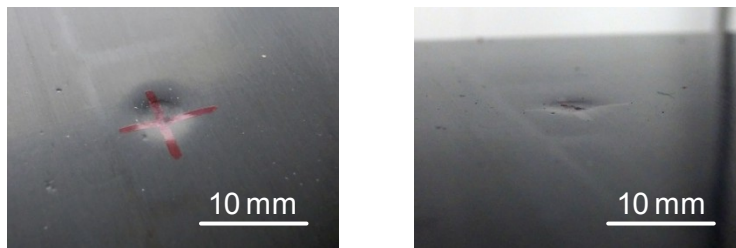


Figure 6.43 Residual damage in the face sheet after 2000 N indentation loading.

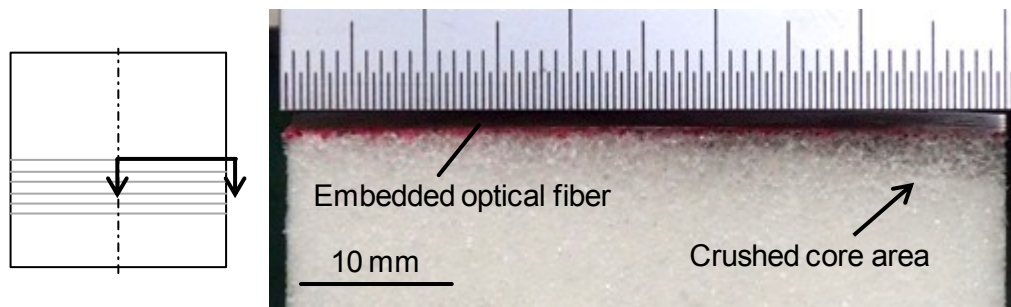


Figure 6.44 Cross section photograph of the sandwich panel at the indentation location after 2000 N loading.

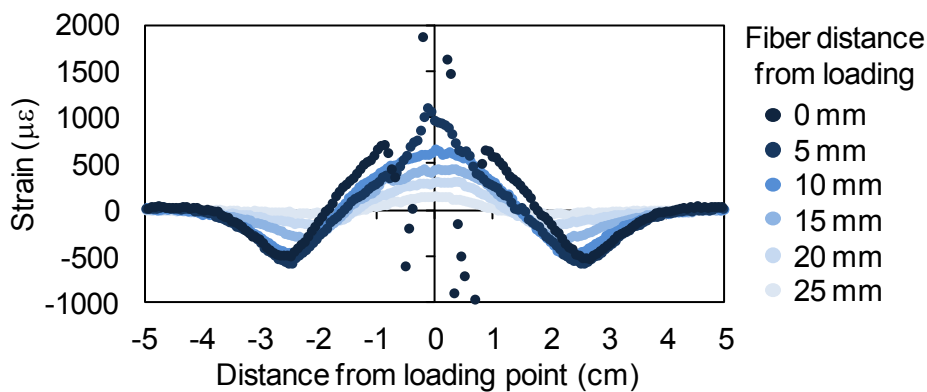


Figure 6.45 Residual strain distributions immediately after 2000 N indentation loading.

Figure 6.46 shows the predicted residual strain distribution in the adhesive layer after indentation loading cycle for an example case of 1.524 mm maximum indentation corresponding with 1000 N maximum loading. Size of the plastic deformation area in the core is also depicted. Region of high compressive strains can be seen at the damaged core area near the edge of the area. This corresponds with the observations in the sandwich beam model in section 4.4.4 where the tensile peak was seen to be near the edge of the damaged core area.

Looking at the predicted strains at the embedded fiber locations, as shown in Figure 6.47, it can be seen that further away from the loading point the residual strains are decreased and the tensile peak in the distribution moves closer to the loading point. This behavior is similar with the experimental results even though the predicted strains are higher due to plastic deformations and damage being ignored in the model. Disregarding any damages that might occur, the shape of the strain distributions measured by the fibers is mainly related with the shape of the dent in the face sheet, which becomes shallower further away from the loading point as can be seen from Figure 6.48.

It therefore seems that in the case of the sandwich panels, the size of the damage in the core can be estimated by observing the location of the tensile strain peaks measured by the monitoring system. In the case studied here, the fibers are however embedded to measure the strain in only in one direction. Estimation of the damage size can thus become more difficult further away from the loading point as the dent profile at the fiber locations becomes shallower. Accuracy of the damage size estimation could therefore be improved by including fibers also in the perpendicular direction, forming a grid network.

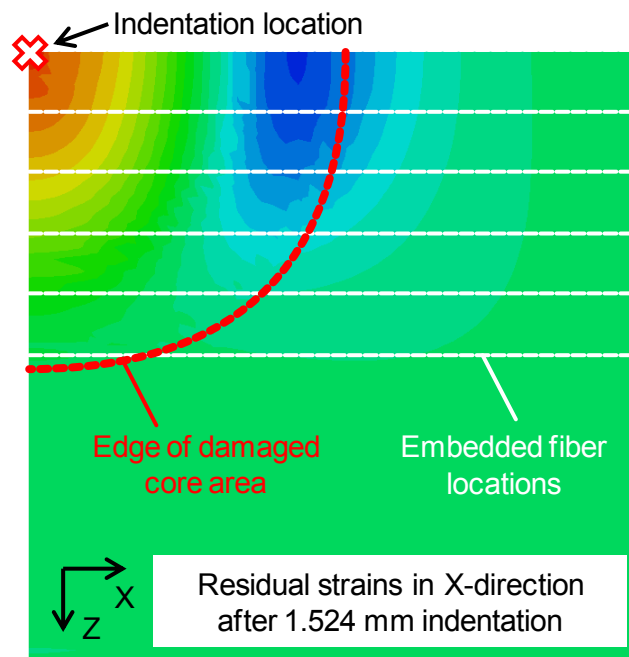


Figure 6.46 Residual X-direction strain distribution in the adhesive layer of sandwich panel after 1.524 mm maximum indentation.

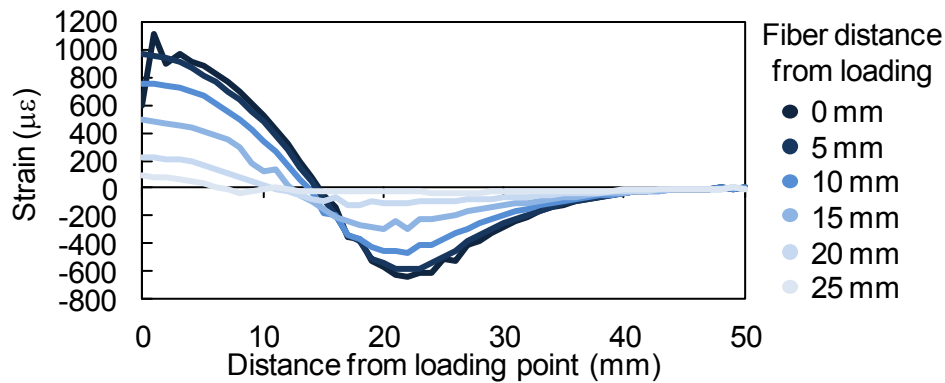


Figure 6.47 Predicted residual strain distributions in the adhesive layer of sandwich panel at embedded fiber locations (Figure 6.46) after 1.524 mm maximum indentation.

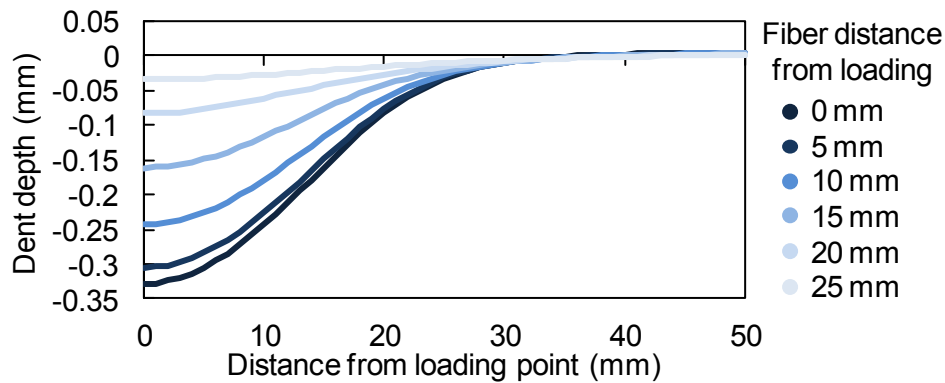


Figure 6.48 Predicted residual face sheet dent profiles of sandwich panel at embedded fiber locations (Figure 6.46) after 1.524 mm maximum indentation.

Based on these experimental and numerical analysis observations, it was shown that the monitoring system seems to be capable of detection indentation damage even in panel structures. For the current configuration, a 20 mm fiber spacing seems to be sufficient for the monitoring system to be able to detect the damage right as it has initiated. The location and size of the damage could also be estimated accurately from the residual strain measurement data.

## 6.7. Damage detection demonstrator sandwich panel

In real life applications of sandwich structures, there is very high probability for impact damage to occur. As the impact even is short in time, the damage detection must rely on the residual state of the structure. Also depending on the location of the impact, the damage might be difficult to detect due to variations in the thickness of the core and face sheets. Thus, in this section the low velocity impact damage detection ability of the used monitoring system on real life foam core sandwich applications is verified using a large scale demonstrator.

### 6.7.1. Sandwich panel

A sandwich panel, as shown in Figure 6.49 was manufactured by Kawasaki Heavy Industries. The faces were made of Kawasaki's proprietary high performance and low cost KMS-6115 carbon fiber composite manufactured using VARTM method and Rohacell 51 WF foam was used for the core. Center region of the panel had thinner face sheet than the taper region. The monolithic edge parts had 12 layers of cross-ply fabrics with the stacking sequence of  $[(0/90)/(+45/-45)]_{3S}$ . At the taper region the thickness was halved, so that the stacking sequence became  $[(0/90)/(+45/-45)]_3$ . The thickness was then further reduced at the ply drop region so that at the center part of the panel the stacking sequence was  $[(0/90)/(+45/-45)]$ . The face sheet configuration is also explained in Figure 6.50.

A normal diameter high delta optical fiber (Heatop 300, Totoku Electric Co., Ltd., outer diameter: 150  $\mu\text{m}$ , cladding diameter: 125  $\mu\text{m}$ ) was embedded into core-face sheet interface to form distributed fiber network over the whole panel as depicted in Figure 6.50. The network was divided in to four regions. Two of these covered the middle part of the panel with thinner face sheet. The other two covered the taper area and adjacent face sheet ply drop area at the edges of the panel. Ends of the embedded fibers were routed to come out from the back side of the panel.



Figure 6.49 Photograph of the impact tested sandwich panel.

### 6.7.2. Test method

For the impact tests, the panel was fixed to a supporting structure by clamps at all four corners. This provided simply supported boundary conditions for the panel. Impact tests were conducted on the taper and center region of the panel. On the taper region the face sheet thickness is constant but the core thickness varies. In the mid region the face sheet thickness and the core thickness both are constant. Impact locations were chosen so that they were over and between the embedded fibers as depicted in Figure 6.51. In the taper region five impact location groups were chosen as indicated by numbers 1 to 5 in Figure 6.51. In groups 1, 3 and 5 the impact was located over the embedded fiber and in groups 2 and 4 between two adjacent fibers. Also the core thickness increases gradually from group 1 to group 5 as the impact locations move closer to the middle of the panel. In the center region of the panel, two groups of impact locations were chosen. One over the fiber and one between two fibers.

An impactor with hemispherical head of diameter 15.75 mm and weight of 5.6 kg was used in the tests. The test configuration is depicted in Figure 6.52. Drop heights of the impactor were selected as 50, 100, 150 and 200 mm so that various impact energies were achieved as listed in Table 6.3. However, the test was ended if clearly visible impact damage occurred. All of the tests were conducted at 22°C and 58%RH ambient room conditions.

The scattering response along the embedded fibers were measured before and immediately after the impacts. These two sets of data were then compared and the strains produced by the impact event were calculated using 10 mm gage length and 5 mm sensor spacing. The strain data was then studied against the contact force and impactor displacement data.

Table 6.3 Used impactor drop heights and corresponding impact energies.

Drop height	50 mm	100 mm	150 mm	200 mm
Impact energy	2.7459 J	5.4917 J	8.2376 J	10.9835 J

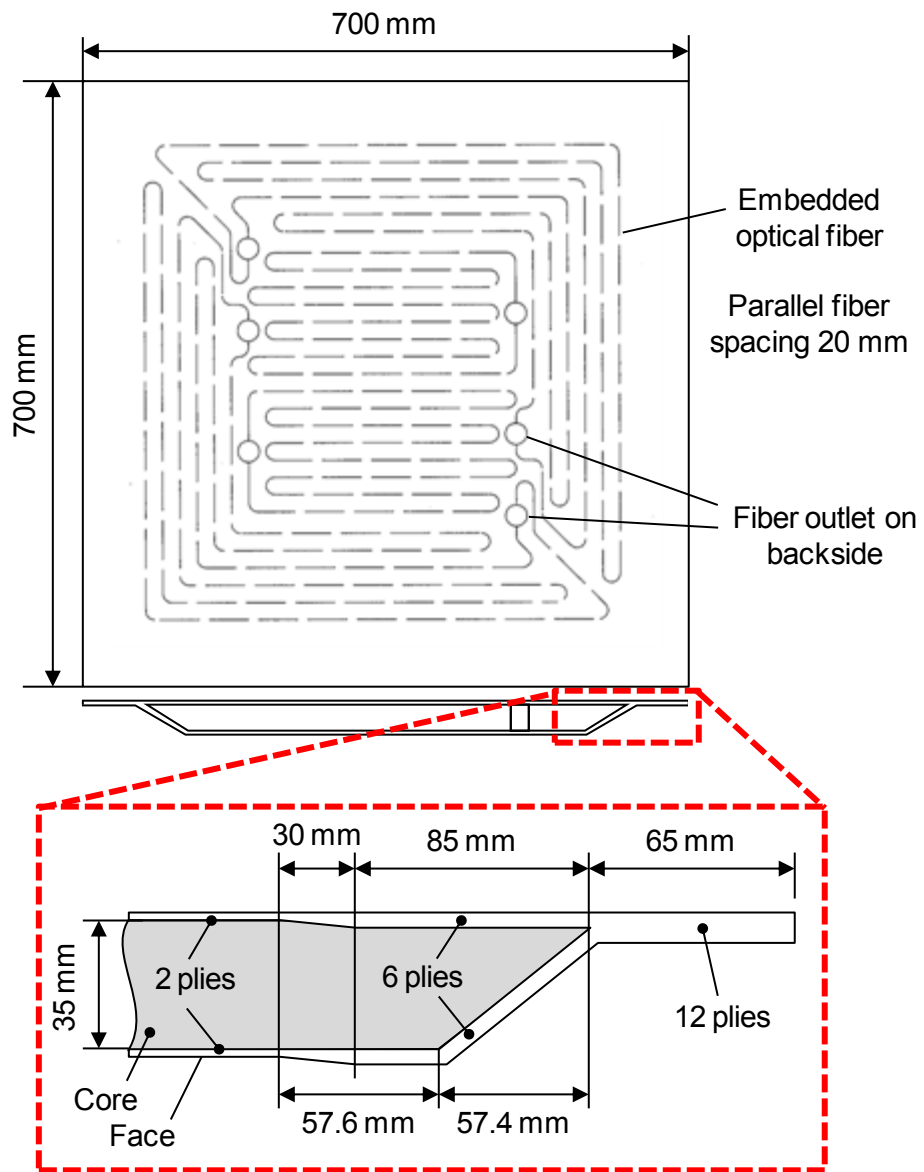


Figure 6.50 Schematic of the sandwich panel showing embedded fiber location and face sheet configuration.

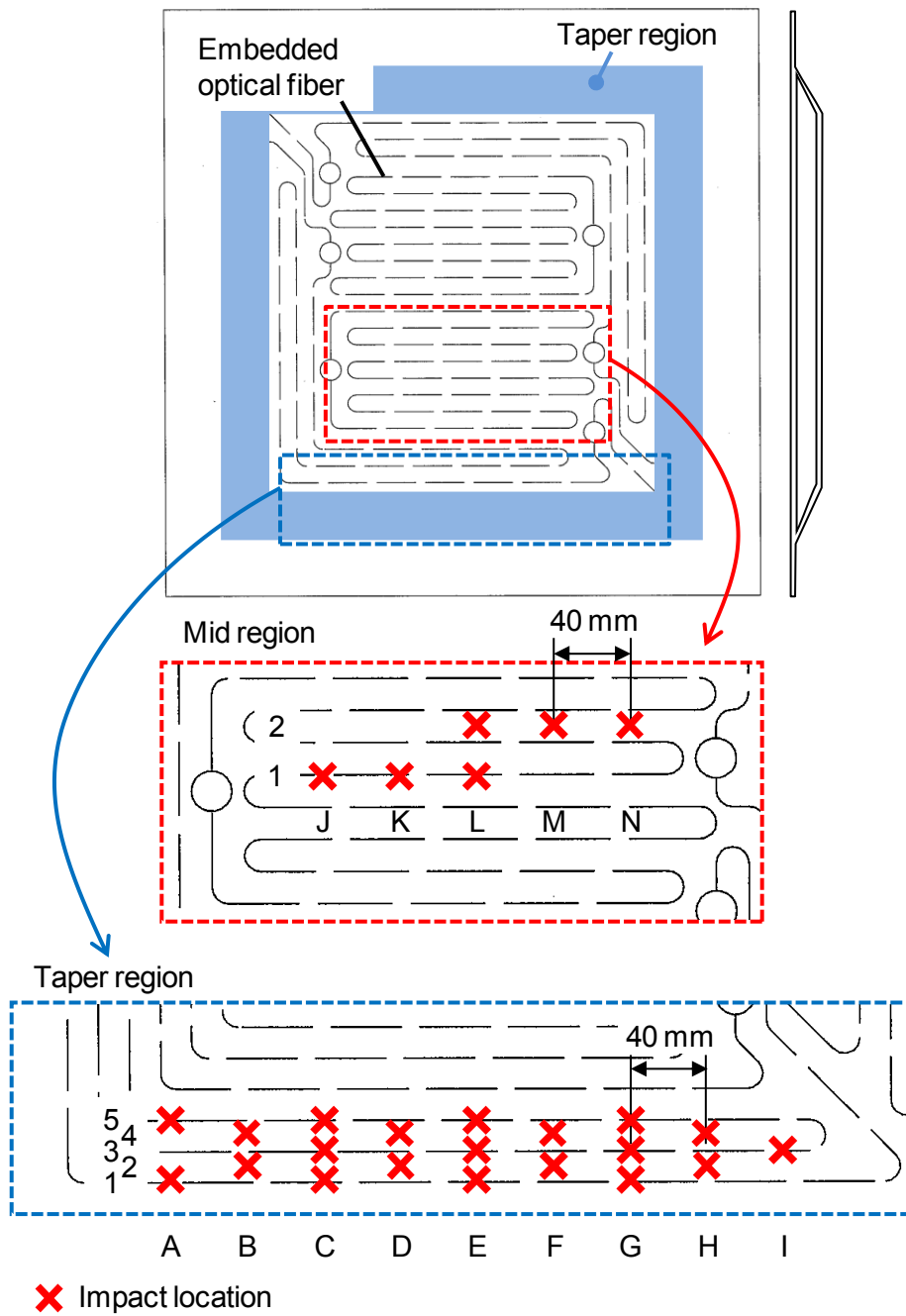


Figure 6.51 Impact locations in the center and taper regions in the sandwich panel.

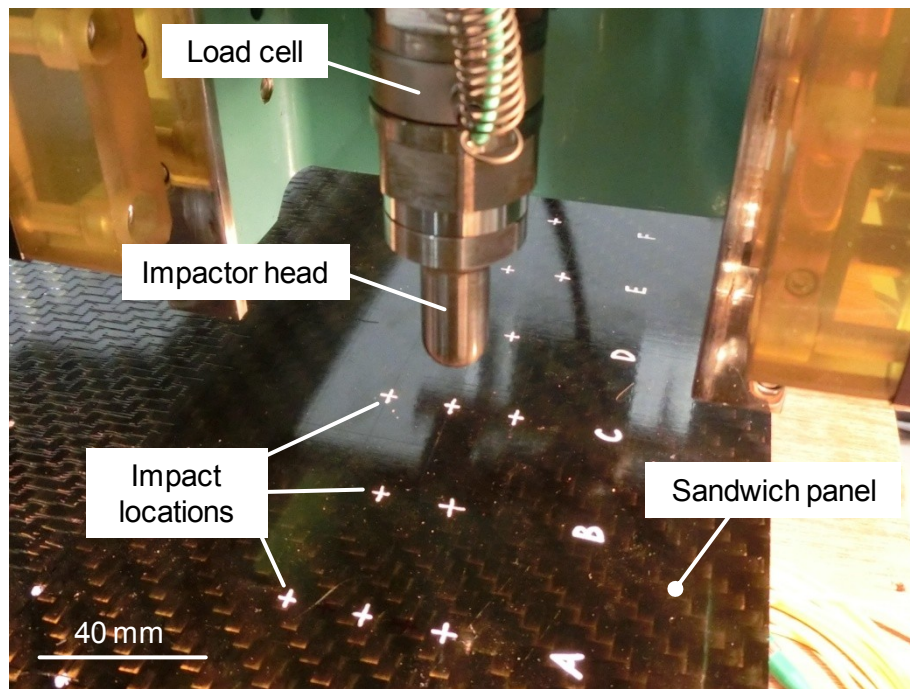


Figure 6.52 Impact test configuration.

### 6.7.3. Results – Taper region

Contact force-displacement curves for the taper region impact groups are shown in Figure 6.53. Near the edge of the panel where the core is thinner, the initial slope of the curve is steep and gets shallower as the impact location moves towards the middle of the panel. This is partly caused by the effect of the boundary conditions restricting global deformation near the edges, but also due to the varying thickness of the core. Also the maximum displacement seems to increase as the thickness of the core at the impact location increases. It can also be seen that the loading curve flattens at the maximum loadings in the thinner core impact regions due to crushing of the core. Similar flattening can also be seen on the thicker core regions, but the change is less abrupt due to global bending of the panel and thicker core. A second peak is seen in the loading response over time. This corresponds with the “hook” shape after the maximum loading in the load-displacement curves and is caused by the panel bending under the impact and during the unloading phase slamming back at the indenter. Near the edges of the panel, the global deformations are smaller, and thus the panel can return faster back to its initial state causing this kind of behavior.

Figure 6.54 shows an example of how the residual strains after impact were observed along the fiber. The residual strain distribution after one impact event located between to fibers is presented. At the fibers on both sides of the fiber a clear strain peak can be observed due to the damage. Also a small strain peak is observable on the third fiber further away from the impact location. The strains become larger further away from the

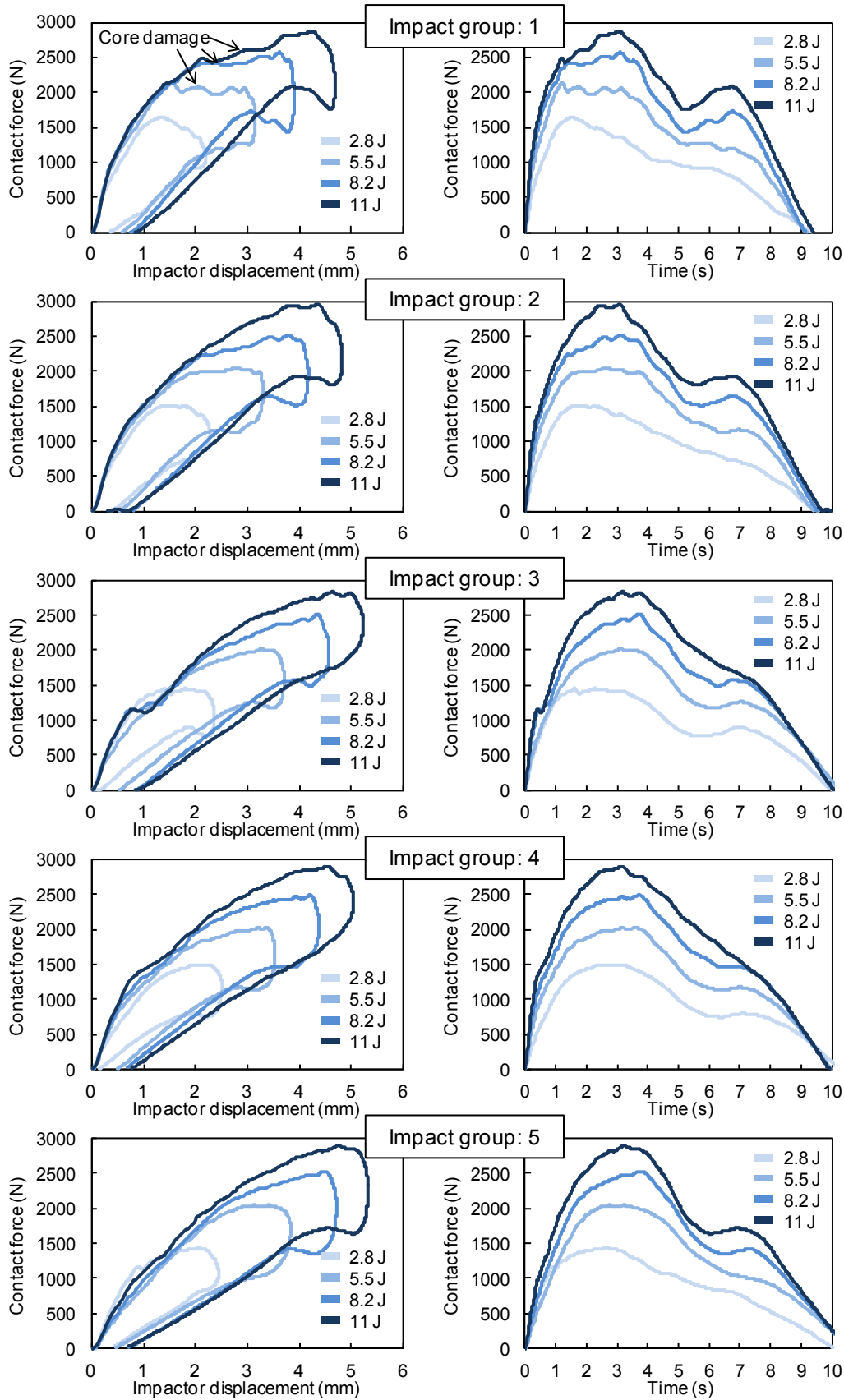


Figure 6.53 Contact force response at taper region.

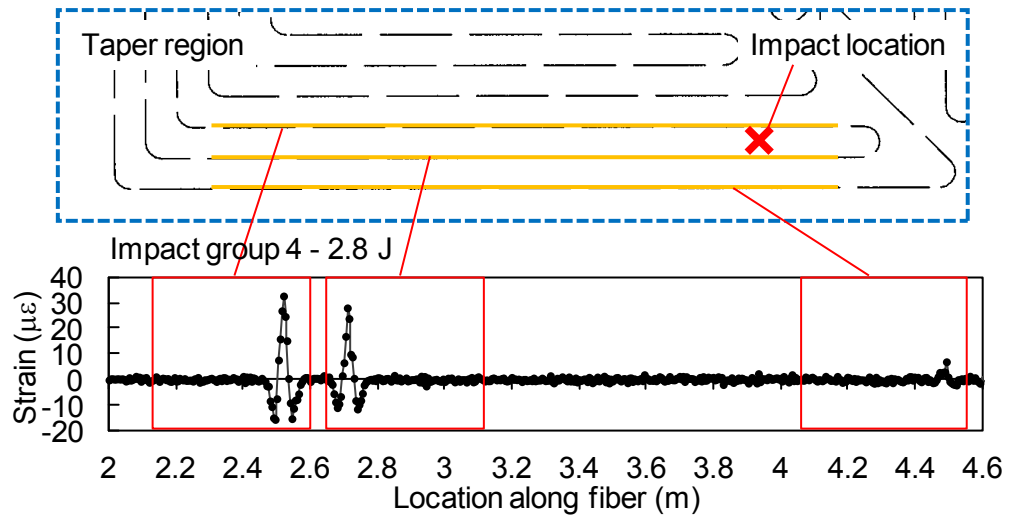


Figure 6.54 Example of residual strain data after 2.8 J impact event at the taper region.

edge of the panel, as the thickness of the core increases and thus amount of crushing in the core also increases. The location of the damage can thus be easily estimated from the residual strain data.

Residual strain distribution data for all impact groups are included in Appendix C. For all impact groups, the damage was detectable at every impact energy when 10 mm gage length was used. This allowed for accurate detection of even smallest changes in the strains. When the impact was located over the embedded fiber, it caused a very local and high strain peak which was easy to locate. Strain data for impacts on region 3 and 5

showed quite notable noise as can be seen in Figure 6.55. This might be caused by vibration of the structure during measurement or by previous impact damages. A distinct indicator of the impact damages was still however observable. Also, when the impact was located immediately over the optical fiber, a very high and local strains were experienced in the impact location which caused difficulties for the correlation algorithm of the monitoring system. This caused notable jumps in the strain values as was seen in the sandwich panel test in section 6.6.

Figure 6.56 shows an example of the progression in residual strain after each impact event. With the used distance of 40 mm between the impact locations, each impact can be distinctly detected from the residual strain data. After all impact events, the maximum residual strains of the earlier impact damages were reduced by 10 to 20  $\mu\epsilon$ , which can be assumed to be caused by the relaxation in the core. The system therefore seems to be capable to detect multiple damages in the structure.

The residual damage on the face sheet in the taper region was hardly visible. Figure 6.57 depicts the damage in the face sheet after 11 J impact in group 5. This was the most visible damage remaining in the face sheet in the taper region. The size of the dent is

small, about 5 mm in diameter, compared to the size of the damage in the core which was estimated from the residual strains to be around 10 cm. The monitoring system can therefore accurately detect the location and size of the damage in the taper region where the face sheet is thick and the thickness of the core be very small.

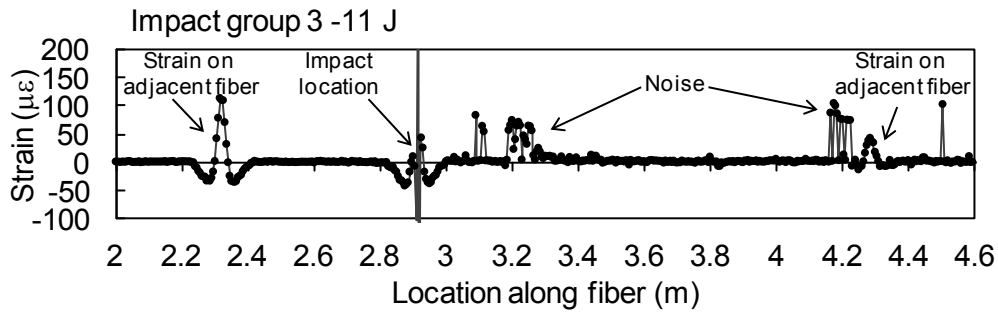


Figure 6.55 Noise in residual strain distribution.

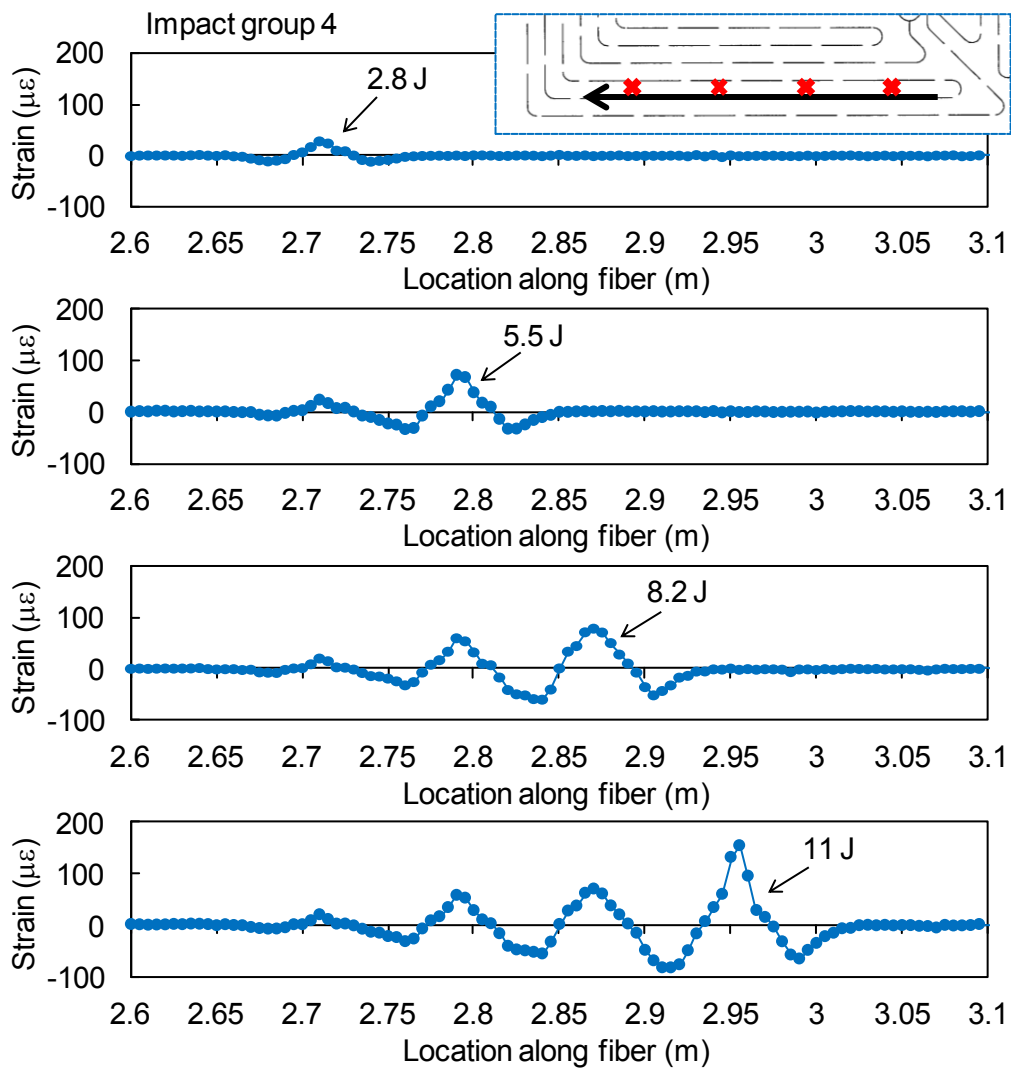


Figure 6.56 Residual strain distribution after consecutive impact events at the taper region.

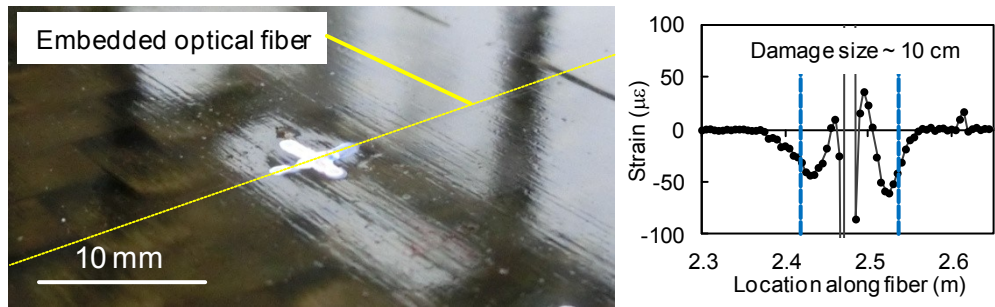


Figure 6.57 Residual damage on the face sheet after 11 J impact in group 5 at the taper region with corresponding residual strain distribution.

#### 6.7.4. Results – Mid region

Contact force-displacement curves for the mid region impact groups are shown in Figure 6.58. Compared to the taper region, the maximum displacements are larger due to the thinner face sheet having less bending stiffness. Therefore crushing of the core starts to initiate earlier and a clear change in the slope can be observed in the beginning of the loading curves. However, the lowest energy impact seem to leave no residual deformation in the face sheets. At 8.2 J impact energy damage initiated in the face sheet and thus higher energy levels were not tested. The face sheet damage can be seen as notable load drop in the contact force curves.

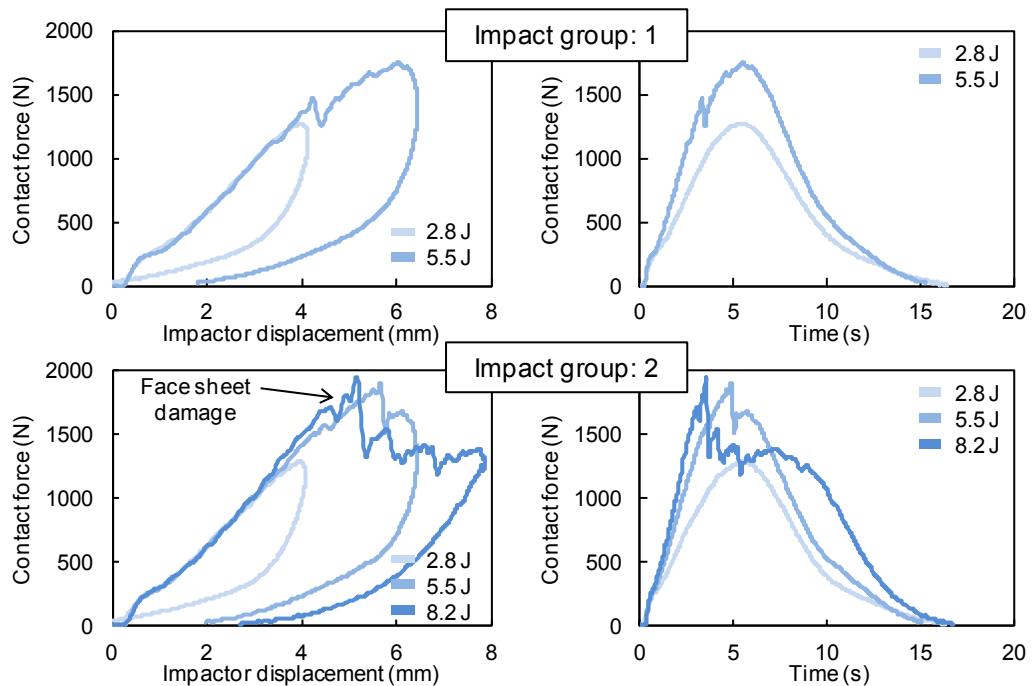


Figure 6.58 Contact force response at mid region.

An example of the measured residual strain distributions is shown in Figure 6.59. Again, highest strain are observed in the fibers at both sides of the impact location allowing for easy detection of the damage location. For the 5.5 J and 8.2 J impacts, the residual strains were observed even in fibers up to 70 mm away from the impact location. Due to the thin face sheet and thick core in the mid region of the panel, notable residual deformations remained even for the smallest impact energies making the damage easy to detect. Figure 6.60 shows the measured residual strains after each consecutive impact. Again, multiple impact events can be detected even though the maximum strains of the previous impacts can drop by 100 to 200  $\mu\epsilon$ .

8.2 J impact caused significant increase in the residual strains as seen in Figure 6.60 and also resulted in notable damage in the face sheet. Figure 6.61 shows the face sheet of impact group 2 after the tests where notable damage can be seen at the 8.2 J impact location while lower impact energies left no clearly visible dent in the face sheet.

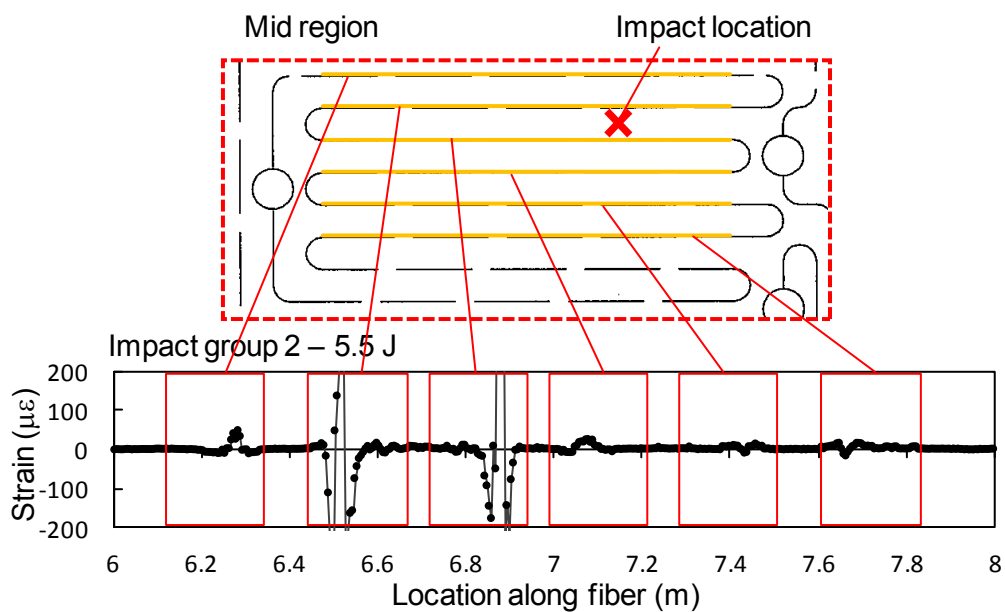


Figure 6.59 Example of residual strain data after 5.5 J impact event at the mid region.

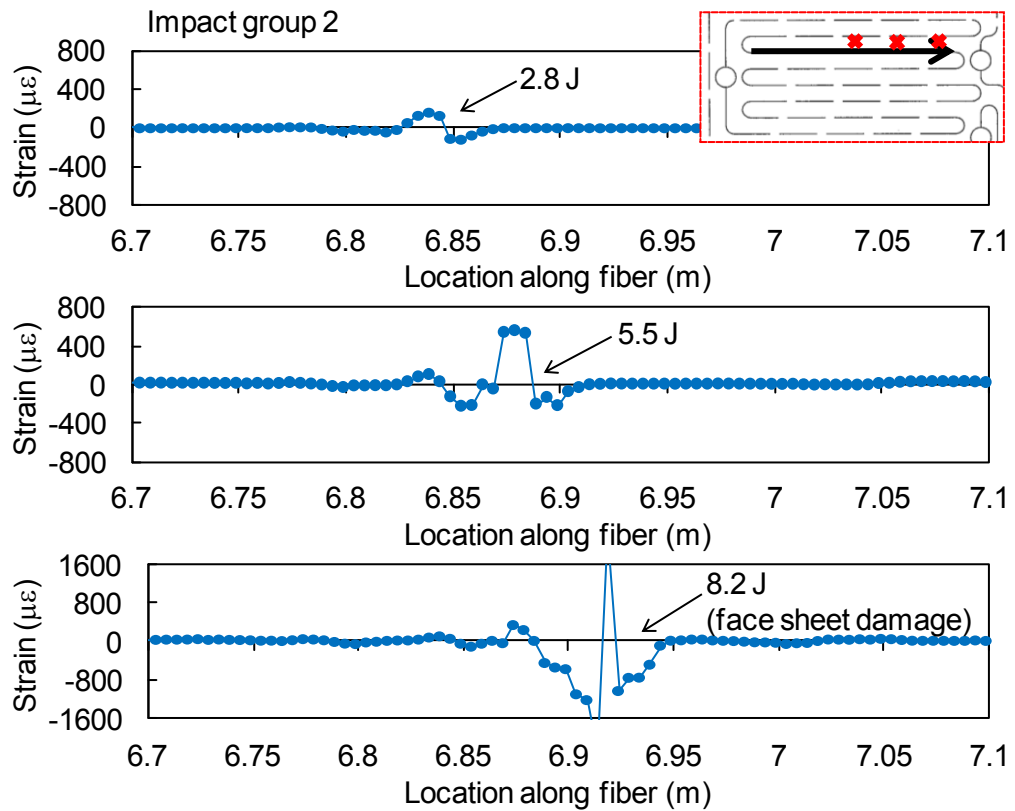


Figure 6.60 Residual strain distribution after consecutive impact events at the mid region.

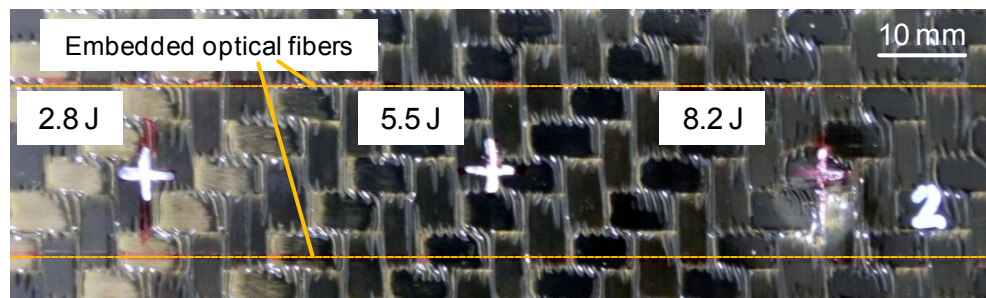


Figure 6.61. Residual damage on the face sheet at mid region impact group 2.

## 6.8. Conclusion

A distributed fiber optic strain monitoring system based on Rayleigh backscattering was applied into foam core sandwich structures. The strain measurement during indentation loading was studied using sandwich beam specimens with optical fiber embedded in the adhesive layer. The system could measure the strain distribution continuously during the indentation loading cycle with very high resolution. Damage in the sandwich beam could be detected from the residual strain distribution as soon as even slightest residual dent remained after unloading. Changes in the strain distribution after unloading were also measured to verify the effect of stress relaxation in the core.

Tests were conducted at various temperature and humidity conditions to observe the effect of environmental conditions on the strain distribution. High temperature and humidity degraded the properties of the core which lead to notable deformations in the core. This was seen as the strains spreading on larger area and also as notably larger residual strains when comparing cases with same maximum indentation loading. The measured strains also corresponded quite well with numerical analysis results and helped in evaluation of the material models used in the analysis.

Indentation test was also conducted with sandwich panel. Due to the added dimension, the deformation was highly local compared to the sandwich beams. The damage, however, was detectable almost immediately after initiating and the location and size of the damage could be estimated quite accurately from the residual strain data. Also, needed spacing and configuration of the fibers in the monitoring network were discussed.

Finally low velocity impact tests were conducted using a large scale sandwich panel similar to real life applications. The center and taper regions of the panel were impacted with various low energy impacts. When the impact location was immediately over the embedded fiber, the very high and local strains caused notable scatter in the measured strains. Nonetheless, this did not affect the monitoring system's ability to detect the impact damages. The system could therefore accurately detect low velocity impact damage in the mid and taper regions of the sandwich panel.

## Chapter 7. Conclusion

This study focused on the indentation response and damage monitoring of foam core sandwich structures. Especially the effect of environmental conditions was considered. Indentation response of sandwich structures at various temperature and humidity conditions was studied experimentally and by finite element analysis. Also the compressive and tensile behavior of the foam core material was studied as the indentation response depends on the loading response of the core material. A fiber optic distributed strain monitoring system was applied to monitor the sandwich structures and to detect the barely visible indentation and low velocity impact induced damage.

In Chapter 2 the loading response of the PMI foam core material was studied experimentally by conducting compression-tension loading cycle tests at various temperature and humidity conditions. Effect of the environmental conditions on the foams properties was then observed. The high temperature and humidity conditions degraded the properties of the foam as its polymer material was softened and plasticized by the temperature and diffused moisture. Conditioning at humid environment for even a short period caused notable reduction in the foams compressive properties. The combined effect of temperature and humidity was notably larger than the effect of only temperature or humidity. The response of the foam also changed from brittle to ductile as the moisture content of the foam increased.

Chapter 3 studied the indentation response of sandwich structures. Indentation loading tests were conducted with beam specimens at various temperature and humidity conditions. The indentation strength and stiffness of the sandwich specimens was notably degraded by high temperature and humidity conditions and was closely related to the foams loading behavior at the same conditions. Also the size of the residual dent increased with increasing temperature and especially with increasing humidity.

In Chapter 4, a finite element analysis of the indentation loaded sandwich beams was conducted. The crushable foam material model in the ABAQUS software was used for the core of the sandwich beams. Material properties and loading behavior of the core were adjusted based on the experimental results in Chapter 1. The indentation loading behavior was predicted well with the used material data. Response at high humidity and temperature conditions however differed from the experiments due to different moisture content of foam core in the sandwich beams and the foam specimens used in Chapter 1. The size of damage in the core was also related with the residual strains for damage

detection purposes. However, prediction of the unloading behavior and residual state was less accurate due to the simplified tensile behavior of the crushable foam model.

Chapter 5 suggested an improved material model for the core material to be used in the finite element analysis. The new model was based on the crushable foam in ABAQUS. Degradation of elastic modulus during compression and tensile response of the foam were implemented based on experimental data. The predicted unloading behavior of indentation loaded sandwich beams was notably improved by the new model compared to the crushable foam model. The new model was also able to provide more accurate prediction of the residual state as was later shown in Chapter 6.

Chapter 6 presented a fiber optic distributed strain monitoring system for damage monitoring in foam core sandwich structures. A Rayleigh scattering based system was used to monitor strain distribution along optical fibers embedded in the adhesive layer of sandwich structures. The system provided high resolution strain data during indentation loading. Damage detection ability of the system was studied by conducting experiments using sandwich beam and panel specimens. Sandwich beam specimens were indentation loaded at various temperature and humidity conditions and the strain distribution in the adhesive layer was monitored. The effect of environmental conditions on the indentation response was also seen in the measured strains. Comparison with analysis results showed good correlation, especially with the improved model. Indentation damage detection ability was also verified on sandwich panel specimen. Finally, a sandwich panel demonstrator closer to real life applications was used to show the system's ability to detect low velocity impact damage. Damage was detected and the location and size of the damages could be estimated even when no damage was visible in the face sheets.

This thesis has therefore shown the indentation response of foam core sandwich structures at various temperature and humidity conditions experimentally and by finite element analysis. Also the residual state after indentation could be predicted with good accuracy using an improved material model for the foam core. Also, a fiber optic distributed monitoring system was presented for accurate indentation and low-velocity impact damage detection and its operation was verified experimentally. Based on the analysis results, the size of the damage can also be accurately estimated from the monitoring data.

### **7.1. Future works**

Some future topics for future works based on the results of this research are suggested as follows:

- A way to accurately determine the moisture content of the foam should be developed, as it has notable effect on the foams loading response but keeps changing constantly

with the surrounding conditions. The moisture content could then be related with the mechanical properties of the foam.

- Effect of humidity and low temperatures on the response of the foam material. Freezing of moisture in the foam might damage the polymer material and thus lead to unpredictable response under compressive or tensile loading.
- Inclusion of viscoelastic effects in the finite element analysis to improve the indentation loading prediction, but also to predict the residual state after relaxation in the core has occurred.
- Monitoring during manufacturing of sandwich panels to possibly detect voids or insufficient bonding of core and face sheet. Also accurate measurement of thermal strains and their utilization in indentation analysis can provide improved prediction on the strength of the structures.

## References

- [1] D. Zenkert (Ed.), *The Handbook of Sandwich Construction*, EMAS Publishing, 1997.
- [2] Y. Hirose, K. Kosugi, M. Nishitani, H. Sashikuma, M. Imuta, H. Fukugawa and H. Kikukawa, "The CFRP Sandwich Panel for Aircraft Nose Structure," *Proceedings of 23rd Congress of the International Council of the Aeronautical Sciences*, 2002.
- [3] L. Herbeck, H. Wilmes, B. Kolesnikov and M. Kleineberg, "Technology and Design Development for a CFRP Fuselage," *Proceedings of SAMPE Europe 2003*, 2003.
- [4] M. Zuardy and A. Herrmann, "An Advanced Centre Box of a Vertical Tail Plane With a Side Panel from CFRP Foam-Core Sandwich Structure," *CEAS Aeronautical Journal*, vol. 2, pp. 253-269, 2011.
- [5] L. Maia and P. de Oliveira, "Crashworthy Composite Fuselage Section Concept for Next Generation General Aviation," *SAE Technical Paper 2005-01-4011*, 2005.
- [6] M. Akay and R. Hanna, "A Comparison of Honeycomb-Core and Foam-Core Carbon-Fibre/Epoxy Sandwich Panels," *Composites*, vol. 21, no. 4, pp. 325-331, 1990.
- [7] J. Tomblin, K. Raju, J. Liew and B. Smith, "Impact Damage Characterization and Damage Tolerance of Composite Sandwich Airframe Structures. Final Report," *DOT/FAA/AR-00/49*, 2001.
- [8] J. Tomblin, K. Raju, J. Acosta, B. Smith and N. Romine, "Impact Damage Characterization and Damage Tolerance of Composite Sandwich Airframe Structures - Phase II. Final Report," *DOT/FAA/AR-02/80*, 2002.
- [9] J. Lejten, H. Bersee, O. Bergsma and A. Beukers, "Experimental Study of the Low-velocity Impact Behaviour of Primary Sandwich Structures in Aircraft," *Composites: Part A*, vol. 40, pp. 164-175, 2009.
- [10] F. Edgren and L. B. P. Asp, "Compressive Failure of Impacted NCF Composite Sandwich Panels - Characterisation of the Failure Process," *Journal of Composite Materials*, vol. 38, no. 6, pp. 495-514, 2004.
- [11] T. Anderson and E. Madenci, "Experimental Investigation of Low-Velocity Impact Characteristics of Sandwich Composites," *Composite Structures*, vol. 50, no. 3, pp. 239-247, 2000.
- [12] L. J. Gibson, M. F. Ashby, *Cellular Solids: Structure & Properties - Second Edition*, Cambridge, UK: Cambridge University Press, 1999.
- [13] Q. Li, R. Mines and R. Birch, "The Crush Behavior of Rohacell-51 WF Structural Foam," *International Journal of Solids and Structures*, vol. 37, pp. 6321-6341, 2000.
- [14] Q. Li and R. Mines, "Strain Measured for Rigid Crushable Foam in Uniaxial Compression," *Strain*, vol. 38, pp. 132-140, 2002.
- [15] D. Zenkert and M. Burman, "Tension, Compression and Shear Fatigue of a Closed Cell Polymer Foam," *Composites Science and Technology*, vol. 69, pp. 785-792, 2009.
- [16] D. Zenkert, A. Shipsha and M. Burman, "Fatigue of Closed Cell Foams," *Journal of Sandwich Structures and Materials*, vol. 8, pp. 517-538, 2006.
- [17] S. Arezoo, V. Tagarielli, N. Petrinic and J. Reed, "The Mechanical Response of Rohacell Foams at Different Length Scales," *Journal of Materials Science*, vol. 46, pp. 6863-6870, 2011.
- [18] V. Koissin and A. Shipsha, "Residual In-plane Mechanical Properties of Transversely

- 
- Crushed Structural Foams," *Journal of Sandwich Structures and Materials*, vol. 11, no. 2-3, pp. 199-211, 2009.
- [19] V. Koissin and A. Shipsha, "Deformation of Foam Cores in Uniaxial Compression-Tension Cycle," *Journal of Sandwich Structures and Materials*, vol. 8, pp. 395-406, 2006.
- [20] I. Grace, V. Pilipchuk, R. Ibrahim and E. Ayorinde, "Temperature Effect on Non-Stationary Compressive Loading Response of Polymethacrylimide Solid Foam," *Composite Structures*, vol. 94, pp. 3052-3063, 2012.
- [21] S. Zhang, J. Dulieu-Barton, R. Fruehmann and O. Thomsen, "A Methodology for Obtaining Material Properties of Polymer Foam at Elevated Temperatures," *Experimental Mechanics*, vol. 52, pp. 3-15, 2012.
- [22] S. Arezoo, V. Tagarielli, C. Siviour and N. Petrinic, "Compressive Deformation of Rohacell Foams: Effects of Strain Rate and Temperature," *International Journal of Impact Engineering*, vol. 51, pp. 50-57, 2013.
- [23] H. Katzman, R. Castaneda and H. Lee, "Moisture Diffusion in Composite Sandwich Structures," *Composites: Part A*, vol. 39, pp. 887-892, 2008.
- [24] A. Ionita and Y. Qeitsman, "A Model for Fluid Ingress in Closed Cell Polymeric Foams," *Mechanics of Materials*, vol. 39, pp. 434-444, 2007.
- [25] J. S. Earl and R. A. Shenoi, "Determination of the Moisture Uptake Mechanism in Closed Cell Polymeric Structural Foam During Hygrothermal Exposure," *Journal of Composite Materials*, vol. 38, no. 15, pp. 1345-1366, 2004.
- [26] F. Aviles and M. Aguilar-Montero, "Moisture Absorption in Foam-Cored Composite Sandwich Structures," *Polymer Composites*, vol. 31, no. 4, pp. 714-722, 2012.
- [27] M. John, R. Schlimper, M. Rinker, T. Wagner, A. Roth and R. Schäube, "Long-Term Durability of CFRP Foam Core Sandwich Structures," *CEAS Aeronautical Journal*, vol. 2, pp. 213-221, 2011.
- [28] O. Ishiai, C. Hiel and M. Luft, "Long-Term Hygrothermal Effects on Damage Tolerance of Hybrid Composite Sandwich Panels," *Composites*, vol. 26, no. 1, pp. 47-55, 1995.
- [29] D. Granville, "Moisture Effects of Polymethacrylimide Foam and Honeycomb Core in Sandwich/Skin Structures," *Proceedings of 43rd Annual Forum of American Helicopter Society*, vol. 2, pp. 907-914, 1987.
- [30] Y.-J. Yu, K. Hearon, T. Wilson and D. Mailand, "The Effect of Moisture Absorption on the Physical Properties of Polyurethane Shape Memory Polymer Foams," *Smart Materials and Structures*, vol. 20, pp. 1-6, 2011.
- [31] F. Aviles and M. Aguilar-Montero, "Mechanical Degradation of Foam-Cored Sandwich Materials Exposed to High Moisture," *Composite Structures*, vol. 92, pp. 122-129, 2010.
- [32] "Rohacell WF Product Information," Evonik Rohm GmbH., [Online]. Available: [www.rohacell.com/product/rohacell/en/products-services/rohacell-wf/](http://www.rohacell.com/product/rohacell/en/products-services/rohacell-wf/).
- [33] J. Crank, *The Mathematics of Diffusion - 2nd Ed.*, New York: Oxford University Press Inc., 1975.
- [34] Q. Li, I. Magkiriadis and J. Harrigan, "Compressive Strain at the Onset of the Densification of Cellular Solids," *Journal of Cellular Plastics*, vol. 42, no. 5, pp. 371-392, 2006.
- [35] A. Hanssen, O. Hopperstad, M. Langseth and H. Ilstad, "Validation of Constitutive Model Applicable to Aluminium Foams," *International Journal of Mechanical Sciences*, vol. 44, pp. 359-406, 2002.
- [36] D. Zenkert, A. Shipsha and K. Persson, "Static Indentation and Unloading Response
-

- of Sandwich Beams," *Composites: Part B*, vol. 35, pp. 511-522, 2004.
- [37] V. Koissin and A. Shipsha, "Residual Dent in Locally Loaded Foam Core Sandwich Structures - Analysis and Use for NDI," *Composites Science and Technology*, vol. 68, pp. 57-74, 2008.
- [38] S. Minakuchi, T. Uezono and N. Takeda, "Formation and Relaxation of Residual Dent on Foam-Core Sandwich Structures by Localized Transverse Loading," *Journal of Sandwich Structures and Materials*, vol. 15, no. 1, pp. 71-91, 2012.
- [39] D. Zenkert, Shipsha, B. P. A and B. Hayman, "Damage Tolerance Assessment of Composite Sandwich Panels With Localised Damage," *Composites Science and Technology*, vol. 65, no. 15-16, pp. 2597-2611, 2005.
- [40] A. Nettless and M. Douglis, "A Comparison of Quasi-Static Indentation to Low-Velocity Impact," *NASA Technical Report*, 2000.
- [41] P. Schubel, J.-J. Luo and I. Daniel, "Low Velocity Impact Behavior of Composite Sandwich Panels," *Composites: Part A*, vol. 36, pp. 1389-1396, 2005.
- [42] S. Abrate, "Localized Impact on Sandwich Structures with Laminated Facings," *Applied Mechanics Reviews*, vol. 50, no. 2, pp. 69-82, 1997.
- [43] F. Shuaieb and P. Soden, "Indentation Failure of Composite Sandwich Beams," *Composites Science and Technology*, vol. 57, pp. 1249-1259, 1997.
- [44] A. Petras and M. Sutcliffe, "Indentation Resistance of Sandwich Beams," *Composite Structures*, vol. 46, pp. 413-424, 1999.
- [45] R. Mines, C. Worrall and A. Gibson, "The Static and Impact Behaviour of Polymer Composite Sandwich Beams," *Composites*, vol. 25, no. 2, pp. 95-110, 1994.
- [46] E. Gdoutos, I. Daniel and K. Wang, "Indentation Failure in Composite Sandwich Structures," *Experimental Mechanics*, vol. 42, no. 4, pp. 426-431, 2002.
- [47] P. Soden, "Indentation of Composite Sandwich Beams," *Journal of Strain Analysis and Engineering Design*, vol. 31, no. 6, pp. 353-360, 1996.
- [48] O. Thomsen, "Analysis of Local Bending Effects in Sandwich Plates with Orthotropic Face Layers Subjected to Localised Loads," *Composite Structures*, vol. 25, pp. 511-520, 1993.
- [49] E. Flores-Johnson and Q. Li, "Experimental Study of the Indentation of Sandwich Panels with Carbon Fibre-Reinforced Polymer Face Sheets and Polymeric Foam Core," *Composites: Part B*, vol. 42, pp. 1212-1219, 2011.
- [50] V. Rizov, A. Shipsha and D. Zenkert, "Indentation Study of Foam Core Sandwich Composite Panels," *Composite Structures*, vol. 69, pp. 95-102, 2005.
- [51] S. Minakuchi, Y. Okabe and N. Takeda, "'Segment-Wise Model' for Theoretical Simulation of Barely Visible Indentation Damage in Composite Sandwich Beams: Part II - Experimental Verification and Discussion," *Composites: Part A*, vol. 38, pp. 2443-2450, 2007.
- [52] V. Pilipchuk, R. Ibrahim and I. Grace, "Low Temperature Brittle Debond Damage Under Normal Compression of Sandwich Plates: Analytical Modeling and Experimental Validation," *Composite Structures*, vol. 98, pp. 24-33, 2013.
- [53] A. Singh and B. Davidson, "Effects of Temperature, Seawater and Impact on the Strength, Stiffness, and Life of Sandwich Composites," *Journal of Reinforced Plastics and Composites*, vol. 30, pp. 269-277, 2011.
- [54] D. Veazie and K. S. K. Robinson, "Effects of the Marine Environment on the Interfacial Fracture Toughness of PVC Core Sandwich Composites," *Composites: Part B*, vol. 35, pp. 461-466, 2004.
- [55] N. Joshi and A. Muliana, "Deformation in Viscoelastic Sandwich Composites Subject to Moisture Diffusion," *Composite Structures*, vol. 92, pp. 254-264, 2010.

- 
- [56] R. Scudamore and W. Cantwell, "The Effect of Moisture and Loading Rate on the Interfacial Fracture Properties of Sandwich Structures," *Polymer Composites*, vol. 23, pp. 406-417, 2002.
- [57] AF163-2 Data Sheet, 3M Co..
- [58] J. Mackerle, "Finite Element Analyses of Sandwich Structures: A Bibliography (1980-2001)," *Engineering Computations*, vol. 19, no. 2, pp. 206-245, 2002.
- [59] N. Mills, R. Stampfli, F. Marone and P. Bruhwiler, "Finite Element Micromechanics Model of Impact Compression of Closed-Cell Polymer Foams," *International Journal of Solids and Structures*, vol. 46, pp. 677-697, 2009.
- [60] S. Nammi, P. Myler and G. Edwards, "Finite Element Analysis of Closed-Cell Aluminium Foam Under Quasi-Static Loading," *Materials and Design*, vol. 31, pp. 712-722, 2010.
- [61] J. Wang, H. Wang, X. Chen and Y. Yu, "Experimental and Numerical Study of the Elastic Properties of PMI Foams," *Journal of Materials Science*, vol. 45, pp. 2688-2695, 2010.
- [62] N. Mills, "Deformation Mechanisms and the Yield Surface of Low-Density, Closed-Cell Polymer Foams," *Journal of Materials Science*, vol. 45, pp. 5831-5843, 2010.
- [63] Y. Song, Z. Wang, L. Zhao and J. Luo, "Dynamic Crushing Behavior of 3D Closed-Cell Foams Based on Voronoi Random Model," *Materials and Design*, vol. 31, pp. 4281-4289, 2010.
- [64] C. Tekoglu and P. Onck, "Size Effects in the Mechanical Behavior of Cellular Materials," *Journal of Materials Science*, vol. 40, pp. 5911-5917, 2005.
- [65] C. Tekoglu, L. Gibson, T. Pardoen and P. Onck, "Size Effects in Foams: Experiments and Modeling," *Progress in Materials Science*, vol. 56, pp. 109-138, 2011.
- [66] M. Alkhalder and M. Vural, "A Plasticity Model for Pressure-Dependent Anisotropic Cellular Solids," *International Journal of Plasticity*, vol. 26, pp. 1591-1605, 2010.
- [67] I. Jeon, T. Asahina, K.-J. Kang, S. Im and T. Lu, "Finite Element Simulation of the Plastic Collapse of Closed-Cell Aluminum Foams with X-Ray Computed Tomography," *Mechanics of Materials*, vol. 42, pp. 227-236, 2010.
- [68] N. Daphalapurkar, J. Hanan, N. Phelps, H. Bale and H. Lu, "Tomography and Simulation of Microstructure Evolution of a Closed-Cell Polymer Foam in Compression," *Mechanics of Advanced Materials and Structures*, vol. 15, pp. 594-611, 2008.
- [69] S. Youssef, E. Maire and R. Gaertner, "Finite Element Modelling of the Actual Structure of Cellular Materials Determined by X-Ray Tomography," *Acta Materialia*, vol. 53, pp. 719-730, 2005.
- [70] V. S. Deshpande and N. A. Fleck, "Isotropic Constitutive Models for Metallic Foams," *Journal of the Mechanics and Physics of Solids*, vol. 48, pp. 1253-1283, 2000.
- [71] G. Machado, M. Alves, R. Rossi and C. Silva Jr., "Numerical Modeling of Large Strain Behavior of Polymeric Crushable Foams," *Applied Mathematical Modelling*, vol. 35, pp. 1271-1281, 2011.
- [72] M. Alkhalder and M. Vural, "An Energy-Based Anisotropic Yield Criterion for Cellular Solids and Validation by Biaxial FE Simulations," *Journal of Mechanics and Physics of Solids*, vol. 57, pp. 871-890, 2009.
- [73] M. Nielsen, R. Krieg and H. Schreyer, "A Constitutive Theory for Rigid Polyurethane Foam," *Polymer Engineering and Science*, vol. 35, no. 5, pp. 387-394, 1995.
- [74] R. Mohamed, F. Zhang, B. Sun and B. Gu, "Finite Element Analyses of Low-Velocity Impact Damage of Foam Sandwiched Composites with Different Ply Angles Face
-

- Sheets," *Materials and Design*, vol. 47, pp. 189-199, 2013.
- [75] R. Mines and A. Alias, "Numerical Simulation of the Progressive Collapse of Polymer Composite Sandwich Beams Under Static Loading," *Composites: Part A*, vol. 33, pp. 11-26, 2002.
- [76] V. Rizov, "Non-Linear Indentation Behavior of Foam Core Sandwich Composite Materials - A 2D Approach," *Computational Materials Science*, vol. 35, pp. 107-115, 2006.
- [77] V. Rizov, "Indentation of Foam-Based Polymer Composite Sandwich Beams and Panels Under Static Loading," *Journal of Materials Engineering and Performance*, vol. 18, pp. 351-360, 2009.
- [78] ABAQUS 6.11 Users Manual, Dassault Systemes Inc..
- [79] *Torayca Technical Reference*, Toray Industries.
- [80] E. Flores-Johnson, Q. Li and R. Mines, "Degradation of Elastic Modulus of Progressively-Crushable Foams in Uniaxial Compression," *Journal of Cellular Plastics*, vol. 44, no. 5, pp. 415-434, 2008.
- [81] N. Takeda, S. Minakuchi and Y. Okabe, "Smart Composite Sandwich Structures for Future Aerospace Application -Damage Detection and Suppression-: a Review," *Journal of Solid Mechanics and Materials Engineering*, vol. 1, no. 1, pp. 3-17, 2007.
- [82] E. Bocherens, S. Bourasseau, V. Dewynter-Marty, S. Py, M. Dupont, P. Ferdinand and H. Berenger, "Damage Detection in a Radome Sandwich Material with Embedded Fiber Optic Sensors," *Smart Materials and Structures*, vol. 9, pp. 310-315, 2000.
- [83] S. Minakuchi, Y. Okabe, T. Mizutani and N. Takeda, "Barely Visible Impact Damage Detection for Composite Sandwich Structures by Optical-Fiber-Based Distributed Strain Measurement," *Smart Materials and Structures*, vol. 18, pp. 1-9, 2009.
- [84] J. Siivola, S. Minakuchi and N. Takeda, "Application of Fiber-Optic Distributed Sensing System to CFRP-Foam Core Sandwich Panel and Its Detection Ability of Local Indentation Damage," *Proceedings of ASC 27th Technical Conference*, pp. 228-243, 2012.
- [85] B. Soller, D. Gifford, M. Wolfe and M. Froggatt, "High Resolution Optical Frequency Domain Reflectometry for Characterization of Components and Assemblies," *Optics Express*, vol. 13, no. 2, pp. 666-674, 2005.
- [86] R. Duncan, B. Soller, D. Gifford, S. Kreger, R. Seeley, A. Sang, M. Wolfe and M. Froggatt, "OFDR-Based Distributed Sensing and Fault Detection for Single- and Multi-Mode Avionics Fiber-Optics," *Proceedings of 10th Joint DOD/NASA/FAA Conference on Aging Aircraft*, pp. 10-14, 2007.
- [87] B. Soller, D. Gifford, M. Wolfe, M. Froggatt, M. Yu and P. Wysocki, "Measurement of Localized Heating in Fiber Optic Component with Millimeter Spatial Resolution," *Proceedings of Optical Fiber Communication Conference*, 2006.
- [88] LUNA Optical Backscatter Reflectometer Model 4600, User Guide 5, Blacksburg VA: Luna Technologies, 2012.
- [89] M. Nishio, "分布ひずみデータの形状特性評価に基づくモデル状態変化にロバストな CFRP 構造の変位同定法に関する研究," 2008.
- [90] J. Siivola, T. Uezono, S. Minakuchi and N. Takeda, "Damage Monitoring of Indentation Loaded Foam-Core Sandwich Beam Using Fiber-Optic Distributed Sensing," *Proceedings of JISSE-12*, 2011.
- [91] M. R. Vanlandingham, R. F. Eduljee and J. W. Gillespie Jr., "Moisture Diffusion in Epoxy Systems," *Journal of Applied Polymer Science*, vol. 71, pp. 787-798, 1999.

## Appendix A. Empirical model for foam parameters

Based on the foam loading tests experimental results, an expression can be proposed to estimate the foams properties related to the combined temperature and humidity conditions. The parameters can be plotted against the moisture content of the foam by using the moisture contents estimated for the foam specimens at the tested humidity conditions in section 2.3. The elastic modulus, for example, seems to degrade nearly linearly with increasing moisture content as shown in Figure A.1. The actual moisture content might however differ notably from the estimated values, so more profound study on the subject is needed.

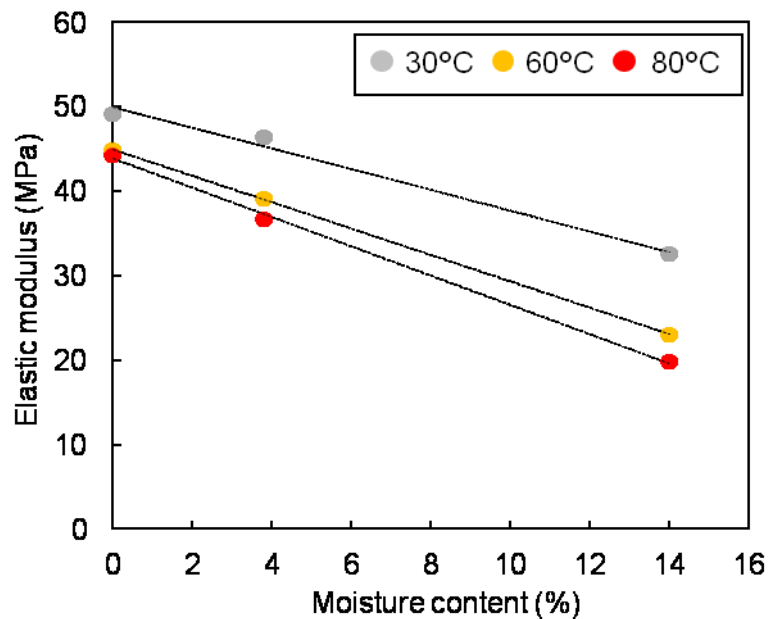


Figure A.1 Elastic modulus plotted against moisture content of the foam specimens.

## Appendix A. Empirical model for foam parameters

---

According to Gibson and Ashby [12] the Young's modulus  $E$  and compressive yield stress  $\sigma_y$  of closed cell foam can be estimated by equations

$$\frac{\sigma_y}{E_s} = 0.05 \left( \frac{\rho^*}{\rho_s} \right)^2 + \frac{p_0 - p_{el}}{E_s} \quad (A.1)$$

$$\frac{E}{E_s} = C_1 \phi^2 \left( \frac{\rho^*}{\rho_s} \right)^2 \quad (A.2)$$

where  $E_s$  is the elastic modulus of the foams parent polymer material,  $\rho^*$  is the foams density,  $\rho_s$  is the parent materials density,  $p_0$  is outside air pressure,  $p_{el}$  is the air pressure inside the cells,  $C_1$  is material parameters and  $\phi$  is the fraction of solid contained in the cell edges. The latter part in Equation A.1 can be ignored as the pressure inside the cells is close to normal air pressure when the cells start to collapse. Therefore the Young's modulus and yield stress of the foam are linearly related to the elastic modulus of the polymer material of the foam. For the Young's modulus of the polymer material at different temperatures, Gibson and Ashby [12] also provide equation

$$E_s(T) = E_{s0} \left( 1 - \alpha_m \frac{T}{T_g} \right) \quad (A.3)$$

where  $E_{s0}$  is the parent materials elastic modulus at  $0^\circ\text{C}$ ,  $T_g$  is the glass transition temperature of the parent material and  $\alpha_m$  is a material parameter. The stiffness of the polymer thus reduces as the temperature gets closer to the glass transition temperature of the parent polymer material. By substituting Equation A.3 into Equation A.1 and A.2 and grouping all constant values gives

$$\sigma_y = A_{\sigma 0} (1 - B_\sigma \cdot T) \quad (A.4)$$

$$E = A_{E0} (1 - B_E T) \quad (A.5)$$

where  $A_{\sigma 0}$  and  $A_{E0}$  are parameters related to the  $0^\circ\text{C}$  temperature condition and  $B_\sigma$  and  $B_E$  are material parameters. At constant temperatures humidity can be thought to have similar kind of response on the foam as the temperature in Equations A.4 and A.5 due to the polymer being plasticized by diffused moisture. However, humidity also reduces the glass transition temperature of the parent polymer material of the foam [91]. This means that the effect of temperature and humidity cannot be regarded as separate phenomena, but are related to each other. Based on these considerations, a model for the combined effect of temperature and humidity on the foams material properties is now proposed as

$$f(T, M) = f_0 (1 - B_T \cdot T - B_M \cdot M - B_{TM} \cdot T \cdot M) \quad (A.6)$$

where  $f_0$  is the value of the material property at 0 °C temperature and 0 % moisture content,  $B_T$  and  $B_M$  are constants for the effect of temperature and moisture content respectively, and  $B_{TM}$  is constant for the combined effect of temperature and moisture.

Equation A.6 was fitted into experimentally obtained data on the foams Young’s modulus and yield stress by least squares method using the estimated moisture contents of 2.8% and 8% for the ambient and wet conditions respectively. The fitted values obtained for the parameters are as shown in Table A.1. The fitted data for the elastic modulus is depicted in Figure A.2 in the temperature, moisture content space and shows how the modulus decreases with increasing temperature and moisture content. It should be noted that at higher temperatures near the glass transition temperature of the material, the behavior of the foam might change notably and is thus out of the scope of the current model.

Table A.1 Fitted parameter values for foam material properties.

	Young’s modulus E	Yield stress $\sigma_y$
$f_0$	53.40661188	1.152405923
$B_T$	0.002356504	0.003780831
$B_M$	0.017404675	0.023357569
$B_{TM}$	0.000190656	0.000095233

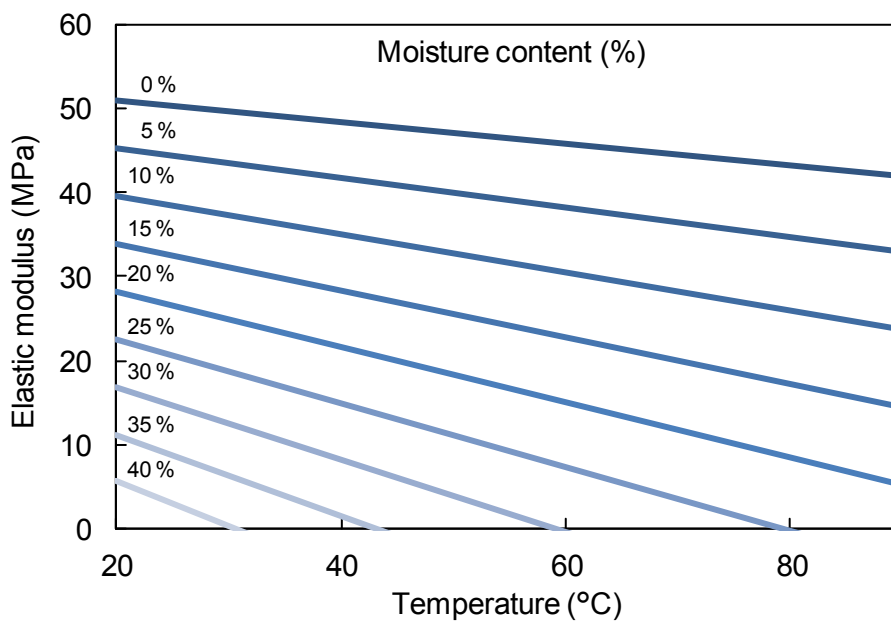


Figure A.2 Elastic modulus as function of temperature and moisture content.

## Appendix B. Humidity and density of the foam

Uniaxial compressive loading tests were conducted also with other densities of the PMI foam to study if the effect of humidity changes with the density of the foam. The tested foam densities are shown in Table B.1. Results for different densities are now compared using the analytical model by Gibson and Ashby [12]. They give an expression for the elastic buckling stress normalized by the elastic modulus of the parent material as

$$\frac{\sigma_{el}}{E_s} = C \left( \frac{\rho^*}{\rho_s} \right)^2 \quad (B.1)$$

where  $E_s$  is the elastic modulus of the parent polymer material,  $\rho^*$  is the density of the foam and  $\rho_s$  is the density of the parent polymer. The coefficient  $C$  depends on the geometry of the foams cell structure and is now obtained by fitting the model with the experimental data from dry conditions and is now approximately 0.085.

Figure B.1 show the correspondence of the experimental and predicted values. For the dry and ambient condition foams the experimental values fit rather well with the model, but for the wet foams the experimental values are higher than the predicted. The difference might be caused by the plasticizing effect of the moisture in the polymer. In the ambient and dry foams the initial yield will mostly happen by elastic buckling of the cell walls as the moisture content is low. In the wet foam, however, the polymer starts to deform plastically before the cell walls should buckle elastically. Also the elastic modulus of the polymer material is reduced with increasing moisture content. The model should therefore include some corrector which would take the effect of moisture into account.

Table B.1 Used foam materials and their densities.

Foam	Density (Measured)	Density (Manufacturer [32])
WF 51	59.9 kg/m <sup>3</sup>	52 kg/m <sup>3</sup>
WF 51(Old batch)	53.5 kg/m <sup>3</sup>	52 kg/m <sup>3</sup>
WF 110	110.9 kg/m <sup>3</sup>	110 kg/m <sup>3</sup>

Adding correction factors for the elastic modulus of the polymer and for the effect of moisture on the elastic buckling into Equation B.1 gives

$$\frac{\sigma_{el}}{C_{\rho M} E_s} = C \left( \frac{\rho^*}{\rho_s} \right)^2 + C_M M \quad (B.2)$$

where  $C_{\rho M}$  defines the effect of moisture on the polymer materials elastic modulus,  $C_M$  defines the effect of moisture on the yield stress and  $M$  is the moisture content of the foam. Assuming that the stiffness of the polymer drops by 10% at the wet conditions defines  $C_{\rho M}$  as 0.9.  $C_M$  can be defined by fitting the model to the experimental results of the wet foam, which then gives a value of  $-6.57 \cdot 10^{-6}$ . The new values are shown in Figure B.2 and fit well with the experiments. Similar procedure should be possible also for the elastic modulus of the foam which has similar expression.

It seems that the behavior of the foam material at various humidity conditions is similar for all densities. This verifies that the humidity mostly affects the parent polymer material of the foams. With the suitable correction factors taking the effect of humidity into account, the response of other foam densities can be evaluated by experimental data done with just one density.

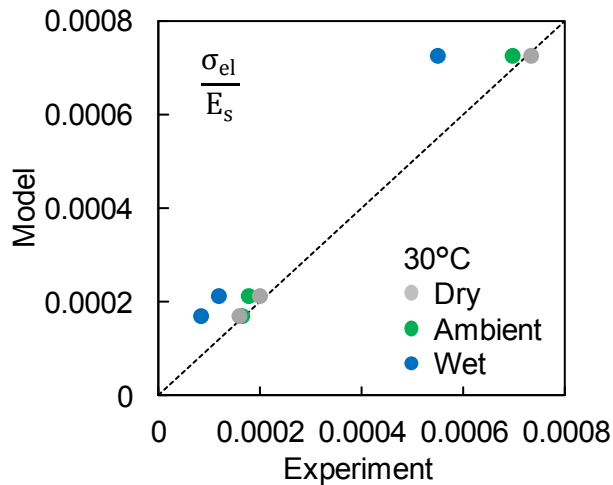


Figure B.1 Comparison of experimental and predicted normalized yield stresses.

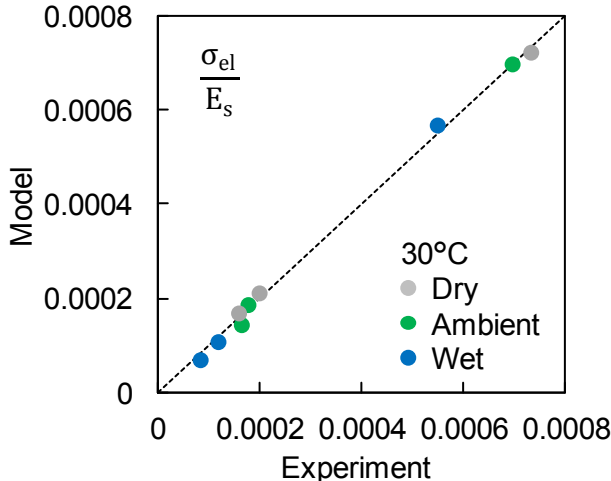


Figure B.2 Comparison with moisture corrected predicted values.

## Appendix C. Impact test strain distribution data

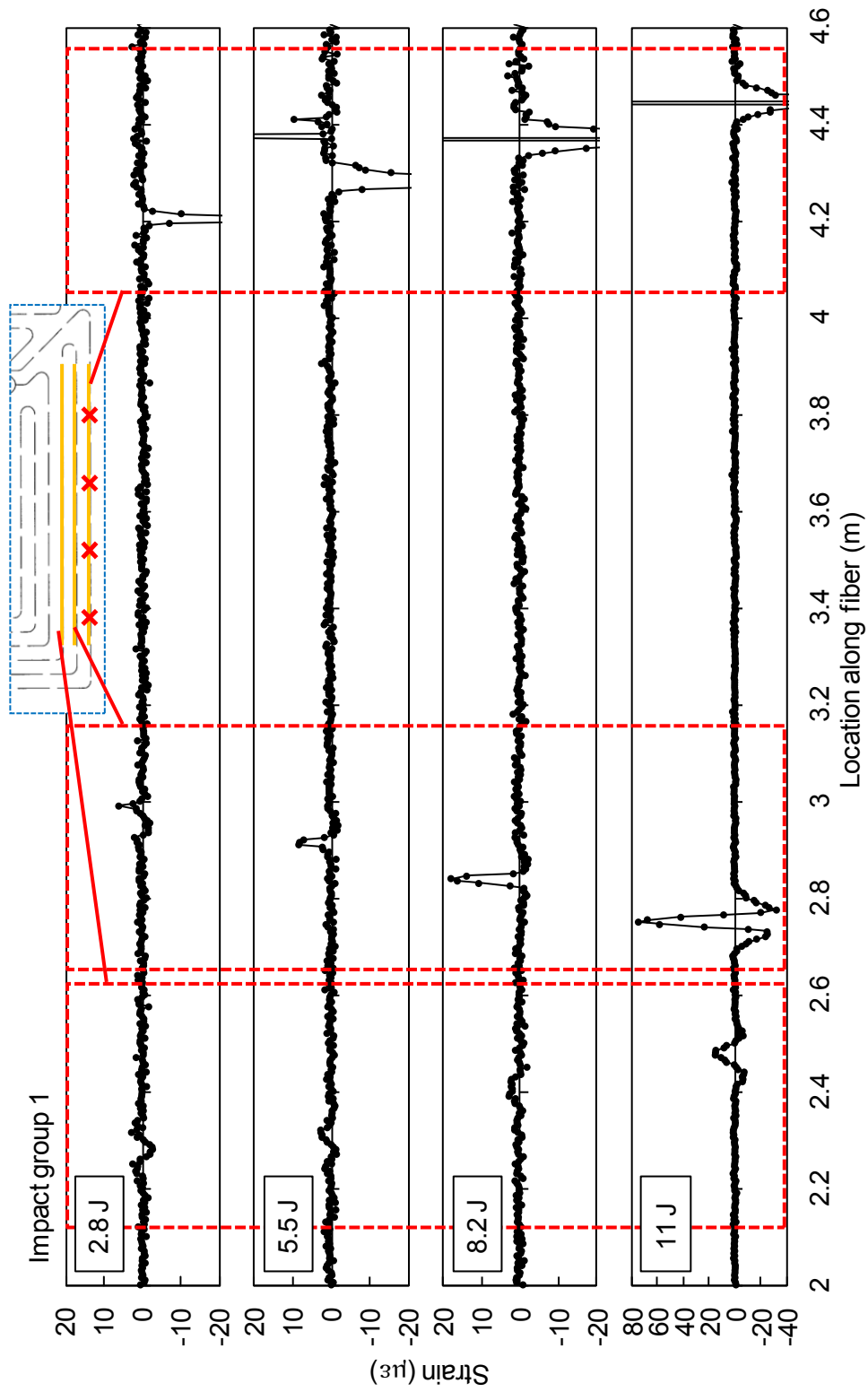


Figure C.1 Residual strain distributions for impact group 1 on the taper region.

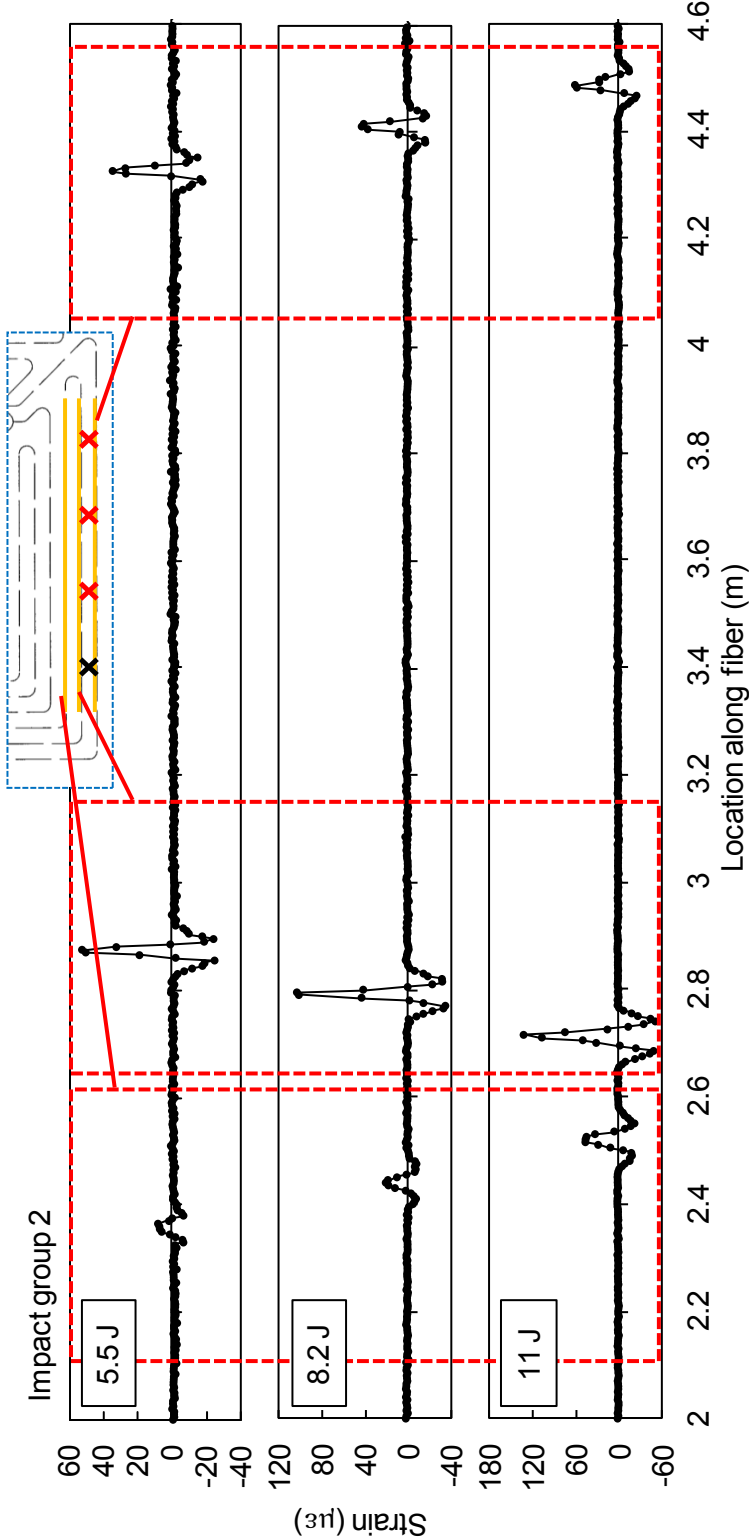


Figure C.2 Residual strain distributions for impact group 2 on the taper region. 2.8 J impact was not recorded due to calibration error.

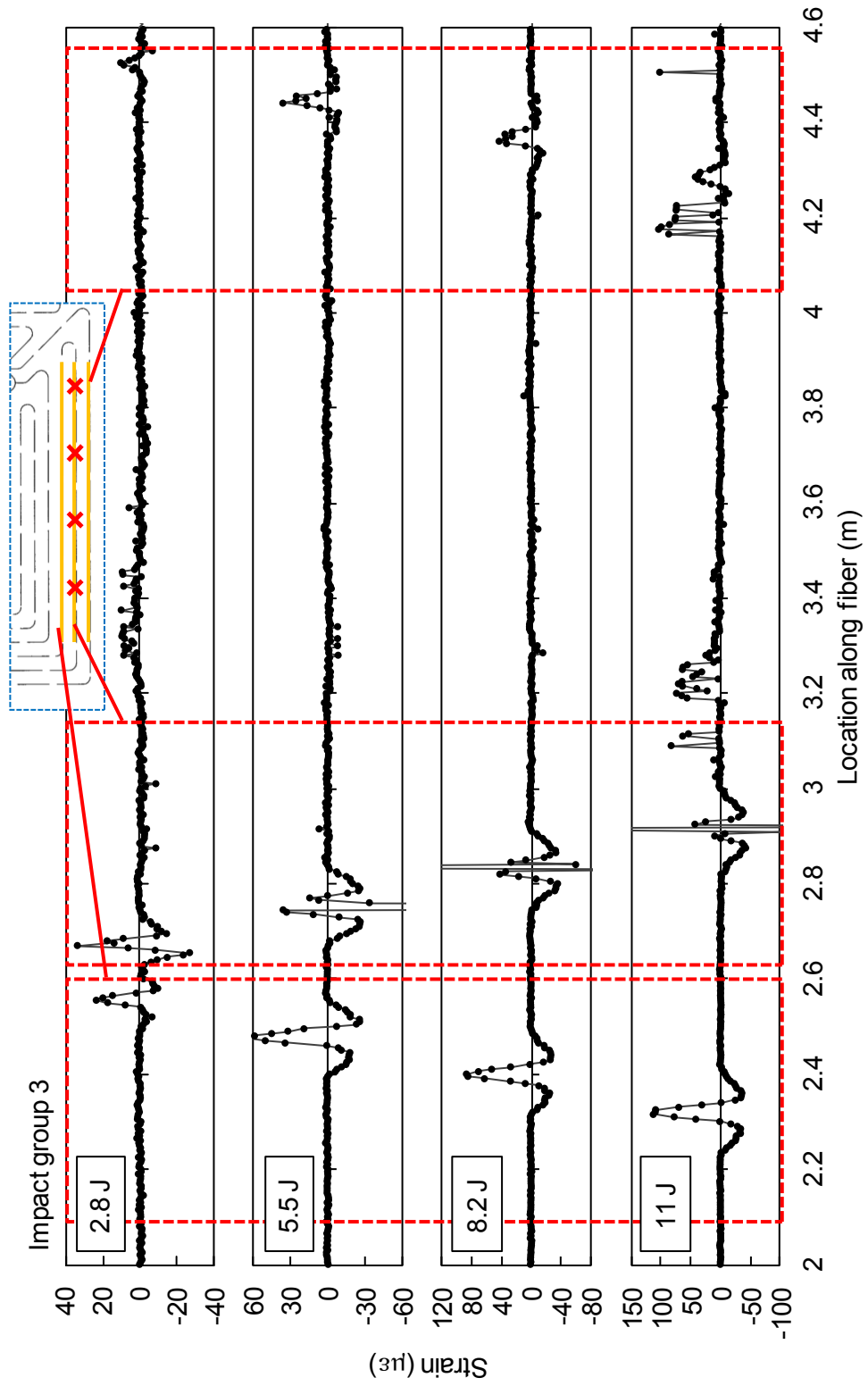


Figure C.3 Residual strain distributions for impact group 3 on the taper region.

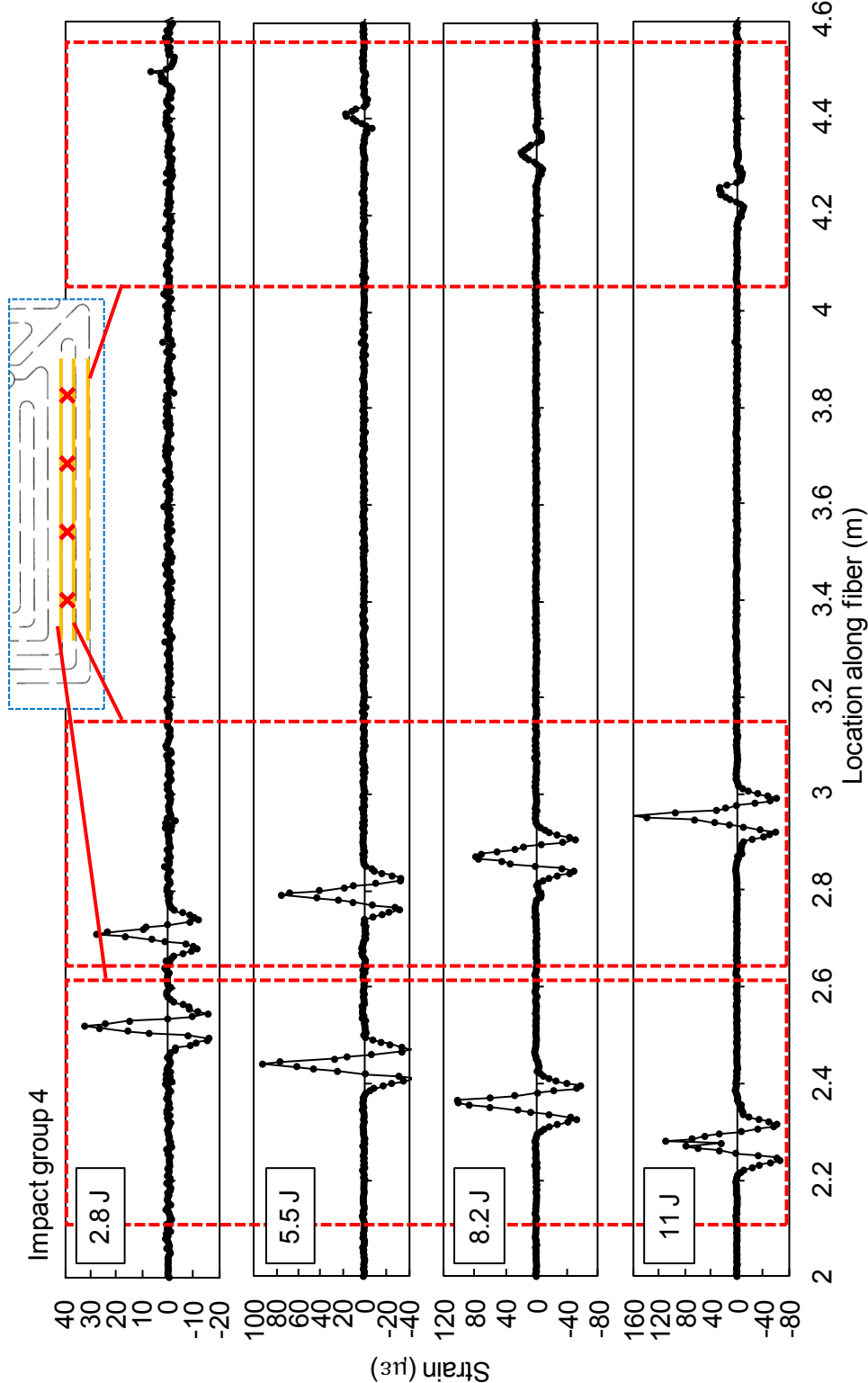


Figure C.4 Residual strain distributions for impact group 4 on the taper region.

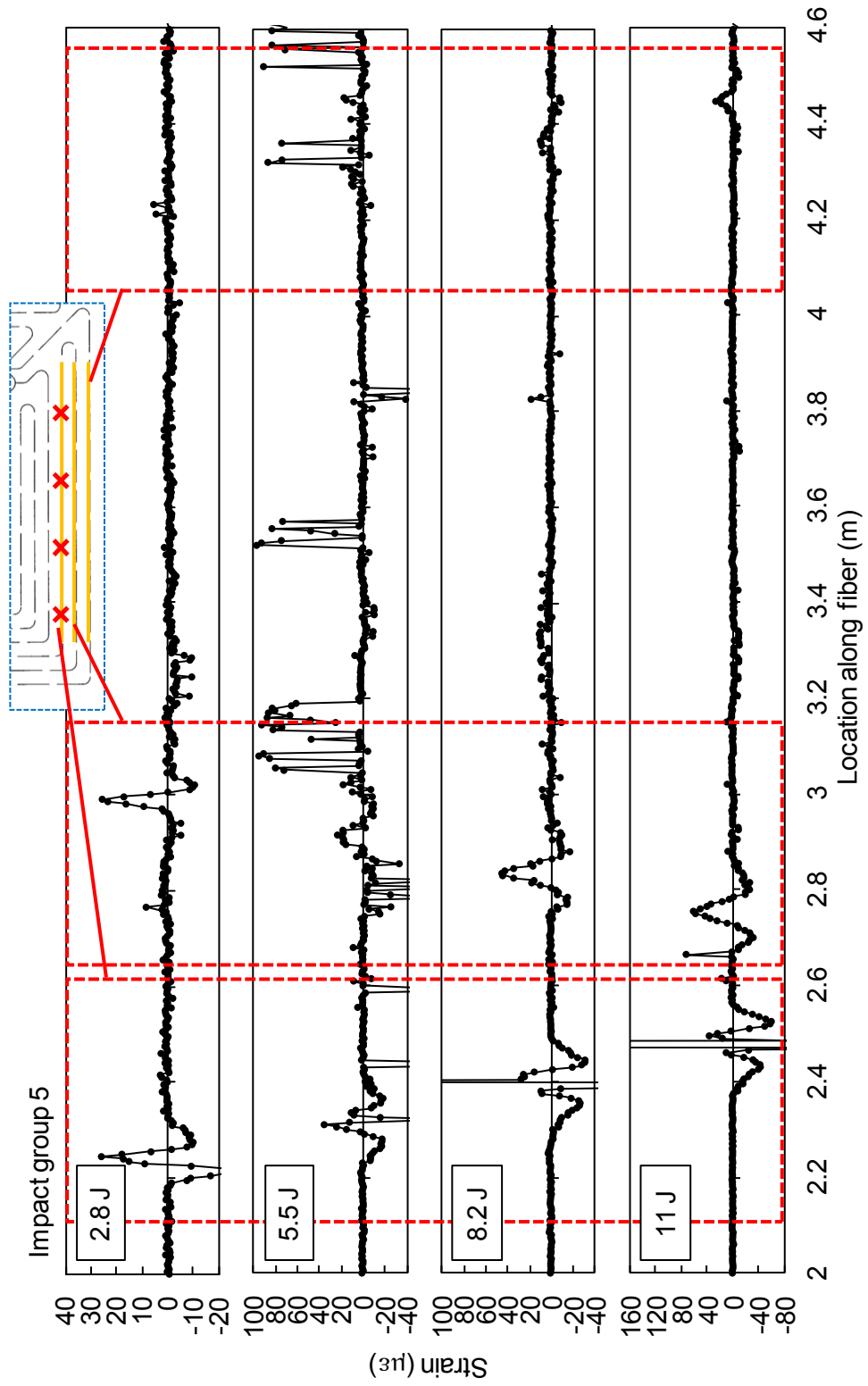


Figure C.5 Residual strain distributions for impact group 5 on the taper region.

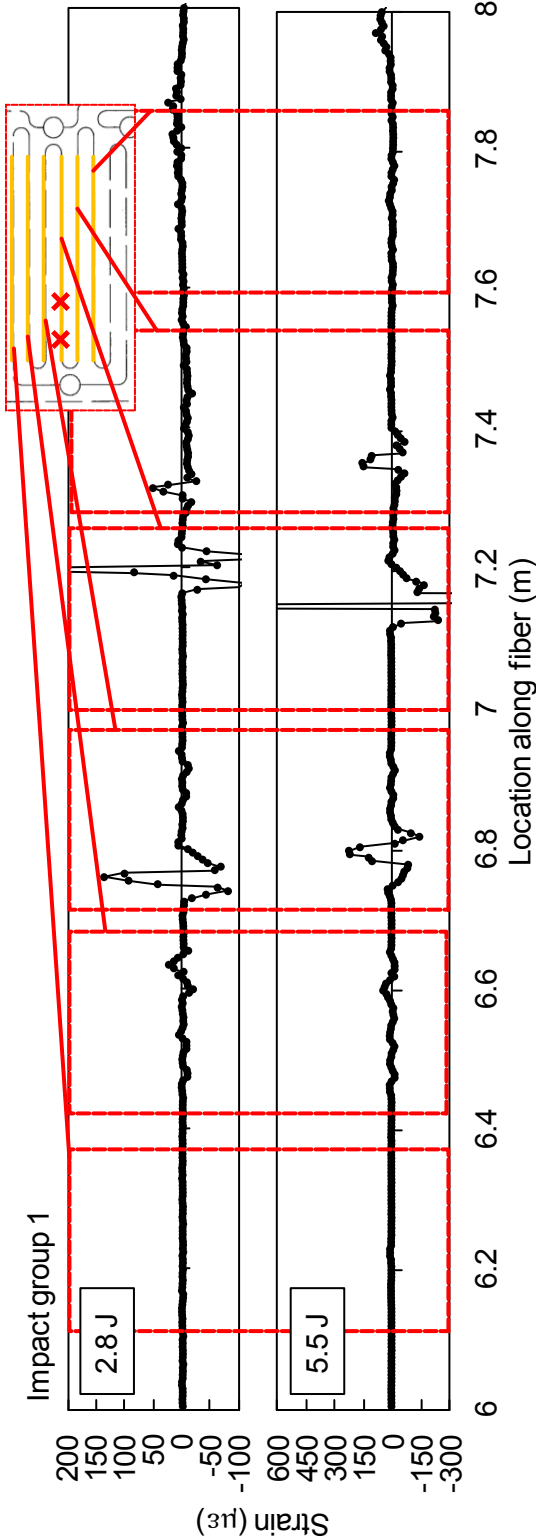


Figure C.6 Residual strain distributions for impact group 1 on the mid region.

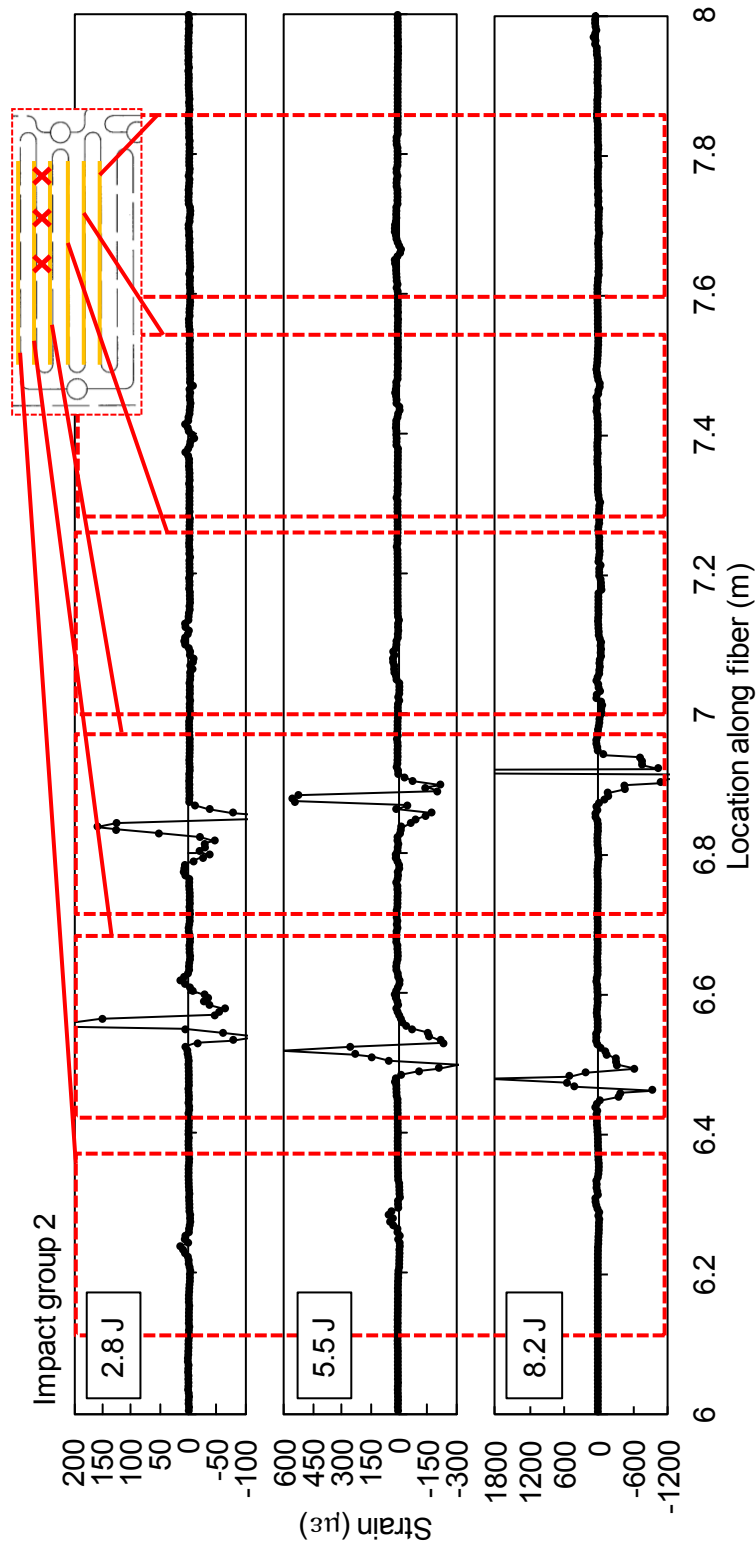


Figure C.7 Residual strain distributions for impact group 2 on the mid region.

## Acknowledgements

My time at the Smart Composite Systems Laboratory at the University of Tokyo has been a great and invaluable experience. During this time I have met many new people while facing new challenges and learning something new every day. I would like to express my gratitude to all those who have been involved.

I would like to express my deepest gratitude to Professor Nobuo Takeda for giving the opportunity to work on this research and for providing a supporting environment to work at. His continuous support and encouraging advice that always inspired to keep moving forward are very much appreciated.

I am also grateful to Dr. Shu Minakuchi for his support. His knowledge, advice and suggestions have been of great help throughout this study.

I would like to thank Dr. Tadahito Mizutani of JAXA for providing access to the LUNA OBR strain monitoring system used in the monitoring part of this thesis.

Assistance of Mr. Kento Kikuchi and Mr. Naoya Sakurayama during the experiments was also greatly appreciated.

I am also thankful to the members of the examination board Professor Kojiro Suzuki, Professor Kimiya Komurasaki, Professor Toshio Ogasawara and Associate Professor Tomohiro Yokozeki for their comments and advice during my final preparations.

Furthermore, I would like to extend my thanks to my fellow doctoral course students over these years: Mr. Sangchul Park, Mr. Takeaki Nadabe, Dr. Yusaku Ito and Dr. Terumasa Tsuda for their support, advice on various topics, and interesting discussions about nearly anything. I am grateful to have been surrounded by such friendly people.

Days working and studying at the laboratory were long but never boring, thanks to all the members of the laboratory and other friends at the campus over the years. I would therefore like to offer special thanks to my fellow students and friends who have made life in Kashiwa truly enjoyable.

Finally, I would like to thank my parents and my brother for their support and understanding throughout the years. They have allowed me to explore new opportunities and to find my own path in life. I could not have made it this far without them.

Kashiwa, December 2013

Juho Siivola